UNIVERSITY OF SOUTHAMPTON

FACULTY OF ENGINEERING, SCIENCE AND MATHEMATICS

School of Engineering Sciences

Accurate Aeroacoustic Measurements in Closed-Section Hard-Walled Wind Tunnels

by

Benjamin A. Fenech

A thesis submitted for the degree of Doctor of Philosophy

June 2009

UNIVERSITY OF SOUTHAMPTON

ABSTRACT

FACULTY OF ENGINEERING, SCIENCE AND MATHEMATICS
SCHOOL OF ENGINEERING SCIENCES

Doctor of Philosophy

Accurate Aeroacoustic Measurements in Closed-Section Hard-Walled Wind Tunnels

by Benjamin A. Fenech

Noise emissions from aircraft are of major concern to aircraft manufacturers. There are various analytical, empirical and numerical tools to help in the design of quieter aircraft, however aeroacoustic measurements in wind tunnels are still required. There is a growing interest in simultaneous aerodynamic and aeroacoustic measurements in hard-walled closed-section wind tunnels. The research hypothesis of this work is whether accurate aeroacoustic measurements are possible in this type of wind tunnel. Two issues are of particular concern: the reverberant sound field and high background noise levels. De-reverberation, based on an Image Source Model (ISM), is proposed to tackle the first issue by incorporating the reflections in the focused beamformer. This technique is computationally fast and easy to implement. Source Power Integration and deconvolution techniques are shown to be still valid in de-reverberation. Measurements in a closed section wind tunnel have shown that an ISM gives a better estimate of the Green's functions, when compared to free-space Green's functions. Furthermore de-reverberation yielded more accurate source strength estimates from the beamformer. Qualitatively, deconvolved results were no different than when using free-space Green's functions. Simulations have shown that the ISM can become unstable at high frequencies if position errors are present. It is therefore recommended to limit the application of the ISM to frequencies below 10 kHz. At low frequencies the accuracy of beamforming levels is highly dependant on the level of noise contamination of the input data. Removing the diagonal of the cross spectral matrix might not be sufficient to eliminate this noise.

Table of Contents

Abstract **i**

List of Figures **v**

List of Tables **viii**

Acknowledgements **ix**

Nomenclature **x**

1 Introduction **1**
1.1 Research Hypothesis 4

2 Beamforming **6**
2.1 Discrete Spatial Sampling of a Finite Size Array 6
2.2 Delay and Sum Beamforming 9
2.3 The Focused Beamformer 11
2.4 The Point Spread Function 16
2.5 Practical Limitations 19
2.6 CSM Diagonal removal 22
2.7 Advanced Techniques 24
2.7.1 Analysis of the Wavenumber Spectrum 24
2.7.2 Deconvolution 25
2.8 Levels from Beamforming 31
2.8.1 Source Power Integration 33
2.8.2 Effect of CSM Diagonal Removal on SPI 34
2.8.3 Levels from CLEAN-SC 37
2.9 Inverse Methods 38
2.9.1 Singular Value Decomposition and the Condition Number . 40
2.9.2 Regularisation Techniques 42
2.9.3 Sensitivity to Errors 46
2.10 Summary 47

3 De-Reverberation **49**
3.1 Analytical Methods 52
3.2 Numerical Methods 55

3.3 Experimental Methods . . . 57
3.3.1 Conventional Sources . . . 57
3.3.2 Impulse Tests . . . 59
3.3.3 Alternative methods . . . 62
3.4 Summary . . . 63

4 The Image Source Model 64
4.1 The Point Spread Function when using an ISM . . . 65
4.1.1 Effect on Source Power Integration . . . 67
4.2 Validating the Image Source Model . . . 69
4.3 Sensitivity to Errors . . . 73
4.3.1 Effectiveness of CSM Diagonal Removal . . . 75
4.3.2 De-reverberation . . . 77
4.4 Summary . . . 81

5 Beamforming with De-Reverberation 82
5.1 Experimental Setup . . . 83
5.1.1 Wind Tunnel . . . 83
5.1.2 Calibration Source . . . 83
5.1.3 Cavity Model . . . 86
5.1.4 Microphone Array and Ancillary Hardware . . . 86
5.1.5 Microphone Array Calibration . . . 90
5.2 Post Processing . . . 90
5.3 Image Source Model . . . 91
5.4 Results . . . 91
5.4.1 De-reverberation . . . 92
5.4.2 Levels from SPI and CLEAN-SC . . . 97
5.4.3 Effect of SPI threshold . . . 99
5.4.4 Effect of flow on de-reverberation . . . 100
5.4.5 Effectiveness of CSM diagonal removal . . . 102
5.4.6 Effect of partially lining the wind tunnel test section . . . 104
5.5 Realistic Sources . . . 111
5.6 Summary . . . 112

6 Conclusions 113
6.1 Recommended future work . . . 117

A SotonArray System 119
A.1 The Microphone Array . . . 119
A.1.1 Microphone Choice . . . 119
A.1.2 Sensor Distribution . . . 121
A.1.3 Array design for the 2.1×1.5 m wind tunnel . . . 126
A.1.4 Array Calibration . . . 133
A.2 Wind Tunnel Duct Liner . . . 135
A.3 Data Acquisition and Processing . . . 136

A.4 Post Processing 137
A.5 Benchmarking 139

B Challenges of implementing Impulse Response Measurements 141
B.1 Impulse Responses 141
B.2 Issues with the Measurements 143
B.3 PSF and SPI when using the measured Impulse Responses 147

C Additional Beamforming Plots 150

D Publications 163

References 164

List of Figures

2.1 Plane wave impinging on line transducer. 7
2.2 Rectangular aperture function 8
2.3 Pattern function of discrete line array 9
2.4 The focused beamformer as a digital filter 12
2.5 Schematic of beamforming planes. 16
2.6 PSF of a 56 microphone array. 18
2.7 Effect of recessing the microphone array 21
2.8 Recessing of the individual microphones in an array 21
2.9 Effectiveness of BiCLean algorithm. 26
2.10 CLEAN-SC vs. CLEAN and DAMAS 32
2.11 PSF for the CSM with Diagonal Removal 36
2.12 Simple source-receiver arrangement: 2 line arrays 44
2.13 Reconstruction of source strengths using Tikhonov regularisation . . 45
2.14 Sensitivity of inverse method to errors in pressure 46
2.15 Sensitivity of inverse method to errors in input parameters 47

3.1 Beamformer errors in a semi-reverberant environment 50
3.2 Correspondence between predicted and measured steering vectors . 51
3.3 Images sources for an infinitely long duct 53
3.4 Image source model output 54
3.5 Green's functions measurement schematic 58
3.6 Directivity of a pseudo-impulsive source 62
3.7 Green's function measurements using secondary sources 63

4.1 PSF using an ISM, 2.1×1.5 m wind tunnel 66
4.2 PSF using an ISM, 4.2×3 m wind tunnel 68
4.3 Green's function measurement setup - photo 1 70
4.4 Green's function measurement setup - photo 2 71
4.5 Green's function measurement setup - schematic 71
4.6 Measured and predicted Green's functions 72
4.7 Schematic of geometry for beamforming simulations. 74
4.8 Effect of CSM DR – high noise levels 76
4.9 Effect of CSM DR – low noise levels 77
4.10 Sensitivity of CSM DR to errors in source position 77
4.11 Errors from reverberant field, low noise levels 78
4.12 Errors from reverberant field, high noise levels 79

4.13 Beamforming errors for a position error of 0.01 m 80

5.1 KA558 calibration source. 84
5.2 Measured directivity of the calibration source 87
5.3 Calibration source centred in cavity model 88
5.4 Cavity model in wind tunnel. Downstream view. 88
5.5 Cavity model in wind tunnel. Array view. 89
5.6 Schematic representation of ISM-1.5 and ISM-0.8 91
5.7 Levels: comparison of free-space with ISM-1.5 93
5.8 Levels: comparison of free-space with ISM-0.8 95
5.9 BF maps: Conventional BF, no flow, ISM-1.5 96
5.10 Narrowband power spectrum of source estimated from beamforming 97
5.11 Levels: SPI vs. CLEAN-SC; source centred 98
5.12 Spectra: SPI with and without threshold, CLEAN-SC 100
5.13 Levels: effect of flow, conventional BF and ISM 101
5.14 Levels: effect of CSM diagonal removal 103
5.15 Spectra with and without flow; SPI and CLEAN-SC 104
5.16 BF maps: Conventional BF, flow, full CSM 105
5.17 BF maps: Conventional BF, flow, CSM with DR 106
5.18 BF maps: CLEAN-SC, flow, full CSM 107
5.19 Levels: effect of absorbing liner, no flow 108
5.20 Levels: effect of absorbing liner, flow at 30m/s 110

A.1 Array azimuthal and solid collection angles 122
A.2 Effect of array size on measured spectra 123
A.3 Co-arrays of a square and circular array 125
A.4 Multi-arm logarithmic spiral array 126
A.5 7×9 array 127
A.6 9×7 array 127
A.7 PSFs of chosen array at 2.5 kHz 128
A.8 PSFs of chosen array at 8 kHz 129
A.9 PSF source behind scan plane, f=2.5kHz 129
A.10 PSF source behind scan plane, f=8kHz 130
A.11 Beamforming plots of point source from measured data. 131
A.12 Concentrating sensors away from centre 132
A.13 PSF square and circular arrays 133
A.14 Absorption coefficient of duct liner 136
A.15 SotonArray – CSM 138
A.16 SotonArray – Beamforming 140

B.1 Impulsive source triggering device 142
B.2 Measured impulse response – time domain 144
B.3 Artifact in measured impulse 144
B.4 Impulse response: original and reconstructed 145
B.5 Impulse in time domain: repetitions 145

B.6 Smoothed Impulse Responses 146
B.7 Impulse duration vs. microphone number and trial number 146
B.8 PSF for Impulse Measurements 148

C.1 Calibration source: Conventional BF, free space 151
C.2 Calibration source: CLEAN, free space 152
C.3 Calibration source: CLEAN-SC, free space 153
C.4 Calibration source: Conventional BF, ISM-1.5 154
C.5 Calibration source: CLEAN, ISM-1.5 155
C.6 Calibration source: CLEAN-SC, ISM-1.5 156
C.7 Calibration source: Conventional BF, ISM-0.8 157
C.8 Calibration source: CLEAN, ISM-0.8 158
C.9 Calibration source: CLEAN-SC, ISM-0.8 159
C.10 Calibration source: Conventional BF, Impulse 160
C.11 Calibration source: CLEAN, Impulse 161
C.12 Calibration source: CLEAN-SC, Impulse 162

List of Tables

2.1 Effectiveness of Source Power Integration. 34
2.2 Effectiveness of Source Power Integration with threshold. 35

4.1 SPI applied to de-reverberation 69

5.1 Sound Power of the calibration source 85

B.1 SPI for Impulse Measurements 149

Acknowledgements

Various people have contributed to this research project. In particular I would like to express my thanks to

- Dr. Kenji Takeda, my PhD supervisor, for his excellent guidance and for keeping things in perspective;
- my PhD advisor Professor Phil Nelson, together with Dr. Keith Holland and Dr. Pieter Sijtsma for plenty of recommendations that have significantly improved the scientific quality of this work;
- Dr. Malcolm Smith from ISVR Consulting for his interest in this work, especially throughout the early stages;
- my fellow colleagues within the Aerodynamics and Flight Mechanics Group and ISVR, in particular Matthew Spiteri, Koen Boorsma and Alexander Carballo Crespo for providing plenty of food for thought;
- Mike Tudor-Pole, wind tunnel technician, for his constant willingness to help; and
- David Johnson-Newell, Airbus-UK, for his interest and feedback from an industrial perspective.

I would also like to acknowledge the small yet significant contributions from people I have met during conferences and project meetings, whose feedback has helped shape this research. In particular I would like to mention professors Louis Cattafesta and Mark Sheplak from the University of Florida, and professor Finn Jacobsen from the Technical University of Denmark.

Finally I would like to thank my loved ones, for their continued support.

Nomenclature

β	Tikhonov regularisation parameter
γ	signal-to-noise ratio
δ	Dirac-delta function
θ	arrival angle
θ_{DA}	array solid collection angle
λ	acoustic wavelength
σ	singular value
Σ	matrix of singular values used in Singular Value Decomposition
ω	angular frequency
C	normalisation factor in the Source Power Integration method
c_0	speed of sound in air
$\mathbf{D}$	Degraded CSM in CLEAN, CLEAN-SC
G	Green's function
$\mathbf{g}$	vector of Green's functions
H_1	Frequency response function
J	cost function
k	acoustic wavenumber
$\vec{M}$	Mach number of flow
M	total number of array sensors

n	noise component
$\mathbf{n}$	vector of noise components
O	order number of Image Source Model
p	acoustic pressure
p	output from microphone
Q	source strength
r	radial distance (scalar)
S	total number of sources included in the inverse method
s	signal incident on microphone due to true source
S_{pp}	Cross Spectral Matrix of sensor outputs (CSM)
Δt_0	time delay due to sound propagation
$\Delta t_{0,c}$	time delay due to convected sound propagation
$\vec{U}$	mean flow velocity
w	weighting function
$\mathbf{w}$	microphone weight vectors
$\mathbf{W}_{\text{opt}}$	optimum filter matrix for inverse method
$\mathbf{w}_{\text{opt}}$	optimum filter vector for focused beamformer
$\vec{x}_m$	vector location of mth microphone
$\vec{y}_0$	vector location of point source
$\vec{y}_p$	vector location of grid point
$(\cdot)^*$	complex conjugate
d	differential operator
$E[\cdot]$	expectation operator
e	exponential operator
$[\cdot]^\dagger$	Hermitian transpose (complex conjugate transpose)

i	imaginary unit
$\kappa(\cdot)$	condition number
$[\cdot]^T$	matrix transpose
$\tilde{(\cdot)}$	transformation in the spatial domain
$\langle\cdot\rangle$	time average
$\mathrm{Tr}(\cdot)$	trace of matrix

Chapter 1

Introduction

Noise emissions from aircraft have become a major factor that can limit growth in the air transportation industry. Communities living near airports are becoming increasingly aware of noise disturbance and its effect on their quality of life, and new legislation has given them more say and more power to take legal action. Pressure builds up on airport operators and airline carriers, who in turn put pressure on certification authorities and airframe and aircraft propulsion manufacturers to produce and operate quieter designs.

Noise from present aircraft is significantly lower than from aircraft manufactured a few decades ago, mostly due to noise reduction technologies applied to propulsion systems. This has made the contribution of airframe noise to the overall noise emissions significant, especially on approach. Features such as slats, flaps and landing gear have been identified as major noise sources. A lot of research has been commissioned to produce quieter designs, and strict noise requirements are being integrated from the very early design stages of a product development cycle. Numerical tools such as Computational Fluid Dynamics (CFD) and Computational Aeroacoustics (CAA) have become indispensable to optimise component design for lower noise emissions. However aeroacoustic measurements are still required to verify predictions, and in the case of complex geometries, measurements are the only reliable analysis tool available to date.

Aeroacoustic measurements tend to be carried out in the same controlled environment used for aerodynamic measurements, i.e. the wind-tunnel. The biggest challenge for any type of acoustic measurement in a wind tunnel is to separate the sources of interest from the high background noise levels present in such an environment. In most cases, single microphone measurements yield very limited

results because of poor signal-to-noise ratios; furthermore it is impossible to identify where the noise is being generated.

The first major breakthrough in aeroacoustic measurements in wind tunnels was achieved by borrowing the concept of the lens from optics. The "acoustic mirror" was thus developed [1], where a microphone is mounted at one of the two foci of an elliptic dish and the arrangement is positioned in such a way that the suspected noise source is at the other focus. Background noise is therefore suppressed, and the arrangement can be used for source localisation purposes [2]. The biggest disadvantage is that it requires physical movement of often large measuring setups, implying very long data acquisition times and expensive mechanical systems. Moreover, the acoustic mirror cannot be used for unobtrusive measurements in closed-section wind tunnels.

In the last decade, the interest has shifted onto arrays of sensors which can be "steered" electronically using post-processing techniques. The same principle still applies: the array can reject background noise by "listening" only to a particular direction or point in space. These kind of arrays of sensors have been in use for a number of years in various disciplines including astronomy, seismology and sonar [3]. Besides the ability to suppress background noise, a microphone array gives the possibility to "scan" an aircraft body and identify noise-generating regions. The key advantage of such a phased array is that there is no mechanical movement of the setup, and if the sensors are all in a flat plane, the array can be flush-mounted in a boundary of a closed-section wind tunnel. Using arrays of sensors used to be prohibitively expensive (the total cost scales with the channel count of the system, and depends not only on the sensors, but also on the data acquisition systems and the related hardware for processing and storing the large amounts of data generated). Luckily the price of computing power and data storage continues to fall, which means that arrays are becoming increasingly affordable to industry and research institutions. Assuming that one invests in an array with the highest possible channel count that the budget allows, the focus is on using the post-processing technique which yields the most useful amount of information from the same set of data.

The first successful instances of aeroacoustic measurements using microphone arrays that are recorded in literature were performed in large, open-jet facilities, where the microphone array could be situated out of the flow, and the test section boundaries could be acoustically treated to reduce background noise levels and reflections [2, 4, 5]. However more recent work has identified a significant

problem with this kind of environment. Sound propagating through the jet shear layer suffers from coherence loss, thereby degrading the quality of the aeroacoustic measurements, especially at high frequencies [6]. There are also physical limitations: open jet wind tunnels cannot be pressurised to simulate realistic Reynolds numbers, and building and running these facilities can be more costly compared to closed section wind tunnels. Furthermore, an open-jet facility is not an ideal environment to make aerodynamic measurements, since the flow jet is bound by a "soft" shear layer, rather than a hard rigid boundary. This gives rise to uncertainties in the actual testing parameters that are hard to quantify. Therefore routine aerodynamic tests during an aircraft development cycle would still have to be performed in closed section wind tunnels. It would be ideal if the latter environment could be used for both aerodynamic and aeroacoustic testing.

This has led to an increased interest in the last few years in microphone array measurements in closed section wind tunnels [6, 7, 8, 9]. If the microphone array is flush-mounted in a test section boundary, the aeroacoustic measurement system becomes completely unobtrusive, and enables back-to-back aeroacoustic and aerodynamic testing. This can have a dramatic advantage in terms of cost and time. Closed-section wind tunnels also allow for shorter setup times, quick model configurations changes and in most cases shorter distances between array and model (taking advantage of a better array resolution). The challenges in this case are significantly higher background noise levels, a highly reverberant sound field, and microphones in contact with the turbulent boundary layer.

With the current state of the art techniques, and with a sufficiently high number of microphones to counteract the higher background noise levels, aeroacoustic measurements in closed-section wind tunnels can give similar qualitative results to measurements in open jet tunnels [6]. For many, the biggest concern is the accuracy of the beamforming levels obtained from a closed test section. This is a justified preoccupation, given that for example, flush-mounted microphones are subjected to levels that are up to 50 dB higher [10] than their out-of-flow open-jet equivalents. Also of concern is the highly-reverberant nature of a typical hard-walled closed section wind tunnel, since the large number of reflections in the test section gives rise to additional image sources and a build-up of energy that can lead to inaccurate source strength estimates.

1.1 Research Hypothesis

This research project aims at answering the question "Is it possible to perform accurate aeroacoustic measurements in hard-walled closed-section wind tunnels?". The underlying theory behind the post beamforming is discussed first in Chapter 2. In particular, the beamformer is shown to be a spatial filter that accepts sound coming from a particular direction or location in space. Practical limitations give rise to inherent limitations in this technique, namely poor resolution at low frequencies and spatial noise at high frequencies. However recent advances in deconvolution techniques, such as DAMAS and all its variants [11], CLEAN and CLEAN-SC [12] means that these issues are no longer of particular concern. Quantitative results can be extracted from beamforming maps using the Source Power Integration technique [4]. Low-frequency noise can be removed by decomposing the cross spectral matrix of measured pressures [13]. For closed section wind tunnels there are two further issues: the noise due to the turbulent boundary layer and the reverberant field. The former has been traditionally dealt with by removing the diagonal of the cross spectral matrix of measured pressures. This works if the noise is uncorrelated over the array microphones. The reverberant field was shown to have an influence on the beamforming results, and some preliminary work was done by Guidati et al. [14] and Sijtsma and Holthusen [15] to correct for this. However their work does not quantify the absolute contribution of the test section boundaries to the beamforming levels. The aim of this work is to determine to what extent the reflections affect the beamforming levels by building on this previous work. A de-reverberation technique is proposed to correct for the influence of these reflections, and is designed to be easily integrated in beamforming.

In Chapter 3 various techniques that can be used to de-reverberate the measurement environment are developed and discussed. These techniques include analytical, numerical and experimental methods. In Chapter 4 one of the techniques proposed, de-reverberation using an Image Source Model, is investigated in more detail using both simulations and measurements. Finally, in Chapter 5 the de-reverberation technique is validated using a calibration source of known sound power. The same chapter includes a discussion on the implications of using de-reverberation for a more complex and realistic distribution of sources. The main conclusions are then summarised in Chapter 6, together with recommended future work.

A significant part of this research project involved the design of a microphone

array system which could be used for the experimental validations. An overview of this system can be found in Appendix A. Appendix B describes an attempt to quantify transfer functions in a hard-walled test section using measured impulse responses, which was of limited success. Appendix C includes a number of plots that compliment the results presented in Chapter 5.

Chapter 2

Beamforming

Aeroacoustic measurements in hard-walled wind tunnels are normally carried out using an array of microphones. The acquired data is then processed using a beamforming algorithm. The first part of this chapter describes the underlying theory of beamforming. Implementing beamforming with data measured in a real environment gives rise to a number of issues, and a number of techniques have been proposed in literature to enhance and extend the applicability of beamforming. These techniques will be discussed in detail in the second part of this chapter.

2.1 Implications of Discrete Spatial Sampling of a Finite Size Array

One of the most advantageous capabilities of an array of sensors is that it can be focused or "steered" to a particular direction or location in space. Before investigating how this is done, it is worth investigating the implications of using an array of sensors first; in particular the implications of using an array of finite size sampled by a discrete number of sensors. For the sake of simplicity the initial arguments will be applied to a one-dimensional array, however the same reasoning can be extended to two dimensions. A more in-depth analysis can be found in Nelson [16].

Consider a harmonic acoustic plane wave with wavenumber $k = \omega/c_0 = 2\pi/\lambda$, where ω is the angular frequency, c_0 is the speed of sound and λ is the acoustic wavelength, impinging on a hypothetical line transducer at an angle of incidence

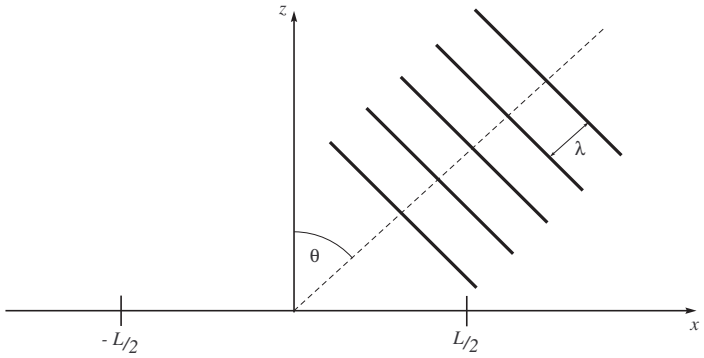

FIGURE 2.1: A harmonic acoustic planar wave impinging on a hypothetical line transducer.

θ, as shown in figure 2.1. If the transducer is of infinite length, the output is:

$$W(\theta) = \int_{-\infty}^{\infty} w(x)\, p(x)\, \mathrm{d}x, \tag{2.1}$$

where p is the acoustic pressure, given by $p(x) = \mathrm{e}^{\mathrm{i}k\sin(\theta)x} = \mathrm{e}^{\mathrm{i}k_x x}$, and w is a weighting function. k_x is frequently referred to as the trace wavenumber. Equation 2.1 can be rewritten as

$$W(k_x) = \int_{-\infty}^{\infty} w(x)\, \mathrm{e}^{\mathrm{i}k_x x}\mathrm{d}x, \tag{2.2}$$

in order to emphasise the dependence on k_x.

The simplest choice for the weighting function w is in the form of a rectangular aperture window, which effectively limits the transducer to a finite length L,

$$w(x) = \begin{cases} 1/L & -L/2 \leq x \leq L/2 \\ 0 & \text{elsewhere.} \end{cases} \tag{2.3}$$

Inserting into equation 2.2 and evaluating the integral yields [16]

$$W(k_x) = \frac{\sin\left[\left(\frac{kL}{2}\right)\sin(\theta)\right]}{\left(\frac{kL}{2}\right)\sin(\theta)}, \tag{2.4}$$

which is a sinc function with a characteristic shape shown in figure 2.2. The first zero crossings of this sinc function are given by $(kL/2)\sin\theta = \pm\pi$, and thus the range of angles for which the output from the transducer is non zero is given by

$$\theta_B = \pm\sin^{-1}\left(\frac{\lambda}{L}\right) \approx \pm\frac{\lambda}{L} \qquad \text{for } \lambda << L. \tag{2.5}$$

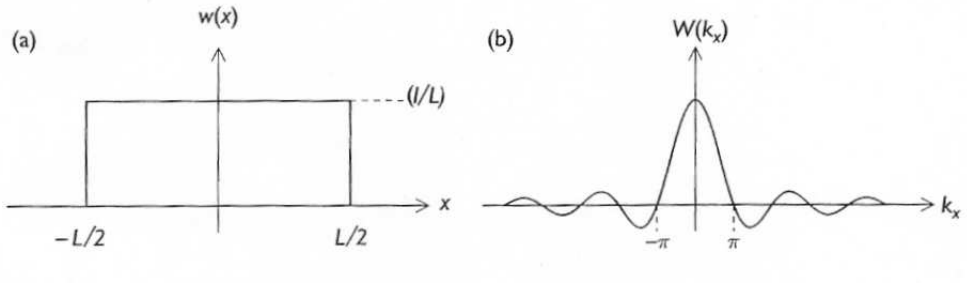

FIGURE 2.2: (a) The rectangular aperture function and (b) the corresponding spatial Fourier transform. From ref. [16].

This means that within the range of angles $-\lambda/L < \theta_B < \lambda/L$ the transducer will yield a non-zero output, even if the incoming wave is at a single angle θ. This range defines the width of the mainlobe of the line transducer. The width of the mainlobe is inversely proportional to the length of the transducer L, so that the smaller L, the wider the mainlobe and the more difficult it becomes to discriminate between arrival angles.

The transducer can be "steered" to be selective to sound impinging from a particular angular location θ_0 by defining the weighting function

$$w_s(x) = w(x)\,\mathrm{e}^{-\mathrm{i}k_0 x}, \tag{2.6}$$

where $k_0 = k\sin\theta_0$. This effectively shifts the spatial Fourier transform along the k_x-axis by an amount k_0, such that the mainlobe can capture the energy impinging from this angle.

The second limitation to be imposed is that of discrete spatial sampling, i.e. having a finite number of sensors rather than a continuous one. It can be shown that the Fourier transform of the aperture function associated with an array of discrete transducers spaced Δx apart can be written as [16]

$$W\left(\mathrm{e}^{\mathrm{i}k_x\Delta x}\right) = \frac{1}{M}\frac{\sin\left[\left(kM\dfrac{\Delta x}{2}\right)\sin\theta\right]}{\sin\left[\left(k\dfrac{\Delta x}{2}\right)\sin\theta\right]}, \tag{2.7}$$

where M is the total number of sensors. The Fourier transform repeats at integer multiples of the spatial sampling frequency $2\pi/\Delta x$. Figure 2.3 shows polar plots of $W\left(\mathrm{e}^{\mathrm{i}k_x\Delta x}\right)$ as a function of θ, for different inter-sensor spacings. Once Δx exceeds half a wavelength, the directional response of the array is no longer dominated by

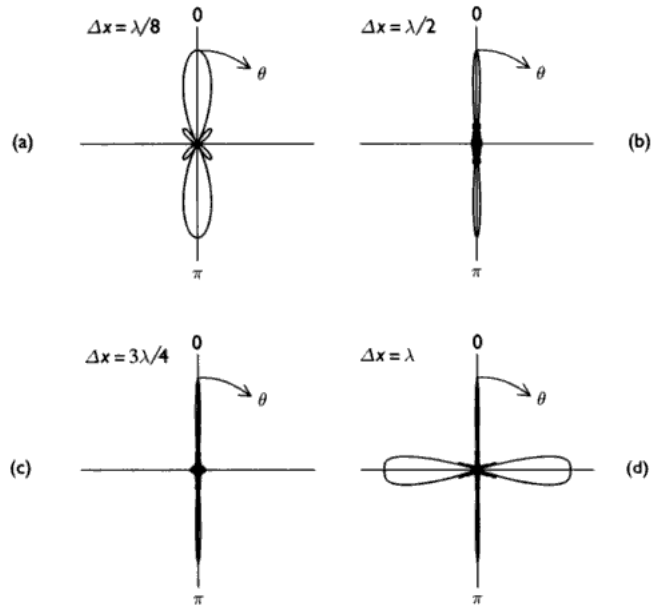

FIGURE 2.3: The pattern function of a discrete line array of sensors, as given in eq. 2.7, for four different inter-sensor spacing Δx. From ref. [16].

the mainlobe: a number of sidelobes are produced. This phenomenon is often referred to as "spatial aliasing", and is analogous to temporal aliasing if the Nyquist criterion is not satisfied.

Therefore an array of finite size and having a finite number of sensors will have two distinctive features: a mainlobe of finite width and a number of sidelobes. These features limit the array's performance in the lower and higher frequencies, respectively. The resulting effects for two-dimensional arrays, and ways how to minimise these negative aspects are discussed later on in this chapter.

2.2 Beamforming in the Time Domain – Delay and Sum Beamformer

The simplest post-processing technique that can be used to steer an array of sensors is delay-and-sum beamforming, which literally describes the concept of delaying a set of time signals by a predefined amount, and then summing all the signals together.

To illustrate the delay and sum concept, consider a signal $\sigma(t)$ emitted by a point source at $\vec{y}_0$. Several other sources may be present, and the combined wavefield

is denoted by $p(\vec{x}, t)$. Next, consider an array of M sensors located at $\{\vec{x}_m\}, m = 1, 2, ..., M$. The phase centre of the array is defined as the vector quantity $\sum \vec{x}_m$, and is conveniently chosen to coincide with the array centre,

$$\vec{0} = \sum_{m=1}^{M} \vec{x}_m. \tag{2.8}$$

Each sensor samples the wavefield spatially at the respective sensor location, and the waveform measured by the m^{th} sensor is $p_m(t) = p(\vec{x}_m, t)$. In delay-and-sum beamforming, a time delay Δ_m and amplitude weight w_m are applied to the output of each sensor, and then the resulting signals are added to give the beamformer's output signal:

$$y(t) \equiv \sum_{m=1}^{M} w_m p_m(t - \Delta_m). \tag{2.9}$$

w_m is often referred to as the array's shading or taper coefficient, and can be used to optimise the beamformer's beam shape, and to reduce sidelobe levels.

A source-receiver acoustic problem has the associated concepts of near and far fields.[1] Beamforming is no exception, and one can choose to focus the array's beam on signals propagating

i.) from a particular direction, denoted by the unit vector $\vec{\xi}_0$, or

ii.) from a particular point $\vec{y}_0$ in space.

The former applies when the source is in the far field, and the sound field at the sensor locations can be approximated by plane waves. The direction of propagation is approximately equal for each sensor. In this case beamforming can be used to locate this direction of propagation, but it is very difficult to locate the *exact* location of the source. On the other hand, when the source is located in the near-field, the wavefronts within the array's aperture are curved, and the wave propagation direction varies with sensor location. A set of unit propagation vectors $\left\{\vec{\xi}_{0,m}\right\} \quad m = 1, 2, ..., M$ is therefore defined as the direction from the source to the m^{th} sensor, together with $\vec{\xi}_0$, which, in this case, is defined at the array centre. For a nonrefractive medium straight-line propagation gives

$$\vec{\xi}_0 = \frac{-\vec{y}_0}{r_0}, \qquad \vec{\xi}_{0,m} = \frac{(\vec{x}_m - \vec{y}_0)}{r_{0,m}}, \tag{2.10}$$

[1] In ref. [17], the far-field is referred to as the Fraunhofer region, whereas the near-field is termed the Fresnel region.

where $r_0 = |\vec{y}_0|$ and $r_{0,m} = |\vec{y}_0 - \vec{x}_m|$.

The delay-and-sum technique can be used to "scan" an imaginary plane to locate areas with maximal output energy. The beamformer response is plotted as a contour map having a bandwidth and lobe structure. A maximum output is obtained when the focus location coincides with the source location. The process assumes that all the measurements are made in the presence of a distribution of small, spatially distinct, mutually independent point sources (monopoles). The presence of coherent or closely -spaced monopoles, dipoles, quadruples or continuously distributed sources results in variations in the noise field coherence, amplitude and phase within the array's aperture. Spatial variations of the source can cause moderate to severe errors in source amplitude, resolution and localisation. Phase variations are interpreted by the array as retarded time delays, resulting in localisation errors. Amplitude and coherence variations modify the relative contribution of each microphone to the array output. Such errors can be minimised by keeping the array's aperture small. The accurate localisation of source distribution depends on the smallest wavelength of interest.[4]

The advantage of delay-and-sum beamforming lies in its simplicity. There is no need to transform the data: the beamformer simply acts as a spatiotemporal filter that selectively passes waves propagating from a narrow range of directions or locations. This means that processing requirements are small; furthermore sources that vary with time can be investigated. The biggest drawback is that temporal averaging cannot be performed. This limits the applicability of the delay-and-sum beamformer in measuring environments prone to high levels of background noise contamination, such as closed-section wind tunnels. Furthermore, acoustic measurements are in general more informative if presented in the frequency domain.

2.3 Beamforming in the Frequency Domain – the Focused Beamformer

Delay-and-sum beamforming can be considered to be the simplest technique one can apply to array data. Further benefits can be achieved by performing a similar analysis in the frequency domain, where time delays are expressed as linear phase shifts. The preceding analysis was also "data independent", since no assumption was made on the nature of the time histories. In the following analysis, an isolated point source in space is considered. The main objective is to get an estimate of the

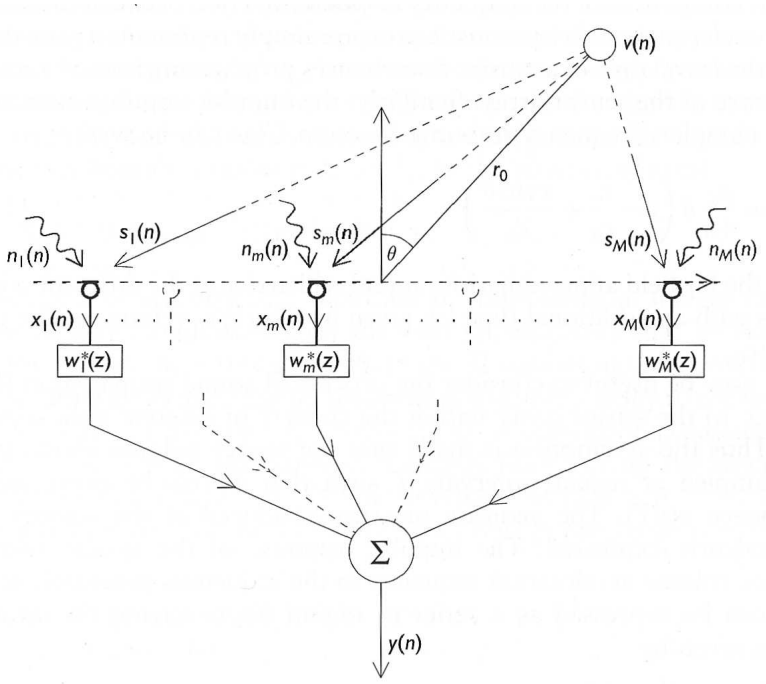

FIGURE 2.4: Schematic showing an array of M sensors and a single source. The signals at the sensors consist of the sound from the source (s_m) and noise n_m. The outputs from the sensors ($x_m = p_m$) are passed through digital filters w_m to give the beamformer output y. From ref. [16].

source strength of the source from the time histories recorded at the microphones, taking into account the presence of noise which might be contaminating the sensor data. Discrete sampling in space and time is assumed. Time varying quantities will be shown as a function of a discrete integer n; the dependence on a time interval T will be assumed but not shown. A more detailed analysis can be found in Nelson [16].

Figure 2.4 shows a schematic of the problem under consideration. A single point source with source strength $q(n)$ (depicted by $v(n)$ in figure 2.4) emits sound that propagates to an array of M microphones, resulting in a sound field $s_m(n)$ at the mth microphone. It is further assumed that the mth microphone is also subjected to a noise signal $n_m(n)$. The output from the mth microphone $p_m(n)$ (depicted as $x_m(n)$ in figure 2.4) can be expressed as a sum of these two signal components,

$$p_m(n) = s_m(n) + n_m(n)\,. \tag{2.11}$$

The Fourier transformed source strength is linked to the Fourier transformed source signal by the transfer function $G_m\left(\mathrm{e}^{\mathrm{i}\omega}\right)$. Thereby equation 2.11 can be

re-written in vector notation as:

$$\begin{aligned} \mathbf{p} &= \mathbf{s} + \mathbf{n} && (2.12)\\ &= q\left(\mathrm{e}^{\mathrm{i}\omega}\right)\mathbf{g} + \mathbf{n}, && (2.13) \end{aligned}$$

where the vectors $\mathbf{p}$, $\mathbf{g}$ and $\mathbf{n}$ are defined as

$$\begin{aligned} \mathbf{p}^T &= \left[P_1\left(\mathrm{e}^{\mathrm{i}\omega}\right), P_2\left(\mathrm{e}^{\mathrm{i}\omega}\right), \ldots, P_M\left(\mathrm{e}^{\mathrm{i}\omega}\right)\right] && (2.14)\\ \mathbf{g}^T &= \left[G_1\left(\mathrm{e}^{\mathrm{i}\omega}\right), G_2\left(\mathrm{e}^{\mathrm{i}\omega}\right), \ldots, G_M\left(\mathrm{e}^{\mathrm{i}\omega}\right)\right] && (2.15)\\ \mathbf{n}^T &= \left[N_1\left(\mathrm{e}^{\mathrm{i}\omega}\right), N_2\left(\mathrm{e}^{\mathrm{i}\omega}\right), \ldots, N_M\left(\mathrm{e}^{\mathrm{i}\omega}\right)\right]. && (2.16) \end{aligned}$$

In beamforming terminology, vector $\mathbf{g}$ is often called the "steering vector", since essentially it is this vector which steers the array to a particular point in space.

During the process of beamforming, the signals are passed through a digital filter with frequency response function $W^*\left(\mathrm{e}^{\mathrm{i}\omega}\right)$. The Fourier transformed output of the beamformer can also be expressed in vector notation,

$$Y\left(\mathrm{e}^{\mathrm{i}\omega}\right) = \mathbf{w}^\dagger \mathbf{p}, \tag{2.17}$$

where

$$\mathbf{w}^\dagger = \left[W_1^*\left(\mathrm{e}^{\mathrm{i}\omega}\right), W_2^*\left(\mathrm{e}^{\mathrm{i}\omega}\right), \ldots, W_M^*\left(\mathrm{e}^{\mathrm{i}\omega}\right)\right], \tag{2.18}$$

and $[\cdot]^\dagger$ denotes the complex conjugate transpose.

The optimum choice of $\mathbf{w}$ is that for which the beamformer output $Y\left(\mathrm{e}^{\mathrm{i}\omega}\right)$ is as close as possible to the actual source strength $q\left(\mathrm{e}^{\mathrm{i}\omega}\right)$. Using the least squares criterion, the cost function can be defined as

$$\begin{aligned} J &= E\left[\left|Y\left(\mathrm{e}^{\mathrm{i}\omega}\right) - q\left(\mathrm{e}^{\mathrm{i}\omega}\right)\right|^2\right]\\ &= E\left[\left(\mathbf{w}^\dagger\mathbf{p} - q\left(\mathrm{e}^{\mathrm{i}\omega}\right)\right)\left(\mathbf{w}^\dagger\mathbf{p} - q\left(\mathrm{e}^{\mathrm{i}\omega}\right)\right)^*\right], && (2.19) \end{aligned}$$

where $E[\cdot]$ is the expectation operator. Equation 2.19 can be expanded and simplified by introducing three quantities:

- $\mathbf{S}_{pp} = E\left[\mathbf{p}\mathbf{p}^\dagger\right]$, the matrix of cross spectra of the sensor outputs;
- $\mathbf{s}_{pq} = E\left[\mathbf{p}q^*\left(\mathrm{e}^{\mathrm{i}\omega}\right)\right]$, the vector of cross spectra between sensor outputs and source strength;
- $S_{qq} = E\left[q\left(\mathrm{e}^{\mathrm{i}\omega}\right)q^*\left(\mathrm{e}^{\mathrm{i}\omega}\right)\right]$, the power spectrum of the acoustic source strength,

thus giving

$$J = \mathbf{w}^{\dagger}\mathbf{S}_{pp}\mathbf{w} - \mathbf{w}^{\dagger}\mathbf{s}_{pq} - \mathbf{s}_{pq}^{\dagger}\mathbf{w} + S_{qq}. \tag{2.20}$$

This is optimised by choosing [16]

$$\mathbf{w}_{\text{opt}} = \mathbf{S}_{pp}^{-1}\mathbf{s}_{pq}. \tag{2.21}$$

Therefore the optimum choice for the filter $\mathbf{w}$ still requires some information about the source strength. Moreover, a matrix inversion is required.

$\mathbf{s}_{pq}$ can be expressed as $E\left[(\mathbf{s}+\mathbf{n})\,Q^{*}\left(\mathrm{e}^{\mathrm{i}\omega}\right)\right]$. If the noise is assumed to be uncorrelated with the signal, then this reduces to $\mathbf{s}_{pq} = \mathbf{g}S_{qq}$. Similarly, the cross spectrum matrix $\mathbf{S}_{pp}$ can be expanded to $S_{qq}\mathbf{g}\mathbf{g}^{\dagger} + \mathbf{S}_{nn}$, where $\mathbf{S}_{nn}$ is the cross spectral matrix of noise signals. The optimum filter can then be written as[16]

$$\mathbf{w}_{\text{opt}} = \left[S_{qq}\mathbf{g}\mathbf{g}^{\dagger} + \mathbf{S}_{nn}\right]^{-1}\mathbf{g}S_{qq}. \tag{2.22}$$

If it is also assumed that the noise signals at the sensors are uncorrelated with each other, the noise cross spectral matrix $\mathbf{S}_{nn}$ can be approximated by $S_{nn}\mathbf{I}$, and, by introducing the signal to noise ratio $\gamma = S_{nn}/S_{qq}$, equation 2.22 reduces to

$$\mathbf{w}_{\text{opt}} = \left[\mathbf{g}\mathbf{g}^{\dagger} + \gamma\mathbf{I}\right]^{-1}\mathbf{g}, \tag{2.23}$$

which can be shown [16] to be equal to

$$\mathbf{w}_{\text{opt}} = \left[\gamma + \mathbf{g}^{\dagger}\mathbf{g}\right]^{-1}\mathbf{g}. \tag{2.24}$$

In the particular case when no noise is present, $\gamma = 0$, and

$$\mathbf{w}_{\text{opt}} = \left[\mathbf{g}^{\dagger}\mathbf{g}\right]^{-1}\mathbf{g}. \tag{2.25}$$

For this special case, $\mathbf{w}_{\text{opt}}$ is easily computed, since *(a)* no *a priori* information is required about the acoustic source strength, and *(b)* no matrix inversions are involved, since the product in the squared brackets reduces to a single value.

Equation 2.25 can be inserted into equation 2.17 to yield the optimum beamformer output

$$Y_{\text{opt}}\left(\mathrm{e}^{\mathrm{i}\omega}\right) = \left[\mathbf{g}^{\dagger}\mathbf{g}\right]^{-1}\mathbf{g}^{\dagger}\mathbf{p}. \tag{2.26}$$

Most common aeroacoustic sources emit random noise with stationary statistical properties, which means that the magnitude and phase of q vary with time. In

this case, averaging the beamformer output Y_{opt} gives zero. Therefore mean square values are normally used, giving

$$\begin{aligned} Q_{\text{opt}} = \langle |Y_{\text{opt}}|^2 \rangle &= \frac{\mathbf{g}^\dagger < \mathbf{p}\mathbf{p}^\dagger > \mathbf{g}}{\left[\mathbf{g}^\dagger \mathbf{g}\right]^2} \\ &= \frac{\mathbf{g}^\dagger S_{\mathbf{pp}}\, \mathbf{g}}{\left[\mathbf{g}^\dagger \mathbf{g}\right]^2} = \mathbf{w}^\dagger \mathbf{S}_{\mathbf{pp}} \mathbf{w}, \end{aligned} \tag{2.27}$$

where $\langle \cdot \rangle$ denotes averaging over time. $\mathbf{w}$ is often referred to as the "microphone weight vector". Q_{opt} represents the best estimate for the true mean square source strength. Averaging the cross spectral matrix (CSM) $\mathbf{S_{pp}}$ yields a robust measurement, because the relative phase information is known precisely.[18]

The only unknown in equation 2.27 is the steering vector $\mathbf{g}$ relating source to receiver. For a point source (monopole), the vector components $G_m = G_m\left(\mathrm{e}^{\mathrm{i}\omega}\right)$ are solutions to the inhomogeneous Helmholtz equation

$$\nabla^2 G + \frac{1}{c^2} \left(2\pi f\right)^2 G = -\delta(\vec{x} - \vec{y}_0)\,, \tag{2.28}$$

where $\delta(\cdot)$ is the Dirac-delta function. In free-space conditions, which are a reasonable approximation to the sound field in large, open-jet wind tunnels, the solution to equation 2.28 (without flow) can be expressed as

$$G(\omega) = \frac{\mathrm{e}^{-\mathrm{i}\omega \Delta t_0}}{4\pi r_0}. \tag{2.29}$$

If the source is in a wind tunnel with a uniform flow velocity $\vec{U}$, equation 2.28 becomes

$$\nabla^2 G - \frac{1}{c^2} \left(\mathrm{i}2\pi f + \vec{U} \cdot \nabla\right)^2 G = -\delta(\vec{x} - \vec{y}_0)\,, \tag{2.30}$$

and the corresponding solution can be expressed as [18]

$$g(\vec{x}, f) = \frac{\mathrm{e}^{-\mathrm{i}\omega \Delta t_{0,c}}}{4\pi \sqrt{\left(\vec{M} \cdot (\vec{x} - \vec{y}_0)\right)^2 + \beta^2 \|\vec{x} - \vec{y}_0\|^2}}, \tag{2.31}$$

where $\vec{M} = \vec{U}/c$ is the Mach number of the flow, and $\beta = \sqrt{1 - \|\vec{M}\|^2}$. In an open jet wind tunnel, further corrections have to be introduced to factor for refraction effects at the jet shear layer.[19]

Equation 2.27 forms the basis of the focused beamformer, which has been used extensively in the last decade to investigate airframe noise. The most powerful

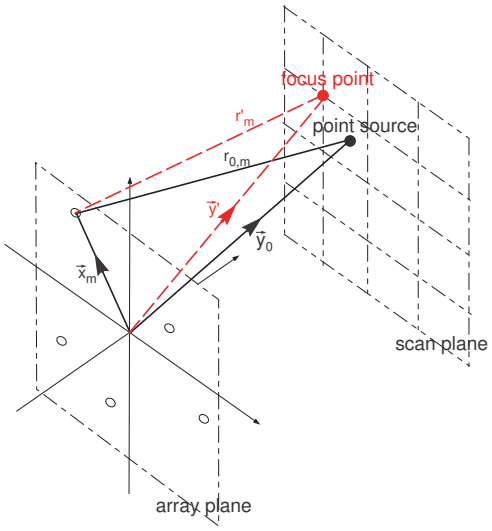

FIGURE 2.5: The focused beamformer is based on two planes - the measurement plane and the scan plane. The latter is subdivided into a number of grid points; the beamformer's output is maximum for the grid point closest to the true source position.

feature of this formulation is that no *a-priori* information is required on the source distribution. Instead, an imaginary scan plane is defined on the model under investigation, and the beamformer's output is calculated at a number of grid points that sample this plane. Figure 2.5 shows a schematic of the array and scan planes. Maximum resolving power is achieved within a scan plane that is parallel to the array plane.

The simplicity of the focused beamformer also means that even with a fast personal desktop computer, a spatial plot consisting of thousands of grid points can be generated in minutes, if not seconds. This is very useful for the noise investigators, and enables the most efficient use of available wind tunnel time by dynamically changing the test programme as results come out. Some examples of the use of the focused beamformer in wind tunnels can be found in Piet and Elias, 1997 [17], Mosher et al., 1999 [5], Dobrzynski et al., 2000 [2], Soderman et al., 2002 [7], Brooks and Humphreys, 2003 [20], Oerlemans and Sijtsma, 2004 [6], Smith et al., 2006 [8], and Quayle et al., 2007 [9].

2.4 The Point Spread Function

Since the focused beamformer is essentially a spatial filter, its performance can be quantified by its response to an acoustic point excitation, in a similar way that an

impulse response function quantifies the response of a linear system to an impulse excitation. The beamformer's response is often referred to as the Point Spread Function (PSF) or the array pattern.

A unit source at $\vec{y}_j$ induces a CSM

$$\mathbf{S}_{pp,j} = \mathbf{g}_j \mathbf{g}_j^{\dagger}, \tag{2.32}$$

where $\mathbf{g}_j^T = [G(\vec{x}_1 : \vec{y}_j), G(\vec{x}_2 : \vec{y}_j), \ldots, G(\vec{x}_M : \vec{y}_j)]$. The beamformer output at a number of k grid points due to the unit source at $\vec{y}_j$ is

$$Q_{jk} = \mathbf{w}_k^{\dagger} \mathbf{S}_{pp,j} \mathbf{w}_k = \mathbf{w}_k^{\dagger} \left[\mathbf{g}_j \mathbf{g}_j^{\dagger} \right] \mathbf{w}_k. \tag{2.33}$$

Equation 2.33 is the defining equation for the PSF. It is a function of the steering vector $\mathbf{g}$, and therefore depends on the positions of the microphone array and scan plane, the measuring environment and frequency.

Ideally $Q_{jk} = 1$ for $j = k$ and $Q_{jk} = 0$ elsewhere. However in Section 2.1 it was shown that this is not possible for an array of finite size sampled by a discrete number of sensors. This can be illustrated by taking a practical example. Figure 2.6 shows the PSF for a 56 sensor array having an aperture of 0.65 m. Full details of the design of this array can be found in Appendix A. The scan plane is a 1×1 m square consisting of 100×100 grid points, and is situated at a perpendicular distance of 1 m from the array plane, with the centre of the scan in line with the centre of the array. The point source is situated at the centre of the scan plane. Free space Green's functions, of the form shown in equation 2.29, are used. The array patterns are shown at four discrete frequencies. Levels are shown in dB, normalised to the peak level.

The plots shown in figure 2.6 illustrate very clearly the concepts of a mainlobe and multiple sidelobes that have been discussed in Section 2.1. In all of the four cases, the mainlobe is coincident with the location of the point source, i.e. at the centre of the scan plane. However, at the lower frequencies, the width of the mainlobe is so large that, for example, at 2 kHz it would be difficult to discriminate between sources that are within 0.5 m of each other. As the frequency increases, the ratio λ/L in equation 2.5 gets smaller, and the resolving power of the array increases. At the same time, the ratio $\Delta x/\lambda$ increases, and sidelobes start to be visible. Thus the 16 kHz plot is contaminated by spatial noise, which makes it more difficult to distinguish between true and spurious sources. Note that the PSFs shown in figure

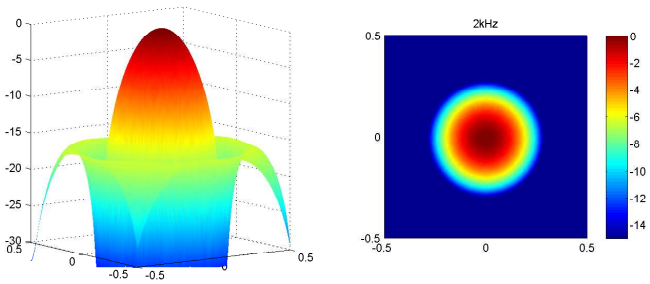

(a) 2 kHz

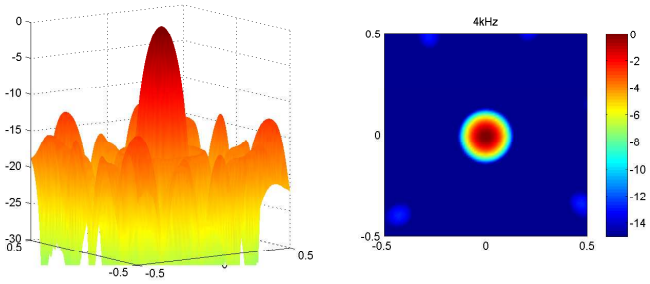

(b) 4 kHz

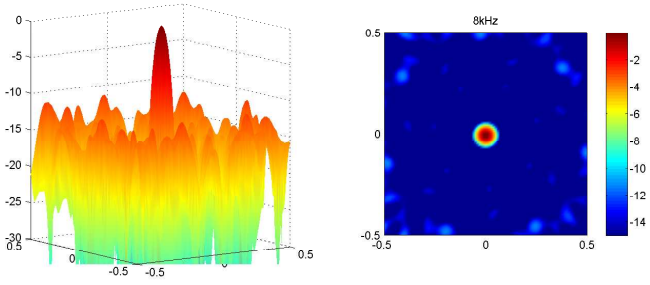

(c) 8 kHz

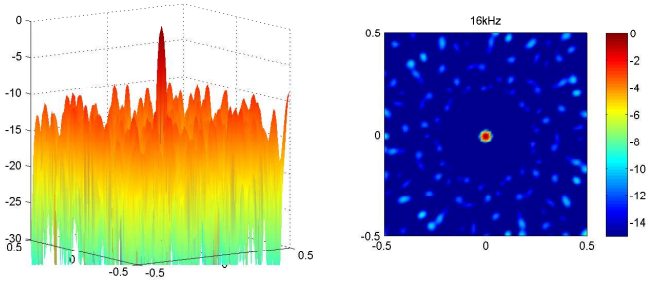

(d) 16 kHz

FIGURE 2.6: Point Spread Functions of a 56 sensor array due to a single unit point source centred on the scan plane, assuming free-space Green's functions. Plots on the right are clipped at -15 dB.

2.6 correspond to an array with good sidelobe suppression characteristics.[2] For an unoptimised array the sidelobes will be significantly higher, especially at high frequencies.

2.5 Practical Limitations

The Point Spread Function (PSF) highlights the two major limiting factors of microphone arrays, i.e. a poor resolution at low frequencies and spatial noise at high frequencies. Aeroacoustic measurements tend to have a very broad frequency range of interest, depending on the physical scale of the model being tested. Typical frequencies range from 500 Hz to 50 kHz, a span of two decades. This means that the wavelength of the sound of interest can vary anywhere between 5 mm and 0.5 m. To cover this entire frequency range, the ideal array has to be very large, and with many sensors tightly packed together. In practice, there are limitations in terms of the maximum size of an array that can be installed in a particular wind tunnel, and the maximum number of channels that can be afforded.

The requirement for a large number of sensors can be relaxed by using different arrays for low and high frequencies. These can either be entirely separate arrays or nested arrays, i.e. a single array with microphones tightly packed in the centre and more widely distributed on the outside. Sidelobes can be further controlled by taking advantage of the fact that spurious lobes in an array pattern require a coherent buildup of elemental signals at angles other than the steering angle. Irregular and aperiodic designs are often used to eliminate periodicity in the sensor locations; further details can be found in Appendix A. Whilst these techniques significantly reduce the influence of sidelobes, they cannot eliminate them completely (as is evident in the bottom plot in figure 2.6).

Given an optimally-designed array, the resulting plots can be further enhanced using deconvolution techniques. These "subtract" the artifacts introduced by the array's response, thereby improving the resolution capabilities and reduce the spatial noise. Deconvolution is discussed in Section 2.7.2.

Beamforming can also yield quantitative results; these will also be contaminated by resolution and sidelobes effects. When the source of interest is well isolated and well defined, its strength can be extracted from the peak level of the mainlobe coinciding with its position. However in most practical cases the noise coming

[2] A detailed discussion of the design of this array can be found in section A.1.3 on page 126.

from an area, say the slats on an aircraft's wing, is of interest. In this case it is necessary to integrate the levels over that area, however such a summation will be contaminated by the width of the mainlobe and any sidelobes present. Furthermore comparisons between frequencies are not possible, as the resolution and sidelobe behaviour are frequency dependent. Brooks and Humphreys[21] have suggested a Source Power Integration (SPI) method which "subtracts" these contaminating factors using information from the PSF. This method is described in more detail in Section 2.8.1.

The next set of limitations are due to the original assumptions stated when formulating the focused beamformer. In particular, the beamformer estimates the source strength of omnidirectional uncorrelated point sources. Most aeroacoustic sources tend to be distributions of highly-directional dipoles, quadrupoles and line sources, and typically exhibit some degree of coherency with adjacent sources. This gives rise to errors, particularly in the quantitative results. In this case, the beamformer has to be reformulated to take into account multiple sources. These Inverse Methods are discussed in Section 2.9.

The last set of limitations arise when applying beamforming to data acquired in closed-section wind tunnels. In order to satisfy non-intrusive conditions, microphone arrays in these types of wind tunnels will usually be flush-mounted in a test-section boundary, and therefore the microphone diaphragms are in direct contact with the turbulent boundary layer. This generates noise which can be considerably stronger than that from the aeroacoustic sources of interest, especially at the lower frequencies. Noise from the boundary layer can be assumed to be uncorrelated over the array aperture,[3] and can be removed by removing the diagonal of the cross spectral matrix (CSM). This technique will be discussed in Section 2.6.

Alternatively the influence of this noise can be suppressed physically. Jaeger et al. [23] investigated the recessing of a microphone array behind a tightly-stretched porous cloth, and found significant benefits in terms of suppressed background noise up to approximately 20 kHz (see figure 2.7). Unfortunately this setup comes with its own drawbacks; in particular the transfer function between source and receivers became significantly altered and hard to predict. At frequencies above 20 kHz additional noise was being generated by the porous cloth, and it could no longer be assumed to be acoustically transparent. Koop and Ehrenfried[13] describe a different method where each individual microphone is recessed behind

[3] See for example Blake [22].

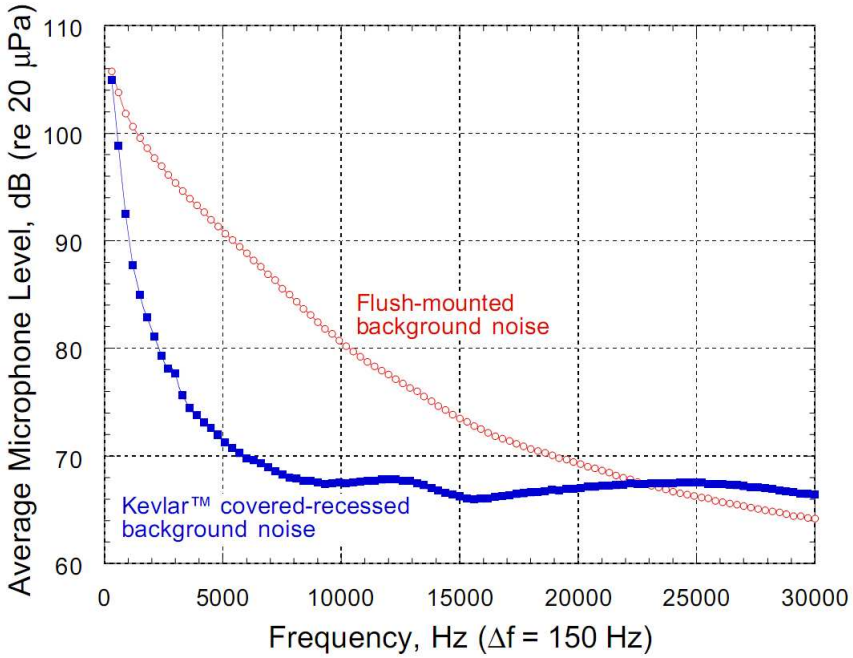

FIGURE 2.7: Comparison of measured spectra in the NASA Ames 40×80 ft. hard walled wind tunnel using microphones that are flush-mounted or recessed 12.7 mm behind a tightly stretched Kevlar cloth. From ref. [24].

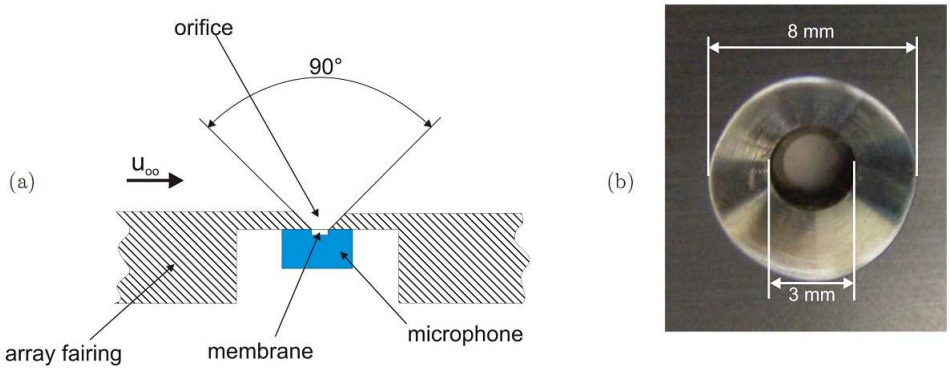

FIGURE 2.8: Array microphone mounting as described by Koop and Ehrenfried. Figure *(a)* shows a cross-section of the array with a microphone recessed behind a conical opening. Figure *(b)* shows the orifice from the top-side which is exposed to the flow. From ref. [13].

an orifice having a cone angle of 90°, as shown in figure 2.8. The final goal was also to reduce the influence of the wall pressure fluctuations caused by the turbulent boundary-layer on the microphone membranes. However in this case the cone shaped orifice provides an approximate acoustic impedance-matching between the sound field in the test section and the microphone membrane. In this way, the source-receiver path is unobstructed. It is not clear if the orifice affects the steering vectors.

In a wind tunnel additional background noise is generated by the fan and flow impinging on the turning vanes and any openings in the test section. In a closed loop tunnel, this noise propagates almost undamped inside the facility and generates a noise signal at the microphones which is correlated over the array microphones. Therefore this background noise cannot be reduced by removing the diagonal of the CSM. Reasonable success has been achieved by doing an eigenvalue decomposition in the wavenumber subdomain using delay-and-sum beamforming with an infinite focal distance.[13, 25] This technique is discussed further in Section 2.7.1.

The final issue is with the reverberant nature of a hard-walled closed-section wind tunnel. In most reported instances of beamformer applications, free-space Green's functions are used. This can be a poor approximation when there are nearby rigid surfaces that give rise to coherent reflections and a complex interference pattern in the test section. This problem will be discussed further in Chapter 3, and forms the basis of the work presented in the subsequent chapters.

2.6 CSM Diagonal removal

Noise arising from the turbulent boundary layer in contact with a flush-mounted array limits the performance benefits of beamforming. This noise can be assumed to be uncorrelated over the array microphones, and one can therefore expect that in the CSM this noise will average to zero except on the leading diagonal. This can be shown mathematically by expanding the simple model described in equation 2.11 to include a source region $q(\vec{y}_s, n)$ instead of just a point source q_s at $\vec{y}_0$. The output from the mth microphone can then be expressed as the volume integral of the product between the source distribution strength and the corresponding transfer function $G_m(\vec{y}_s)$, plus the channel noise term $n_m(n)$,

$$p_m(n) = \int G_m(\vec{y}_s)\, q(\vec{y}_s, n)\, \mathrm{d}^3\vec{y}_s + n_m(n)\,. \tag{2.34}$$

In this case the channel noise term is assumed to be dominated by the turbulence in close proximity to the microphone. The beamformer output when focused on $\vec{y}_0$, which is within the source region, is $Q_{\mathrm{opt}} = \langle |\mathbf{w}\,(\vec{y}_0)^{\dagger}\,\mathbf{p}|^2 \rangle$, which can be expanded

to give[19]

$$\begin{aligned} Q_{\text{opt}} &= \sum_{m=1}^{M} |w_m(\vec{y}_0)|^2 \left[\int |G_m(\vec{y}_s)|^2 Q(\vec{y}_s)\, \mathrm{d}^3\vec{y}_s + F_m \right] \\ &+ \sum_{m \neq m'} \int G_m(\vec{y}_s)\, G^*_{m'}(\vec{y}_s)\, Q(\vec{y}_s)\, \mathrm{d}^3\vec{y}_s, \end{aligned} \tag{2.35}$$

where

$$F_m = \langle |W^*_m(\vec{y}_0)\, N_m|^2 \rangle \tag{2.36}$$

is the averaged square channel noise term, and $m, m' = 1, 2, \ldots, M$. From equation 2.35 it is evident that the channel noise F_m enters in the beamforming expression only through the diagonal elements of the CSM (i.e. when $m = m'$). Furthermore, by expressing the mth element of the microphone weight vector as

$$W_m(\vec{y}_0) = \alpha(\vec{y}_0)\, \frac{\mathrm{e}^{-\mathrm{i}\omega\Delta t(\vec{x}_m, \vec{y}_0)}}{R(\vec{x}_m, \vec{y}_0)}, \tag{2.37}$$

the beamformer output can also be expressed as[19]

$$\begin{aligned} Q_{\text{opt}} &= \alpha^2(\vec{y}_0) \sum_{m=1}^{M} \frac{1}{R^2(\vec{x}_m, \vec{y}_0)} \left[\mathbf{S}_{\text{pp}}\right]_{mm} \\ &+ 2\alpha^2(\vec{y}_0) \sum_{m'>m} \frac{|\left[\mathbf{S}_{\text{pp}}\right]_{mm'}|}{R(\vec{x}_m, \vec{y}_0)\, R(\vec{x}_{m'}, \vec{y}_0)} \\ &\quad \cos\left\{\omega \left[\Delta t(\vec{x}_m, \vec{y}_0) - \Delta t(\vec{x}_{m'}, \vec{y}_0)\right] - \varphi\big(\left[\mathbf{S}_{\text{pp}}\right]_{mm'}\big)\right\}, \end{aligned} \tag{2.38}$$

where $\varphi\big(\left[\mathbf{S}_{\text{pp}}\right]_{mm'}\big)$ denotes the phase of the mm' CSM element. The diagonal elements are only present in the first term, which does not include any phase information. Therefore the diagonal terms do not contribute to the resolving power of the array.

The diagonal removal technique has become a standard technique applied to measurements in closed section wind tunnel. It has been shown that provided that the noise is uncorrelated over the array microphones, removing the diagonal of the CSM can completely remove the influence of this noise, without affecting the resolving capabilities of the array. However this technique can give rise to non-physical negative source powers in the beamforming maps.[12] This causes problems when extracting quantitative data from beamforming maps, as will be discussed in Section 2.8.1.

2.7 Advanced Techniques

2.7.1 Analysis of the Wavenumber Spectrum

For a typical case of a model being investigated in a closed section wind tunnel, the sound field recorded by the microphones can be regarded as a superposition of waves coming from the model and subsequent reflections from the test section walls, noise coming from the fan or the turning vanes, and incoherent noise from the turbulent boundary layer over the array. Of these, only the first component is of interest; the rest can be considered as contaminating noise.

It has already been shown that by removing the diagonal of the CSM, the incoherent noise component due to the boundary layer can be effectively removed. However beamforming results in closed section wind tunnels often feature strong background noise in the low frequency range which is not removed by the diagonal removal technique. Koop and Ehrenfried suggest that this noise is caused by plane waves that are generated by the fan or the turning vanes downstream of the test section and are reflected by the acoustically hard side wall. These plane waves should be identifiable if the results are analysed in a wavenumber spectrum.

The solution of the wave equation in three dimensions can be expressed as

$$p(\mathbf{x}, \omega_k) = A(\omega_k)\, \mathrm{e}^{-\mathrm{i}\mathbf{k}\ \mathbf{x}}, \tag{2.39}$$

where $p(\mathbf{x}, \omega)$ is the complex amplitude of the pressure signal at frequency ω and $A(\omega)$ is an arbitrary constant. Assuming a uniform flow field with flow velocity U in the x-direction, each plane wave can be described by a wavenumber $\mathbf{k} = (k_x, k_y, k_z)$ with magnitude $|\mathbf{k}| = (\omega - k_x U)/c_0$. Since for a given flow speed $|\mathbf{k}|$ is constant, k_x and k_y can be chosen to be the independent variables. The acoustic domain is then limited within the ellipse defined by[13]

$$\frac{k_x}{k_0} = \frac{\cos\theta}{1 + M\cos\theta} \qquad \text{and} \qquad \frac{k_y}{k_0} = \frac{\sin\theta}{1 + M\cos\theta}, \tag{2.40}$$

where $k_0 = \omega/c_0$ and M is the Mach number.

The sound waves propagating in the closed test section and picked up by the array can be analysed by calculating the wavenumber spectrum in the array plane using the focused-beamformer with an infinite focal plane [13]:

$$\tilde{Q}(\mathbf{k}, \omega) = \tilde{\mathbf{w}}^{\dagger} \mathbf{S}_{\mathbf{pp}}(\omega_k)\, \tilde{\mathbf{w}}, \tag{2.41}$$

where the microphone weight vector $\tilde{\mathbf{w}}$ consists of the components

$$\tilde{w}_m = \mathrm{e}^{-\mathrm{i}(k_x x_m + k_y y_m)}. \tag{2.42}$$

This is the main concept behind the BiCLean algorithm.[13] The objective is to reduce the spurious waves travelling in the reverberant test section. The cross spectral matrix $\mathbf{S_{pp}}$ is split into a first part $\mathbf{S_{pp},1}$, which represents the real sources in the observation plane, and a second part $\mathbf{S_{pp},2}$ representing the spurious waves. This is done in an iterative procedure where in each step a search for the absolute maximum over both maps is carried out. This maximum is either within the scan plane given by equation 2.27 (real source) or in the wavenumber space obtained with equation 2.41. A synthetic cross-spectral matrix $\mathbf{S_{pp}}_{\mathrm{synth}}$ is generated from this maximum and subtracted from the original CSM. The synthetic CSM is added to either $\mathbf{S_{pp},1}$ or $\mathbf{S_{pp},2}$, depending whether the maximum was due to, respectively, a true source or a spurious wave. At the end of this iterative loop, matrix $\mathbf{S_{pp},1}$ is used instead of the original CSM in the focused beamformer (equation 2.27) to calculate an improved source map. Koop and Ehrenfried [13] demonstrated that BiCLean was effective in removing spurious noise from beamforming plots at certain frequencies below 4 kHz, as shown in figure 2.9.

2.7.2 Deconvolution

In Section 2.5 it was shown that the optimum beamformer filter "distorts" the output by introducing undesired effects such as a finite-width mainlobe and additional sidelobes, depending on the geometry of the array and its spatial sampling by a fixed number of sensors. Sidelobes can be suppressed by increasing the channel count and optimising the sensor positioning within the array. However there will always be an upper limit to the number of sensor used, often determined by cost. As regards resolution, the array size is restricted by the physical size of the wind tunnel test section and the allocated space for a flush-mounted array. Therefore these limitations cannot be completely avoided; instead one can try to reduce their effects. Recently a lot of research has been carried out on "deconvolution" techniques, where features in the beamforming plots arising due the processing technique are filtered out. Three of the most popular deconvolution techniques as applied to aeroacoustic measurements are CLEAN, DAMAS and CLEAN-SC.

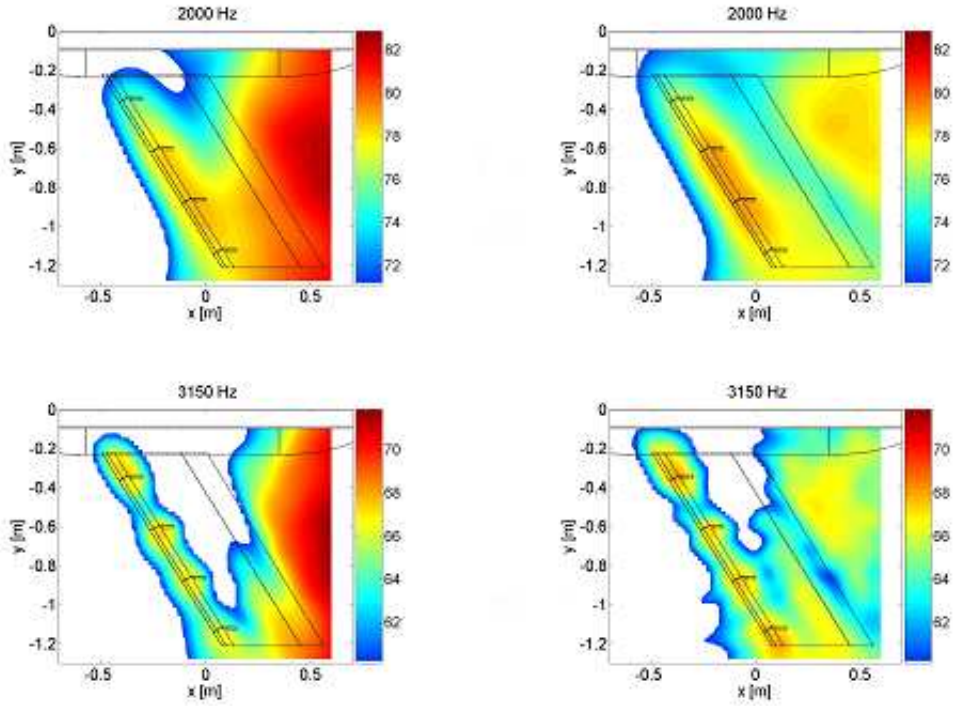

FIGURE 2.9: Comparison of beamforming maps of a swept constant-chord half-model in a closed section wind tunnel, without *(left)* and with *(right)* the Bi-CLean algorithm. Results are shown only for two one-third octave bands with centre frequencies $f_c = 2\,\text{kHz}$ and $3.15\,\text{kHz}$. From ref. [13].

2.7.2.1 CLEAN

CLEAN was developed during the 1960s by the Swedish physicist Jan Högbom for astronomy applications.[26] It was used to remove the spurious responses from a celestial radio image caused by the use of discrete, rather than continuous spacings in deriving the radio image. This is the equivalent problem of removing spurious sidelobes caused by the use of discrete sensors sampling an array. The fundamental assumption is that beamforming maps are built up of theoretical point spread functions (PSFs).

Essentially CLEAN is an iterative procedure, starting with a standard beamforming map (*dirty map*) containing the sources of interest plus spatial noise. The peak location is identified and an appropriately scaled PSF corresponding to that peak is subtracted from the dirty map. This PSF is replaced by a *clean beam* (a beam without the sidelobes) on a *clean map*. The next peak location is identified in the dirty map, and the same procedure repeated until a suitable stop criterion is satisfied.

The iterations start with $i = 0$, where the dirty map is built by determining Q_j at

a number of $\vec{y}_j$ locations using equation 2.27. For the first iteration, the degraded CSM is defined as

$$\mathbf{D}^{(i)} = \mathbf{D}^{(0)} = \mathbf{S}_{\text{pp}}. \tag{2.43}$$

For $i \geq 1$, the peak source location $\vec{y}^{(i)}_{\max}$ is determined from the dirty map, i.e. the grid point for which $Q_j^{(i-1)}$ obtains its maximum $Q^{(i-1)}_{\max}$. The influence of this peak source on the beamforming plot can be expressed by the scaled PSF

$$P_j^{(i)} = Q^{(i-1)}_{\max} \mathbf{w}_j^{\dagger} \left[\mathbf{g}^{(i)}_{\max} \mathbf{g}^{\dagger\,(i)}_{\max} \right] \mathbf{w}_j = \mathbf{w}_j^{\dagger} \mathbf{G}^{(i)} \mathbf{w}_j, \tag{2.44}$$

where $\mathbf{g}^{(i)}_{\max}$ is the steering vector corresponding to $\vec{y}^{(i)}_{\max}$. This PSF is replaced by a clean beam,

$$C_j^{(i)} = Q^{(i-1)}_{\max} \Phi\left(\vec{y}_j - \vec{y}^{(i)}_{\max}\right), \tag{2.45}$$

where the function Φ represents a beam of fixed width, normalised such that $\Phi(0) = 1$.

The degraded CSM becomes

$$\mathbf{D}^{(i)} = \mathbf{D}^{(i-1)} - Q^{(i-1)}_{\max} \mathbf{g}^{(i)}_{\max} \mathbf{g}^{\dagger\,(i)}_{\max}, \tag{2.46}$$

and the updated dirty map is computed by

$$Q_j^{(i)} = \mathbf{w}_j^{\dagger} \mathbf{D}^{(i)} \mathbf{w}_j. \tag{2.47}$$

The procedure is continued for I iterations until the degraded CSM satisfies a suitable stop criterion.[12] The final "cleaned" beamforming map can then be expressed as a summation of the clean beams and the remaining dirty map,

$$Q_{\text{clean},j} = \sum_{i=1}^{I} C_j^{(i)} + Q_j^{(I)}. \tag{2.48}$$

2.7.2.2 DAMAS

DAMAS (Deconvolution Approach for the Mapping of Acoustic Sources) was proposed by Brooks and Humphreys in 2004.[27] The main objectives was to accurately quantify the position and strength of acoustic sources by removing the beamforming characteristics from the output presentation. This algorithm differs from CLEAN in that a number of statistically independent noise sources equal to the number of grid points are assumed, leading to a linear system of equations

which takes into account the reciprocal influence of all the sources at the different locations over the array survey region.

The problem consists of an array of M microphones and a scan plane with N grid points. The pressure at the mth microphone due to a source at n can be expressed as

$$p_{m:n} = \hat{P}_n G^{-1}_{m:n}; \tag{2.49}$$

where $\hat{P}_n$ represents the pressure which would be generated by a source at n at a reference point on the array (say the centre) if there were no convective and refractive effects. $G^{-1}_{m:n}$ is the transfer function that includes all the factors affecting the propagation of sound from n to m that yield $p_{m:n}$.

The $[m, m']$th element of the cross spectral matrix arising from a point source at n is given by $E[(p_{m:n})^* \, p_{m':n}]$, i.e.

$$\begin{aligned} S_{pp,n}(m, m') &= E\left[\left(\hat{P}_n G^{-1}_{m:n}\right)^* \left(\hat{P}_n G^{-1}_{m':n}\right)\right] \\ &= E\left[\hat{P}^*_n \hat{P}_n \left(G^{-1}_{m:n}\right)^* G^{-1}_{m':n}\right]. \end{aligned} \tag{2.50}$$

Thus, the modelled cross-spectral matrix for a single source at n can be expressed as

$$\mathbf{S}_{pp,n\,\mathrm{mod}} = X_n \begin{bmatrix} \left(G^{-1}_1\right)^* G^{-1}_1 & \left(G^{-1}_1\right)^* G^{-1}_2 & \dots & \left(G^{-1}_1\right)^* G^{-1}_M \\ \left(G^{-1}_2\right)^* G^{-1}_1 & \left(G^{-1}_2\right)^* G^{-1}_2 & & \vdots \\ & & \ddots & \vdots \\ & & & \left(G^{-1}_M\right)^* G^{-1}_M \end{bmatrix}_n, \tag{2.51}$$

where X_n is the mean square pressure at microphone m normalised in level for a microphone at a reference point (e.g. the centre of the array).

This approach is extended for the case of N statistically independent sources located at each grid point. The total modelled cross spectral matrix can thus be defined as

$$\mathbf{S}_{pp\,\mathrm{mod}} = \sum_n \mathbf{S}_{pp,n\,\mathrm{mod}} \tag{2.52}$$

The beamformer's output for the nth grid point is

$$\begin{aligned} Q_{n\,\mathrm{mod}}(\mathbf{w}) &= \left[\mathbf{w}^\dagger \mathbf{S}_{pp\,\mathrm{mod}} \mathbf{w}\right]_n \\ &= \mathbf{w}^\dagger_n \sum_{n'} X_{n'} \left[\quad\right]_{n'} \mathbf{w}_n = \sum_{n'} \mathbf{w}^\dagger_n \left[\quad\right]_{n'} \mathbf{w}_n X_{n'} \\ &= \mathbf{A} X_{n'}, \end{aligned} \tag{2.53}$$

where the terms in the square brackets are the same as those in equation 2.51. The components of square matrix $\mathbf{A}$ (size $N \times N$) are

$$A_{nn'} = \mathbf{w}_n^\dagger [\quad]_{n'} \mathbf{w}_n. \tag{2.54}$$

Equating $Q_{n \bmod}(\mathbf{w}_n)$ with the regular beamformer output $Q(\mathbf{w}_n)$ obtained from the measured data (using equation 2.27) gives the defining equation for the DAMAS algorithm,

$$\mathbf{AX} = \mathbf{Q}. \tag{2.55}$$

For standard beamforming, the diagonal terms of $\mathbf{A}$ are equal to unity. If the CSM diagonal removal is used, the diagonal elements of $\mathbf{A}$ are also equal to one, but the off-diagonal components differ and attain negative values when n and n' represent sufficiently distant points from one another, depending on frequency.[27]

Equation 2.55 represents a system of N linear equations relating a spatial field of point locations with corresponding beamformer outputs Q_n to equivalent source distributions X_n at the same point locations, which are also the required quantities. If matrix $\mathbf{A}$ is non-singular, the solution would be given by $\mathbf{X} = \mathbf{A}^{-1}\mathbf{Q}$. However for most practical cases matrix $\mathbf{A}$ turns out to be singular, with a quite small rank[4] (of the order of 0.25 or lower). Brooks and Humphreys [27] found that Singular Value Decomposition with and without regularisation, and special iterative algorithms such as Conjugate Gradient methods could not be implemented successfully. Instead, a physically-necessary positivity constraint was imposed on the $\mathbf{X}$ components, and the solution was obtained iteratively. The authors found that the actual rate and accuracy at which solutions converge depend on the chosen spatial resolution and evaluation region sizes compared to the array beam width. DAMAS has been extended for three-dimensional applications.[28]

The main problems of the standard DAMAS algorithm are slow processing speeds (of the order of hours or even days) and the lack of an explicit regularisation technique to control the high frequency noise during reconstruction. Dougherty [29] has proposed modified algorithms, termed DAMAS2 and DAMAS3, which use assumptions common in the fields of optics and radio astronomy, i.e. restricting the point spread function to a translationally-invariant convolutional form. In order for this to be relevant to aeroacoustic beamforming, a change of the coordinate space is necessary. Drastic speed improvements were achieved by using FFT processing (DAMAS2) and reducing the number of required iterations (DAMAS3). Ehren-

[4] In this context the rank denotes the number of linearly independent equations compared to the total number of grid points N.

fried and Koop [11] discuss two further algorithms, the RichardsonLucy method and a gradient-type nonnegative least-squares (NNLS) approach, that can be embedded in DAMAS to speed up the computations whilst preserving accuracy.

2.7.2.3 CLEAN-SC

The problem with CLEAN and all the DAMAS variants is that they use theoretical point spread functions to eliminate the resolution and sidelobes effects. This approach works well only if all the sources present are incoherent monopoles. Aeroacoustic sources often have a spatial extent or non-uniform directivity; furthermore measurements are prone to loss of coherence.[30] Therefore the theoretical PSFs used to deconvolve the results might not accurately represent beam patterns of the measured sources. In light of this Sijtsma [12] proposed a modified version of CLEAN based on the measured spatial source coherence. This technique, termed CLEAN-SC, takes advantage of the fact that mainlobes are spatially coherent with their sidelobes, as they originate from the same physical source.

CLEAN-SC follows the same methodology as CLEAN. The main difference is in the definition of matrix $\mathbf{G}^{(i)}$ in equation 2.44. Instead of using the steering vectors $\mathbf{g}_{\max}^{(i)}$, a requirement is made that the source cross powers at any grid point $\vec{y}_j$ with the peak location $\vec{y}_{\max}^{(i)}$ are determined entirely by $\mathbf{G}^{(i)}$. This can be expressed as[12]

$$\mathbf{w}_j^{\dagger}\mathbf{D}^{(i-1)}\mathbf{w}_{\max}^{(i)} = \mathbf{w}_j^{\dagger}\mathbf{G}^{(i)}\mathbf{w}_{\max}^{(i)} \quad \text{for all} \quad \mathbf{w}_j, \tag{2.56}$$

where $\mathbf{w}_{\max}$ is the weight vector corresponding to steering vector $\mathbf{g}_{\max}$. This relationship is satisfied when

$$\mathbf{D}^{(i-1)}\mathbf{w}_{\max}^{(i)} = \mathbf{G}^{(i)}\mathbf{w}_{\max}^{(i)}. \tag{2.57}$$

Equation 2.57 does not have a unique solution for $\mathbf{G}^{(i)}$. However it can be assumed that $\mathbf{G}^{(i)}$ is due to a single coherent source component $\mathbf{h}^{(i)}$,

$$\mathbf{G}^{(i)} = Q_{\max}^{(i-1)}\mathbf{h}^{(i)}\mathbf{h}^{\dagger(i)}. \tag{2.58}$$

Equation 2.57 is solved when[12]

$$\mathbf{h}^{(i)} = \frac{1}{\left(1 + \mathbf{w}_{\max}^{\dagger(i)}\mathbf{H}^{(i)}\mathbf{w}_{\max}^{(i)}\right)}^{1/2} \left(\frac{\mathbf{D}^{(i-1)}\mathbf{w}_{\max}^{(i)}}{Q_{\max}^{(i-1)}} + \mathbf{H}^{(i)}\mathbf{w}_{\max}^{\dagger(i)}\right), \tag{2.59}$$

where $\mathbf{H}^{(i)}$ is given by

$$H_{mn}^{(i)} = \begin{cases} 0, & m \neq n \\ h_m^{(i)} h_n^{*(i)} & m = n. \end{cases} \tag{2.60}$$

Equation 2.59 is not an explicit expression for $\mathbf{h}^{(i)}$, because it contains the $\mathbf{H}^{(i)}$ component. However it can be solved iteratively, using $\mathbf{h}^{(i)} = \mathbf{g}_{\max}^{(i)}$ as a first guess. $\mathbf{G}^{(i)}$ is thereby computed using equation 2.58, and the iterative procedure is continued in a similar way to the CLEAN algorithm described in Section 2.7.2.1. Note that in CLEAN-SC, the steering vector $\mathbf{g}_{\max}^{(i)}$ is only used as a first guess for the $\mathbf{h}^{(i)}$ iteration loop.

CLEAN-SC was demonstrated to be superior to CLEAN and DAMAS when applied to realistic aeroacoustic sources. Figure 2.10 shows beamforming plots of a model aircraft exhibiting a dominant source on the wing tip. Both CLEAN and DAMAS fail to clean the sidelobes corresponding to this source, most probably because they do not match the ideal PSF. On the other hand CLEAN-SC successfully cleans these contaminating sidelobes to reveal further sources along the wing slats that are more than 20 dB quieter than the dominant source.

2.8 Levels from Beamforming

Aircraft manufacturers are not only interested in identifying noise-generating regions: they also need to quantify the noise in order to assess the level of benefit offered by potential noise control measures. Furthermore, as advanced techniques further refine the focused beamformer and expand its applicability, there is an increased desire to use these results for aircraft certification purposes, thereby significantly reducing the cost of an aircraft design cycle. When comparing deltas (relative change in levels between different configurations), factors affecting the beamformer output such as the array response are not of significant concern, provided that comparisons are done at the same conditions. However absolute levels necessitate that all the factors introduced by the measuring environment and post processing technique are filtered out.

The focused beamformer is developed on the premise of an isolated point source. In this case, the source strength is simply the peak value of the mainlobe in the plot, i.e. the grid point with the maximum level. Note that this holds only if the grid point coincides with the exact location in space of the source of interest. In practices this is rarely the case; furthermore most cases of interest involve a dis-

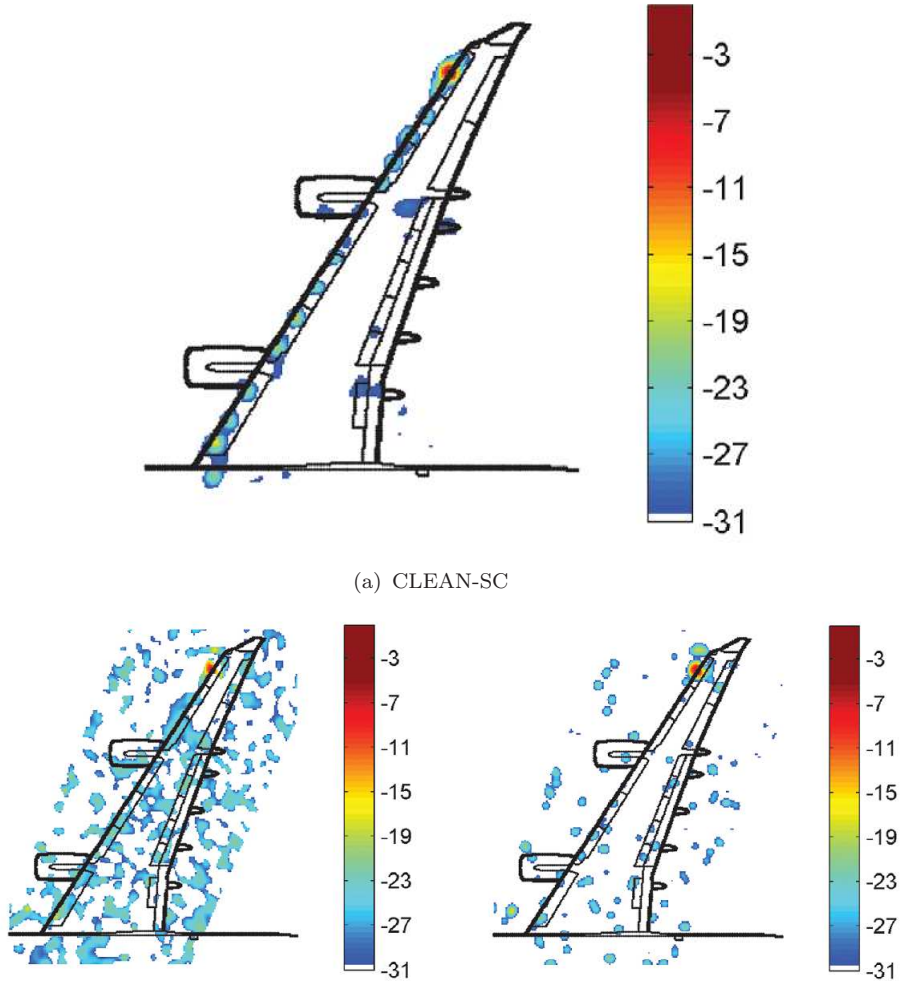

(a) CLEAN-SC

(b) CLEAN

(c) DAMAS

FIGURE 2.10: Deconvolved beamforming plots of an Airbus A340 1:10.6 scale model in a closed section wind tunnel using CLEAN-SC, CLEAN and DAMAS. From ref. [12].

tribution of sources rather than an isolated one, and some sort of area integration becomes necessary.

It has already been shown that the focused beamformer is a spatial filter with a particular response function. Therefore beamforming maps are a convolution of the true sources and this response function, and the results of an area summation would be contaminated by errors due to the finite width of the mainlobes and the presence of sidelobes. In order to recover the specific contribution from the sources of interest, the array response has to be filtered out.

2.8.1 Source Power Integration

To date the standard way of correcting for the array response is by using the Source Power Integration (SPI) method, as proposed by Brooks and Humphreys [21]. An integration area surrounding the source region of interest is defined by $l_L \leq l \leq l_U$ and $n_L \leq n \leq n_U$, where l, n are integers representing grid points sampling the scan plane. If $Q_{l,n}$ is the beamformer output at $[l, n]$, the integrated mean square source strength output of the defined area can be expressed as

$$Q_T = \sum_{l=l_L}^{l_U} \sum_{n=n_L}^{n_U} [Q_{l,n}/C_{l,n}] \tag{2.61}$$

$$C_{l,n} = \left[\sum_{l'=l_{L'}}^{l'_U} \sum_{n'=n_{L'}}^{n'_U} Q_{l',n'} \right]_{l,n} \tag{2.62}$$

$$Q_{l',n'} = \left[\frac{\mathbf{g}^\dagger \mathbf{G}'_{l,n} \mathbf{g}}{[\mathbf{g}^\dagger \mathbf{g}]} \right]_{l',n'} \tag{2.63}$$

$$\mathbf{G}'_{l,n} = \left[\mathbf{g}\mathbf{g}^\dagger \right]_{l,n}. \tag{2.64}$$

Therefore for each grid point $[l, n]$, the beamformer output $Q_{l,n}$ is normalised by the corresponding $C_{l,n}$, the summed contribution of unit influences from all other grid points in the integration region. These unit influences are a function of the synthesised cross-spectral matrix $G'_{l,n}$. This method should give reasonably accurate results provided that the integration area does not contain significant contributions from sources situated outside the integration area. As with beamforming, the source region is assumed to be comprised of uncorrelated point sources.

Due to the large number of grid points used in practical applications (typically in the thousands), computing $C_{l,n}$ for each grid point would be a very computationally-intensive task. Therefore a representative C_{l_0,n_0} is computed at the centre of gravity of the scan plane and used to normalise the output at all grid points.

In order to demonstrate the effectiveness and robustness of SPI, a number of simulations have been carried out to extract a known source strength from beamforming levels. Similar simulations will also be presented in Chapter 4 and Appendix B when discussing the de-reverberation technique. In this way these simulations can demonstrate the effectiveness of different techniques in a consistent way.

A single unit point source is used to calculate the pressures at an array of mi-

TABLE 2.1: Errors (dB) when retrieving the source strength of a unit point source from beamforming plots, using a simple summation and SPI. Three scan plane grids are considered in each case.

Error in source strength (dB)						
	Summation			SPI		
freq (kHz)	0.02 m	0.01 m	0.005 m	0.02 m	0.01 m	0.005 m
2	23.7	29.7	35.7	0.02	0.005	0.001
4	18.8	24.7	30.7	0.06	0.01	0.003
8	17.3	23.2	29.2	0.08	0.02	0.005
16	17.0	23.0	29.0	0.09	0.02	0.006
32	17.3	23.2	29.2	0.08	0.02	0.005

crophones using free space Green's functions. Beamforming is then carried out in the normal way, and the resulting plots are equivalent to the point spread functions. The same array-scan plane discussed in Section 2.4, resulting in the PSFs shown in figure 2.6 on page 18 was used. The source strength was retrieved from the plots using a simple summation and SPI. Table 2.1 shows the errors in the retrieved source strength Q_T in dB (error $= 10 \log Q_T$). The errors are shown for five discrete frequencies: 2, 4, 8, 16 and 32 kHz. Three grids of different resolutions are considered: $\Delta x = \Delta y = 0.02$ m, $\Delta x = \Delta y = 0.01$ m and $\Delta x = \Delta y = 0.005$ m where Δx, Δy refer to the inter-grid spacing in the x and y directions, respectively. The approximate version of SPI, using a single representative C_{l_0,n_0}, was used.

The results in Table 2.1 show that a simple summation of the grid points within the area of interest yields significant errors, even for the simplest case of an isolated point source. The levels are also dependent on the inter-grid spacing. The increase in the errors when doubling the grid resolution is 6 dB, corresponding to a quadrupling of the total number of grid points. At the lower frequencies, the errors are mainly due to the width of the mainlobe. At the higher frequencies, contamination from sidelobes becomes more significant.

The errors when using the Source Power Integration method are very small, and can be assumed to be negligible. These very small errors might be due to using a representative C_{l_0,n_0}, rather than computing a unique $C_{l,n}$ for each grid point.

2.8.2 Effect of CSM Diagonal Removal on SPI

In Section 2.6 it was shown that by removing the diagonal of the cross spectral matrix, the influence of the boundary layer noise over a flush-mounted array can

TABLE 2.2: Errors (dB) when retrieving the source strength of a unit point source from beamforming plots for which the CSM diagonal removal technique has been applied. Grid resolution is 0.01 m.

Error in source strength (dB)				
freq (kHz)	Summation	SPI	SPI + threshold	
			12 dB	16 dB
2	28.6	0.006	0.005	0.005
4	19.5	0.05	0.02	0.02
8	-4.3	0.95	0.05	0.05
16	10.1	-0.4	0.06	0.06
32	2.2	-1.7	0.05	0.05

be, in theory, eliminated completely. It was also shown that this technique does not affect the resolving power of the array, however some adverse effects on absolute levels could be introduced. In order to investigate this effect, the same point spread function is considered once again, however this time the leading diagonal of the CSM $\mathbf{S}_{pp,j}$ in equation 2.32 is replaced by zeros. The resulting PSFs at 2, 4, 8, and 16 kHz are shown in figure 2.11. Comparing with figure 2.6 on page 18, one can indeed confirm that the resolution of the array is unchanged; furthermore the sidelobes are somewhat more suppressed. This apparent effect arises because non-physical negative source strengths are produced at certain grid point locations. Although this phenomenon can be considered as advantageous to the qualitative data, it gives rise to errors when performing area integrations.

Table 2.2 shows the errors in source strength when performing an area integration on the plots shown in figure 2.11. Only one grid resolution, $\Delta x = \Delta y = 0.01$ m, is considered. The results from a simple summation show that the diagonal removal leads to a reduction in the overall levels, although the peak mainlobe level remains unchanged. In particular, at 8 kHz the error becomes an underestimation rather than an overestimation.

When the Source Power Integration method is used, the errors in estimated source strength are no longer negligible. Furthermore, there is no obvious trend in the results: the error increases from 2 to 8 kHz, and then drops for the 16 kHz and 32 kHz plots.

Sijtsma [18] attributes these errors to the negative source powers introduced as a result of removing the CSM diagonal. He therefore suggests the introduction of a threshold parameter to the SPI technique. Using this formulation, equation 2.61

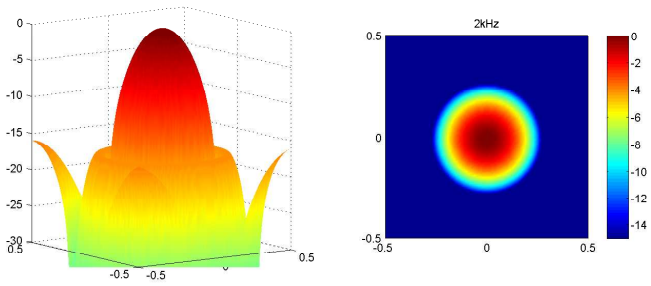

(a) 2 kHz

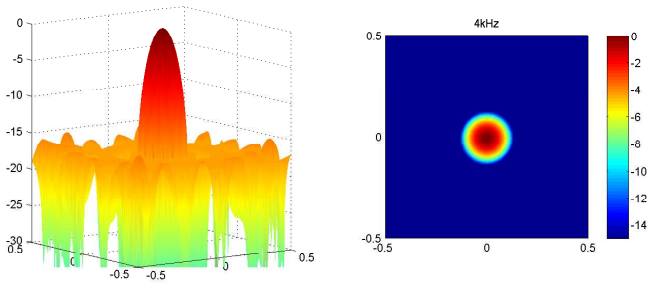

(b) 4 kHz

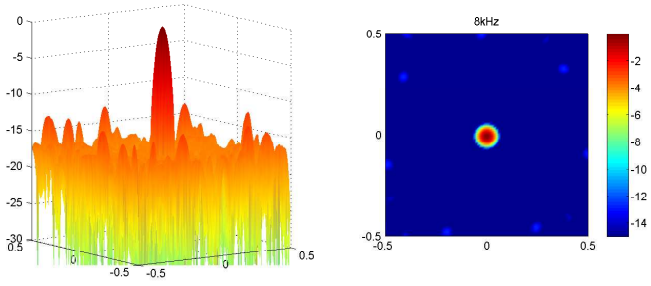

(c) 8 kHz

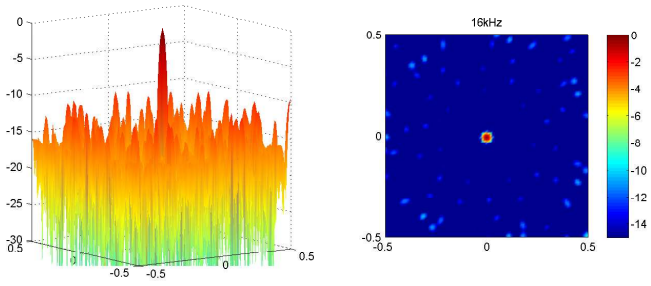

(d) 16 kHz

FIGURE 2.11: Point Spread Functions for the same case as shown in figure 2.6, but using the CSM diagonal removal technique.

can be re-written as

$$Q_T = \frac{\sum_{l=l_L}^{l_U}\sum_{n=n_L}^{n_U}\{Q_{l,n}; \quad Q_{l,n}/\max(Q_{l,n}) \geq \lambda\}}{\sum_{l=l_L}^{l_U}\sum_{n=n_L}^{n_U}\{C_{l,n}; \quad C_{l,n}/\max(C_{l,n}) \geq \lambda\}}, \tag{2.65}$$

where $0 \leq \lambda \leq 1$ is the preset threshold. Sijtsma found that a value of 12 dB works well for data of a half aircraft model.

If the SPI with threshold is used to recover the source strength from the plots shown in figure 2.11, the errors are systematically reduced, as shown in the right-most two columns of Table 2.2. When using a threshold of 12 dB, the errors at the five frequencies become less than 0.1 dB, and therefore can be assumed to be negligible. There was no advantage observed when the threshold was increased to 16 dB.

2.8.3 Levels from CLEAN-SC

The purpose of the Source Power Integration method is to filter out the level contributions from the source mainlobe and corresponding sidelobes. However these effects were also filtered out by the deconvolution techniques discussed in Section 2.7.2. Therefore it should be possible to extract levels directly from the deconvolved data. This idea is demonstrated here using CLEAN-SC as an example, as originally proposed by Sijtsma [12].

CLEAN-SC is based on an iterative approach that extracts discrete sources from the "dirty" plot based on a level ranking. After I iterations, the original cross spectral matrix (CSM) can be expressed as[12]

$$\mathbf{S_{pp}} = \sum_{i=1}^{I} Q_{\max}^{(i-1)} \mathbf{h}^{(i)} \mathbf{h}^{\dagger\,(i)} + D^I, \tag{2.66}$$

where D^I is the degraded CSM from which no further information can be extracted. If after I iterations $\|D^I\| << \|\mathbf{S_{pp}}\|$, then it is safe to assume that the first term on the right hand side of equation 2.66 contains most of the information on the sources of interest. Therefore the summed microphone autospectra due to the sources of interest,

$$\sum_{m=1}^{M} \mathbf{S}_{\mathbf{pp},mm'} = \sum_{i=1}^{I} Q_{\max}^{(i-1)} \sum_{m=1}^{M} h_m^{(i)} h_{m'}^{(i)}, \tag{2.67}$$

can be assumed to represent the sum of all the source strengths, without any resolution/sidelobe contamination.

2.9 Inverse Methods

The discussion up to now has been focused on a single isolated point source. In fact, the focused beamformer formulation is only valid for a distribution of uncorrelated point sources. Many aeroacoustic sources exhibit some sort of coherency. Holland and Nelson [31] have demonstrated the dependence of the beamformer's output on the level of coherency between interfering sources in the vicinity of the original source. To eliminate such errors, all contributing sources have to be taken into account as a combined system.

One technique, often referred to as the inverse method [31, 32], seeks to optimise the output of S beamformers operating simultaneously, S being the total number of sources present. This technique requires *a priori* knowledge of the source distribution, and therefore is not meant to substitute beamforming, but rather complement it. The true source distribution can be modelled as a finite number S of discrete sources at specific locations. The analysis presented in the beginning of this chapter can then be extended to include multiple sources. In this case, $Q\big(\mathrm{e}^{\mathrm{i}\omega}\big)$ is replaced by the vector $\mathbf{q}$, and the vector $\mathbf{g}$ is replaced by a matrix of Green's functions $\mathbf{G}$ mapping the sth source to the mth microphone. The desired filter is now a matrix $\mathbf{W}$,

$$\begin{aligned} \mathbf{p} &= \mathbf{s} + \mathbf{n} = \mathbf{G}\mathbf{q} + \mathbf{n} && (2.68) \\ \mathbf{y} &= \mathbf{W}^{\dagger}\mathbf{p}. && (2.69) \end{aligned}$$

Using the least squares criterion to minimise the sum of squared errors $\mathbf{e} = \mathbf{y} - \mathbf{q}$ implies that the cost function is defined as

$$\begin{aligned} J = E\big[\mathbf{e}^{\dagger}\mathbf{e}\big] &= \mathrm{Tr}\big\{E\big[\mathbf{e}\mathbf{e}^{\dagger}\big]\big\} \\ &= \mathrm{Tr}\Big\{E\Big[\big(\mathbf{W}^{\dagger}\mathbf{p} - \mathbf{q}\big)\big(\mathbf{W}^{\dagger}\mathbf{p} - \mathbf{q}\big)^{\dagger}\Big]\Big\}, \end{aligned} \qquad (2.70)$$

where $\mathrm{Tr}\{\cdot\}$ denotes the trace (sum of diagonal elements) of a matrix. This can be expanded, and by using the expectation operator, reduces to

$$J = \mathrm{Tr}\big\{\mathbf{W}^{\dagger}\mathbf{S}_{pp}\mathbf{W} - \mathbf{W}^{\dagger}\mathbf{S}_{qp}^{\dagger} - \mathbf{S}_{qp}\mathbf{W} + \mathbf{S}_{qq}\big\}, \qquad (2.71)$$

where the spectral density matrices $\mathbf{S}_{qp}$ and $\mathbf{S}_{qq}$ are defined by

$$\mathbf{S}_{qp} = E\left[\mathbf{q}\mathbf{p}^{\dagger}\right] \tag{2.72}$$
$$\mathbf{S}_{qq} = E\left[\mathbf{q}\mathbf{q}^{\dagger}\right]. \tag{2.73}$$

The cost function is minimised by choosing [16]

$$\begin{aligned} \mathbf{W}_{\text{opt}}^{\dagger} &= \mathbf{S}_{qp}\mathbf{S}_{pp}^{-1} \qquad \text{or} \\ \mathbf{W}_{\text{opt}} &= \mathbf{S}_{pp}^{-1}\mathbf{S}_{pq}. \end{aligned} \tag{2.74}$$

This result is effectively a superposition of multiple solutions as given in the single source problem (cf. equation 2.21). The optimum filter matrix $\mathbf{W}_{\text{opt}}$ consists of S column vectors $\mathbf{w}_{\text{opt}} = \mathbf{S}_{pp}^{-1}\mathbf{s}_{ps}$, where $\mathbf{s}_{ps} = E\left[\mathbf{p}_M Q_s^*\left(\mathrm{e}^{\mathrm{j}\omega}\right)\right]$. The properties of $\mathbf{S}_{pp}$ are determined from the number of sources present, their degree of correlation, and the properties of interfering noise.

It is ideal to have an optimum filter solution which does not require *a priori* information about the source strengths.[5] If the noise signals $\mathbf{n}$ are assumed to be uncorrelated with the source strengths $\mathbf{q}$, then

$$\mathbf{S}_{pp} = E\left[\left(\mathbf{G}\mathbf{q}+\mathbf{n}\right)\left(\mathbf{G}\mathbf{q}+\mathbf{n}\right)^{\dagger}\right] = \mathbf{G}\mathbf{S}_{qq}\mathbf{G}^{\dagger} + \mathbf{S}_{nn}, \tag{2.75}$$

where $\mathbf{S}_{nn} = E\left[\mathbf{n}\mathbf{n}^{\dagger}\right]$. Similarly,

$$\mathbf{S}_{qp} = E\left[\mathbf{q}\left(\mathbf{G}\mathbf{q}+\mathbf{n}\right)^{\dagger}\right] = \mathbf{S}_{qq}\mathbf{G}^{\dagger}, \tag{2.76}$$

and, inserting into equation 2.74 gives

$$\mathbf{W}_{\text{opt}}^{\dagger} = \mathbf{S}_{qq}\mathbf{G}^{\dagger}\left[\mathbf{G}\mathbf{S}_{qq}\mathbf{G}^{\dagger} + \mathbf{S}_{nn}\right]^{-1}, \tag{2.77}$$

which, after some manipulation, can be rewritten as [16]

$$\mathbf{W}_{\text{opt}}^{\dagger} = \left[\mathbf{S}_{qq}^{-1} + \mathbf{G}^{\dagger}\mathbf{S}_{nn}^{-1}\mathbf{G}\right]^{-1}\mathbf{G}^{\dagger}\mathbf{S}_{nn}^{-1}. \tag{2.78}$$

Furthermore, assuming that both source strengths and noise are uncorrelated between sources and microphones, i.e. $\mathbf{S}_{qq} = S_{qq}\mathbf{I}$ and $\mathbf{S}_{nn} = S_{nn}\mathbf{I}$, and by introducing the signal to noise ratio $\gamma = S_{nn}/S_{qq}$,

$$\mathbf{W}_{\text{opt}}^{\dagger} = \left[\gamma\mathbf{I} + \mathbf{G}^{\dagger}\mathbf{G}\right]^{-1}\mathbf{G}^{\dagger}. \tag{2.79}$$

[5] Note however that the number and location of the sources need to be known beforehand.

In the case of no noise, i.e. as $\gamma \to 0$,

$$\mathbf{W}_{\text{opt}}^{\dagger} = \left[\mathbf{G}^{\dagger}\mathbf{G}\right]^{-1}\mathbf{G}^{\dagger} = \mathbf{G}^{+}, \tag{2.80}$$

where $\mathbf{G}^{+}$ is the pseudo-inverse of $\mathbf{G}$. Note that in this special case, no information about the source cross spectral matrix is required.

The same result is obtained from a deterministic least squares approach of the estimate of $\mathbf{q}$, which seeks to minimise the error between the output $\mathbf{p}$ from the sensors and the signals $\mathbf{s} = \mathbf{G}\mathbf{q}$ produced by the assumed model.[32] Thus the cost function to be minimised is a quadratic

$$\begin{aligned} J &= (\mathbf{p} - \mathbf{G}\mathbf{q})^{\dagger}(\mathbf{p} - \mathbf{G}\mathbf{q}) \\ &= \mathbf{q}^{\dagger}\mathbf{G}^{\dagger}\mathbf{G}\mathbf{q} - \mathbf{q}^{\dagger}\mathbf{G}^{\dagger}\mathbf{p} - \mathbf{p}^{\dagger}\mathbf{G}\mathbf{q} + \mathbf{p}^{\dagger}\mathbf{p}, \end{aligned} \tag{2.81}$$

which gives

$$\mathbf{q}_{\text{opt}} = \left[\mathbf{G}^{\dagger}\mathbf{G}\right]^{-1}\mathbf{G}^{\dagger}\mathbf{p}. \tag{2.82}$$

A unique minimum for the cost function J exists only provided $\left[\mathbf{G}^{\dagger}\mathbf{G}\right]$ is positive definite. Note that this analysis holds only if $M \geq S$; with $M < S$, no solution exists. When $M = S$, then $\mathbf{q}_0 = \mathbf{G}^{-1}\hat{\mathbf{p}}$. In most practical cases, the matrix $\mathbf{G}$ is ill-conditioned, and even if the system can be solved, the solution becomes unstable. Regularisation techniques have to be used to condition the matrix of Green's functions.

2.9.1 Singular Value Decomposition and the Condition Number

Singular value decomposition (SVD) can be used to decompose the transfer matrix $\mathbf{G}$ in the form [32]

$$\mathbf{G} = \mathbf{U}\mathbf{\Sigma}\mathbf{V}^{\dagger}. \tag{2.83}$$

When $M > S$,

$$\mathbf{\Sigma} = \begin{bmatrix} \sigma_1 & 0 & \cdots & 0 \\ \vdots & \sigma_2 & & \vdots \\ & \vdots & \ddots & \\ 0 & 0 & \dots & \sigma_S \\ 0 & 0 & \dots & 0 \\ \vdots & \vdots & & \vdots \\ 0 & 0 & \dots & 0 \end{bmatrix},$$

where σ_s is the s^{th} singular value of $\mathbf{G}$, usually arranged in descending order of magnitude. Matrices $\mathbf{U}$ and $\mathbf{V}$ are unitary matrices of order $(M \times S)$ and $(S \times S)$ respectively, the columns of which contain the left and right singular vectors of $\mathbf{G}$, respectively. Using the unitary properties of the matrices, i.e. $\mathbf{U}^\dagger\mathbf{U} = \mathbf{U}\mathbf{U}^\dagger = \mathbf{I}$ and $\mathbf{V}^\dagger\mathbf{V} = \mathbf{V}\mathbf{V}^\dagger = \mathbf{I}$, equation 2.82 can be expressed as[32]

$$\mathbf{q}_{\text{opt}} = \mathbf{V}\mathbf{\Sigma}^+\mathbf{U}^\dagger\mathbf{p} = \mathbf{W}_{\text{opt}}^\dagger\mathbf{p}. \tag{2.84}$$

$\mathbf{\Sigma}^+$ is the pseudo-inverse of $\mathbf{\Sigma}$, and has the form

$$\mathbf{\Sigma}^+ = \begin{bmatrix} \frac{1}{\sigma_1} & 0 & \cdots & 0 & 0 & 0 & \cdots & 0 \\ 0 & \frac{1}{\sigma_2} & & \vdots & \vdots & \vdots & & \vdots \\ \vdots & \vdots & \ddots & & & & \ddots & \\ 0 & 0 & \dots & \frac{1}{\sigma_S} & 0 & 0 & & 0 \end{bmatrix}.$$

Therefore small singular values give rise to large terms in the solution of the inverse matrix.

The sensitivity of the solution for $\mathbf{q}$ due to small errors in $\mathbf{G}$ and $\mathbf{p}$ is determined by the condition number of $\mathbf{G}$. The condition number is defined as [32]

$$\kappa(\mathbf{G}) = \|\mathbf{G}\|\|\mathbf{G}^+\|, \tag{2.85}$$

where $\|\mathbf{G}\|$ denotes the Frobenius norm[33] (also called two-norm) of matrix $\mathbf{G}$. When matrix $\mathbf{G}$ is square $(M = S)$, equation 2.85 reduces to $\kappa(\mathbf{G}) = \|\mathbf{G}\|\|\mathbf{G}^{-1}\|$. The condition number can also be expressed in terms of the singular values,[32]

$$\begin{aligned} \kappa(\mathbf{G}) &= \sigma_{\max}/\sigma_n, \quad M > S; \\ \kappa(\mathbf{G}) &= \sigma_{\max}/\sigma_{\min}, \quad M = S, \end{aligned} \tag{2.86}$$

where σ_n is the smallest non-zero singular value of $\mathbf{G}$. It can be shown that errors

in the computed source strengths, $\delta\mathbf{q}$ are related to errors in the signals, $\delta\mathbf{s}$, by [32]

$$\frac{\|\delta\mathbf{q}\|}{\|\mathbf{q}\|} \leq \kappa(\mathbf{G}) \frac{\|\delta\mathbf{s}\|}{\|\mathbf{s}\|}. \tag{2.87}$$

Therefore extraneous noise introduced in the measurements of the acoustic pressures will have a disproportionately large effect on the solution for the source strengths if $\kappa(\mathbf{G})$ is large, i.e. if the matrix is ill-conditioned. If the auto- and cross-spectra of the source strengths and acoustic pressures are used, then the errors are proportional to $(\kappa(\mathbf{G}))^2$, making the solution even more sensitive to errors. Therefore in order to ensure a stable solution, it is necessary to identify which parameters contribute the most to the condition number. Nelson and Yoon [32] have carried out a comprehensive study on the relationship between the most common parameters in acoustic testing and the condition number. In general, they observed that

- the matrix of transfer functions $\mathbf{G}$ becomes badly conditioned as frequency decreases and as the sources move away from the receiver array – in the latter case, the receiver array fails to capture the acoustic evanescent field associated with the high spatial frequencies in the source distribution, and
- the inverse problem is best conditioned when the number of sensors and sources is small, when the geometrical arrangement of the sensors matches the assumed source distribution, when the sources and sensors are equally spaced apart and when the sensor array is symmetrically placed with respect to the sources.

2.9.2 Regularisation Techniques

There are two well-established ways how to avoid problems with very small singular values. The first is to keep only the largest D singular values and discard the rest, i.e. set the terms $1/\sigma_{D+1}$, $1/\sigma_{D+2}$, ..., $1/\sigma_{S-1}$, $1/\sigma_S$ equal to zero, to give a modified matrix of singular values $\mathbf{\Sigma}_\mathbf{D}^+$ This approach stabilises the final solution, however it also acts as a spatial low-pass filter of the true source distribution.[32] Furthermore, it is not always obvious up to which singular values to discard.[34] The other method, known as Tikhonov regularisation, is based on a redefinition of the cost function that penalises not only the sum of squared errors, but also the sum of squared source strengths. The cost function can be reformulated as [32]

$$J_R = \mathbf{e}^\dagger\mathbf{e} + \beta\mathbf{q}^\dagger\mathbf{q}, \tag{2.88}$$

where β is a small regularisation parameter. The solution in this case is [32]

$$\mathbf{q}_R = \left[\mathbf{G}^\dagger\mathbf{G} + \beta\mathbf{I}\right]^{-1}\mathbf{G}^\dagger\mathbf{p}. \tag{2.89}$$

The contribution of the regularisation parameter β can be identified by using singular value decomposition on the solution, to yield

$$\mathbf{q}_R = \mathbf{V}\mathbf{\Sigma}^+_{\mathbf{R}}\mathbf{U}^\dagger\mathbf{p}, \tag{2.90}$$

where

$$\begin{aligned}\mathbf{\Sigma}^+_{\mathbf{R}} &= \left[\mathbf{\Sigma}^\dagger\mathbf{\Sigma} + \beta\mathbf{I}\right]^{-1}\mathbf{\Sigma}^\dagger \qquad (2.91)\\ &= \begin{bmatrix} \frac{\sigma_1}{(\sigma_1^2+\beta)} & 0 & \cdots & 0 & 0 & 0 & \cdots & 0 \\ 0 & \frac{\sigma_2}{(\sigma_2^2+\beta)} & & \vdots & \vdots & \vdots & & \vdots \\ \vdots & \vdots & \ddots & & & & \ddots & \\ 0 & 0 & \cdots & \frac{\sigma_S}{(\sigma_S^2+\beta)} & 0 & 0 & & 0 \end{bmatrix}.\end{aligned}$$

Therefore the parameter β helps to stabilise the inverse, without having to omit any singular values. However this comes at a cost. Figure 2.13 shows the reconstructed source strength distribution of the source-receiver arrangement shown in figure 2.12. The source strength is equal to unity for the source in the middle and zero for the other sources, as shown in the "true" plot (a). For small values of β, large errors are introduced in the solution. As β is increased, the solution converges to a more accurate solution, and then the solution deteriorates again. Similar to singular value discarding, it is not always straightforward what is the optimum value for β. Furthermore, even the best solution (plot (d) in figure 2.13) is marred by resolution problems, similar to the case of the focused beamformer. It can be shown [16] that this phenomenon can be explained by SVD, where, in the noise-free case, the vectors of signals from the microphones $\mathbf{p}$ and source strengths $\mathbf{q}$ can be transformed in the spatial domain to $\tilde{\mathbf{p}} = \mathbf{U}^\dagger\mathbf{p}$ and $\tilde{\mathbf{q}} = \mathbf{V}^\dagger\mathbf{q}$ such that

$$\tilde{\mathbf{p}} = \mathbf{\Sigma}\tilde{\mathbf{q}}. \tag{2.92}$$

Therefore the ith singular value relates the ith "spatial mode" of the source distribution to the ith "spatial mode" of the sensor distribution. Since the higher spatial frequencies tend to be associated with the smallest singular values, any form of suppression of the contribution from the latter will result in a degradation in the spatial resolution.

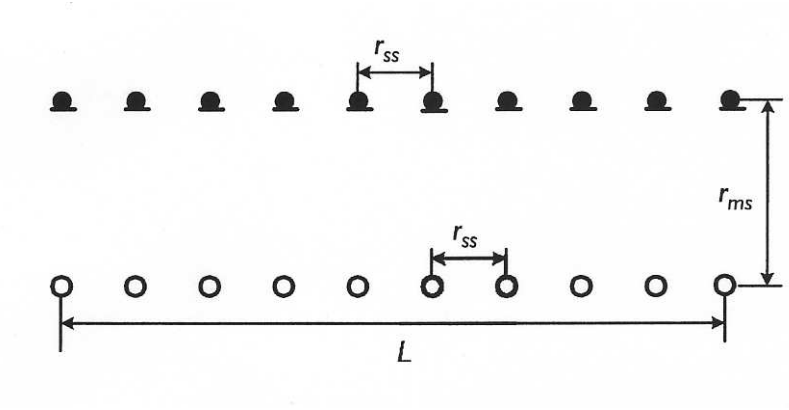

FIGURE 2.12: A source - receiver arrangement consisting of two linear arrays with 9 elements each. From ref. [16].

Holland and Nelson [35] have shown that it is possible to reformulate the inverse model to exploit known spatial correlation structures within large distributed sources, thereby drastically reducing the number of sensors required. This is especially relevant to large sources at high frequencies, where the correlation lengths may be small.

Recently Suzuki [36] has proposed a redefinition of the cost function presented in equation 2.88 with the aim of increasing the resolution of the inverse approach. The proposed cost function is of the form

$$J_R = \mathbf{e}^{\dagger}\mathbf{e} + \sum |\mathbf{q}|, \tag{2.93}$$

which avoids the spreading of the amplitude distribution. Unfortunately there is no direct solution to this cost function, and the author used an iterative approach to solve $\mathbf{q}$ whilst continuously trying to reduce the components of $\mathbf{q}$ (which is equivalent to narrowing the source region). In order to stabilise the problem, only the first few eigenvalues are used, and a Gaussian spatial filter is used to remove spurious spikes in the noise-source maps.[36] The author showed an improvement over conventional beamforming with deconvolution for a line source and a correlated monopole-dipole distribution. The biggest drawback of this method is that it does not automatically converge to the right solution. Furthermore, the sources under investigation need to be well defined before setting up the problem.

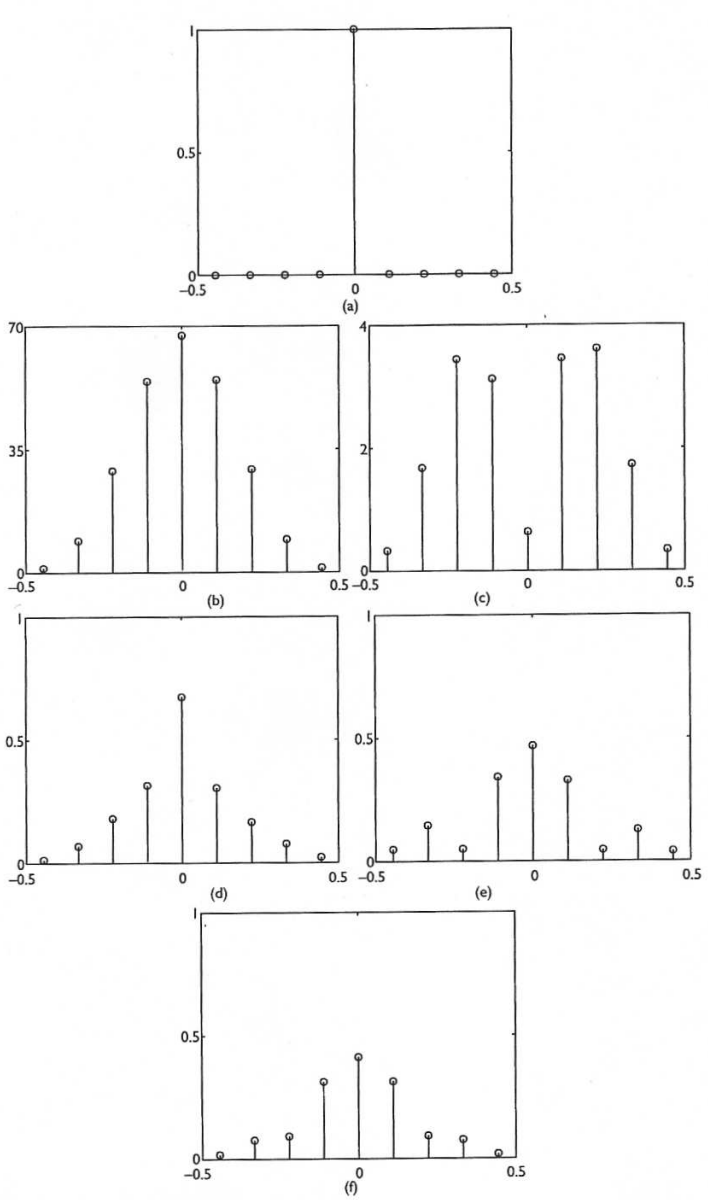

FIGURE 2.13: Reconstructed source distribution for the source-receiver arrangement shown in figure 2.12, with $r_{ms} = 2L$ and $r_{ss} = \lambda/2$. The true source distribution is shown in plot (a). Plots (b) to (f) show the reconstructed source strengths using equation 2.89 with $\beta = 0$, 0.1, 1, 100, 10^4, respectively. Results from calculations using 10% noise contamination in the pressures. From ref. [16].

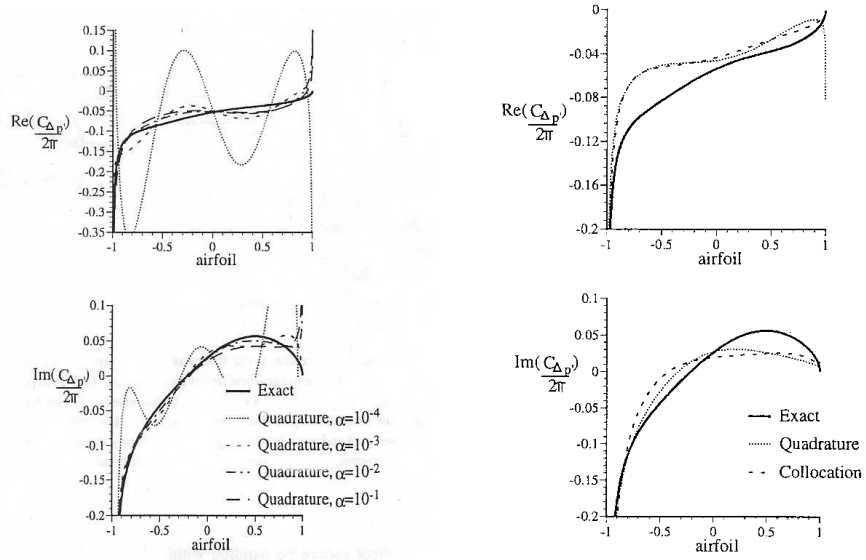

(a) Slight noise contamination

(b) 20% noise contamination

FIGURE 2.14: Real and imaginary parts of the non-dimensional unsteady surface pressure jump along a flat-plate aerofoil reconstructed from far-field pressure data contaminated by noise. The solid line represents the exact solution. From ref. [34].

2.9.3 Sensitivity of Inverse Method to Errors in the Input Parameters

The sensitivity of the inverse method to errors in the measured data is governed by the condition number of the Green's functions matrix $\mathbf{G}$. In this case, an optimum choice for the regularisation parameter can make the solution less prone to these kind of errors. Patrick Grace et al. [34] discuss the importance of this parameter when reconstructing the unsteady surface pressure of a flat-plate aerofoil from simulated far-field pressures contaminated with noise. Figure 2.14(a) shows the real and imaginary parts of the unsteady surface pressure along the aerofoil obtained using the exact and reconstructed solutions, for a slight noise contamination in the far-field data. The solution oscillates widely for a very small regularisation value, but improves as the same parameter is increased. On the other hand, figure 2.14(b) shows the reconstructed data using far-field pressures contaminated with a significant 20% error, and an optimum regularisation value. Although the deviation from the exact solution is not negligible, the solution is still satisfactory considering the large amount of noise injected. For similar cases, improvements were also achieved by careful selection of the receiver locations.

The far-field pressure data is not the only input parameter for the inverse problem.

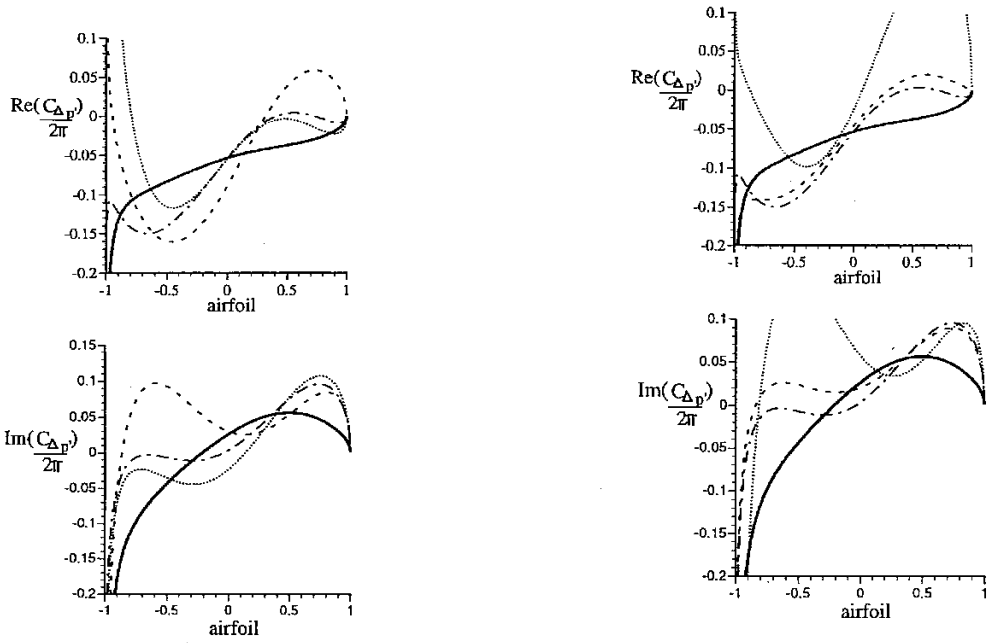

FIGURE 2.15: Real and imaginary parts of the non-dimensional unsteady surface pressure jump along a flat-plate aerofoil reconstructed using noise-free far-field data. Left plots generated with a 5% error in the Mach number M; right plots generated with a 5% error in the reduced frequency k_1. From ref. [34].

The same authors have also looked at the sensitivity due to errors in the Mach number M and the reduced frequency $k_1 = \omega c_0/2U_\infty$. The results, shown in figure 2.15, show that even small 5% errors in either parameter give significant errors in the reconstructed solutions. Moreover, no improvement is obtained by altering the regularisation method or parameter, or by optimising the sensor locations. Thus, the inverse aeroacoustic problem can be much more sensitive to errors in input parameters than to errors in the input data.

2.10 Summary

The focused beamformer is a spatial filter that enables an array of microphones to focus on a point in space, thereby rejecting noise emanating from other directions. This makes this technique ideal for measurements in a noisy environment such as a wind tunnel. Physical limitations give rise to artifacts in the results, such as poor resolution at low frequencies and spatial noise at high frequencies. Both these effects can be minimised by careful array design and using deconvolution techniques. Errors arising from coherent sources can in theory be minimised by applying multiple simultaneous beamformers using inverse methods. For a flush-

mounted array, noise is also generated by the turbulent boundary layer. This noise can be reduced by removing the leading diagonal of the cross spectral matrix, or by physically separating the microphones from the boundary layer. All these enhancements have improved the accuracy and applicability of beamforming. However there is still one fundamental issue with measurements in closed-section wind tunnels: the effect of reflections on the beamforming results. The following chapters aim to quantify this effect, and discuss ways how to correct for it.

Chapter 3

De-Reverberation

The focused beamformer is a powerful tool able to identify and quantify aeroacoustic sources in wind tunnel tests. Various techniques have been presented to deal with some of the shortcomings of beamforming, such as poor resolution at low frequencies, spatial noise at high frequencies, and high background noise levels contaminating the microphone signals. One potential problem that has not been discussed in detail yet is the effect of reflections from the wind tunnel boundaries on the beamforming results, qualitatively and quantitatively.

In ref. [19] Dougherty describes the effect of wind tunnel boundaries using the concept of image sources. This is a common model used in acoustics to describe the sound field in an enclosed space, especially at high frequencies.[37] Dougherty argues that image sources are significantly suppressed by a combination of spherical divergence and the array's sidelobe pattern. His argument is based on a point source centred in a wind tunnel. The following three counterarguments show that Dougherty's hypothesis is not necessarily valid. First, reflections off the wind tunnel boundaries are normally coherent with the source, and therefore have a much more significant impact on source level estimates than uncorrelated sources. Second, the array's sidelobe suppression performance deteriorates at low frequencies. Third, aeroacoustic sources in real wind tunnel tests do not always occur in the centre of the test section. For example a half aircraft model mounted directly on a wind tunnel boundary can exhibit several sources that are situated very close to a hard surface.

In terms of quantitative effects, Holland and Nelson[31] have demonstrated an error in beamformer output when using free-space Green's functions to represent the case of a single source under semi-reverberant conditions. This environment

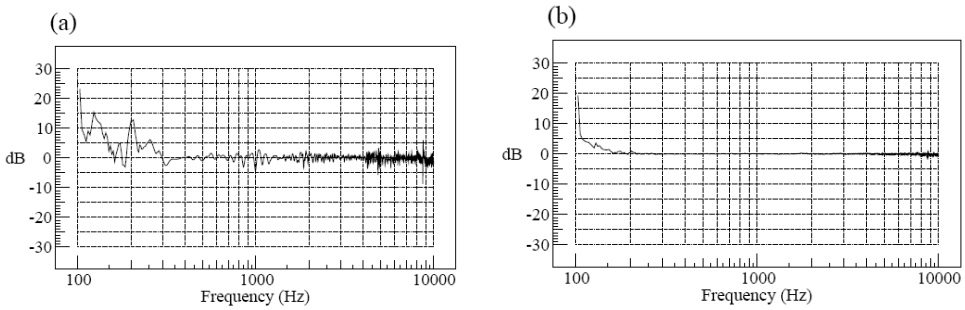

(a) Free-space (b) Measured

FIGURE 3.1: Error in source strength estimate using free-space and measured Green's functions. Semi-reverberant measuring environment, no flow conditions. From Holland and Nelson [31].

was modelled by placing reflective boards in an anechoic chamber. The free-space Green's functions give rise to an overestimate of the source strength at frequencies below 300 Hz, as shown in figure 3.1*(a)*. The authors managed to reduce significantly this error by "de-reverberating" the space (figure 3.1*(b)*), using measured Green's functions instead of free-space ones.

At higher frequencies, which are of most interest in beamforming, the errors vary within approximately $\pm$ 4 dB. Although these errors are small, one has to keep in mind that measurements were performed in a modified anechoic chamber at very low background noise levels. More significant errors might occur in a highly reverberant closed-section wind tunnel. Furthermore, as aircraft manufacturers push to obtain certification-quality results from wind tunnel measurements, even such small errors become significant.

It should also be noted that reflections arising in a hard-walled wind tunnel can modify the array's point spread function (PSF), as pointed out by Dougherty [19]. Advanced deconvolution techniques such as CLEAN and DAMAS (discussed in Section 2.7.2) rely on the theoretical PSF, and therefore their performance might be limited when applied to measurements carried out in a reverberant environment.

Guidati et al. [14] acknowledged the influence of reflections in a closed section wind tunnel, and proposed a technique which they referred to as "reflection canceller" (RC), which combines the reflections in the beamforming process using the concept of image sources. In the same study, the authors compare the Green's function generated by the RC to measured Green's functions in a 0.73×2.7 m hard walled wind tunnel, and found them to be more similar than conventional free-space Green's functions. Figure 3.2 shows a comparison of the degree of correspondence T between measured steering vectors and predictions using free-space

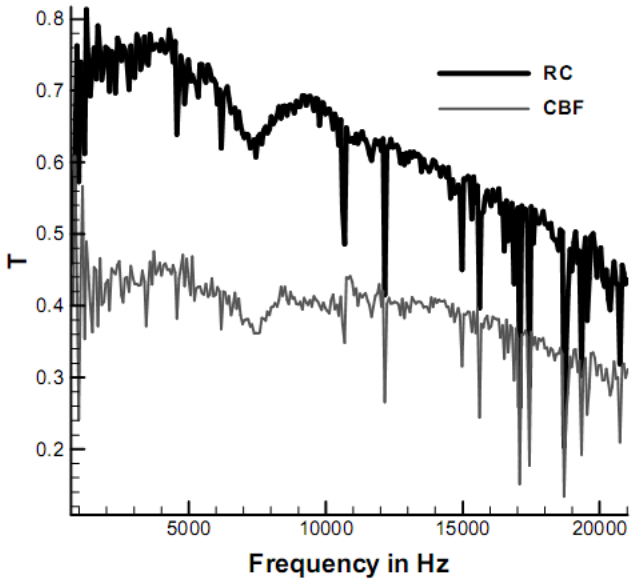

FIGURE 3.2: Correspondence between measured and predicted steering vectors. Predicted steering vectors are calculated using free-space Green's functions (CBF) and the Reflection Canceller (RC). From ref. [14].

Green's functions and the RC. The RC gave a clear advantage at low frequencies, although the correspondence diminishes rapidly above 10 kHz. The measured Green's functions were obtained in an empty wind tunnel. The authors also observed that beamforming using the RC produced a better resolution in the axis perpendicular to the two parallel boundaries, at the expense of higher sidelobe levels.

Sijtsma and Holthusen [15] followed on the work of Guidati et al., and showed that even the most simple version of the RC (taking into account only one image source, corresponding to the reflection from the nearest boundary) gives an improvement in beamforming accuracy at the lower frequencies. Their formulation is based on *a priori* knowledge of the exact source location. The authors also showed that the RC is highly sensitive to position errors at high frequencies, and propose an alternative model that essentially puts a further constraint on the cost function of the conventional beamformer (c.f. equation 2.19) to minimise the influence of the image source. This method was shown to be more robust at high frequencies, however it involves a matrix inversion, which limits its applicability in practice.

The work presented by Guidati et al. and Sijtsma and Holthusen proves that the influence of reflections in closed section wind tunnels cannot be ignored. Moreover, it is possible to correct for these effects. The scope of this chapter is to build on this previous work in order to develop a satisfactory de-reverberation technique

that offers improved accuracy in beamforming levels. It was deemed important to develop a technique that would be easy to implement, in terms of the input parameters and computational time penalties. This made the formulation by Guidati et al. more attractive. De-reverberation should give a better estimate for the beamforming steering vector $\mathbf{g}$ (c.f. equation 2.27), which represents the transfer functions between each grid point and the array microphones. This better estimate can be obtained by modelling the sound field in an enclosed space either analytically, numerically or experimentally.

3.1 Analytical Methods

Two frequently used methods to model sound fields in enclosed spaces are the modal technique and the image source model. The modal technique assumes the sound field in the room to consist of a superposition of modes. Because the modal density gets very high as the wavelength becomes small compared to the enclosure dimensions, this method is more suit for low frequencies. At high frequencies, the wavelengths become small compared to the boundary dimensions, and it can be assumed that the enclosed space is bound by rigid walls of infinite extent. The boundaries can then be replaced by an infinite set of mirror image sources situated outside the enclosed space. Since beamforming is of particular interest at high frequencies, such an image source model (ISM) is the preferred method.[1]

The test section of a closed-section wind tunnel is effectively a duct, and can be modelled by a twofold infinity of image sources lying in a plane transverse to the duct, as shown in figure 3.3.[37] The sound field in the duct will therefore consist of the sum of contributions from the true source and all the resulting image sources.

For a rectangular duct, it is easy to determine the locations of the image sources based on the position of the true source with respect to the wind tunnel boundaries. Figure 3.4 shows a schematic downstream view of a $2.1 \times 1.5\,\mathrm{m}$ wind tunnel test section, with a point source close to the floor. It is convenient at this stage to group image sources into order numbers, referring to imaginary rectangles of increasing size that encloses a subset of image sources. For example, for a rectangular duct, an ISM of order zero will represent the eight images closest to the true source, order one represents the nearest 24 images, and so on. Indeed, if O represents the

[1] This method is similar to the "Reflection Canceller" technique suggested by Guidati et al. [14].

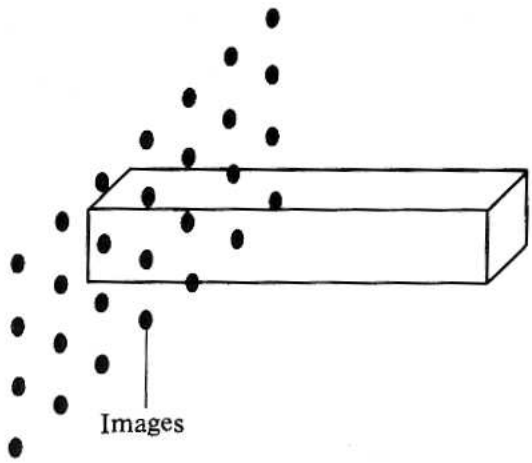

FIGURE 3.3: Distribution of image sources for a source in an infinitely long rectangular duct. The array of sources has a repetition distance of twice the distance between the walls. From ref. [37].

order of the ISM, the total number of image sources J included in the model is

$$J = \sum_{o=0}^{O} 8\,(o+1)\,. \tag{3.1}$$

This grouping is based on the propagation distance between source and receiver: the sound from the first set of eight image sources would arrive first, then from the next group of 16 images, and so on.

The pressure at the mth microphone due to a distribution of discrete identical point sources within a volume V can be expressed as

$$\begin{aligned} p(\vec{x}_m) &= \int_V \Bigg[\mathrm{i}\omega\rho_0 q_s \delta(\vec{y}-\vec{y}_1)\,\frac{\mathrm{e}^{-\mathrm{i}kr_1}}{4\pi r_1} \\ &+ \mathrm{i}\omega\rho_0 q_s \delta(\vec{y}-\vec{y}_2)\,\frac{\mathrm{e}^{-\mathrm{i}kr_2}}{4\pi r_2} \\ &+ \mathrm{i}\omega\rho_0 q_s \delta(\vec{y}-\vec{y}_3)\,\frac{\mathrm{e}^{-\mathrm{i}kr_3}}{4\pi r_3} + \ldots \Bigg]\,\mathrm{d}V \\ &= \mathrm{i}\omega\rho_0 q_s \frac{\mathrm{e}^{-\mathrm{i}kr_1}}{4\pi r_1} + \mathrm{i}\omega\rho_0 q_s \frac{\mathrm{e}^{-\mathrm{i}kr_2}}{4\pi r_2} + \mathrm{i}\omega\rho_0 q_s \frac{\mathrm{e}^{-\mathrm{i}kr_3}}{4\pi r_3} + \ldots \\ p(\vec{x}_m) &= \frac{\mathrm{i}\omega\rho_0 q_s}{4\pi}\left[\frac{\mathrm{e}^{-\mathrm{i}kr_1}}{r_1} + \frac{\mathrm{e}^{-\mathrm{i}kr_2}}{r_2} + \frac{\mathrm{e}^{-\mathrm{i}kr_2}}{r_2} + \ldots\right], \end{aligned} \tag{3.2}$$

where $r_j = |\vec{y}_j - \vec{x}_m|$ and $\vec{y}_j$ denotes the location of the jth image source. In practice, only a finite number of image sources can be taken into account. This is justifiable because the further away the image sources (corresponding to a large

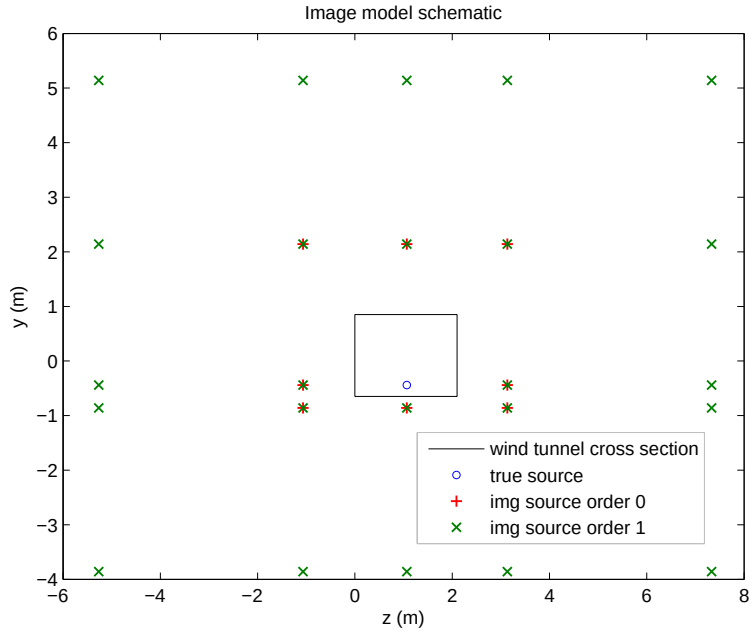

FIGURE 3.4: Image source positions generated by a 0th and 1st order image source models. The wind tunnel cross section (upstream view) is modelled as a rectangle for simplicity.

number of boundary interactions), the lesser their impact due to spherical spreading and dissipation losses.

From equation 3.2 the case of a true point source at $\vec{y}_0$ and a finite number J of image sources located at $\vec{y}_j \quad j = 1, 2, \ldots, J$ can be modelled by an effective transfer function

$$G(\vec{x}_m|\vec{y}_0) = \frac{\mathrm{i}\omega\rho_0}{4\pi} \sum_{j=0}^{J} \frac{\mathrm{e}^{-\mathrm{i}kr_j}}{r_j}. \tag{3.3}$$

In practice there will be dissipation of energy with each boundary interaction and during sound propagation (especially at high frequencies). The dissipation during sound propagation can be factored in by using a complex wavenumber $\tilde{k}$.[38] To take into account the losses at the boundaries, each reflection needs to be taken into consideration. Assuming the jth image source has a corresponding total number of boundary interactions I_j, then

$$G(\vec{x}_m|\vec{y}_0) = \frac{\mathrm{i}\omega\rho_0}{4\pi} \left[\frac{\mathrm{e}^{-\mathrm{i}\tilde{k}r_0}}{r_0} + \sum_{j=1}^{J} \frac{\mathrm{e}^{-\mathrm{i}\tilde{k}r_j}}{r_j} \prod_{i=1}^{I_j} R^{\mathrm{d}}_{i,j} \right], \tag{3.4}$$

where $R^{\mathrm{d}}_{i,j} = R_{i,j}(\theta_i)$ is the complex reflection coefficient of the boundary responsible for the ith reflection of the jth image source (which is dependent on the angle

of incidence θ). This step complicates the ISM considerably: complex reflection coefficients are very difficult to predict, and to compute the angle of incidence for each reflection requires a very complex geometrical model. In this case, it makes more sense to use numerical techniques such as ray tracing methods. As a first approximation, all boundaries can be assumed to have the same angle-independent reflection coefficient R^{i}, in which case equation 3.4 becomes

$$G(\vec{x}_m|\vec{y}_0) = \frac{\mathrm{i}\omega\rho_0}{4\pi}\left[\frac{\mathrm{e}^{-\mathrm{i}\tilde{k}r_0}}{r_0} + \sum_{j=1}^{J}\frac{\mathrm{e}^{-\mathrm{i}\tilde{k}r_j}}{r_j}\left(R^{\mathrm{i}}\right)^{I_j}\right]. \tag{3.5}$$

This formulation satisfies the two initial requirements in terms of speed and input parameters. No matrix inversions are involved, which means that this method is not limited to specific scenarios. Furthermore no extra wind tunnel time is required. However there are many implications to the simplifying assumptions. If the wind tunnel test section is not perfectly rectangular, determining the exact locations of the image sources becomes more complicated. The presence of the model and any support structures, which often have a complex geometry, is not taken into account. Errors can therefore be expected if the dimensions of the test model are comparable to the wind tunnel test section. The accuracy of the ISM deteriorates at the lower frequencies, depending on the wind tunnel test section dimensions. Reflections are assumed to obey geometrical laws, and scattering and diffraction effects are assumed to be negligible.

3.2 Numerical Methods

When the wind tunnel test section has a complex geometry, or the size of the test model is significant, an analytical ISM is not a viable solution. Numerical techniques can be used in this case, keeping the advantage of zero extra wind tunnel time required. At low frequencies, modal techniques such as finite element and boundary element methods are normally used. However, as beamforming is normally used for high frequencies, geometrical acoustic simulation techniques may be more suitable.

Geometrical acoustics, such as ray tracing and beam tracing methods are widely used to simulate the acoustic field within enclosed spaces at high frequencies. The beam tracing method assumes that the wave propagation can be described by the travel of beams carrying the energy quantity, whose propagation can be

determined entirely by the geometrical shape of the enclosure. An emitted beam will possess a certain amount of energy at the starting point, and loses some of this energy during propagation due to air attenuation and absorption when hitting the enclosure surfaces. The accuracy of this method is poor at low to mid frequencies for two main reasons: the phase information is neglected, which means that interference phenomena are ignored, and statistically-determined frequency-averaged material properties are used. The phased beam tracing method (PBTM) was suggested to overcome the inherent problems of energy methods by including the phase information in the geometrical acoustics, thus extending its applicability into the mid frequencies.[38] In this context, *low*, *mid* and *high* frequencies refer to the the modal density in the enclosure, and the Schroeder cutoff frequency f_c is usually used as an approximative boundary indicator: frequencies below f_c are considered to be *low* frequencies, *mid*-frequencies fall within f_c and $4f_c$, whilst higher frequencies can be considered as *high*. The estimated[2] Schroeder frequency for the $2.1 \times 1.5\,\mathrm{m}$ wind tunnel test section at the University of Southampton is approximately 400 Hz, which means that it's safe to assume that all frequencies above 1.6 kHz can be considered as *high*.

The phased beam tracing method involves two complex quantities:

- the complex pressure reflection coefficient R^{d} (dependent on the angle of incidence θ) representing the acoustical properties of the enclosure boundaries, and
- the complex wavenumber $\tilde{k} = k - \mathrm{i}m/2$[38] (where k is the wavenumber in a lossless free field and m is the air attenuation factor) which models the phase change during the propagation of sound in air.

The complex pressure reflection coefficient R^{d} can be calculated from the measured surface impedance Z_w and radiation impedance $Z_r(\theta)$ of the boundary,

$$R^{\mathrm{d}} = R(\theta) = \frac{Z_w - Z_r(\theta)}{Z_w + Z_r(\theta)}. \tag{3.6}$$

Approximate solutions for Z_w and Z_r are given in ref. [38].

As a rough approximation, it can be assumed the reflection coefficient is a real-valued quantity and that the surface is locally reacting, such that the reflection

[2]The test section of a wind tunnel can be considered as an enclosure with two sides having infinite absorption, which means that only axial and tangential modes exist. The estimated value for f_c was obtained by calculating the number of modes within the half-power bandwidth of one third-octave bands, and selecting the lowest band where the number of modes is equal to three.

coefficient becomes angle independent,

$$R^{\mathrm{i}} = \pm\sqrt{1-\alpha_s}, \tag{3.7}$$

where α_s is the absorption coefficient of the boundary material in a diffuse sound field. Most materials have a positive value of R^{i}; negative values correspond to pressure release boundaries, such as an open pipe end [39].

Jeong et al. [38] observed a noticeable improvement with the phased beam tracing method when simulating the energy impulse response of a medium-size room, when compared to the conventional BTM. Using an angle dependent reflection coefficient yielded more accurate results at the mid frequencies ($f_c < f < 4f_c$), however the computational time penalty was significant: results using R_θ^{d} took 31 times longer to compute than when using R^{i}. As a final note, the authors recommend the use of complex reflection coefficients from measured data if the best accuracy is required.

3.3 Experimental Methods

Numerical simulations can be an effective way how to model a realistic wind tunnel test section and test model setup, however unless some approximations are made, the modelling and computational efforts might not be viable. In some cases, the experimental determination of the transfer functions between source and receiver might be the only viable method. This can be done in a number of ways.

3.3.1 Conventional Sources

The simplest way how to determine an acoustic transfer function is to place a source of known strength at $\vec{y}_0$ and measure the resulting pressure at the receiver. In typical beamforming applications, a scan plane sampled by 100×100 grid points is common. Since each grid point is a hypothetical source position, this means that 10,000 individual measurements would be necessary.

This requirement can be relaxed by assuming that the measured Green's function can be extrapolated and still be valid within a sphere of radius equal to half a wavelength of the frequency of interest. At the lower frequencies this assumption reduces the required measuring point considerably. For example, for a scan plane of one squared metre the minimum number of unique source positions required

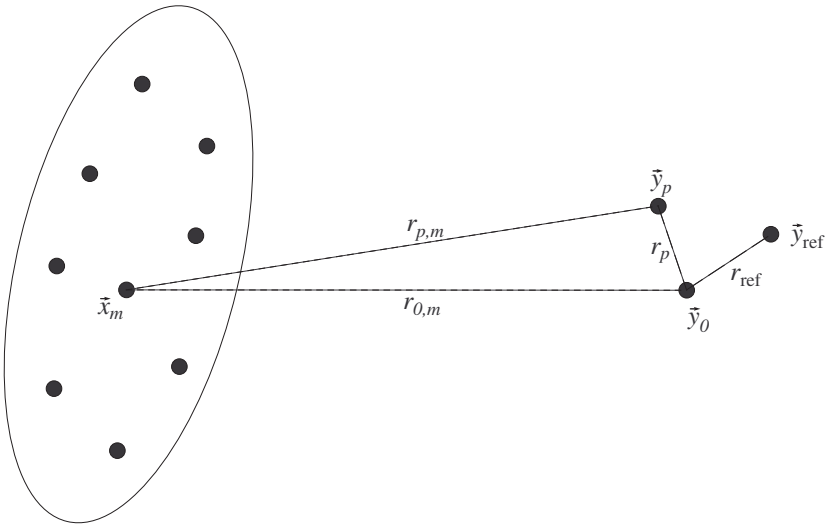

FIGURE 3.5: Schematic showing the location of the mth microphone ($\vec{x}_m$), the point source ($\vec{y}_0$), the reference microphone ($\vec{y}_{\text{ref}}$) and grid point ($\vec{y}_p$) as used to measure the Green's functions.

at 2 kHz is 43. The number of required locations increase quadratically with frequency, so that at 4 kHz, 173 positions are required.

Figure 3.5 shows the geometry involved to measure the transfer functions $G(\vec{x}_m|\vec{y}_p)$ using a compact, omni-directional source of unknown strength. The source is placed at $\vec{y}_0$ and a reference microphone is placed at $\vec{y}_{\text{ref}}$. If the pressure due to the compact source is assumed to be of the form

$$p = \frac{S\mathrm{e}^{-\mathrm{i}kr}}{r}, \quad S = \frac{\mathrm{i}\omega\rho_0 Q_s}{4\pi}, \tag{3.8}$$

then the transfer function between the source position and the mth microphone can be expressed as

$$G(\vec{x}_m|\vec{y}_0) = \frac{p(\vec{x}_m)}{p(\vec{y}_{\text{ref}})}\frac{\mathrm{e}^{-\mathrm{i}kr_{\text{ref}}}}{4\pi r_{\text{ref}}} = H_1\frac{\mathrm{e}^{-\mathrm{i}kr_{\text{ref}}}}{r_{\text{ref}}}, \tag{3.9}$$

where H_1 is the measured frequency response function between the mth array microphone and the reference microphone.

In order to estimate the transfer function to the grid point $\vec{y}_p$, the scalar distance $r_{p,m}$ can be expressed in terms of $r_{0,m}$ and a new dummy variable r_δ such that

$$r_{p,m} = r_{0,m} + r_\delta. \tag{3.10}$$

This gives

$$\begin{aligned} G(\vec{x}_m|\vec{y}_p) &= \frac{\mathrm{e}^{-\mathrm{i}k[r_{0,m}+r_\delta]}}{(r_{0,m}+r_\delta)} \\ &= \frac{\mathrm{e}^{-\mathrm{i}kr_{0,m}}}{r_{0,m}} \frac{\mathrm{e}^{-\mathrm{i}kr_\delta}}{1+\frac{r_\delta}{r_{0,m}}} \\ &= G(\vec{x}_m|\vec{y}_0) \frac{\mathrm{e}^{-\mathrm{i}kr_\delta}}{1+\frac{r_\delta}{r_{0,m}}}. \end{aligned} \tag{3.11}$$

Using equation 3.9 finally gives

$$G(\vec{x}_m|\vec{y}_p) = H_1 \frac{\mathrm{e}^{-\mathrm{i}kr_{\mathrm{ref}}}}{r_{\mathrm{ref}}} \frac{\mathrm{e}^{-\mathrm{i}kr_\delta}}{1+\frac{r_\delta}{r_{0,m}}}. \tag{3.12}$$

In free field conditions this extrapolation of Green's functions would be subject to the condition

$$|\vec{y}_p - \vec{y}_0| < \frac{\lambda}{2}, \tag{3.13}$$

where λ is the shortest wavelength of the sound of interest. In a reverberant environment, this method is approximate and should only be used if the wind tunnel test section is large compared to the wavelength, and $\vec{y}_0, \vec{y}_p$ and $\vec{y}_{\mathrm{ref}}$ are close together.

The extrapolation constraint is the most significant limitation of this method, due to the physical size of most commercial broadband speakers. It might be necessary to make use of the principle of reciprocity and place microphones at the grid positions and the source at the array microphone locations. It can also be difficult to find a sufficiently small speaker that can emit sufficient energy in the entire frequency range of interest.

3.3.2 Impulse Tests

A further challenge of measuring Green's functions in wind tunnels is the wide frequency range of interest in aeroacoustic measurements. The source has to emit sufficient energy in a very wide frequency band (for example 1 - 50 kHz), yet it has to be sufficiently small so that it does not significantly alter the sound field in the test section. Furthermore, ideally measurements should be carried out with the test model in situ, which puts further constraints on the physical size of the sound source. An impulse can be better suit to satisfy these requirements.

The impulse response function provides complete information on the acoustic re-

sponse of an enclosed space. It is extensively used to quantify the acoustic properties of auditoria and performing spaces. Traditionally the room is excited by a transient noise of short duration, such as a gun shot. With advances in signal processing, other methods such as Maximum Length Sequence (MLS) or sine sweeps have become more popular.[40] These methods use autocorrelation techniques to yield the impulse response from a deterministic signal, and have the advantage of being less prone to noise. The main disadvantage is that a conventional source is required.

An ideal impulse (delta function in mathematical terms) can be thought of as a function having zero length in time and infinite amplitude. This concept is widely used for mathematical analyses due to its unique time and frequency domain properties. An ideal impulse is not physically realisable, however impulse-like physically realisable signals can be generated which are adequate over typical frequency ranges of interest, and pose little or no theoretical compromises in measurement accuracy if proper techniques are utilised.

An impulse-like transient should satisfy the following criteria:[41]

- it must have a relatively short time span;
- it should be wide enough to contain sufficient power spectral density for a good signal to noise ratio;
- the spectrum must be adequately uniform over the desired frequency range;
- is must not possess any non-linear propagation characteristic problems;
- and it must be a physically realisable signal.

3.3.2.1 Use of Impulse Tests in Literature

Singh and Katra[41] used an acoustic impulse to measure the transmission loss of mufflers. The isolated incident, reflected and transmitted pulses were captured by appropriately located pressure transducers. Time domain averaging was used to eliminate flow noise components. They described the technique as reliable, efficient and versatile. The major drawbacks were a somewhat limited dynamic range, cost and complexity of hardware and software and limited applicability for the study of non-linear phenomena. The authors used a horn driver to produce the acoustic impulse in the muffler. Data acquisition was performed at 4096 Hz,

which gives a time resolution of 0.25 ms. FFT analysis was done with a block size of 512 (time window = 0.125 s).

Salikuddin et al. [42] used the impulse technique to determine the jet nozzle acoustic transmission coefficient. They attribute the limited dynamic range obtained by Singh and Katra to the low energy intensity of the impulse generated by the horn driver, and propose a high voltage spark discharge as a high intensity alternative. This was chosen because of its flatter, more uniform spectrum, pulse uniformity and ease of operation. The main disadvantage was that the very high voltages caused electrical and electromagnetic interference problems. Once again, the frequency of interest was limited up to 2.5 kHz.

Salikuddin et al. [43] investigated yet another acoustic impulse application, this time to quantify the magnitude of the reflections in a hard-walled wind tunnel, and determine the viability of measuring propfan noise signals from microphones mounted on a model aeroplane. Due to the nature of the wind tunnel (transonic), the maximum background noise was about 130 dB (at M = 0.8); furthermore, the propfan noise dictated a frequency range of interest up to 8 kHz. Two impulsive sources were tested: a high voltage spark discharge as discussed previously, and a system of 19 electro-acoustic drivers interconnected by a system of tubes. The purpose of the tubes was to ensure long propagation times of the high intensity pulses, resulting in non-linear propagation effects which in turn result in a steeper pulse than the individual generated pulses. A detailed analysis of the output from the source exit as a function of input pulse magnitude and width, together with the directivity characteristics of the source with and without flow was carried out. Of particular interest is the observation that the shear layer of the jet depletes high frequency information. The electro-acoustic driver source was eventually chosen due its superior repeat rate (shorter averaging times).

In all these three cases, an impulse was primarily chosen because the duration is sufficiently short that the incident, reflected and transmitted pulses are separated in time.

Arana et al. [44] tackle the main limitations of using electro-acoustic sources to generate impulses: while generation and amplification of the impulsive electric signal can be efficiently done, emission through amplifiers distorts the impulsive signal, due to the inertia of the amplifier acoustic system. Furthermore these kind of sources can be highly directional at high frequencies. The authors therefore analyse pseudo-impulsive sources, in the form of small explosive charges closed in cylindrical cartridges, as a possible alternative. They found these sources to

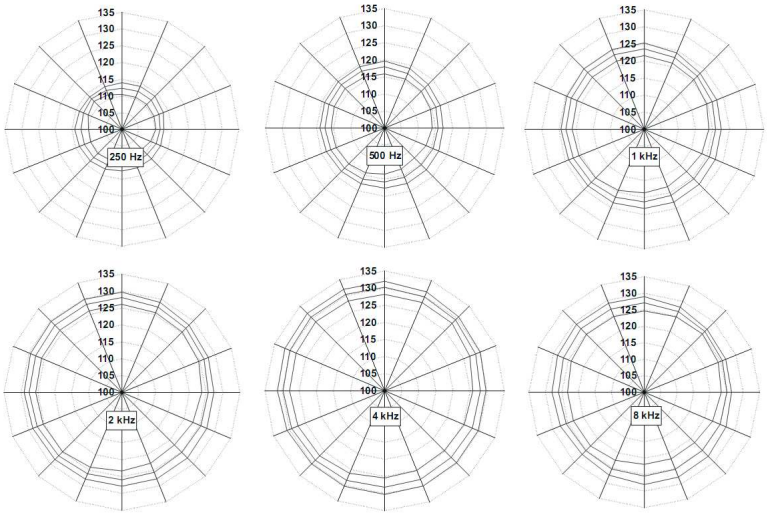

FIGURE 3.6: Measured directivity of a pseudo-impulsive source, averaged over 20 explosions. From ref. [44].

be omnidirectional, repeatable and with a sufficient spectral power throughout the frequency range of interest. Figure 3.6 shows the measured directivity, in octave bands, of these pseudo-impulsive sources. Of particular interest is the nearly perfect uniform directivity achieved at 8 kHz. Unfortunately data was only presented up to 8 kHz, so the characteristics at higher frequencies are not clear.

3.3.3 Alternative methods

One of the biggest drawback of any Green's function measurement strategy is the large number of measurement positions required, this is further complicated if a test model is present. Innovative solutions may have to be found. One possibility is to borrow the concept of grid refining often used in numerical computations, where the grid is made very fine only where it is necessary. In the same way, the spatial sampling of the measurements can be varied depending on the geometry of the model, with more measurements carried out, for example, along the slats and flaps on the wing of an aircraft. Other possibilities could be devised by borrowing concepts from underwater acoustics. For example, Roux and Fink [45] outline a way how to estimate Green's functions between two points A and B without using either as source, by introducing the concept of secondary sources. With reference to figure 3.7, the Green's function between points A and B is computed by averaging the correlation of the signals received at A and B due to the secondary sources S. The problem described is two dimensional (A, B and S are coplanar), and S has to span the whole depth of the space. However this theory could

FIGURE 3.7: Problem definition for measuring the Green's function between points A and B using secondary sources S. From ref. [45].

potentially be extended to three dimensions, with the secondary sources spanning a two-dimensional plane (i.e. the wind tunnel test section).

3.4 Summary

There are few instances in literature where the importance of steering vector choice is discussed in detail. The two most relevant studies are by Guidati et al. and Sijtsma and Holthusen. The former proposed the reflection canceller to incorporate the reflections in the beamformer, however there is no indication on the effect this has on beamforming levels. Sijtsma and Holthusen use a simplified variant of this method to show the improvements in the results, however their study is based on a priori knowledge of the exact source position.

In this chapter an analytical method similar to the reflection canceller has been developed to take into account reflections in a hard-walled wind tunnel. This Image Source Model (ISM) includes a correction factor for dissipation of energy at the test section boundaries. In the following two chapters the ISM is analysed in terms of its applicability, stability, and performance benefits.

There are other ways to model Green's functions in an enclosed space. The proposed Image Source Model can only be implemented for simple test section geometries. More complex scenarios necessitate the use of numerical or experimental techniques.

A proof of concept impulse response measurement technique was also developed as part of this work. Unfortunately this technique was of limited success. Details can be found in Appendix B.

Chapter 4

The Image Source Model

A number of methods can be used to obtain a better estimate for the steering vector $\mathbf{g}$ when beamforming in a reverberant closed-section wind tunnel (as opposed to the conventional use of free-space Green's functions). As discussed in the previous chapter, an Image Source Model (ISM) offers certain advantages over the other methods. An ISM aims to reconstruct the sound field in an enclosure by replacing the boundaries with a finite number of discrete image sources. To simplify the model, dissipation at the walls can be assumed to be purely resistive and independent of the angle of incidence. The Green's functions then take the form expressed in equation 3.5, where the angle-independent reflection coefficient R^{i} is given by equation 3.7. This makes it a semi-analytical model, which means that it will be computationally fast compared to fully numerical tools like CAA and phased ray tracing methods. Furthermore it requires minimum additional information compared to conventional beamforming: the relative positions of the array and scan plane with respect to the wind tunnel test section, and an estimate of the absorption coefficients of the wind tunnel boundaries.

Given the assumptions considered to obtain this semi-analytical model, it is necessary to evaluate its performance. In this chapter the performance is assessed in terms of the point spread function, sensitivity to errors and an experimental validation of the resulting transfer functions. In the next chapter the performance is assessed with respect to the absolute beamforming levels.

4.1 The Point Spread Function when using an ISM

The point spread function (PSF) describes the array's response to a unit point source, and is a function of the steering vectors (c.f. equation 2.33 on page 17). Since the ISM gives a modified estimate for the steering vector, the array response will change, which will be reflected by a modified beamforming plot.

To illustrate this effect, the same microphone array-scan plane combination considered in Section 2.4 will be used. However this time $\mathbf{g}$ is generated using equation 3.5 on page 55, assuming an ISM of order 0 (only the first set of eight image sources included). The array is assumed to be flush mounted centrally in the ceiling of a rectangular duct 2.1 m wide and 1.5 m high. The 1×1 m scan plane is parallel to the array plane and at a perpendicular distance of 1 m below it. The inter-grid spacing is $\Delta x = \Delta y = 0.01$ m. All the boundaries are assumed to be rigid and uniform, with $R^i = +\sqrt{1-\alpha}$ estimated from the following absorption coefficient (α) values[1]:

- 0.01 for $f \leq 1$ kHz;
- 0.05 for $1 < f \leq 2$ kHz;
- 0.10 for $2 < f \leq 4$ kHz;
- 0.12 for $4 < f \leq 8$ kHz;
- 0.15 for $f > 8$ kHz.

The complex wavenumber $\tilde{k}$ was calculated using $\tilde{k} = k - \mathrm{i}m/2$, as suggested in ref. [38]. The value for the air attenuation factor m was approximated by $m \approx 4.66 \times 10^{-13}\omega^2$ [Nepers per metre].[46]

The resulting PSFs at 2, 4, 8 and 16 kHz are shown in figure 4.1. The x-axis is parallel to the length of the duct. This means that the walls of the wind tunnel would be represented by two horizontal lines parallel to the x-axis. These PSFs can be compared to those in figure 2.6 on page 18, which were generated using free-space Green's functions.

[1] These values are based on generic data found in literature for acoustically hard surfaces. It is assumed that these values are independent of flow, although this could not be validated.

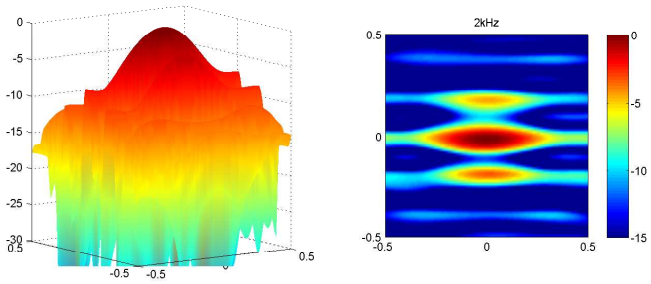

(a) 2 kHz

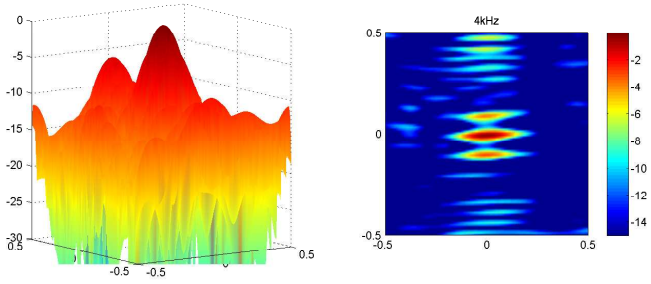

(b) 4 kHz

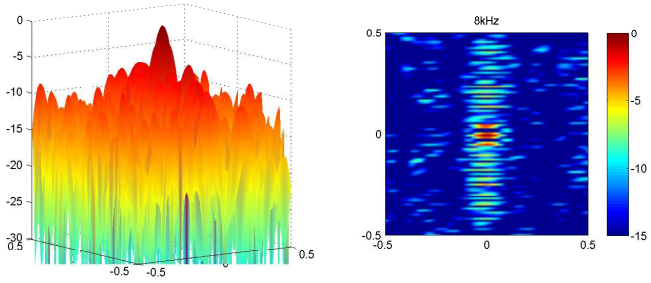

(c) 8 kHz

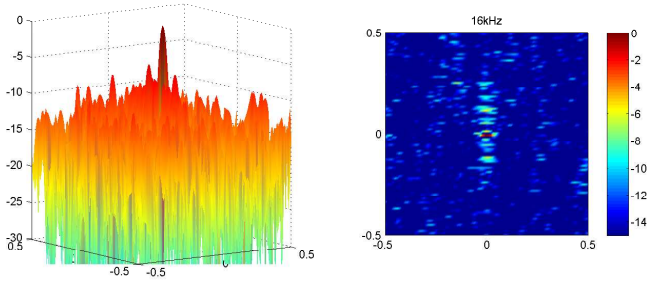

(d) 16 kHz

FIGURE 4.1: Point Spread Functions of a 56 microphone array for a point source centred on the scan plane, using an Image Source Model based on a wind tunnel test section of 2.1 × 1.5 m (see text for details).

It is evident that de-reverberation has a significant effect on the array's response. The most noticeable effect is that the mainlobe is flattened along the axis perpendicular to the wind tunnel boundaries. Furthermore a number of sidelobes are introduced with a peak level comparable to that of the mainlobe. The most significant sidelobes are situated very close to the mainlobe. Both these features could prove to be problematic to beamforming, especially the sidelobes. Similar behaviour was observed by Sijtsma and Holthusen [15].

The ISM is mainly dependent on two factors: the losses at the boundaries and the size of the wind tunnel test section. As the losses increase (boundaries made more acoustically absorbent), the point spread functions will change such that in the limit of $\alpha = 1$, the PSF becomes the same as for free-space Green's functions. The size of the test section also has an effect. Figure 4.2 shows the resulting PSFs for a wind tunnel having the same type of walls but double the cross-section of that considered in figure 4.1, i.e. $4.2 \times 3\,\mathrm{m}$. In this case the mainlobe is less distorted, and the influence of sidelobes is less pronounced. Therefore a larger wind tunnel is less prone to the influence of image sources.

In theory this complex beam pattern should cancel out an equally-complex response in the wind tunnel caused by all the coherent reflections. In practice errors and inaccuracies in the de-reverberation formulation might mean that these two complex responses do not cancel out, giving rise to degraded conventional beamforming results. This is especially relevant to measurements in smaller wind tunnels with highly-reflective walls, and may be the reason why to date de-reverberation has not been investigated in further detail. However, using the ISM formulation, de-reverberation only changes the steering vectors, and the changes to the array's response are completely integrated in the PSFs. These PSFs can therefore be used to deconvolve these artifacts from the final plots. In fact in the following chapter it will be shown that deconvolved, de-reverberated results can be qualitatively very similar to deconvolved plots based on free-space Green's functions.

4.1.1 Effect on Source Power Integration

Source power integration (SPI), introduced in Section 2.8.1, is the standard way to extract quantitative results from beamforming plots. This technique normalises the sum of all the source powers by the PSF. As de-reverberation changes the PSF significantly, it is necessary to check whether SPI is equally valid when using an

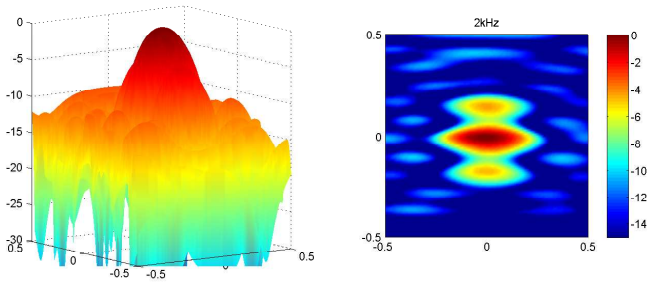

(a) 2 kHz

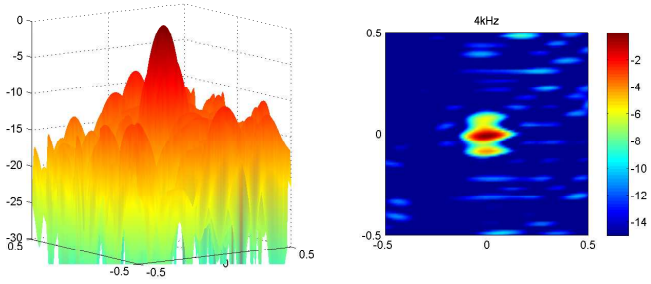

(b) 4 kHz

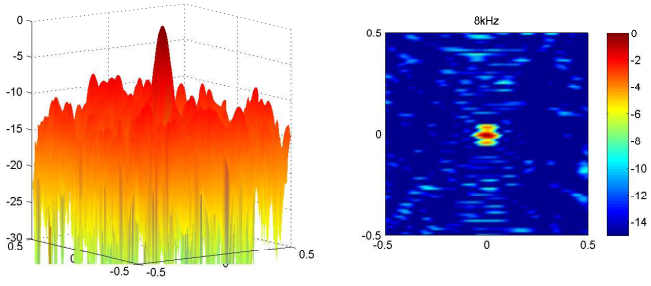

(c) 8 kHz

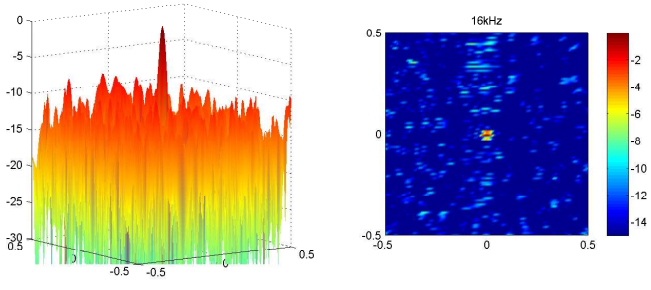

(d) 16 kHz

FIGURE 4.2: Point Spread Functions of a 56 microphone array for a point source centred on the scan plane, using an Image Source Model based on a wind tunnel test section of 4.2×3 m (see text for details).

TABLE 4.1: Errors in levels extracted from beamforming plots using an Image Source Model. Grid resolution is 0.01 m.

Error in source strength (dB)					
	Full CSM		Diagonal Removal		
freq (kHz)	Sum	SPI	Sum	SPI	SPI + threshold
2	29.5	0.005	28.5	0.006	0.006
4	25.7	0.012	22.4	0.02	0.02
8	25.3	0.012	20.2	0.04	0.02
16	23.1	0.022	13.4	0.20	0.05
32	23.3	0.020	8.59	-0.55	0.06

ISM. This check was performed on the PSF plots, which represent the simplest case of a single point source of unit strength. This method is consistent with the analysis presented in Section 2.8.1. Table 4.1 lists the errors in source strength obtained when using a simple summation versus SPI (with and without threshold). Both the full CSM and CSM with diagonal-removal cases are considered.

The results are very similar to those shown in table 2.2 on page 35 (using free-space Green's functions), and confirm that even with de-reverberation,

- with a full CSM, SPI accurately extracts the true source strength;
- when the leading diagonal of the CSM is removed, minor errors are introduced, which can be practically nullified by using a threshold as defined in equation 2.65.

4.2 Validating the Image Source Model

A number of assumptions were made when formulating the ISM, namely that the wind tunnel is an infinite duct with a rectangular cross-section, and that dissipation at the walls is purely resistive. It is necessary to check whether the ISM can accurately model the sound field in a real wind tunnel, in spite of these assumptions. An experimental validation test was therefore carried out in the 2.1×1.5 m wind tunnel at the University of Southampton. The objective was to compare measured Green's functions with those obtained from equation 3.5.

Measured Green's functions were obtained using the conventional source method described in Section 3.3.1. The source was a radiating orifice 10 mm in diameter

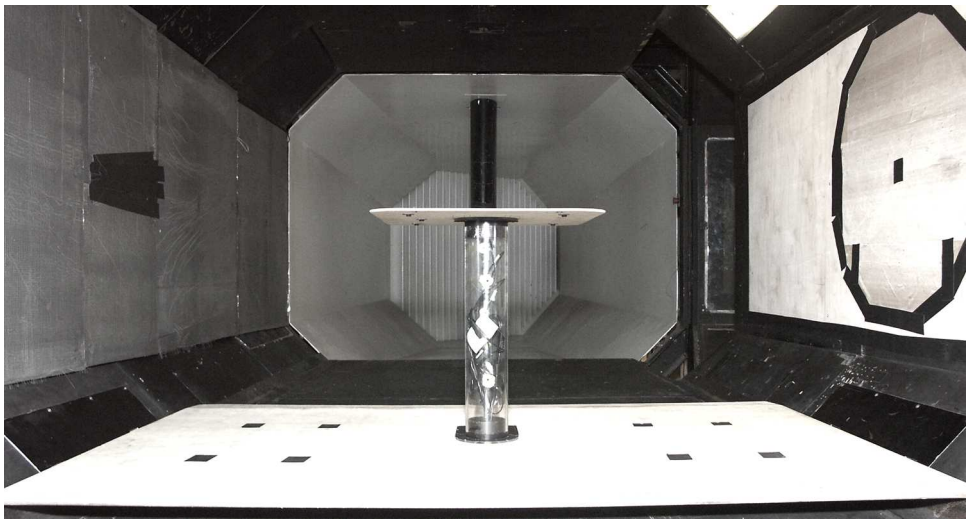

FIGURE 4.3: A downstream view of the Green's functions measurement setup. The microphone array can be seen flush mounted on the wind tunnel wall on the right. A cylindrical strut is mounted between two end plates. The on-surface microphones are on the back of the strut.

coupled to a high-frequency, high-intensity sound source generating broadband noise. Further details of this source can be found in ref. [47]. An unflanged circular pipe of this size radiates sound omnidirectionally to within $\pm 3\,\mathrm{dB}$ up to $10\,\mathrm{kHz}$ [48]. To make measurements more realistic, a physical model was introduced in the test section, in the form of a cylindrical strut mounted between two horizontal end plates, as shown in figure 4.3. The strut featured six on-surface microphones spread equally along it's length, facing downstream. These microphones were used as the reference microphones required to estimate the source strength of the radiating orifice. Further details of the experimental setup can be found in Boorsma and Zhang [49]. Six data sets were acquired, with the source positioned close to each of the six reference microphone, as shown in figure 4.4.

A 56-channel microphone array was flush-mounted on the side of the wind tunnel, in a plane parallel to the vertical strut axis, as shown in figure 4.5. Data was simultaneously acquired from the reference microphone closest to the source and the array microphones, in the form of a $4.3\,\mathrm{s}$ time history sampled at $48\,\mathrm{kHz}$. Measured Green's functions were evaluated for the source position $\vec{y}_0$ using equation 3.12, where H_1 was evaluated from 200 averages of a 1024-sample FFT block size. The diffractive effects of the strut were not taken into account.

Predictions were computed using the simplified ISM based on equation 3.5. All the walls were assumed to have a reflection coefficient of unity, and the air attenuation factor m was assumed to be negligible. The number of image sources included was

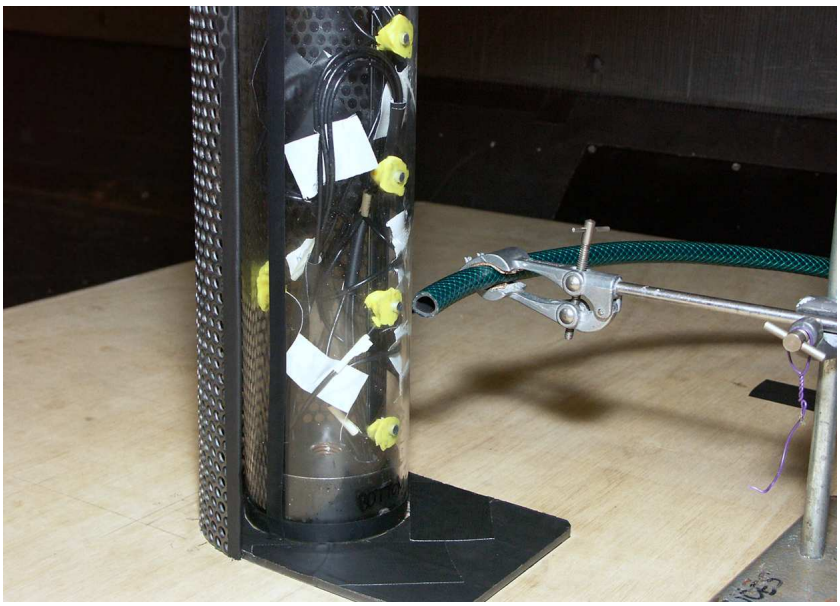

FIGURE 4.4: Detail showing the radiating orifice positioned near one of the on-surface microphones. Part of the experimental setup used to measure Green's functions in the $2.1 \times 1.5\,\mathrm{m}$ wind tunnel.

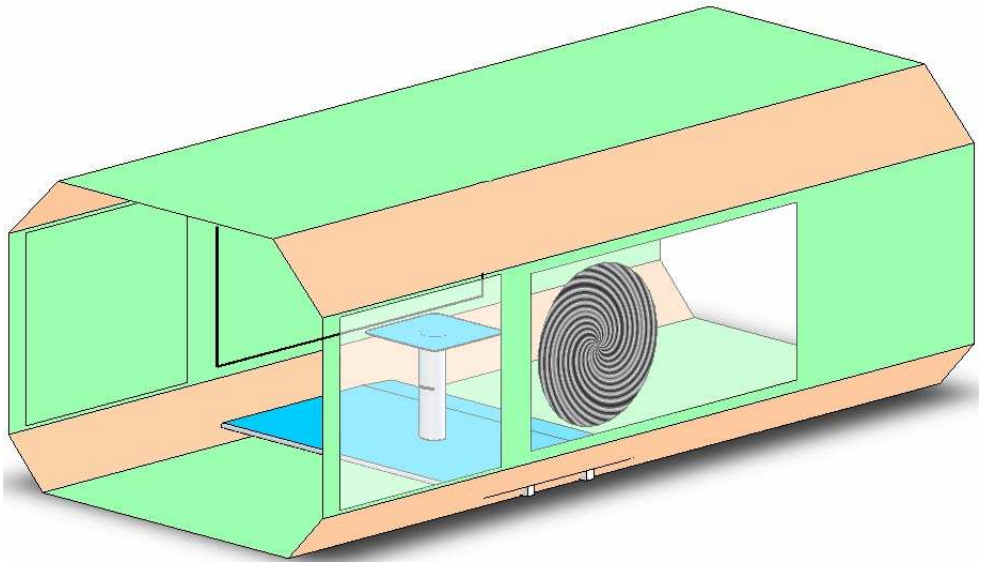

FIGURE 4.5: Rendered drawing showing the setup for Green's functions measurements in the $2.1 \times 1.5\,\mathrm{m}$ wind tunnel. The strut is mounted between two end plates (blue). The array's position is denoted by the spiral shading.

varied to check if including higher order image sources gives any benefit.

As explained previously, only a basic cross-section can be modelled using an ISM. Referring to figure 4.5, the slanting edges coloured in orange, the cylindrical strut and the end plates (rendered in blue) were not taken into account. This was deemed a realistic environment where to test the ISM.

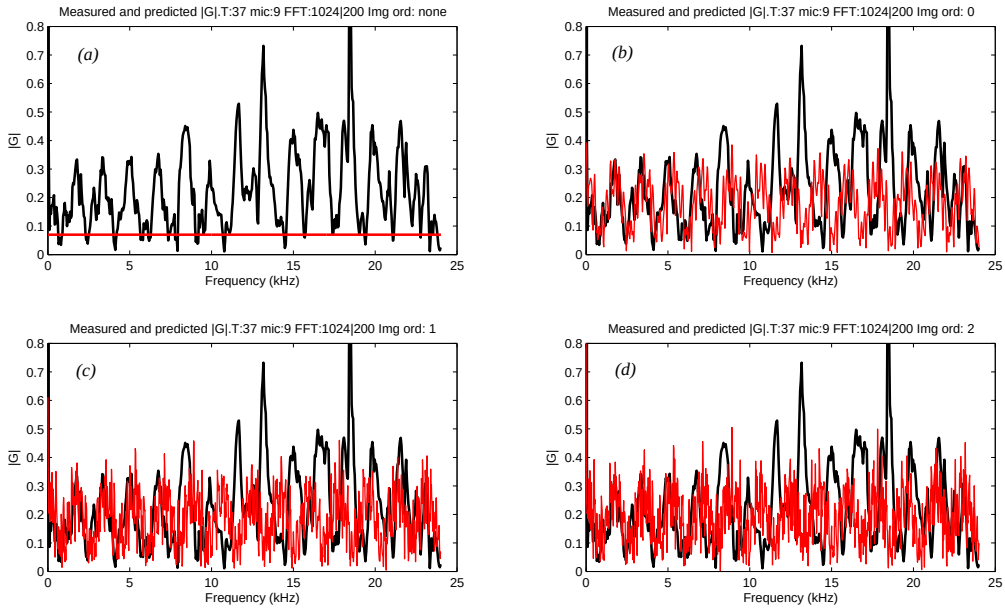

FIGURE 4.6: Comparison between predicted and measured Green's functions. Predicted Green's functions using *a*) free-space, *b*) 0th order ISM, *c*) 1st order ISM and *d*) 2nd order ISM.

Figure 4.6 shows a comparison between the magnitudes of measured and predicted Green's functions.[2] The four plots each show the same measured transfer function compared to *(top-left)* free-space Green's functions, *(top-right)* an ISM of order 0, *(bottom-left)* an ISM of order 1 and *(bottom-right)* an ISM of order 2. The phase of the predicted and measured Green's functions could not be compared directly due to the inherent problems with phase unwrapping of the measured signal.

It is immediately evident that the free-space estimate is a very poor representation of the "true" Green's function in the wind tunnel test section. A 0th order ISM gives a significant improvement, and can be considered as a good approximation for frequencies up to approximately 6 kHz. However it fails to predict the distinctive peaks at approximately 13 and 18 kHz. If the number of image sources is increased from 8 to 24 to 48, the predictions change in terms of narrowband fluctuations superimposed on the same spectrally-modulated signal; however there appears to be no obvious advantage of including the higher order image sources. This might be due to two reasons. First, multiple reflections will eventually need to propagate through the centre of the wind tunnel test section. The presence of a physical body will diffract or scatter the sound, thereby altering the sound field. Secondly, processing is carried out using data blocks of a finite time duration. In

[2] Only results for one source position will be shown; the other five data sets yielded different curves but exhibited the same trends.

this case, the chosen FFT block size of 1024 samples at a sample rate of 48 kHz is equivalent to a sound propagation distance of approximately 7.3 m. From figure 3.4 one can see that image sources with a 1st order ISM are situated on the perimeter of a 7 m radius circle centred at the centre of the array ($[0, 0]$). Sound from higher order reflections will therefore be captured in a different block than that containing sound from the direct path.

This test shows that in spite of the various assumptions, the Image Source Model can yield more accurate estimates for the Green's functions in hard-walled closed-section wind tunnels at low to mid frequencies. There was no obvious benefit observed from using an ISM of order 1 or higher.

4.3 Sensitivity to Errors

Having established that an ISM can give better representative Green's functions, the next step is to investigate the sensitivity of this method to errors in the various input parameters, such as the position of the source and receivers with respect to the wind tunnel test section.

A number of beamforming simulations were carried out using the SotonArray beamforming code.[3] The original code was modified in two ways. First the pressure data, which normally is acquired from the microphones, was simulated directly in the frequency domain using a predefined value of the source strength q_s and the user's choice of Green's functions. Secondly, the beamforming processing was carried out at one grid point ($\vec{y}_p = \vec{y}_0$) for a frequency vector from 0 to 20 kHz at 5 Hz intervals, rather than at one frequency for a large number of grid points. This means that the source strength estimates were obtained directly from the beamformer output, without the use of any integration methods.

To simulate a reverberant field, an image source model, based on Eq. 3.5, was used to generate the simulated pressure data. The model was based on a rectangular duct with a cross-section of 2.1 $\times$ 1.5 m. The dissipative constant α was set to the following values: 0.01 for $f \leq 1$ kHz, 0.1 for 1 kHz $< f \leq 2$ kHz, 0.15 for 2 kHz $< f \leq 4$ kHz, 0.2 for 4 kHz $< f \leq 8$ kHz and 0.4 for $f > 8$ kHz. Air absorption effects were assumed to be negligible, such that $\tilde{k} = k$. The microphone array was assumed to be mounted vertically on the shorter dimension, with the centre of the array situated 0.65 m above the floor. The reference source position

[3] An overview of this code can be found in Appendix A.

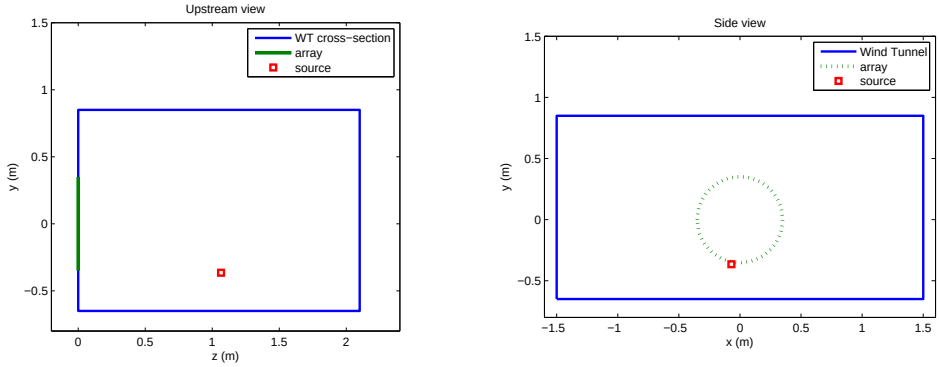

(a) Upstream view

(b) Side view

FIGURE 4.7: Schematic representation of the geometry considered for the beamforming simulations. The plots show the wind tunnel rectangular cross-section to together with the relative positions of the reference array and source positions.

was randomly chosen as [-0.07,-0.365,1.066], with the origin at the array centre. Figure 4.7 shows an overview of the geometry of the problem. Simulations were carried out for the case of no flow and with a mean flow of $\vec{U} = [80, 0, 0]$ [m/s].

Various arrays were used in the simulations. The reference array aperture size was 0.7 m, with sensors distributed using an aperiodic design based on the multi-arm log spiral (see Appendix A for further details). Further simulations were done using a 1.25 m-diameter aperiodic array and an array with a regular sensor distribution. Channel counts of 25, 56, 99 and 112 were considered.

Pseudorandom noise was injected in the simulated pressure data, up to a predefined percentage maximum. Randomness were generated using Matlab's default random number generator, which uses a modified version of Marsaglia's subtract with borrow algorithm.[50] The random number generator was reset to the same initial state for each test case, to ensure that the same errors were used. The Cross Spectral Matrix was generated using averages over 100 independent blocks.

Errors were introduced in a number of input parameters, namely the source and receiver positions, wind tunnel cross-section and Mach number. Errors in source position $\vec{y}_p$ and test section dimensions consisted of a fixed "bias" value. Errors in the receivers positions $\vec{x}_m$ were generated as a random percentage of a maximum "bias" value. Only the x and y values were perturbed. Errors in Mach number were generated as a percentage of the original value.

The simulations were carried out using "true" parameters to generate the pressure data, and the "erroneous" parameters in beamforming. This means that the sound

field created by an ISM is being assumed to be a good representation of the actual reverberant field in a wind tunnel. An ISM assumes rigid planar walls of infinite extent, which means that these simulations will be unable to highlight errors due to edge effects at the boundaries and reactive losses at the boundaries.

The following results are presented in terms of the beamformer error, defined as $10\log\left(\frac{Q_{\text{opt}}}{|q_s^* q_s|}\right)$ [dB], and plotted on a linear frequency scale. A positive error shows an overestimation, whereas a negative error represents an underestimate. A linear abscissa was chosen because *(a)* beamforming is most useful at high frequencies and *(b)* results at very low frequencies can be inaccurate.

In some instances, the use of the diagonal removal (DR) technique gave rise to unexpected behaviour in the simulation results. Therefore a number of simulations were carried out first to get a better understanding on the direct and indirect effects of using this technique. These simulations were carried out using free space Green's functions.

4.3.1 Effectiveness of CSM Diagonal Removal

Figure 4.8 shows the beamformer output error given by a 112-microphone array when the pressure data at the microphones is perturbed with a very large noise component. The noise is incoherent between frequencies and microphones. The amount of noise is expressed as a maximum percentage of the free-field pressure at each microphone due to the source. In this case maximum noise perturbations of 100,000% and 10,000% were chosen to represent the high noise contamination levels exhibited by flush-mounted microphones when compared to their out-of-flow open jet equivalents.[4]

For both cases, the array gives a 20 dB improvement over a single microphone when using the full CSM. The errors from a 56-channel microphone array were approximately 3 dB higher (not shown). The diagonal removal technique was expected to eliminate the remaining errors completely. However in both these two cases, the diagonal removal technique reduces the error by approximately 10 dB. This may seem to be a small amount, however it is equivalent to a further tenfold increase in channel count, and proves the efficiency of this simple operation. Due to computational limitations, it was not possible to investigate what happens when

[4]Wicken and Lindener [10] observe single microphone levels that are 40 to 50 dB higher in closed section wind tunnels.

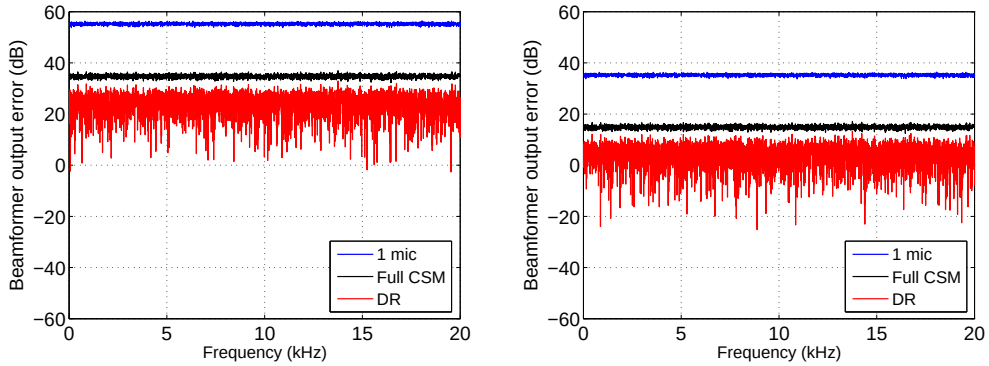

(a) 100,000% noise (b) 10,000% noise

FIGURE 4.8: Error in beamformer due to pressure data contaminated with the specified amount (maximum) of noise, with and without CSM DR. 112-channel array, free-space Green's functions. The error from a single microphone is included for comparative purposes.

the number of averages is significantly increased.[5] Therefore it is not clear whether the remaining errors were entirely due to an insufficient number of averages.

The diagonal removal technique also introduces narrowband fluctuations of more than $\pm 10\,\mathrm{dB}$ in the levels, and hence also in the errors. This phenomenon is directly related to the modified CSM, and is somewhat related to the generation of non-physical source powers discussed in Section 2.8.2. If the noise injected in the simulated pressures is reduced, so does the extent of these fluctuations, as shown in figure 4.9. This leads to the conclusion that the diagonal removal technique is very sensitive to errors in the input data, which was the reason why this technique is used in the first place. Note that in this case, a threshold cannot be defined, since the source strength is obtained directly from the beamforming level at the source position.

The sensitivity of the CSM DR technique to errors in the source position $\vec{y}_p$ and Mach number $\vec{M}$ is presented in Fig. 4.10. Errors in $\vec{y}_p$ arise when the true source does not coincide with a scan plane grid point. Errors in the Mach number are due to a local flow speed which varies from the free-stream velocity. The resulting beamformer error due to errors in $\vec{y}_p$ is a function of frequency, however the DR technique has very little effect on this error. Similar behaviour was observed for errors in the microphone positions $\vec{x}_m$ (not shown).

Errors in $\vec{M}$ (plot *(b)*) give rise to much more significant beamformer errors. An error in Mach number corresponds to beamforming to a location other than the

[5] The expected reduction in the error levels is expected to be $5 \log N$, where N is the number of averages [51].

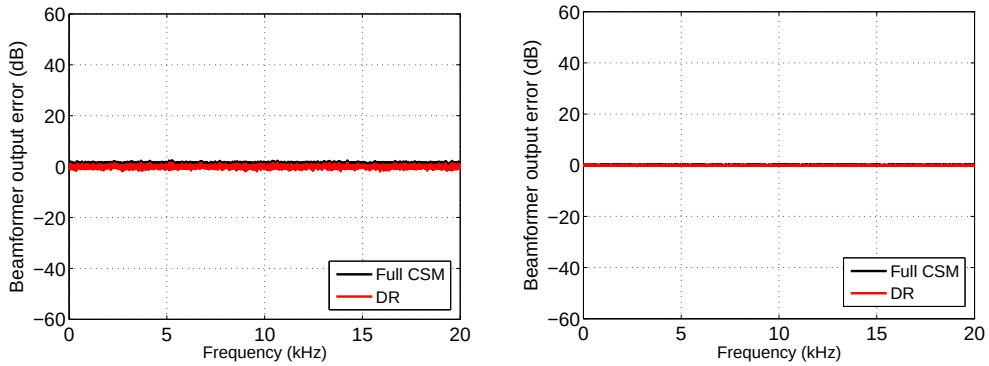

(a) 1,000% noise (b) 200% noise

FIGURE 4.9: Error in beamformer due to pressure data contaminated with the specified amount (maximum) of noise, with and without CSM DR. Free-field conditions.

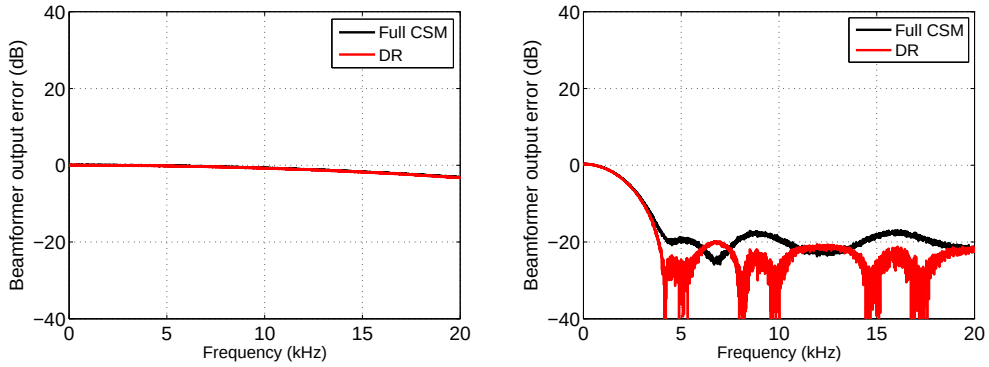

(a) Error of 0.01 m in $\vec{y}_p$ (b) Error of 50% in $\vec{M}$

FIGURE 4.10: Sensitivity of DR technique to errors in source location and Mach number. Free-field conditions. (a) $\vec{U} = 0$; (b) $\vec{U} = [80,0,0]$ m/s.

source position; in this case the 50% error corresponds roughly to a translational error of 0.12 m. The error curve is indirectly representing the beamformer's ability to suppress sources off the focus point, with higher performance at higher frequencies. Removing the CSM diagonal changes the beamformer error curve, due to the reasons given above. Errors in Mach number can be easily avoided by extracting levels from the apparent source location on the beamformer plots, rather than the hypothetical true source location.

4.3.2 De-reverberation

The errors from conventional beamforming in a reverberant environment are shown first. Figure 4.11 shows these errors for three different arrays: two 99-channel

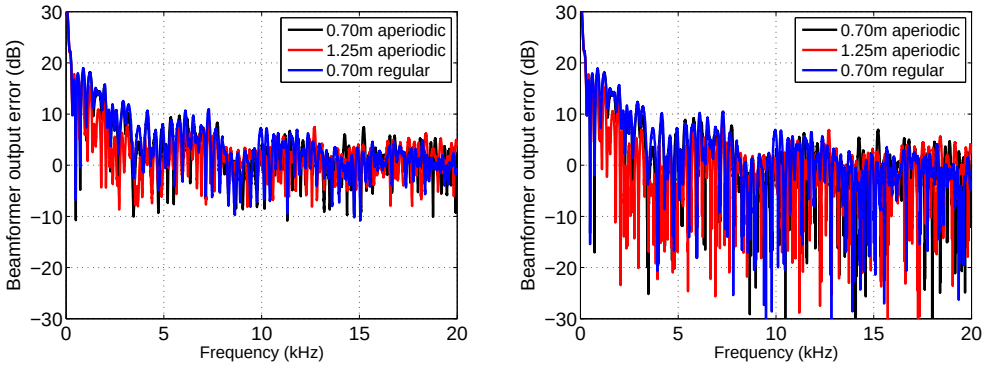

(a) Full CSM

(b) Diagonal removal.

FIGURE 4.11: Errors in beamformer output for three different arrays obtained when using free-space Green's functions to model a reverberant space. 100% noise, no position errors, no flow. Reverberant sound field created using a first order ISM.

aperiodic arrays with apertures of 0.7 and 1.25 m and a square-based 100-channel regular array. The simulated pressures were generated using an ISM of order one. 100% random noise was introduced in the microphone signals; the noise is incoherent between microphones. Beamforming was carried out using free-space Green's functions. No position errors were introduced.

All three arrays exhibit the same behaviour. Maximum errors are at low frequencies, up to 19 dB at 1 kHz. The shape of the three curves is a spectrally modulated signal featuring sharp, narrowband fluctuations. These can be attributed to the complex interference pattern that arises from the resulting 24 coherent image sources. Above 8 kHz the errors are on average bound within ±5 dB: in this frequency range the influence of the image sources is somewhat suppressed by the modest absorption at the boundaries. When the CSM diagonal is removed, the fluctuations in the errors become significantly more pronounced, as discussed in the previous section. Similar behaviour was also observed for arrays with a different channel count (not shown).

The spectral modulation phenomenon was also observed and discussed in detail by Sijtsma and Holthusen [15], when investigating an isolated source situated at 0.31 m from the test section ceiling (for the simulations considered here, the source is at 0.385 m from the floor). This modulation arises when the source is coherent with its image source(s). However in Sijtsma's case, the spectral modulation is only noticeable below 6 kHz, for both simulations and measurements. For the simulated case, Sijtsma only considers one image source, corresponding to the reflection off the ceiling. The measurements were carried out in a 3.0 × 2.22 m wind tunnel,

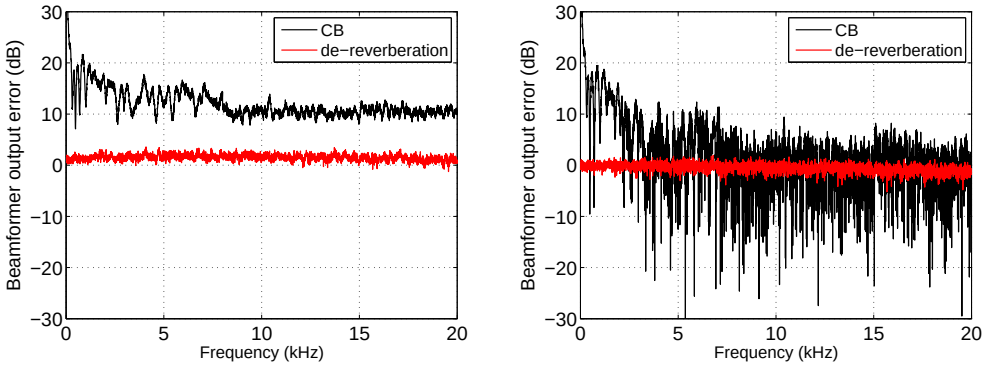

(a) Full CSM (b) Diagonal removal

FIGURE 4.12: Error in beamformer when beamforming in a reverberant space using free-space Green's functions (CB) and de-reverberation. 1000% noise, errors of 0.005 m in $\vec{y}_p$ and 0.001 m (max.) in $\vec{x}_m$. Reverberant sound field created using a first order ISM.

which is significantly larger than the 2.1×1.5 m wind tunnel considered in these simulations. Furthermore, the wind tunnel wall opposite the array was lined with absorbing material, which reduced the influence of some of the image sources.

If the injected noise in the simulated pressures is increased by a factor of ten, the errors with a full CSM change significantly. Figure 4.12 shows the beamformer errors involved in the reverberant environment when using a 112-channel aperiodic array with an aperture of 0.7 m. Once again the reverberant environment was simulated using an ISM of order 1, however this time the pressures were contaminated with 1000% noise. Furthermore the coordinates of the source position $\vec{y}_p$ had a fixed bias error of 5 mm, and the microphone positions had a random error of maximum 1 mm. The two plots show the case of (*left*) a full CSM and (*right*) with diagonal removal (DR) . Results are with flow.

Comparing the conventional beamforming (CB) curve in figure 4.12 *(a)* to that in figure 4.11 *(a)*, one can notice that the behaviour up to 2 kHz is very similar, however for the higher frequencies the extra noise shifts the average beamformer error to +10 dB. At the same time, the sharp fluctuations are noticeably reduced. If the diagonal of the CSM is removed, the curve becomes very similar to the equivalent case with 100% noise (figure 4.11 *(b)*). It is important to note that the 10 dB error shown in the case of 1000% noise with the full CSM is not solely due to the injected noise in the simulated pressures, as the same magnitude of noise in free-space conditions only gives an average error of 1.5 dB (c.f. figure 4.9 *(b)*).

With de-reverberation based on the ISM, the errors are very small. Finite errors are still present due to the source and receiver position errors. It is interesting to

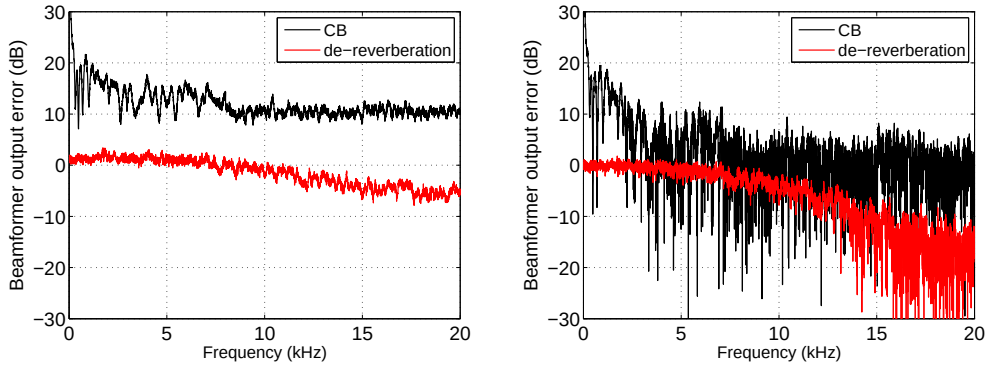

(a) Full CSM (b) Diagonal removal

FIGURE 4.13: Same conditions as for figure 4.12, but with an extra error of 0.01 m in array position.

note that even with CSM DR, the de-reverberation errors are well-contained.

The image source model, on which de-reverberation is based, relies on the accurate locations of the source and receivers with respect to the wind tunnel boundaries in order to give accurate results. Therefore, it can be expected that de-reverberation will be sensitive to errors in wind tunnel cross-section, particularly at high frequencies. Figure 4.13 shows the beamforming errors introduced by a position error of 0.01 m in the relative position of the test section boundaries with respect to the array. All other parameters are the same as in figure 4.12. Similar plots were obtained for different arrays and source positions (not shown).

For this case the beamformer error when using free-space Green's functions remains unchanged, since the test section boundaries position is not an input parameter. With de-reverberation and a full CSM, the absolute value of the beamformer error increases above 10 kHz, settling at approx. 6 dB at 20 kHz. If the DR technique is applied, the beamformer accuracy deteriorates much more drastically. Similar errors were observed for an error of 0.01 m in wind tunnel cross-section dimensions (not shown). However when the noise injected in the pressure data was reduced to 100%, the curves obtained with diagonal removal were identical to those with a full CSM, resulting in well-contained beamforming errors.

The instability of the ISM at high frequencies, as shown in figure 4.13, led Sijtsma and Holthusen to conclude that such a model should be avoided because it is not robust enough [15]. However two counter arguments can be presented. The benefits from de-reverberation are most significant at low to mid frequencies, where the ISM is robust to position errors. The instability of the ISM at high frequencies is amplified when the diagonal removal technique is applied, especially

when high noise levels contaminate the pressure data. This kind of noise could instead be controlled by a combination of array surface treatment and advanced post-processing techniques such as BiCLEAN.

4.4 Summary

In this chapter the performance of de-reverberation based on an Image Source Model was investigated in detail. De-reverberation changes the PSF by distorting the mainlobe and introducing additional sidelobes. Both these effects can be filtered out using deconvolution techniques. The Source Power Integration method is still effective in extracting accurate levels from the beamforming maps, in spite of the changes to the mainlobe and sidelobe structure.

Measurements in a closed section wind tunnel have shown that the ISM gives a better representation of the true transfer functions measured in a closed section wind tunnel, when compared to the free-space approach. Finally, simulations have shown that the ISM is robust to small errors in source and receiver positions. However it becomes unstable at high frequencies ($> 10\,\text{kHz}$) when errors in the array position and test section geometry are present. This limits the applicability of the ISM to low and mid frequencies, were the errors due to the reflections is most pronounced.

Having thus validated the ISM, the final step in answering the research hypothesis question is to investigate whether de-reverberation can yield improvements in the accuracy of beamforming levels. The simulations discussed in this chapter have shown that this should be the case; in the next chapter, measurements will be used to validate the simulated results.

Chapter 5

Beamforming with De-Reverberation

Free space Green's functions can be a poor estimate of the true transfer functions in closed section wind tunnels. An Image Source Model (ISM) can give better estimates with a minimum of additional parameters (test section dimensions, position of the array and absorption of boundaries). Simulations have shown that using an ISM in beamforming can give more accurate levels in reverberant environments.

In this chapter the results from a set of measurements carried out in a closed section wind tunnel will be presented to validate the simulation results. A fundamental issue with the simulations discussed in the previous chapter is that an ISM was used both to simulate the reverberant field and to de-reverberate the results. This means that factors such as the complex impedance of the boundaries, refraction and scattering effects were not taken into account. The measurements presented in this chapter will give a more realistic representation of the performance benefits, if any, of the de-reverberation technique.

The measurements were performed on a single calibration source of known source strength. By comparing the levels obtained from beamforming with the true source strength, it is possible to quantify the beamformer errors. An isolated source helps to reduce the degrees of freedom of the problem, and facilitates the interpretation of the results. However a single source does not give a complete picture of the effects of a reverberant space. Thus at the end of this chapter a brief discussion on the implications of using de-reverberation on a realistic test model (a half-aircraft model) will be presented.

5.1 Experimental Setup

5.1.1 Wind Tunnel

The calibrated source measurements were performed in the 2.1×1.5 m closed section wind tunnel at the University of Southampton. This is a closed-loop hard walled wind tunnel, with the fan situated in the return leg and turning vanes in the four corners. The wind tunnel was designed primarily for aerodynamic measurements, and therefore there are no features installed that reduce the background noise.

One of the aims of this investigation was to test the viability of lining the test section with acoustically absorptive material, in order to reduce the influence of reflections. In this way there would be no need to apply de-reverberation techniques in the post-processing results. One of the key challenges is to find a sufficiently absorptive material that does not alter the flow characteristics of the test section. Normal porous absorptive foam is not ideal, as the rough surface could change the boundary layer structure. For these tests a duct liner was used, consisting of 25 mm thick polyurethane foam covered by an impervious plastic sheet, which acts as a smooth surface in contact with the flow. This impervious sheet has an adverse effect on the absorption capabilities of the foam, and the absorption coefficient, measured in an impedance tube, varies between 0.25 and 0.4.[1] Due to limitations imposed by the facility, only two sides of the test section could be lined: the ceiling where the array was mounted and one of the vertical walls.

5.1.2 Calibration Source

When validating techniques related to beamforming the ideal source should approximate a point source, i.e. compact and with a uniform directivity pattern. In order to be detectable in the high background levels present in a wind tunnel, the source should have high power handling capabilities throughout the frequency range of interest. In practice these are conflicting requirements. In general high power handling implies a large physical size, and at high frequencies most conventional sources become highly directional.

In Section 4.2 a point source was approximated by a radiating orifice coupled to

[1] Further details of this duct liner, including the absorption results, can be found in Appendix A.

(a) Front (b) Back

FIGURE 5.1: KA558 calibration source.

a high-intensity source. This arrangement yielded a loud enough source with a minimum size penalty. However for the purpose of this test such an arrangement proved to be unsuitable. The output of a radiating orifice is highly dependent on the radiation impedance, which is affected by nearby rigid objects. Therefore a conventional high-frequency transducer (tweeter) was chosen as the calibration source. This tweeter could generate sound at sufficiently high levels throughout the frequency range of interest. The main disadvantage is that this source is not as compact as the radiating orifice arrangement.

Figure 5.1 shows two photos of the calibration source. The outer diameter is 88 mm, and the overall height is 73 mm. It features a 38 mm-diameter high temperature Kapton voice coil and a 1.13 kg magnet structure. The frequency response, as quoted by the manufacturer, is 2 – 25 kHz.

The tweeter was driven by software-generated Gaussian white noise with an amplitude of ± 1.0 V passed through a high pass filter having a windowed FIR topology with 121 taps. The amplitude of the signal was unchanged above 4 kHz. At 3 kHz it was approximately 80% of the maximum value; at 2 kHz the amplitude was 20% of the maximum. The amplitude was reduced to zero below 1 kHz. This was done to avoid damaging the speaker when feeding it with low frequency sound at high levels. The signal was amplified using a power amplifier set to a fixed gain.

The sound power of the calibration source driven by the filtered white noise was determined according to BS EN ISO 3741:2000 *Acoustics Determination of sound power levels of noise sources using sound pressure - Precision methods for reverberation rooms.*[2] Measurements were performed in the small reverberation chamber of ISVR Consulting at the University of Southampton. The computation of sound power from sound pressure measurements is based on the premise that, for a source

[2]Full details of these measurements can be found in ref. [52].

Midband frequencies (Hz)	L_w (dB) ± 1.0 V excitation	L_w (dB) ± 1.2 V excitation
1000	30.6	32.8
1250	41.3	44.1
1600	54.8	57.1
2000	67.0	68.5
2500	77.8	79.5
3150	85.7	87.3
4000	90.0	91.6
5000	92.0	93.3
6300	91.0	92.4
8000	88.4	89.8
10000	85.3	86.8
12500	81.7	83.2
16000	77.4	78.5

TABLE 5.1: Sound Power Level of the calibration source determined according to BS EN ISO 3741:2000.

emitting a given sound power in a reverberation test room, the mean-square sound pressure averaged in space and time, $< \bar{p}^2 >$, is directly proportional to the sound power and otherwise depends only on the acoustical and geometrical properties of the room and on the physical constants of air. The determined sound power, in one-third octave bands between 1 kHz and 16 kHz is shown in table 5.1. The lower frequency limit was due to the source and driving signal; the upper frequency limit was due to the measuring environment. The source was mounted in exactly the same way as in the wind tunnel (the setup is shown in figures 5.3 and 5.4), and coupled to the same signal generator and power amplifier. According to the standard, the maximum standard deviation of reproducibility of the sound power levels is 1.5 dB for the one-third octave bands between 1 kHz and 5 kHz, and 3 dB for the bands between 6.3 kHz and 10 kHz. No data is given for the higher frequencies.

Conventional sources tend to get highly directional at high frequencies; this was expected to create problems when interpreting results, since both beamforming and the ISM assume uniform directivity. An estimate of the directivity of the calibration source was therefore obtained from the time-averaged sound pressure level measured in an anechoic chamber along an arc subtending an angle between 30° and 110° with the horizontal. The reference source was situated at the centre of the arc, firing upwards. The arc radius was 2.1 m. The sound field was captured by eight Behringer ECM8000 precision electret condenser measurement microphones mounted on the arc at 10° intervals. Four measurements were taken,

each time rotating the source by 90° about a vertical axis passing through the centre of the source. Figure 5.2 shows the averaged directivity plots computed in one-third octave bands between 1.6 kHz and 20 kHz. The repeatability of the measurements was within ±0.6 dB, and the variations between the two perpendicular measurement planes were within ±2.5 dB. The source can be treated as omnidirectional up to the 3.15 kHz band. Above 6.3 kHz, it is highly directional.

5.1.3 Cavity Model

One of the limitations of an ISM is that it cannot model any diffraction or scattering effects due to an object in the wind tunnel. This is one of the sources of error that was not investigated in the simulations study. For these tests a cavity model was placed in the wind tunnel test section. The presence of this object was solely to recreate this source of error, and was chosen specifically because it does not feature any specific noise generating regions at frequencies above 1 kHz. It consists of a flat plate featuring a rectangular cavity, mounted on four cylindrical legs.[3] The exterior dimensions of the flat plate are 1.065 m long by 0.9 m wide; the cavity dimensions are 0.2 m by 0.9 m by 0.05 m deep. The flat plate is in a plane parallel to the ceiling of the test section, at a perpendicular distance of 0.79m from it. The legs are 60 mm in diameter. Two perspex end plates complete the structure.

During the tests, the calibration source was placed on the cavity model, inside the cavity, as shown in figure 5.3. Tests were performed with the source at two different positions: centred (as shown in figure 5.3), and offset by 0.25 m to one side. These two positions will be referred to as A and B, respectively. Figure 5.4 shows the position of the cavity model in the wind tunnel test section, together with the two source positions, A and B.

5.1.4 Microphone Array and Ancillary Hardware

Pressure data was recorded using a 56-channel microphone array flush-mounted in the ceiling of the test section. The array was designed according to a multi-arm log spiral sensor placement strategy [54], and has an aperture of 0.65 m. Figure 5.5 shows the array's aperture relative to the two calibration source positions. The sur-

[3]Full details on this cavity model can be found in Ashcroft and Zhang [53].

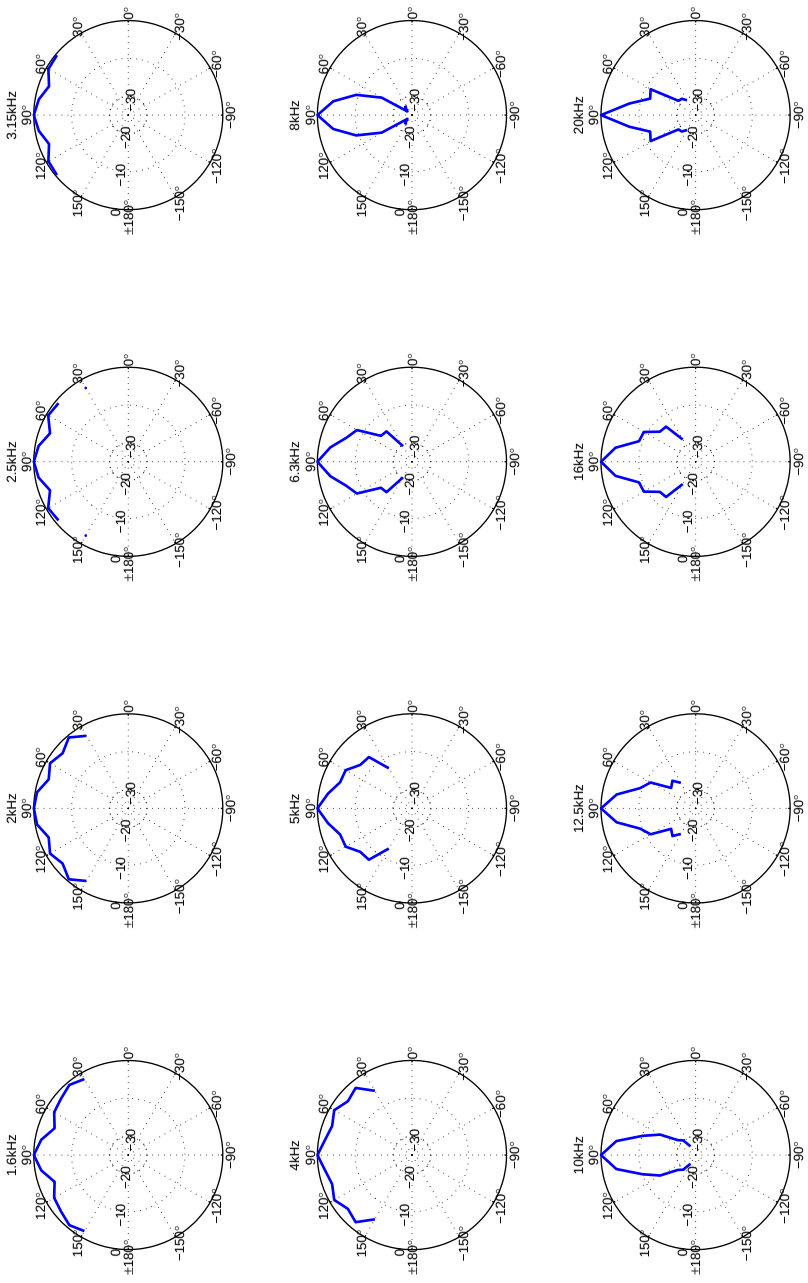

FIGURE 5.2: Directivity plots for the calibration source in one-third octave bands centred between 1.6 and 20 kHz. Data is averaged over two perpendicular planes (see text for details).

FIGURE 5.3: Calibration source centred on the cavity model (position A).

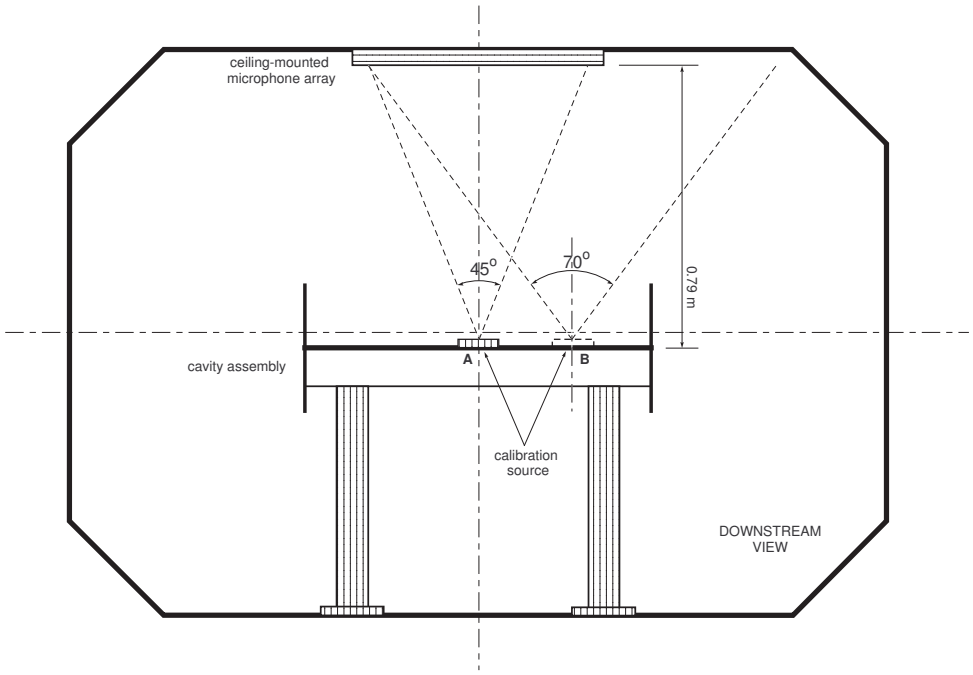

FIGURE 5.4: Schematic of the 2.1×1.5 m wind tunnel test section showing the relative positions of the microphone array and cavity model. The figure also shows the angles subtended by the array's aperture for the two source positions A and B.

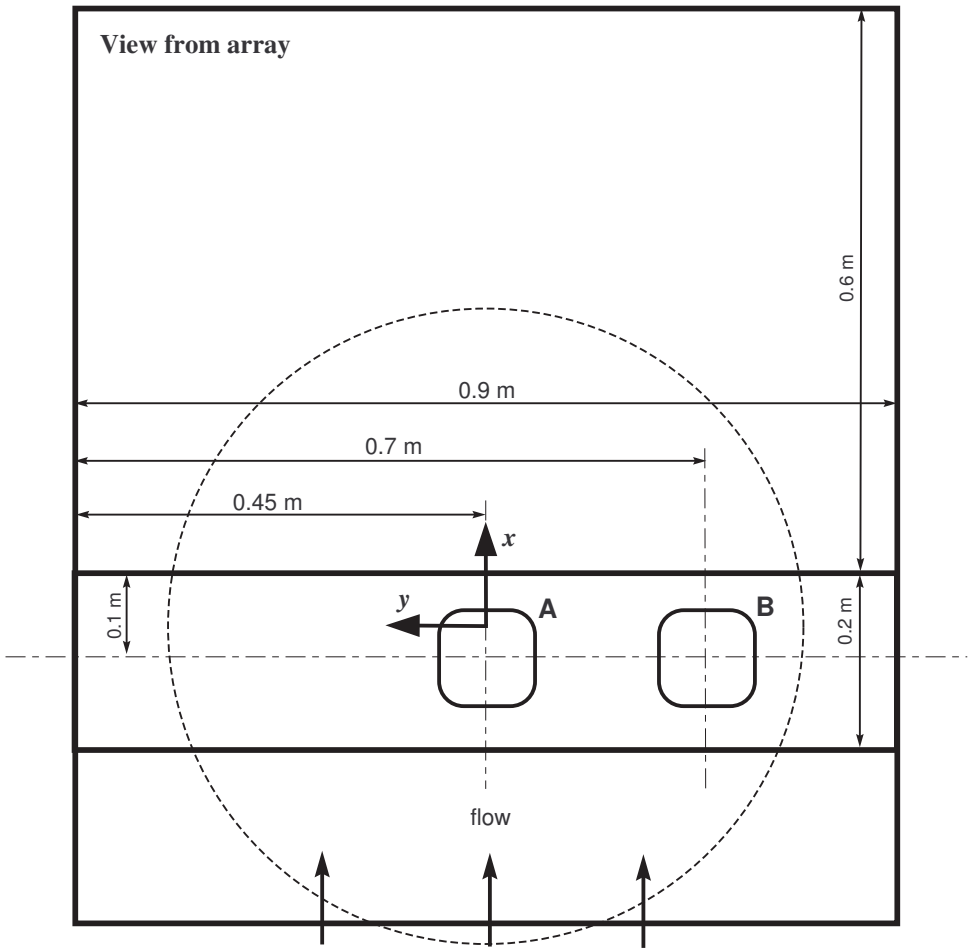

FIGURE 5.5: Schematic of cavity model as viewed from the array, showing the two calibration source positions (A - centred) and (B - offset). The dotted circle represents the array's aperture.

face of the array was covered by a porous cloth.[4] Microphones were of the electret type. Signals from the microphones were amplified using custom-built preamplifiers, which also fed power to the microphones. The amplified signals were then simultaneously acquired and digitised using 24 bit data acquisition cards sampling at a frequency of 96 kHz. For each test run, a 17 s time history was acquired. The data was stored in binary format for later retrieval and post processing. Further details on the microphone array system can be found in Appendix A.

[4]Previous tests had shown that the presence of this cloth reduced the risk of microphones overloading, possibly by creating a more uniform array surface. However it is not well understood whether this surface treatment changes the boundary layer structure.

5.1.5 Microphone Array Calibration

The array microphones were individually calibrated using a frequency response function (FRF) comparison method. Each microphone was placed diaphragm-to-diaphragm with a calibrated, reference instrumentation-grade microphone (GRAS Type 46BE transducer, consisting of a 1/4″ CCP preamplifier Type 26CB and a free field microphone Type 40BE). The sensitivity of the reference transducer was determined prior to the test using a Brüel and Kjær Acoustical Calibrator Type 4230. The two microphones were subjected to white noise, and the transfer function between the two was measured and used to correct the recorded pressures from the array microphones. The calibration had to be performed with the microphones in the array, as the microphones are permanently fixed.

5.2 Post Processing

The post processing was carried out using the SotonArray microphone array software.[5] Pressure data was Fourier transformed using a a block size of 4096 samples; this resulted in a frequency resolution of 23.4 Hz. Averaging was done over 400 independent blocks, with 50% overlap. The scan plane dimensions were 0.9×0.9 m, centred at the array origin, and the inter-grid spacing was $\Delta x = \Delta y = 0.01$ m. In this coordinate system, the coordinates of the calibration source were [-0.044,0] for position A and [-0.044,-0.250] for position B. Beamforming maps were generated using conventional beamforming with and without de-reverberation. These maps were then deconvolved using CLEAN and CLEAN-SC using a frequency independent mainlobe with a resolution of 50 mm. Quantitative levels were obtained from CLEAN-SC and using the Source Power Integration (SPI) technique. For the latter, the integration area was taken as the entire scan plane, and a threshold of 12 dB was used. Results were summed in one third octave bands between 1 and 16 kHz, in order to enable a direct comparison with the "true" calibration source strength given in Table 5.1.

[5] Further details on SotonArray can be found in Appendix A.

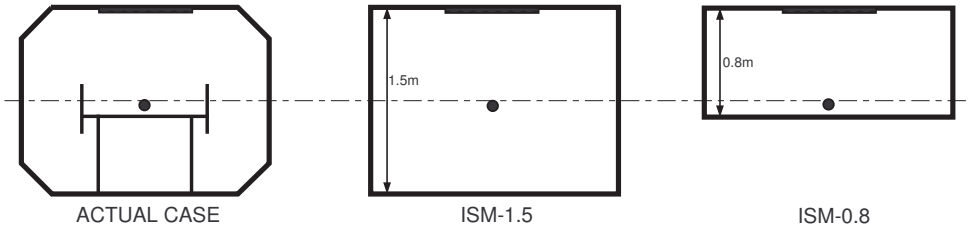

FIGURE 5.6: Schematic representations of the boundaries of two image source models chosen to simulate the sound field of the actual wind tunnel test section. Downstream views, drawings not to scale.

5.3 Image Source Model

De-reverberation was implemented using an ISM of order zero, i.e. taking into account only the first eight image sources. The absorption of the boundaries was assumed to be uniform with the following values: 0.01 for $f < 1\,\text{kHz}$, 0.04 for $1 \leq f < 2\,\text{kHz}$, 0.06 for $2 \leq f < 4\,\text{kHz}$, 0.08 for $4 \leq f < 8\,\text{kHz}$ and 0.1 for $f \geq 8\,\text{kHz}$. Air attenuation was taken into account using a complex wavenumber $\tilde{k} = k - \mathrm{i}m/2$, where the air attenuation factor $m = 4.66 \times 10^{-13}\omega^2$ [46].

Due to the geometry of the setup, it was interesting to consider two ISM formulations. The first models the rectangular test section, without the sloping edges and the cavity model. This will be referred to as ISM-1.5. A second ISM, referred to as ISM-0.8, models the flat plate of the cavity model as the floor of the wind tunnel. Figure 5.6 shows a schematic representation of the "true" setup and the two geometries modelled by the different ISMs. It should be expected that ISM-0.8 is more accurate when the wavelength is short compared to the cavity model dimensions, and vice-versa for ISM-1.5.

5.4 Results

The results presented in this section will focus on the error in beamforming levels, in line with the research hypothesis. The errors are plotted in one-third octave bands centred between 1 kHz and 16 kHz. In some cases, narrowband spectra will be shown; these are normalised to $\Delta f = 1\,\text{Hz}$. A selection of beamforming maps will also be shown in this section to highlight certain issues, or when they can help clarify the interpretation of the quantitative results. Additional beamforming maps can be found in Appendix C.

The beamforming level error, $\epsilon(L_W)$ is defined as $L_{w,\,\text{BF}} - L_{w\,\text{true}}$, i.e. the difference

between the sound power computed using integrated levels from beamforming maps and the sound power of the source as given in Table 5.1. Pressure doubling at the array microphones is taken into account. The repeatability of the levels summed in one-third octave bands was within ±1 dB for frequencies up to 2 kHz and within ±0.5 dB at higher frequencies. The dynamic range of the beamforming plots is 20 dB from the peak level.

5.4.1 De-reverberation

The question of main interest is whether de-reverberation based on an ISM gives a smaller beamformer error than conventional beamforming based on free-space Green's functions. Figure 5.7 shows a comparison of the beamforming errors when using free-space Green's functions (blue) and de-reverberation based on ISM-1.5 (red), for the calibration source in positions A (centred) and B (offset).

The plots can be divided into three frequency sections: low (1 to 2 kHz), mid (2.5 to 5 kHz) and high (6.3 to 16 kHz). In the low and high sections, beamforming gives an overestimation of the source strength. This is consistent with the results obtained from simulations. Using ISM-1.5 reduces the beamforming errors by 1 – 5 dB. In the low frequency bands, when the source is behaving as a compact source, and position errors have a minor influence, the improvements in beamformer accuracy can be solely attributed to the effectiveness of de-reverberation. In the high frequency bands, the directivity of the source, together with the sensitivity of the ISM to position errors makes it more difficult to attribute with certainty the resulting improvements in beamforming accuracy.

It is interesting to note that the beamformer levels change by up to 2.5 dB with source position. This level change occurs even at the low frequencies, where the source can be considered as omnidirectional. This confirms that the nearby reflecting surfaces have an influence on the absolute beamforming levels. In this case, the relative difference in errors when using the two types of steering vectors remains unchanged. This is because the presence of the surfaces closest to the source, especially the end plates, is not modelled by the ISM.

The results in the mid-frequency bands (2.5, 3.15, 4 and 5 kHz) exhibit an unexpected behaviour. In these bands, conventional beamforming gave rise to an underestimation of the source strengths. De-reverberation reduces the source strength estimates even more to take into account the influence of the reverberant field, and hence the magnitude of the errors is increased with de-reverberation. This

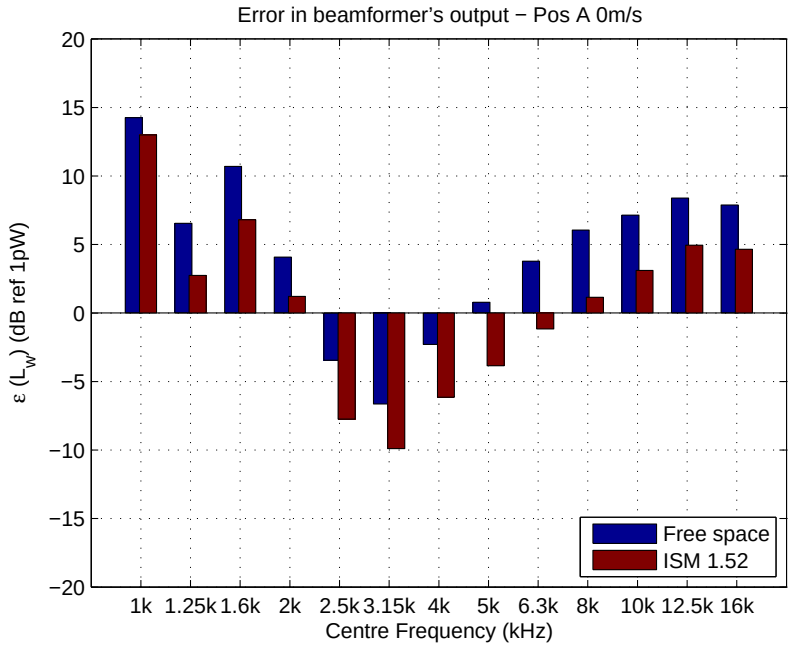

(a) Position A

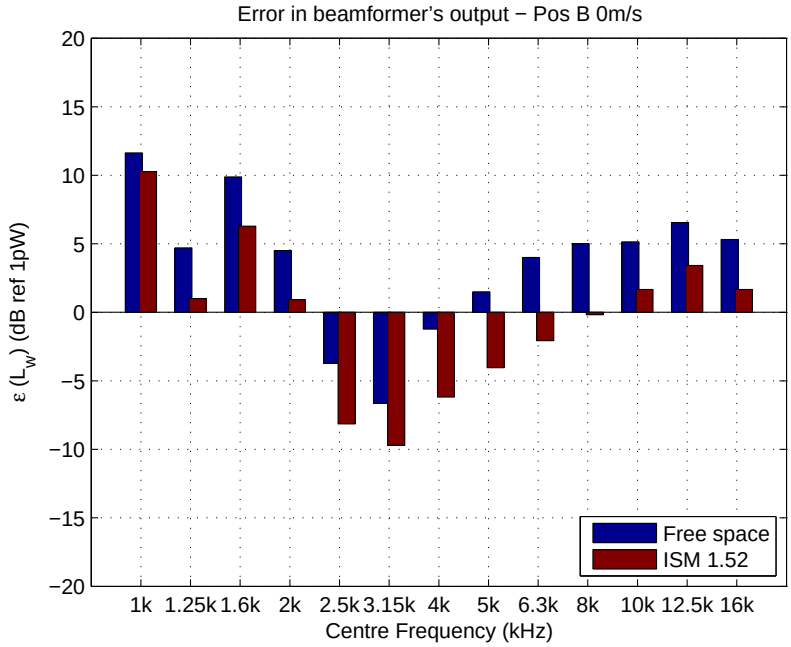

(b) Position B

FIGURE 5.7: Beamforming level errors when using free-space Green's functions and an ISM of order 0 modelling the entire cross-section (ISM-1.5). *(upper)* source centred, *(lower)* source offset.

behaviour at mid-frequencies is recurrent for all the measured data sets, and unfortunately its occurrence cannot be explained with certainty.[6] Such a phenomenon could be due to installation effects, i.e. if the source power spectrum changes between the two measuring environments (reverberation chamber and wind tunnel).[7] Due to these uncertainties results in the mid frequency bands will be discarded, although further investigation of this phenomenon is recommended.

Figure 5.8 shows the equivalent of figure 5.7 but using ISM-0.8. In this case the ISM is modelling the flat plate to be the floor of the test section. Given the rather large size of the flat plate relative to the test section dimensions, this model might be more representative in the frequency range of interest.

For this case the free-space levels are the same as in figure 5.7, since the test section geometry is not an input parameter. Once again de-reverberation gives improvements at the low and high frequencies. However in this case the absolute errors are even smaller; in most cases they do not exceed ± 3 dB. The only exception is the 2 kHz frequency band, where de-reverberation results in an increase in the magnitude of the beamforming error. Varying the source position gives some slight changes (1 dB) in the relative errors produced by the two types of steering vectors, which is not sufficient to take into account the absolute changes in error that occur between the two source positions. Once again this can be explained by the presence of extra reflecting surfaces and the directivity pattern of the source, both of which are not taken into account by the ISM.

One of the concerns when using de-reverberation is the resulting distorted point spread functions (PSFs), as shown in figure 4.1 on page 66. In particular, the unusually high sidelobes close to the source might give rise to problems with source identification.

Figure 5.9 shows beamforming maps at a selection of one-third octave band frequencies of the calibration source in position A, when using de-reverberation based on ISM-1.5. The plots are without deconvolution. One can observe the characteristic sidelobes in the axes perpendicular to the parallel boundaries (y-axis) at the low frequencies, however the effect is much less pronounced than in the PSFs. One important difference is that the plots in figure 4.1 are at one particular frequency, whereas the plots in figure 5.9 are a sum of the plots at all the narrowband

[6] Sijtsma and Holthusen [15] also report a difference in the spectra recorded in anechoic and wind tunnel environments, which was partly due to poor calibration of the array in the closed wind tunnel [51]. In this case the FRF calibration curves did not exhibit any irregular behaviour at these frequencies, so it is unlikely that this was due to instrumentation or calibration effects.

[7] Interestingly, horn loaded speakers exhibit resonances at these frequencies [39].

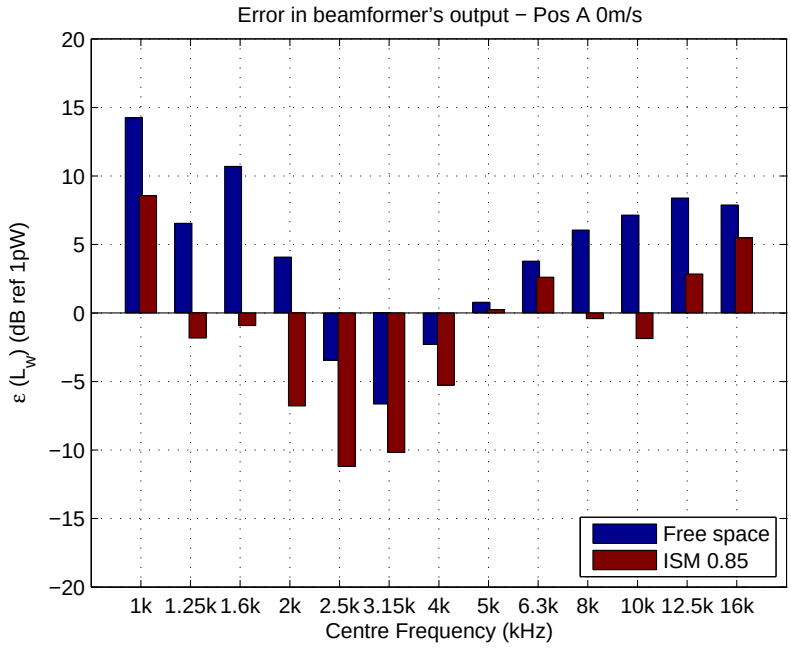

(a) Position A

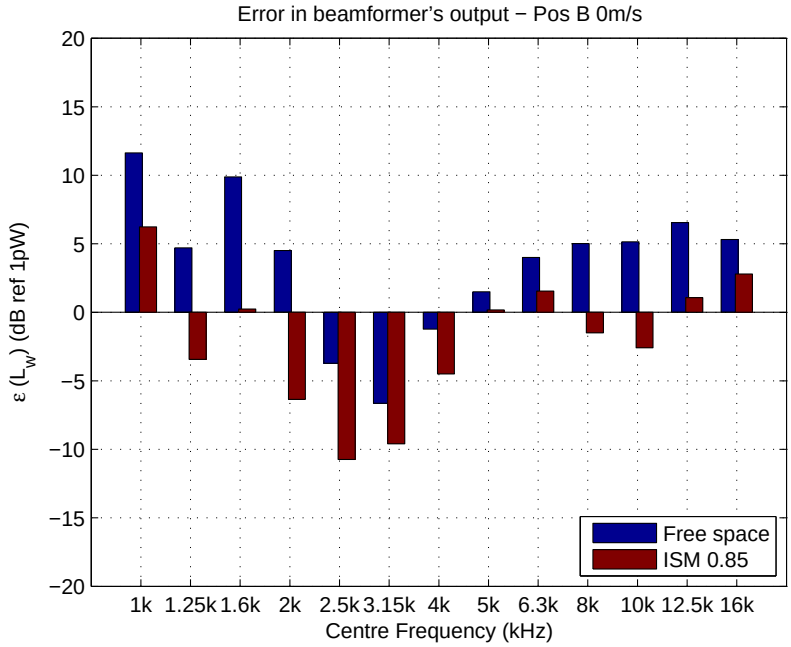

(b) Position B

FIGURE 5.8: Beamforming level errors when using free-space Green's functions and an ISM of order 0 modelling half the cross-section (ISM-0.8). *(upper)* source centred, *(lower)* source offset.

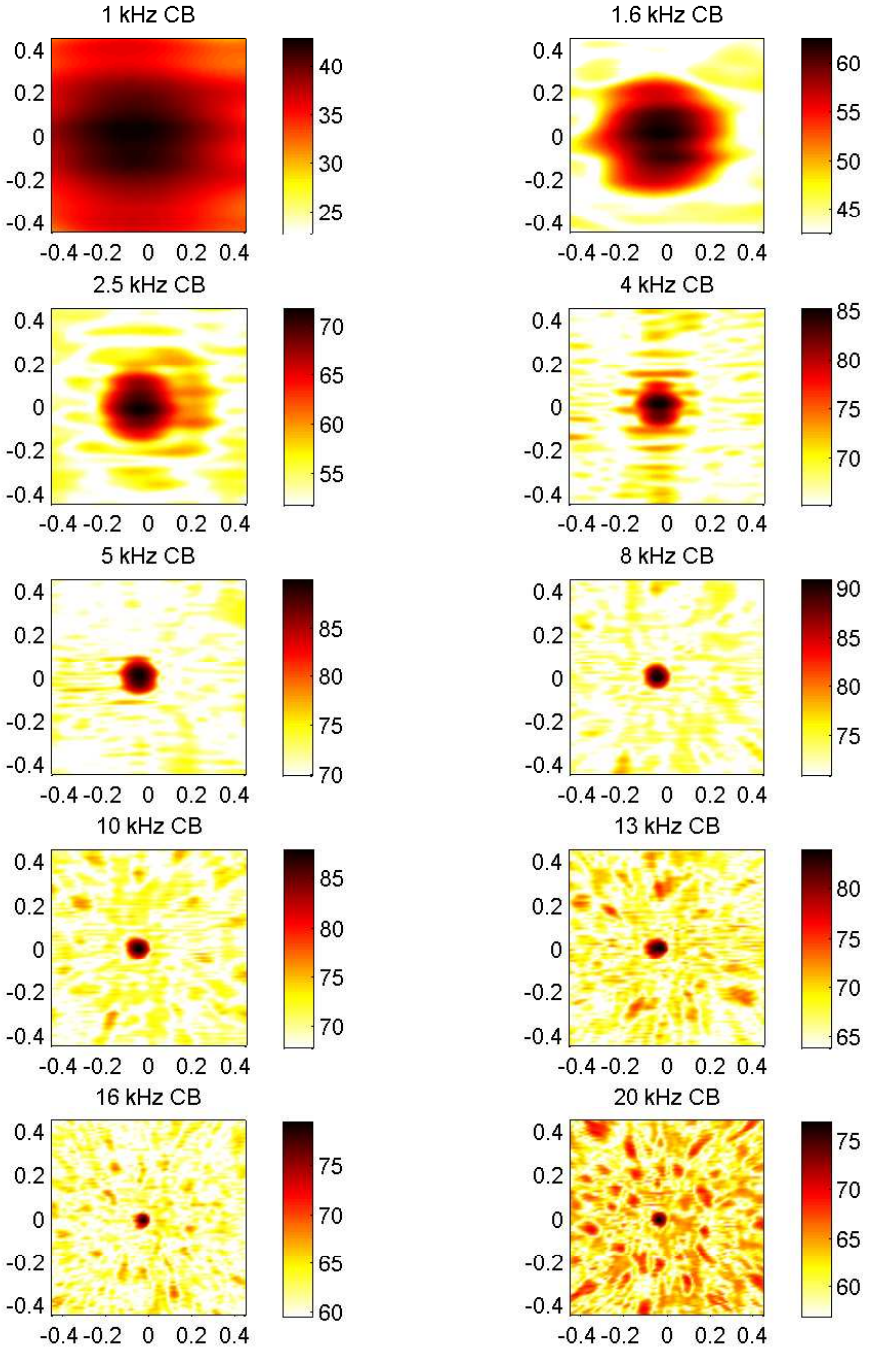

FIGURE 5.9: Beamforming maps of the centred source without flow using de-reverberation based on ISM-1.5.

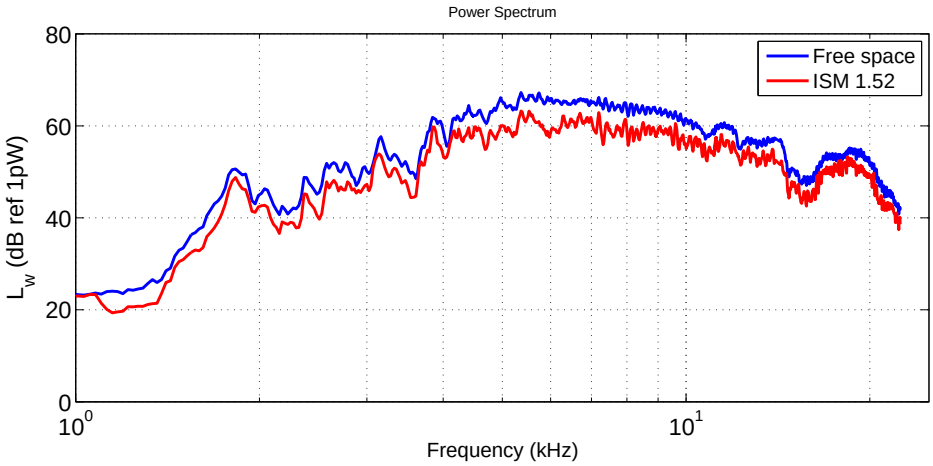

FIGURE 5.10: Narrowband source power spectrum from integrated beamforming plots generated using free-space Green's functions and ISM-1.5. Source centred, no flow.

frequencies within the respective frequency bands. At frequency bands of 8 kHz and above, the plots are very similar to those obtained using free-space Green's functions (as shown in figure C.1 on page 151). It is interesting to note that when using CLEAN (deconvolution based on the PSF) with de-reverberation (c.f. figure C.5), sidelobes on the perimeter of the plots are attenuated, however extraneous sidelobes are introduced at 5, 8, 10, 13 and 16 kHz. CLEAN-SC does not suffer from these drawbacks, and yields qualitatively similar plots irrespective of the type of steering vector used (c.f. figures C.3 and C.6).

Figure 5.10 shows the difference when using free-space Green's functions and de-reverberation based on ISM-1.5 in terms of the narrowband beamformer output spectrum. The shape of the two spectra is very similar. In general the de-reverberated spectrum is between 0 and 8 dB less than the free-space equivalent. One can notice a number of peculiar dips in the power spectrum between 2 and 4 kHz, which might be the reason of the unexpected behaviour of the beamformer errors at these mid frequencies.

5.4.2 Levels from SPI and CLEAN-SC

The standard way of extracting quantitative levels from beamforming plots is using the Source Power Integration technique (see Section 2.8.1). However levels can also be obtained directly from the CLEAN-SC technique, as discussed in Section 2.8.3. Figure 5.11 shows a comparison of the levels obtained from these two techniques, for both the case of free-space Green's functions and de-reverberation.

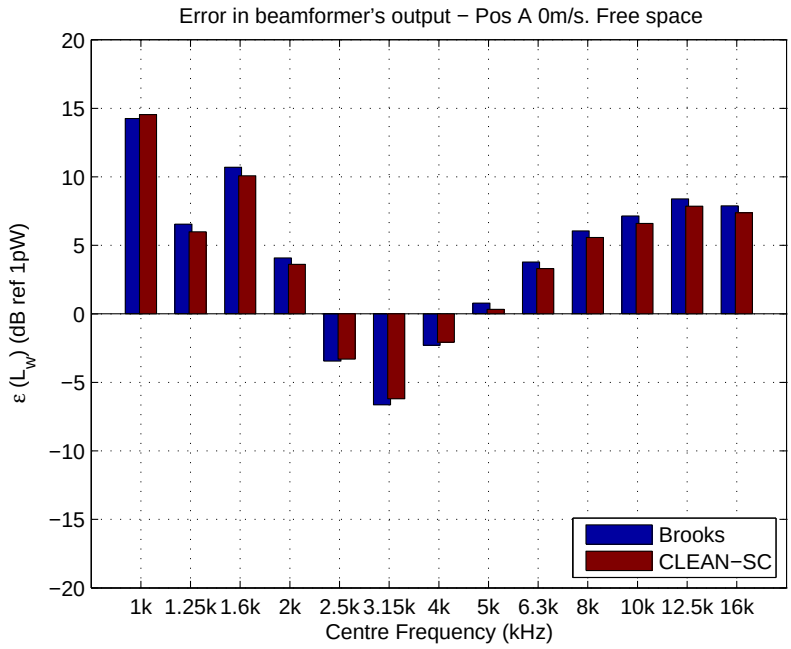

(a) Free space

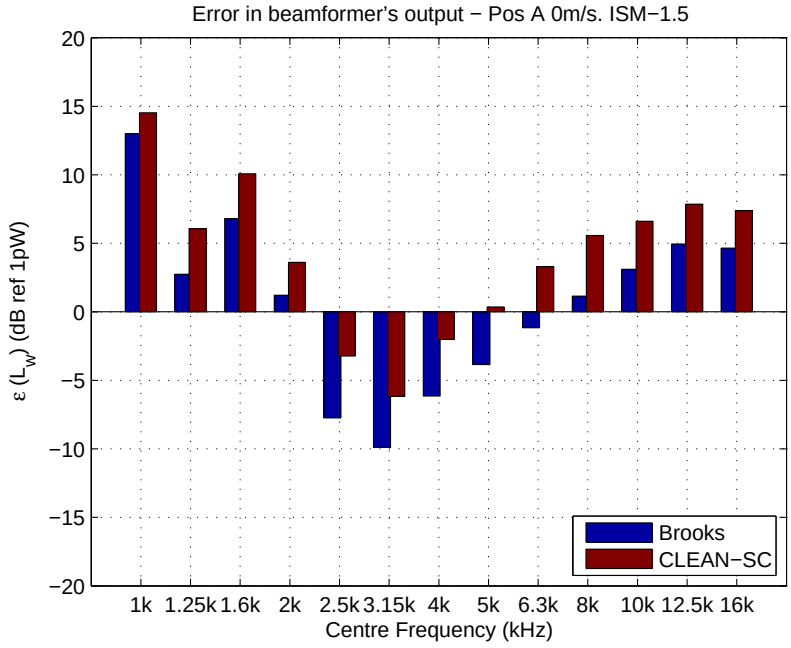

(b) ISM-1.5

FIGURE 5.11: Beamforming level errors resulting from levels obtained from SPI (Brooks) and CLEAN-SC. *(upper)* free-space Green's functions and *(lower)* ISM-1.5. Source centred.

In the free-space scenario, levels from both methods match to ±1 dB, which is consistent with the observations by Sijtsma [12]. However this is not the case with de-reverberation. The levels from CLEAN-SC in plots *(a)* and *(b)* are identical, whereas those from SPI are not. The same behaviour was observed for the source in position B (not shown). This leads to an important conclusion. CLEAN-SC is based on a coherent source component **h**, defined in equation 2.59 on page 30. This source component is obtained iteratively based on the acquired pressure data – the computed steering vectors act only as a first guess. Therefore if the pressures recorded at the microphones are contaminated by the reflections, CLEAN-SC cannot correct for this effect. It is clear that in the present formulation, CLEAN-SC cannot be used to obtain levels from de-reverberated results.

5.4.3 Effect of SPI threshold

When beamforming in closed-section wind tunnels, the diagonal of the Cross Spectral Matrix (CSM) is normally removed to reduce the influence of the turbulent boundary layer noise over the array microphones. In Section 2.8.2 this was shown to introduce errors in the resulting SPI levels, and the use of a threshold was recommended. Figure 5.12 shows the implications of omitting the use of this threshold on the resulting narrowband source power spectrum. The results are for free-space Green's functions, although similar results were observed when using de-reverberation.

Since the plots are using free-space Green's functions, the spectrum obtained from CLEAN-SC is nearly identical to that from SPI when using the threshold. Without the threshold the source power spectrum is similar up to 4 kHz. At higher frequencies it features narrowband fluctuations of significant magnitude (as much as ±25 dB). This behaviour was also observed in the simulated data presented in the previous chapter. It is interesting to note that the fluctuating behaviour varies between the two source positions, in spite of the fact that both spectra were extracted from the same scan plane.

Levels from CLEAN-SC do not require a threshold parameter, since the diagonal of the CSM is reconstructed during the iterations of the deconvolution process.

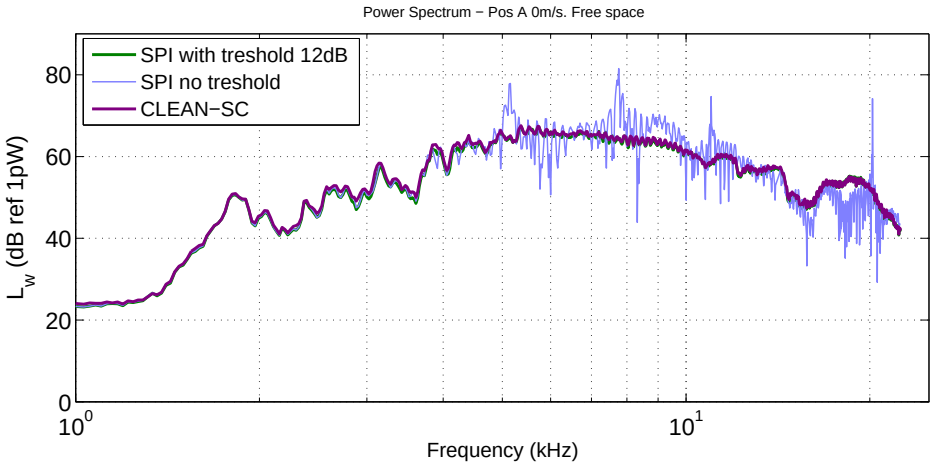

(a) Position A

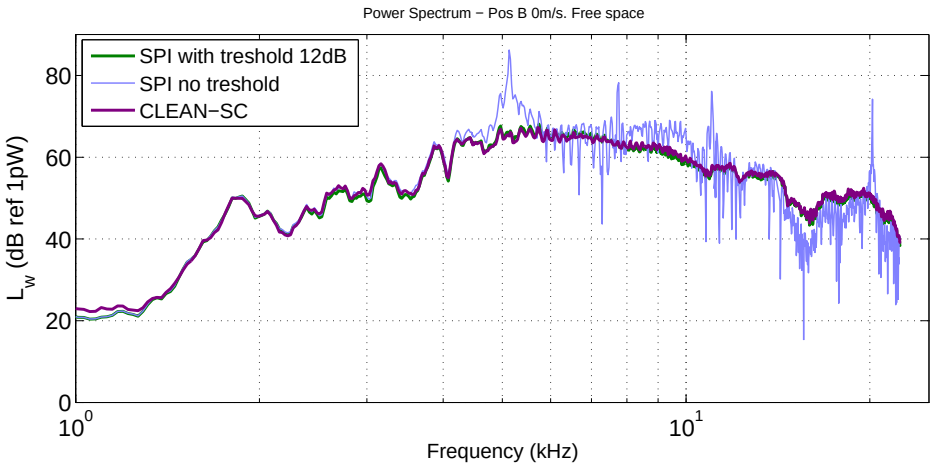

(b) Position B

FIGURE 5.12: Beamforming level spectrum resulting from levels obtained from SPI (with and without threshold) and CLEAN-SC. *(upper)* source centred and *(lower)* source offset.

5.4.4 Effect of flow on de-reverberation

All the results presented up to this stage have been for the case of no flow. It is important to confirm if de-reverberation can be successfully applied to cases with flow. Figure 5.13 shows a direct comparison of the beamformer errors with and without flow, when using the two types of steering vectors. Note that the limits of the ordinate have been increased to include the larger errors.

Both types of steering vectors exhibit the same behaviour in the presence of flow, i.e. much more significant errors at low frequencies, and minor increases of up to 2 dB at the higher frequencies. Note that these results are with CSM diagonal removal (DR). It is clear from these results that the CSM DR technique does not necessarily completely remove the undesired noise component due to flow.

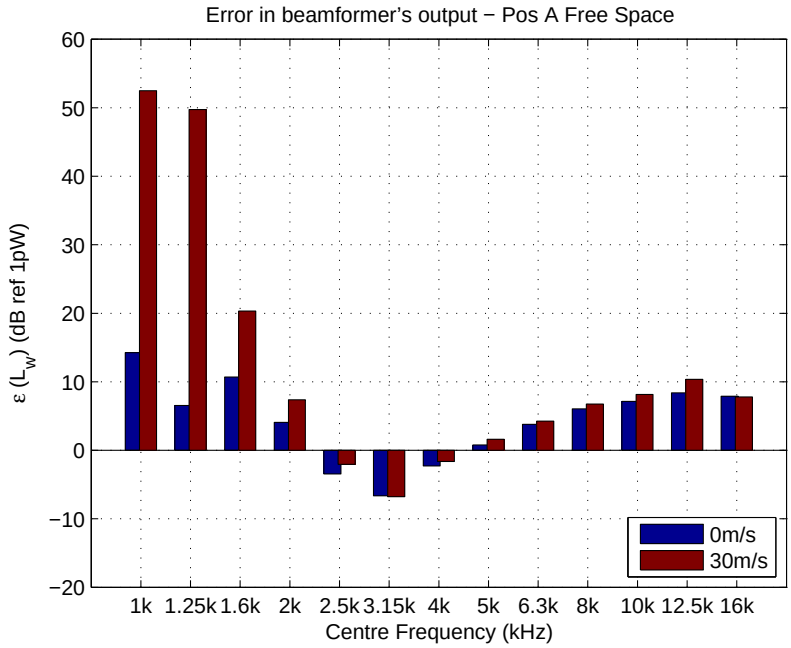

(a) Free space

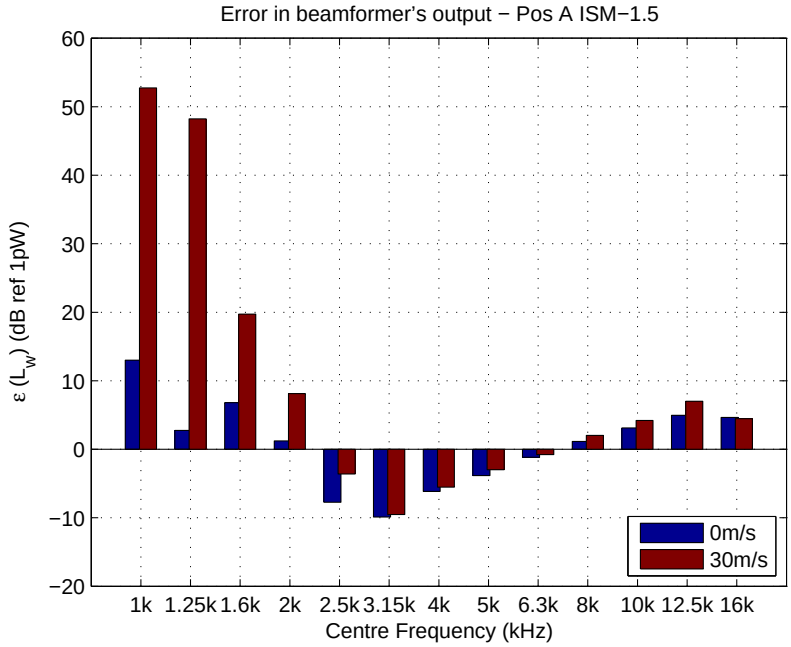

(b) ISM-1.5

FIGURE 5.13: Beamforming level errors with and without flow. *(upper)* free-space Green's functions and *(lower)* ISM-1.5. Source centred.

However these plots do confirm that de-reverberation works equally well in the presence of flow.

5.4.5 Effectiveness of CSM diagonal removal

At this stage it is interesting to quantify the effects achieved by the CSM DR technique. Figure 5.14 shows the beamformer error with and without DR for the centred source using free space Green's functions.

In the case of no flow, removing the diagonal reduces the absolute levels, and hence the errors, by up to 1 dB. This can be attributed to the elimination of uncorrelated channel self-noise generated by the microphones and preamplifier channels. With flow the diagonal removal should in theory completely remove the influence of the turbulent boundary layer in direct contact with the microphones. In practice DR gives a maximum reduction of 10 dB in the 1.6 and 2 kHz bands. Incidentally this maximum reduction of 10 dB was also observed in simulations that were presented in Section 4.3. At mid and high frequencies, DR yields little change. At these frequencies the source level is sufficiently high that the array results are not effected by the boundary layer noise. In the lowest two frequency bands DR is not so effective, and improvements are limited to approximately 5 dB. It is not clear if the very high beamforming levels arise from partially or fully-correlated noise over the array, the sound field in the wind tunnel or aerodynamic noise from the cavity model. A detailed investigation is recommended. The magnitude of the errors suggest that de-noising based on an eigenvalue decomposition of the CSM might be more suitable.

Figure 5.15 shows the effect of flow in terms of the narrowband beamforming power spectrum. Levels obtained from CLEAN-SC are higher than those obtained from SPI with threshold for frequencies below 3 kHz. This can be because CLEAN-SC includes coherent reflections [51]. However it is not clear why in the equivalent case without flow (c.f. figure 5.12 *(b)*) this is not the case.

The significant contamination of background noise at low frequencies has implications even on the qualitative results. Figures 5.16 and 5.17 show beamforming maps at the lowest ten one-third octave bands for the source centred with flow at 30 m/s. Figure 5.16 is for a full CSM, whereas figure 5.17 is with the DR technique. For both cases, the source cannot even be detected in the two lowest frequency bands. Furthermore, with the full CSM the source is barely visible in the next two frequency bands. The plots start to be qualitatively similar at and above 5 kHz.

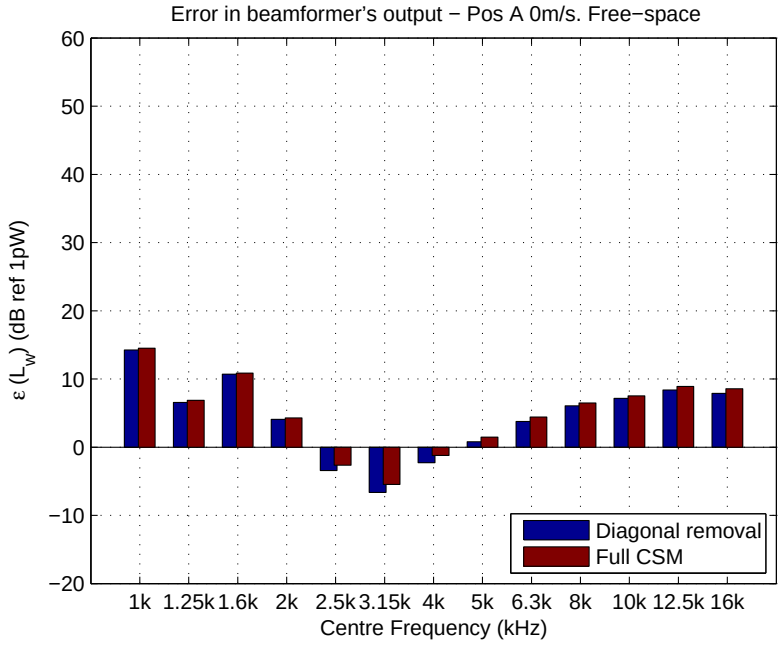

(a) 0 m/s

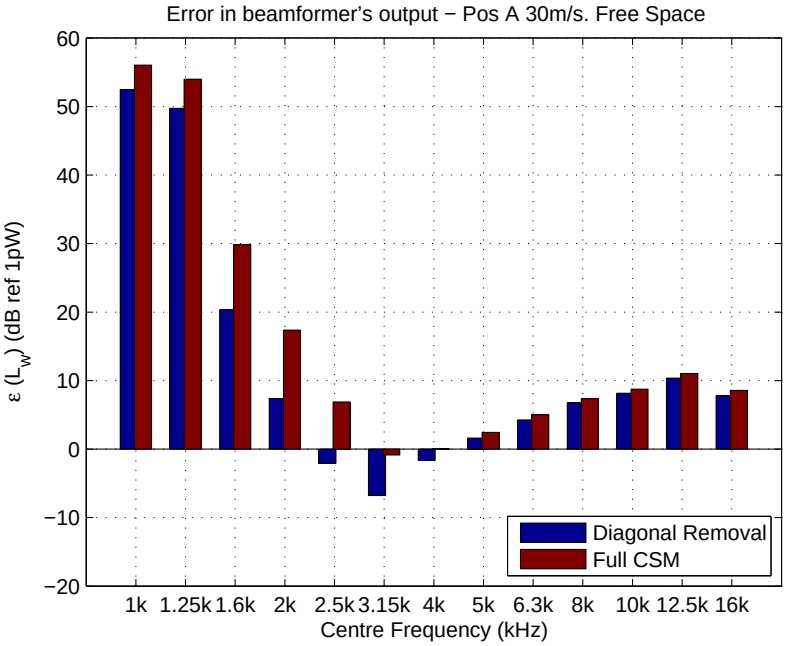

(b) 30 m/s

FIGURE 5.14: Beamforming level errors when beamforming using a full CSM or with the leading diagonal removed. *(upper)* no flow and *(lower)* flow at 30 m/s. Source centred, free space Green's functions.

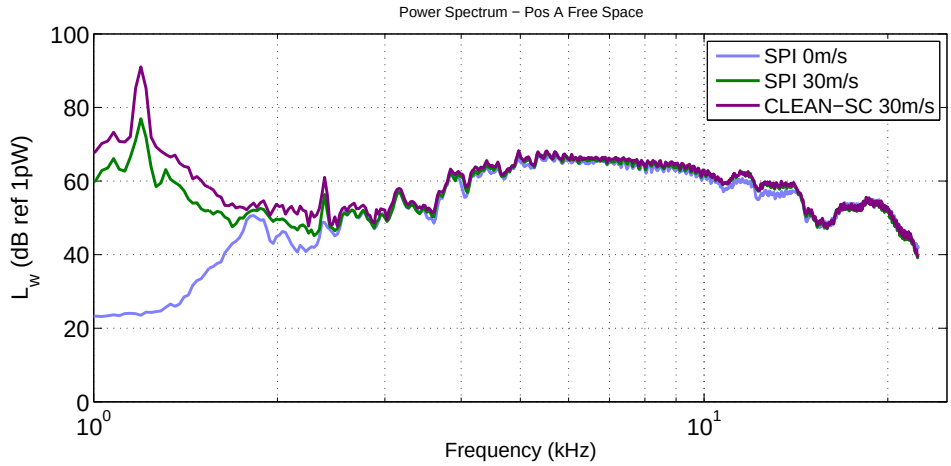

FIGURE 5.15: Source power spectra from integrated beamforming plots and CLEAN-SC with and without flow. Source centred, free space Green's functions.

These results show that although the CSM diagonal removal technique gives significant improvements in both the qualitative and quantitative beamforming results, results at low frequencies can still be inaccurate. At these frequencies noise contamination can be due to the turbulent boundary layer over the array or tunnel noise, or a combination of both. The former can be minimised by using a properly designed microphone array where the microphone diaphragms are in some way physically separated from the boundary layer over the array. One should keep in mind that deconvolution techniques such as CLEAN-SC and DAMAS cannot remove this type of physical noise. Referring to figure 5.18, CLEAN-SC offers little or no improvement to the plots between 1 kHz and 3.15 kHz.

5.4.6 Effect of partially lining the wind tunnel test section

Previous results have confirmed that reflecting surfaces in a closed-section wind tunnels give rise to errors in beamforming levels. An alternative to de-reverberation is to physically attenuate the reflections by lining the test section with absorptive material. Figure 5.19 shows the effect of the duct liner on the beamformer error, for the two different types of steering vectors.

In most frequency bands the difference is 1 dB or less, which falls within measurement errors. This suggests that in this case the liner is not an effective solution. However the effectiveness of this test was limited by two factors. The chosen liner was covered by an impervious plastic sheet in order not to affect the flow characteristics; this seriously limits the absorption characteristics. Secondly, only small parts of the wind tunnel test section could be covered without affecting the stan-

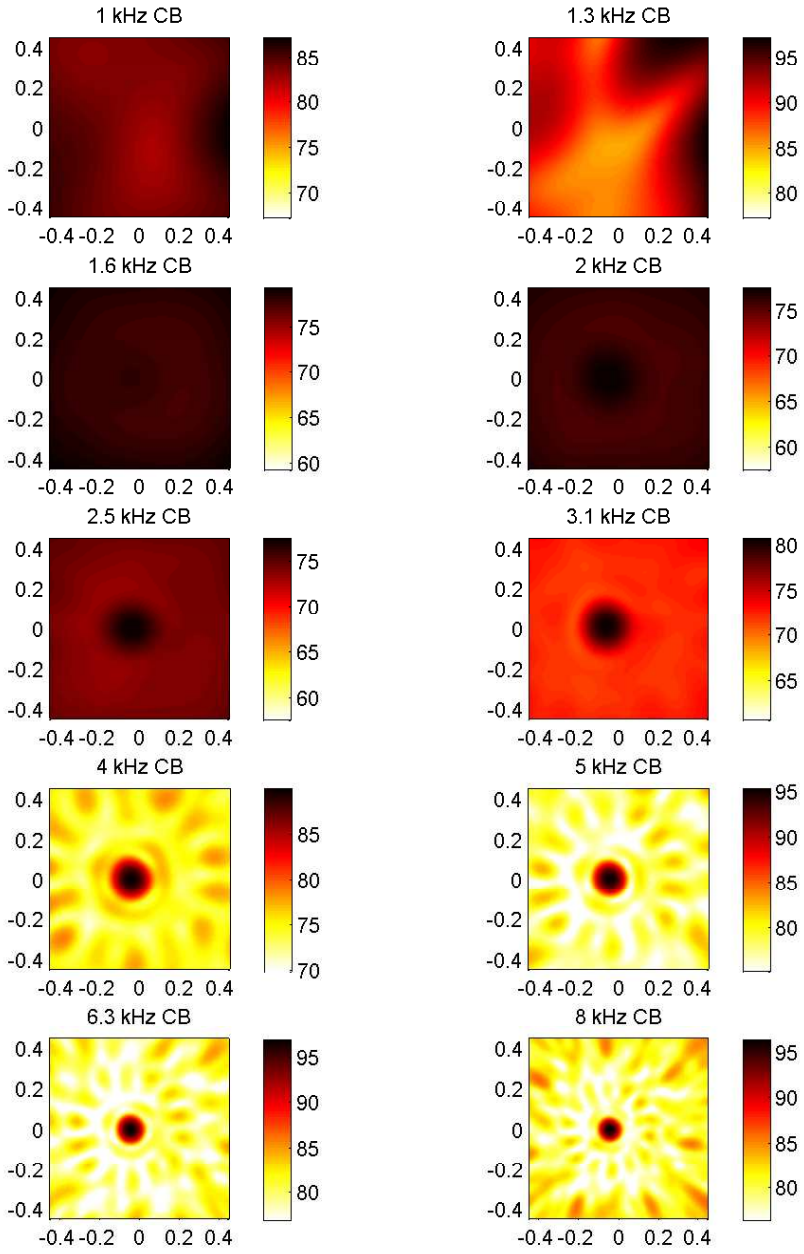

FIGURE 5.16: Conventional beamforming maps of the centred source in the presence of flow at 30m/s, using the full CSM. Free space Green's functions.

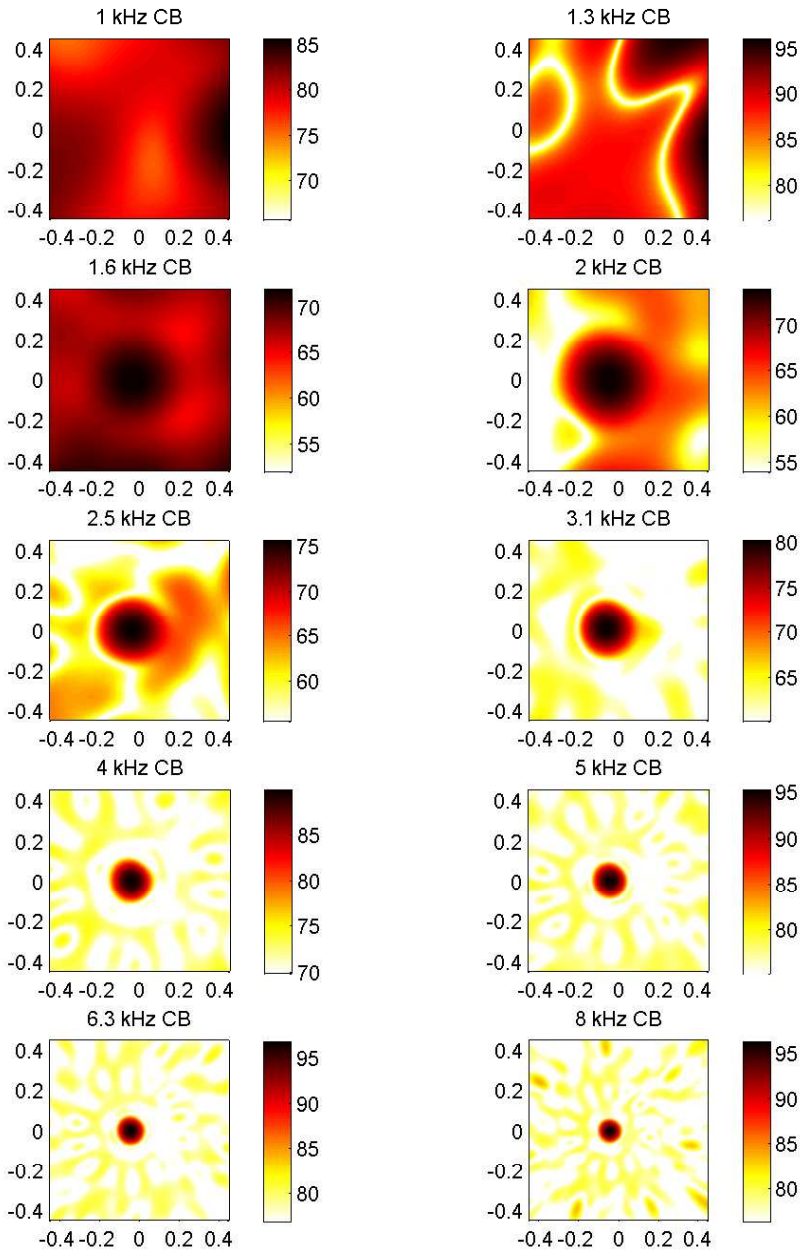

FIGURE 5.17: Conventional beamforming maps of the centred source in the presence of flow at 30m/s, with CSM diagonal removal. Free space Green's functions.

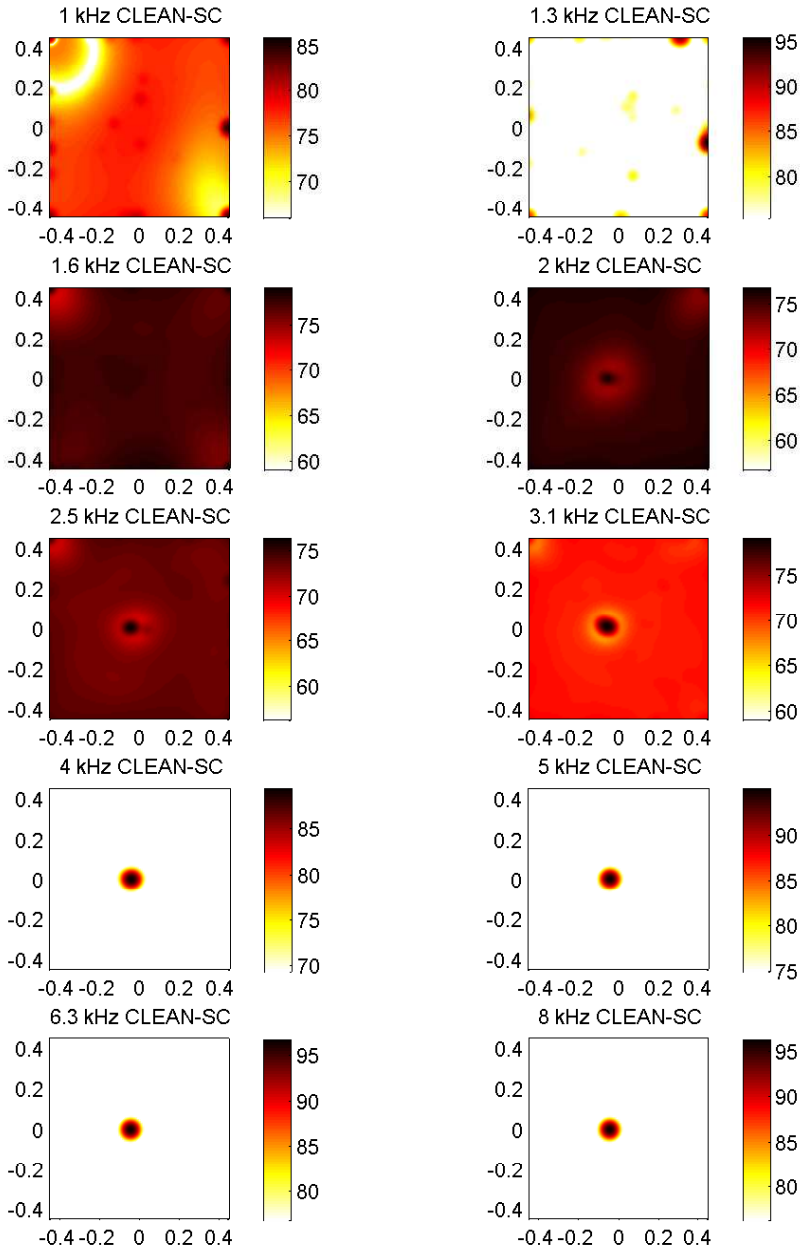

FIGURE 5.18: Deconvolved beamforming maps of the centred source in the presence of flow at 30m/s, using the full CSM. Free space Green's functions.

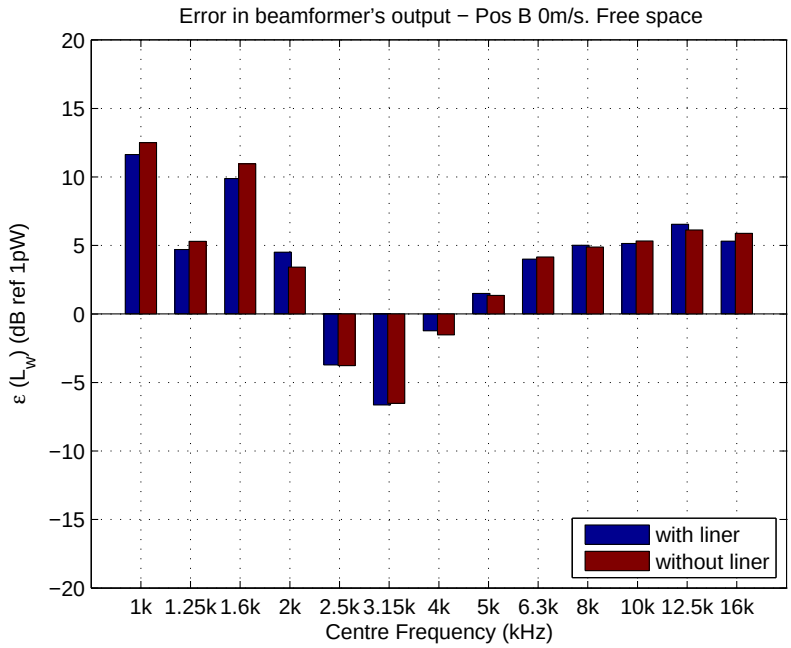

(a) Free space

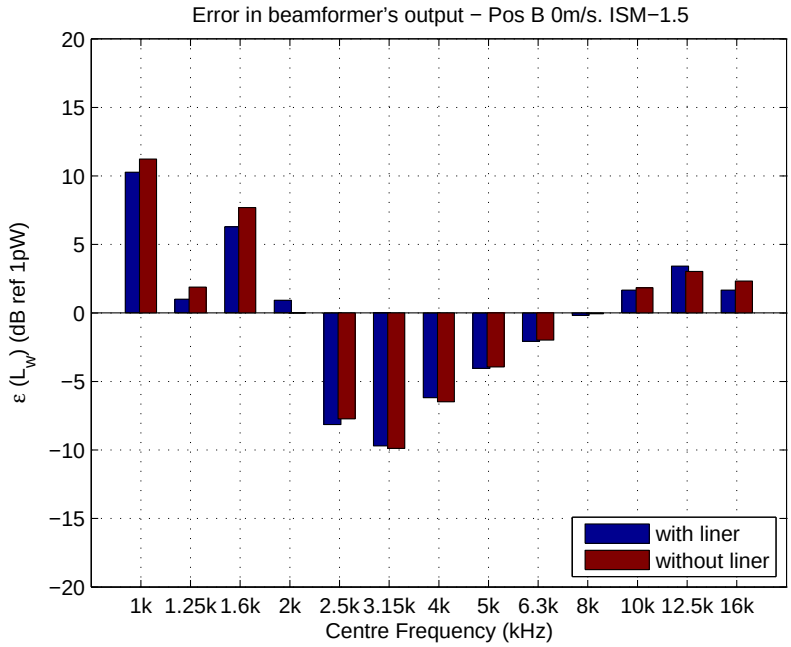

(b) ISM-1.5

FIGURE 5.19: Beamforming level errors with and without the absorptive liner installed. *(upper)* free-space Green's functions and *(lower)* ISM-1.5. Source offset, no flow.

dard operational procedures of the wind tunnel (for example areas covered with glass could not be lined).

Figure 5.20 shows the effect of liner in the presence of flow, when using free space Green's functions. In this case there is a noticeable benefit of up to 5 dB in the lowest frequency bands, which can be observed for both source positions (centred and offset). This can be due to a reduction in wind tunnel noise levels. The beamforming maps at these frequencies show a slight change in the sidelobe behaviour with and without liner, which may indicate the presence of plane wave noise propagating in the wind tunnel as discussed by Koop and Ehrenfried [13]. There is no noticeable increase in the errors at high frequencies when the liner is installed, and the beamforming maps are very similar.

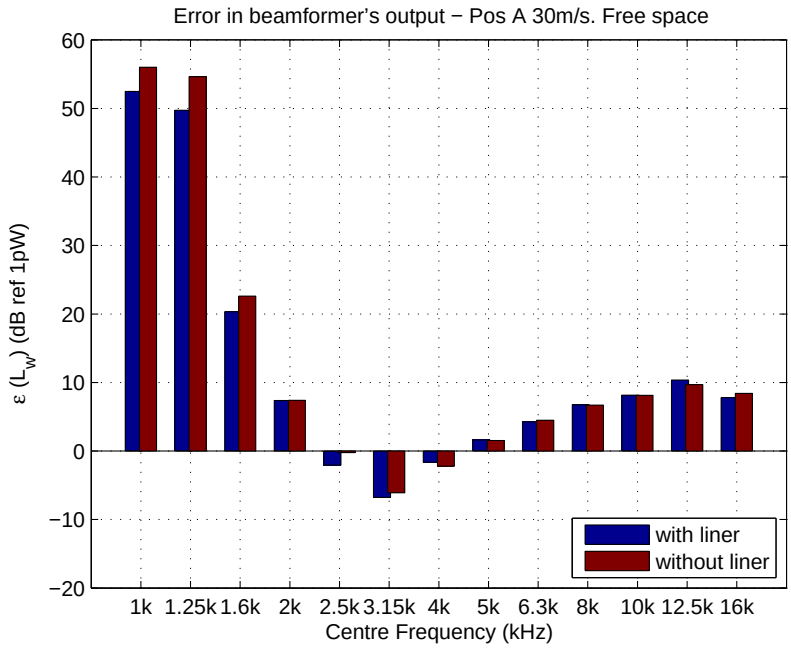

(a) Position A

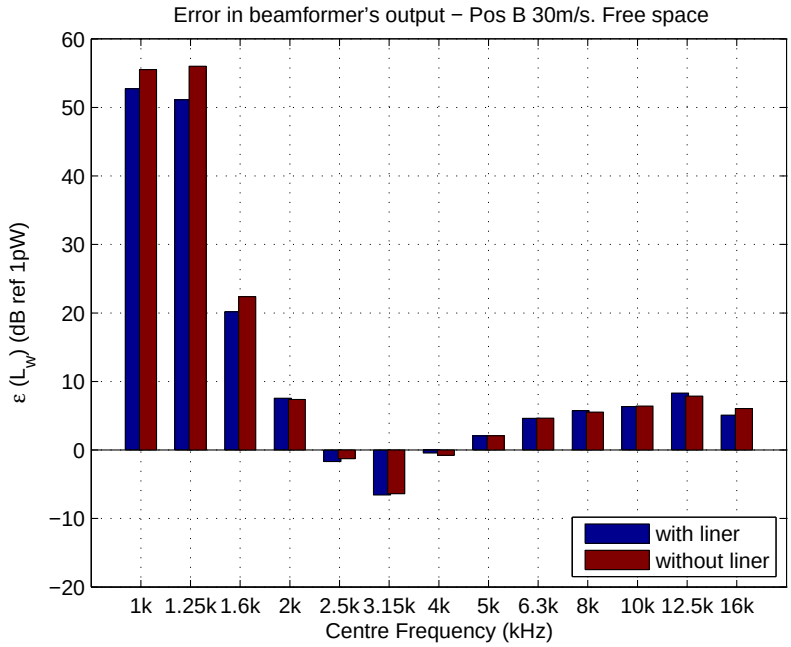

(b) Position B

FIGURE 5.20: Beamforming level errors with and without the absorptive liner installed. *(upper)* source centred and *(lower)* source offset. Flow at 30 m/s, free space Green's functions.

5.5 Realistic Sources

The previous section discusses the effects of de-reverberation in terms of a single calibration source. In practice test models that are installed in wind tunnels typically feature a spatial distribution of noise-generating regions. This can lead to some sources being closer to a boundary than others, and the level contributions from the reflections will be different for each individual source.

This observation was made when applying de-reverberation to data acquired from a half-aircraft model mounted from the ceiling of a hard-walled wind tunnel [55], and comparing the results with those obtained using free-space Green's functions. Unfortunately the results from this test are classified and therefore could not be published. A qualitative description of the key conclusions will be presented instead. The tests were performed using a 144-channel microphone array mounted vertically facing the pressure side of the wing. The array has an aperture of one metre, and the perpendicular distance from array to scan plane was approximately one metre. The following discussion is based on data from the landing configuration (slats and flaps deployed) at 70m/s.

The most significant differences between plots generated using free-space Green's functions and de-reverberation occur in the mid to high frequencies. At these frequencies the array resolution is sufficiently high such that sources are well defined. In this case sources were concentrated along the leading edge of the wing, coinciding with slat tracks and other discontinuities. The major change introduced by de-reverberation is the significant reduction in the apparent level of a source at the wing-fuselage junction. This source is situated very close to the ceiling of the wind tunnel, and de-reverberation yielded a significant reduction. Sources further away from this rigid boundary were also attenuated, but to a lesser extent. This meant that with de-reverberation, the most prominent source was the isolated source on the trailing edge of the wing - using conventional beamforming, the most prominent source was the one at the wing-fuselage junction. This source-reordering can have serious consequences in the noise control strategies taken as a direct results of the aeroacoustic measurement session. Nevertheless one has to be careful how to interpret these results, since the ISM applied to this case assumes sources that have unform directivity, whereas in practice this might not be the case.

In the lower end of the spectrum, the most noticeable difference was that de-reverberation significantly attenuated a number of isolated point sources randomly situated around the wing (which are probably spurious sources), and instead high-

lighted a number of sources along the fuselage. It is not yet clear if these sources along the fuselage have any physical significance. Furthermore, a number of additional sources were introduced along the wing by de-reverberation; once again the existence of these sources in reality could not be confirmed.

Another secondary effect was that de-reverberation resulted in an overall reduction in background noise levels at the lowest frequency bands (0.63, 0.8, 1 and 1.25 kHz). At 630 Hz the reduction was between 5 and 10 dB; for the other three bands the reduction was less than 5 dB.

5.6 Summary

In this chapter the accuracy of beamforming levels in closed-section wind tunnels was investigated using a calibration source of known source strength. De-reverberation based on an ISM yielded improvements in beamforming accuracy in the low and high frequencies, although the improvements at high frequencies cannot be attributed with certainty to de-reverberation. The way the ISM is defined can have a noticeable influence on the improvements that can be achieved: in this case, the most accurate model was not a true representation of the wind tunnel test section. De-reverberation is equally valid for the flow and no-flow scenarios. Levels from CLEAN-SC are not influenced by de-reverberation, therefore quantitative data should be extracted using SPI on the de-reverberated plots (without deconvolution).

The accuracy of results at low frequencies is highly dependant on the level of noise contamination. The CSM diagonal removal technique cannot be assumed to be completely effective in eliminating the influence of this noise.

Applying de-reverberation to a half-aircraft model has highlighted another important effect of the reverberant field. The contribution of reflections depends on the distance of the true source from the rigid boundaries. In a typical model, some sources may be closer to a boundary than others; this may lead to a re-ordering of the source ranking.

Chapter 6

Conclusions

This work was based on the research hypothesis investigating whether accurate aeroacoustic measurements are possible in closed section hard-walled wind tunnels. Inaccuracies can arise due to a number of factors, which can be broadly classified as errors due to physical phenomena, and errors due to the signal processing (beamforming). This work focuses on the former type. In particular, the two main sources of error in closed section hard-walled wind tunnels are the reverberant sound field and the turbulent boundary layer in contact with a flush-mounted microphone array. It was shown that both these phenomena can give rise to significant errors in the beamforming levels.

A technique referred to as de-reverberation, based on an Image Source Model (ISM), was shown to give improvements in the accuracy of beamforming results by taking into account the influence of the walls using the concept of image sources. The improvements that can be achieved vary with the wind tunnel's test section size and the relative position of the sound source, and therefore it is difficult to quantify these improvements in general. Measurements carried out using a calibration source in a $2.1 \times 1.5\,\mathrm{m}$ wind tunnel benefited from a reduction in beamforming level errors of $1 - 5\,\mathrm{dB}$.

When dealing with aeroacoustic measurements, it is a challenging task to quantify what "accurate" is. Results from closed-section tests can be compared with their open-jet equivalents, however it is important to ensure that the test conditions are exactly the same for both cases. Furthermore array measurements in open-jet wind tunnels can suffer from inaccuracies due to coherence loss at high frequencies. For aircraft manufacturers the most accurate data set is from flyover tests, however this data is not available for individual components such as high

lift devices or landing gear. Therefore accuracy studies tend to be carried out using calibration sources. To evaluate the absolute improvements given by de-reverberation, a high-frequency transducer was used as a calibration source. Its total radiated sound power was measured in a reverberation chamber according to international standard BS EN ISO 3741:2000, and the sound power levels obtained from beamforming were compared to these reference levels.

De-reverberation is integrated in the beamforming processing by modifying the steering vector. For a closed test section, an ISM replaces the boundaries with a number of image sources whose positions depend on the relative position of the true source. An infinite duct of rectangular cross section is considered for simplicity. During beamforming, the "true" source is assumed to be at each grid point on the scan plane, and therefore the positions of the image sources vary for each grid point. The modified steering vector is built by summing up the transfer functions between receiver and the grid point and corresponding image grid points. Dissipation at the walls is taken into account by assuming a purely resistive factor. The absorption due to air at high frequencies is also taken into account.

This kind of model offers several benefits. Similar to beamforming, no *a priori* information on the number and location of sources is required. It is computationally efficient: for a simple source, the computational time with de-reverberation was on average 35% longer than standard beamforming. For a more realistic complex source (half aircraft model), the clean wing configuration (no sources visible) also took 35% more time to compute, however the landing configuration took the same amount of time as conventional beamforming. There are no matrix inversions, which makes this technique insensitive to the relative position of each grid point with respect to the boundaries. De-reverberation was shown to work equally well with and without flow. Furthermore, no extra wind tunnel time or test section modifications are required.

The biggest drawback of this technique is that it is sensitive to position errors at high frequencies. Beamforming relies on accurate phase information, and at high frequencies even a small position error corresponds to a significant phase error. However simulations have shown that the influence of the reverberant field is of most concern at the low to mid frequencies ($< 10\,\mathrm{kHz}$). Therefore, unless the position measurements can be guaranteed to be accurate, de-reverberation should only be employed for the low to mid frequencies.

In practice the dissipation at the wind tunnel boundaries will have a reactive part, and it will also be dependent to some extent on the angle of incidence of the

incoming sound waves. This means that an ISM that takes into account purely resistive losses at the boundaries can lead to errors in the beamforming levels. Incorporating a complex angle-dependent impedance at the boundaries into the ISM is possible, however it will complicate the model considerably. In the limit, the model can become a numerical method such as a phased beam tracing method. The computational penalty of using an angle dependent dissipation over an angle independent approximation was given in literature to be equal to a factor of 30 [38].

In theory an Image Source Model creates an infinite number of image sources. In the model implemented in this work, image sources were grouped according to expanding rectangles emanating from the test section boundaries. Measurements showed that including more than the first set of eight images (for a rectangular cross-section) is not likely to yield any further improvements in the accuracy of the beamforming levels. This might be the case because "higher order" reflections correspond to sound waves propagating past the test model in the wind tunnel. This physical body will invariably "break up" the reflections through diffraction and scattering effects.

Beamforming with de-reverberation gives rise to a complex beam pattern featuring a distorted mainlobe and high sidelobe levels. In theory this beam pattern should cancel out the complex acoustic response of the reverberant test section. In practice the de-reverberation formulation will include assumptions and inaccuracies, which means that this degraded beam pattern might not cancel out completely. However since de-reverberation only alters the steering vectors, any remaining noise can be nullified through the use of deconvolution. It was shown that CLEAN-SC was particularly effective. In fact de-reverberation results with CLEAN-SC were qualitatively very similar to those obtained from conventional beamforming with CLEAN-SC. This was the case for both a single calibration source and a realistic half-aircraft model.

In free space conditions quantitative levels can be extracted from beamforming plots using either Source Power Integration (SPI) or directly through CLEAN-SC. In a reverberant environment more accurate results have been achieved when using SPI to extract levels from beamforming plots generated using de-reverberation. In its current formulation levels from CLEAN-SC are only a function of the measured data, i.e. they are not affected by the type of Green's functions used to generate the beamforming plots. Therefore it is suggested that deconvolved plots are used for qualitative purposes, whereas a quantitative analysis is carried out using SPI

on the "dirty" de-reverberated maps.

Inaccuracies in the beamforming levels also arise due to the noise contribution from the turbulent boundary layer in contact with a flush-mounted microphone array. The conventional way of eliminating this noise is by removing the diagonal of the cross-spectral matrix (CSM). This is based on the assumption that the boundary layer noise is uncorrelated across the array microphones. However with the measured data in this investigation, the diagonal removal (DR) technique was only partially effective. In fact both simulations and measurements have shown that the DR technique can only give a maximum of 10 dB reduction in the errors arising due to the flow. This phenomenon is believed to be linked to the surface treatment of the array, although further investigation is required for more definite conclusions. It is suggested that physical measures to separate the microphones from the turbulent boundary layer should be employed.

Simulations have also shown that the DR technique can also amplify the effects of other errors, such as those arising from the reverberant field. It was observed that when various errors were injected in the input parameters, the resulting beamforming level at the source position fluctuated significantly as a function of frequency. Once again, this phenomenon is still not very well understood. It is believed that this effect is related to the non-physical negative source powers that arise in beamforming plots, and that give rise to errors in SPI levels when the DR technique is used. In this case, using a threshold to reject levels below a fixed level was shown to restore the accuracy of the results.

A set of measurements was also carried out with the wind tunnel test section partially lined with acoustic duct liner. This liner yielded benefits in beamforming accuracy at low frequencies (≤ 2 kHz) - quantitative errors were reduced by up to 5 dB, and the plots were more clear. The improvements can be attributed to a reduction in the test section reflections and also a certain degree of absorption of the noise propagating inside the wind tunnel. However installing the liner requires a significant cost and wind tunnel time penalty, and can adversely affect the wind tunnel aerodynamic characteristics. Both these types of noise can be reduced in post-processing: the former by de-reverberation and the latter using BiClean [13] (not investigated in this work).

In spite of the advantages of de-reverberation, it is always better to avoid the influence of reflections in the first place. Carrying out beamforming in larger wind tunnels, where the test model is well away from any rigid boundaries, is therefore recommended.

6.1 Recommended future work

De-reverberation was shown to be an effective technique to improve the accuracy of beamforming, especially at low frequencies. However there are a number of issues that still need to be tackled before aeroacoustic measurements in hard walled wind tunnels can be considered as accurate.

First, a method that is more robust to position errors would be advantageous. A method suggested by Sijtsma which tries to minimise the effect of the image sources through an additional constraint for the minimisation of the cost function was shown to be more robust to phase errors at high frequencies. The problem with this method is that it involves a matrix inversion and therefore depends on the condition number. Essentially this method works well when the steering vectors due to the true source and image sources are independent of each other. This limits the applicability when sources are very close to a boundary (maximum influence on the beamforming levels accuracy), and for reflections from the boundary opposite the array.

Second, beamforming levels for array measurements of the calibration source in the $2.1 \times 1.5\,\mathrm{m}$ wind tunnel exhibited two features that could not be explained with certainty. The levels between $2 - 4\,\mathrm{kHz}$ were underestimated by conventional beamforming. De-reverberation reduced the absolute levels, thereby increasing the level of underestimation, and hence the magnitude of errors. It is believed that this might have been due to the source spectrum changing between the reverberation chamber and inside the wind tunnel test section. The second feature was an increasing error in beamforming levels at the highest frequencies. Simulations have shown that the effect of reverberation is not so significant at high frequencies ($> 10\,\mathrm{kHz}$). The observed errors might be due to the directivity of the source. This effect should be investigated further, possibly by performing array measurements in an anechoic environment.

The issue of source directivity is also important in the formulation of the Image Source Model. The implemented model assumed point monopoles, thereby simplifying the prediction of the image source locations. Realistic aeroacoustic sources tend to be multipole, and therefore the influence of the reflecting boundaries becomes more difficult to predict.

The proposed ISM is a simplistic model, and it does not take into account the presence of any structural struts, or the influence of the test model under investigation. A more accurate representation of the actual transfer functions in the

wind tunnel test section can only be achieved using numerical tools such as phased beam tracing methods and Computational Aeroacoustics (CAA) codes, or determined experimentally. The latter method will ultimately be the most accurate representation, however it is also the most challenging, due to the requirement of accurate phase measurements at high frequencies. Unfortunately an attempt to get an estimate of the true Green's functions using impulse response measurements was of limited success. It is recommended that another attempt is made using a more repeatable source, instrumentation-grade microphones and a data acquisition system with a very high sampling frequency (0.5 MHz).

Appendix A

SotonArray System

As part of this research project, a 64-channel flush mounted microphone array system was designed for the 2.1×1.5 m wind tunnel at the University of Southampton. This chapter describes some of the design considerations of this development. The array system will be divided into three main parts:

- the microphone array (hardware),
- the data conditioning, acquisition and storage hardware, and
- the data processing software.

A.1 The Microphone Array

The microphone array consists of a number of sensors that are positioned in a certain way within a fixed area. Both the actual sensors and their positioning affect the array's performance.

A.1.1 Microphone Choice

The choice of microphones is usually an important decision that has to be made at an early stage of the design stage. The most important considerations when choosing sensors are:

- frequency range: aeroacoustic measurements often involve scale models, which pushes the frequency range of interest to above the audible range: frequencies up to 100 kHz can be of interest in aeroacoustic measurements in wind tunnels [19];
- dynamic range: flush-mounted sensors in closed section wind tunnels have to withstand very high sound pressure levels, especially at low frequencies (c.f. figure 2.7 on page 21), however they should be able to detect weak acoustic signals at the high frequencies;
- phase matching: beamforming is only possible when the data from all the microphones is accurately phase matched (in practice, it has been shown that deviations between microphones within $\pm 10^\circ$ do not affect the accuracy of the results [56]);
- size: the size of the actual microphone plus any necessary hardware will limit how tightly packed the microphones can be and the flexibility of installation of the array;
- stability with respect to environment conditions: this is of most concern in pressurised wind tunnels, where the harsh environmental conditions can significantly alter the performance of the microphones;
- directionality: in most cases, omnidirectional microphones are preferred;
- cost: the available budget will limit the channel count of the system, depending on the price of the sensors (which can vary by up to three orders of magnitude).

Traditionally precision instrumentation-grade microphones have been the preferred choice [54], as they can satisfy the first six conditions discussed above. $1/4''$ and $1/8''$ microphones are preferred due to their small size, lower sensitivity and wider frequency response. The biggest drawback is in terms of cost, which is typically around one thousand pounds per channel, and would normally constitute a significant part of the overall system budget.

An alternative is to use low-cost electret-condenser microphones, which are usually two to three orders of magnitude cheaper. This allows for a higher channel count system for the same cost. The downside is that electret microphones are not designed for precision measurements, which means that the dynamic range, phase matching and stability are inferior to instrumentation microphones. Humphreys

et al. [57] presented a study on the suitability of low-cost electrets for aeroacoustic measurements. The microphones were found to vary in terms of magnitude and phase. Magnitude variations were within ±5 dB. For frequencies between 250 and 16,000 Hz, the phase of individual microphones varied by a maximum of 10°, and therefore no phase corrections were necessary. For higher frequencies (up to 40 kHz), phase variations of ±25° were measured, and phase corrections had to be applied. The lower end of the frequency spectrum was dominated by $1/f$ noise, which is typical of electret microphones. Total harmonic distortion was equal to 1 - 2 % as long as sound pressure levels were lower than 120 dB. Most importantly, the authors found no difference in processed array results up to 20 kHz when compared with equivalent measurements performed using instrumentation microphones.

In recent years there has been a lot of interest in Micro-Electro-Mechanical System transducers, better known as MEMS [58, 59, 60]. These transducers boast a number of advantages: their miniature size allows for a large number of sensors tightly packed in a very low profile sheet that can literally line a complete wind tunnel test section. Material and construction costs are claimed to be reduced by two orders of magnitude when compared to instrumentation microphones [58]. Current designs are based on the piezo-resistive and piezo-capacitive concepts. The current state-of-the art designs are not able to satisfy all the conditions required for aeroacoustic measurements: in particular, a high maximum sound pressure level limit, a large dynamic range and low self noise impose conflicting requirements.

Given the budget, electret microphones (Panasonic WM-61A) were chosen for the SotonArray system. These are omnidirectional, back-electret condenser microphones with a diameter of 6.0 mm. The sensitivity is specified as -35 ± 4 dB (0 dB = 1 V/Pa at 1 kHz), and the SNR is at least 62 dB. The deciding factor for choosing these microphones was that the noise suppression benefits of a higher channel count system far outweighed the drawbacks of magnitude and phase deviations between microphones, which could be corrected by calibration. The choice of microphones imposes a high frequency limit of 30 - 35 kHz (which is equivalent to the first resonance of the capsules), above which the accuracy of the acquired data becomes questionable [61].

A.1.2 Sensor Distribution

In Section 2.1 it was shown that an array of finite size sampled by a finite number of sensors will produce a mainlobe of finite width and a sidelobe pattern. The

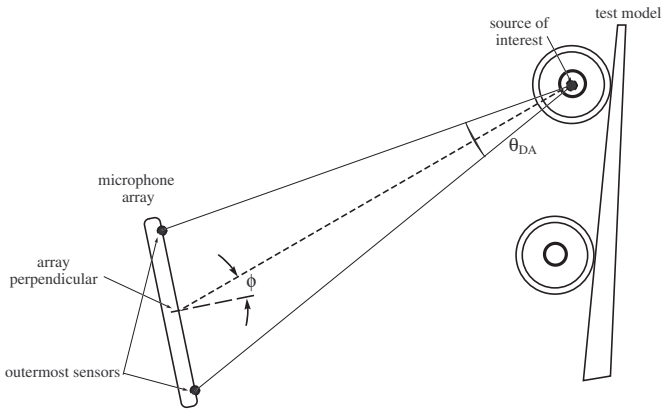

FIGURE A.1: Definition of the array azimuthal angle ϕ_i and solid collection angle θ_{DA}.

width of the mainlobe has an adverse effect on the resolving power of the array at the lower frequencies, whereas sidelobes can make the task of isolating true sources from spurious sources more challenging. Therefore the sensor distribution plays a vital role in the design of an effective array.

A.1.2.1 Aperture size

The aperture size refers to the largest dimension within which the sensors are confined, and will largely determine the resolution of the array – the larger the aperture, the better the array is at discriminating sources close to each other. However a large array poses two challenges: for the same number of microphones, the intersensor distance becomes larger (resulting in more sidelobes); furthermore there is a higher risk of variations in the coherence, amplitude and phase of the noise field over the array surface for directional sources. In references [4, 21] this problem was solved by using two separate arrays for the low and high frequencies. The large-aperture and small-aperture directional arrays (LADA and SADA, respectively) had an approximate diameter of 1.2 and 0.2 metres. The small size of the SADA permitted easy movement around the model under study, and reduced the risk of directivity smearing.

One of the most interesting observation made by the authors was that the array size affected the magnitude of the beamforming levels. In this case, the array size was represented by the solid collection angle θ_{DA}, defined in figure A.1.

Figure A.2 shows the observed effect of array size (represented by θ_{DA}) on the measured spectra of a high-lift NACA $63_2 - 215$ main element airfoil with a 30

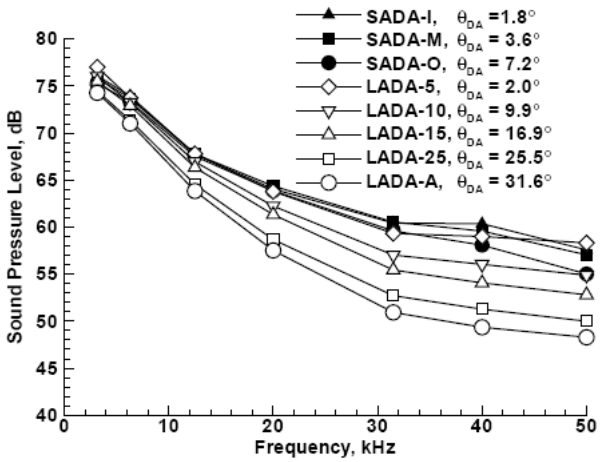

FIGURE A.2: One-third octave spectra of a flat edge flap at M =.17 determined using arrays and sub-arrays of different apertures. From ref. [21].

percent chord half-span Fowler flap at a flow speed of $M = 0.17$. The different solid collection angles were obtained using sub-arrays in both the small- and large-aperture arrays. The general trend is that the larger the array, the lower the spectra. However the Source Power Integration technique was able to recover the total noise spectral output of the different sources irrespective of the array used. The investigators also observed lower absolute levels when using the cross-spectral matrix (CSM) diagonal removal optimisation technique. This can be attributed to coherence loss due to the open-jet shear layer. A closed section wind tunnel does not suffer from such drawbacks.

In closed-section wind tunnels the aperture of the array is often dictated by the geometry of the test section. This is especially relevant to arrays using instrumentation grade microphones with attached preamplifiers; these types of arrays must be installed by physically removing panels in the test section boundaries. If using microphones having a lower profile, the array can be designed in such a way that it can be attached directly to the test section walls. This adds flexibility to its positioning and dimensions. One such array is described in ref. [13], where the microphones were mounted inside a 25 mm thick array fairing with the leading and trailing edges having a slope of 6° to avoid disturbances due to flow separation.

A.1.2.2 Sensor distribution

Once the aperture size has been fixed, the space within has to be spatially sampled with microphones. The most important criterion for this sampling is spatial aliasing, which has already been described in Chapter 2. In order to avoid this,

the array has to be sampled at an interval smaller or equal to half the shortest wavelength of interest. This condition puts severe limitations on the practicality of arrays for aeroacoustic measurements. For example, to measure sounds with frequencies of 50 kHz sensors would have to be spaced 3.53 mm apart. Besides being very close to the physical limit at which the smallest commercially available precision microphones (3.18 mm diameter) can be mounted in an array, such a small inter-sensor spacing would require an unfeasible amount of microphones to fill an array of any reasonable aperture.

An often used solution is to take advantage of the fact that spurious lobes in an array pattern require a coherent buildup of elemental signals at angles other than the steering angle, and can be avoided by eliminating periodicity in the sensor locations. This is achieved by using irregular or aperiodic arrays. The effectiveness of these kind of arrays can be gauged by the peak and average sidelobe levels. The peak sidelobe level depends mainly on the array's channel count. Furthermore, as a general rule of thumb [54],

- the theoretical average sidelobe power level of a random planar array relative to the mainlobe is approximately $10\log(1/M)+3$ dB, where M is the number of sensors in the array;
- the peak sidelobe level is unlikely to exceed the average sidelobe power level by 10 dB.

Ideally, for a given number of sensors, the levels of all sidelobes should be as close to the theoretical average sidelobe level as possible, thus maximising the effective dynamic range of the array. This can be done by optimising even further the sensor placement. Algorithmic aperiodic array design can be used to ensure irregularity in sensor position. More specifically, redundancy in the vector spacings between sensors has to be avoided.

The quickest way how to assess an array's performance is via its co-array, which is the vector spacing view of an array [54]. The co-array gives a good indication of the number of distinct vector spacings for the given array. For an array with M sensors located at $\vec{x}_m$, the co-array is defined as the set of points given by

$$\vec{X}_p = \vec{x}_m - \vec{x}_{m'}, \qquad m = 1, 2, \ldots, M \qquad m' = 1, 2, \ldots, M \tag{A.1}$$

Since $\vec{X}_p$ consists of M^2 vectors, of which M are zero, the maximum number of unique vector spacings in the array is $P_{\max} = M^2 - (M-1)$. For a given array,

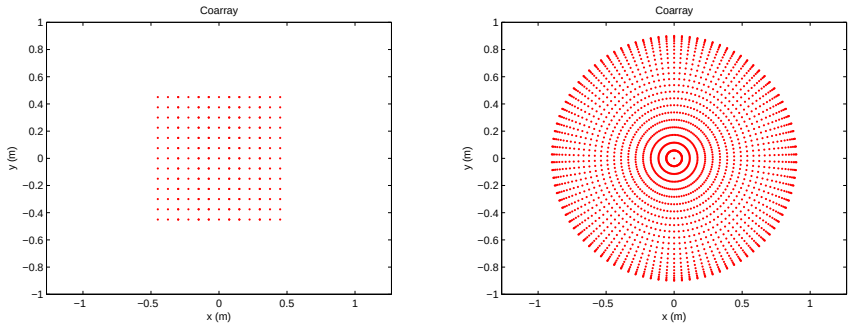

(a) Square array (b) Circular array

FIGURE A.3: Co-arrays of two different arrays, each having 49 sensors. The square co array has 169 unique vector spacings, while the circular array has the maximum possible number of 2353.

a figure of merit can be defined as $F = \frac{P}{P_{\max}} \leq 1$. Figure A.3 shows the co-arrays for two 49-sensor arrays featuring a square or circular sensor placement.

A more thorough analysis of the array's performance can be achieved by plotting the point spread function, which was discussed in Section 2.4. From these plots, the resolution, average sidelobe and peak sidelobe levels can all be quantified.

Many arrays used in practice are based on the logarithmic spiral. One such design, proposed by Underbrink [54], is the multi-arm logarithmic spiral array, shown in figure A.4. A circular aperture is divided into concentric annuli, each having the same area. A logarithmic spiral with a given inner radius and spiral angle is sampled at the radial centre of each annulus. A circular array (containing an odd number of sensors M_c equally spaced on the circumference) is then built, using the pre-positioned sensors as the starting point. The inner circle is divided into M_c sections, and the sensors arranged at the centroid of each resulting sector. An extra circular array is added in the innermost region to 'fill-in' the unsampled space which would otherwise result from this design strategy. Underbrink claims that with this design it is possible to get a peak sidelobe level not more than 5 dB above the average sidelobe level, and dynamic ranges of at least 12 dB over a broad frequency range (1 - 80 kHz).

Other methodologies which have been used to determine sensor positioning include a "simulated annealing" design [24] and a cross-shaped array [17, 62].

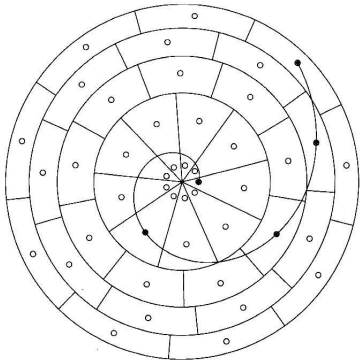

FIGURE A.4: A multi-arm logarithmic spiral array using an equal-aperture-area sampling strategy. Each segmented annular section has the same area. From ref. [54].

A.1.3 Array design for the 2.1×1.5 m wind tunnel

In the case of the 2.1×1.5 m wind tunnel at the University of Southampton, the available space for a flush-mounted microphone array was limited to a rectangular area of dimensions 1.8 x 0.89 metres. For a circular array, this means that the maximum aperture possible is 0.89 m (in practice, this is reduced due to manufacturing constraints). This constraint means that a poor resolution can be expected at frequencies lower than 2.5 kHz. An attempt was made to design a multi-arm spiral array based on concentric ellipses rather than circles. However the resolution is only improved in one axis, and the distorted mainlobe shape could make source map interpretation more difficult. This design was therefore not implemented.

The array design was narrowed down to a 63-channel multi-arm log spiral array with a maximum aperture size of 0.7 m diameter. Scan planes would typically be situated in a region defined by $0.5 \leq z \leq 1.5$ m, where z is the axis perpendicular to the array plane. The only parameters left to vary were the number of concentric circles and the number of sensors in each circle. Four possibilities are 7×9 and 9×7, with and without an inner circle of sensors added. The inner circle reduces sidelobe levels at higher frequencies, at the expense of a poorer resolution. In this notation, the first number corresponds to the number of sensors on each circle whilst the second number denotes the number of concentric circles forming the array. Figures A.5 and A.6 show the sensor arrays and resulting co-arrays of these four different configurations.

The chosen array has seven sensors on nine concentric circles (7×9), without an inner circle, and was chosen because the improvement in resolution was considered

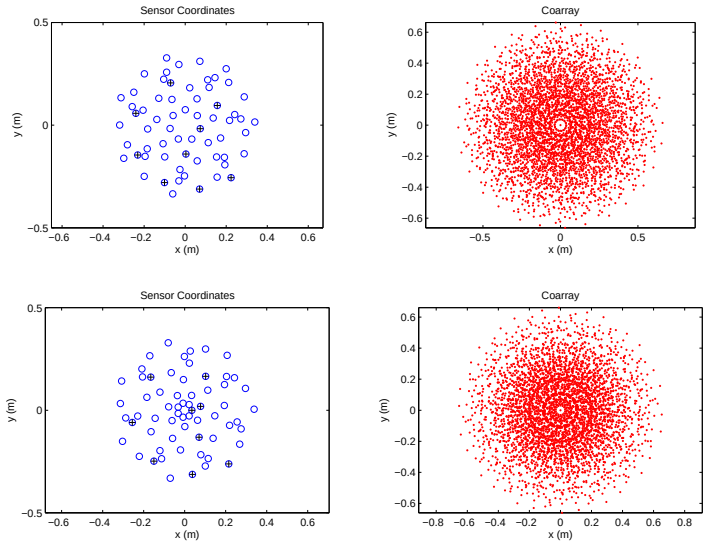

FIGURE A.5: Microphone arrays *(left)* and corresponding co-arrays *(right)* having 7 sensors on each of 9 concentric circles. The bottom plots feature an inner set of sensors.

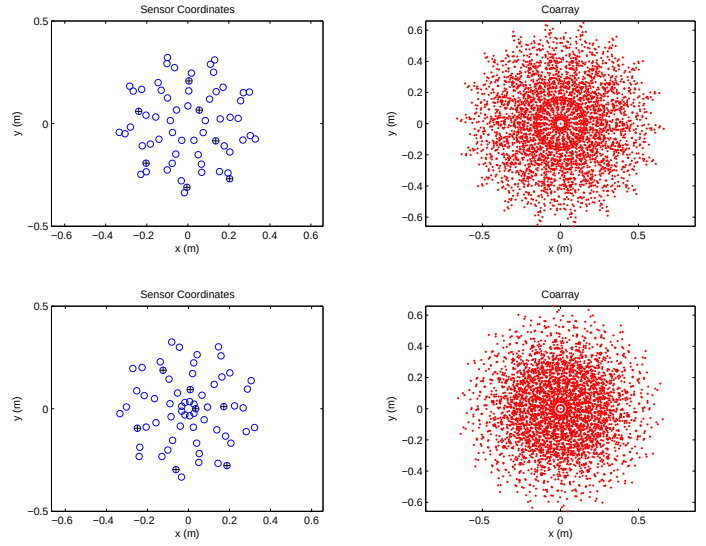

FIGURE A.6: Microphone arrays *(left)* and corresponding co-arrays *(right)* having 9 sensors on each of 7 concentric circles. The bottom plots feature an inner set of sensors.

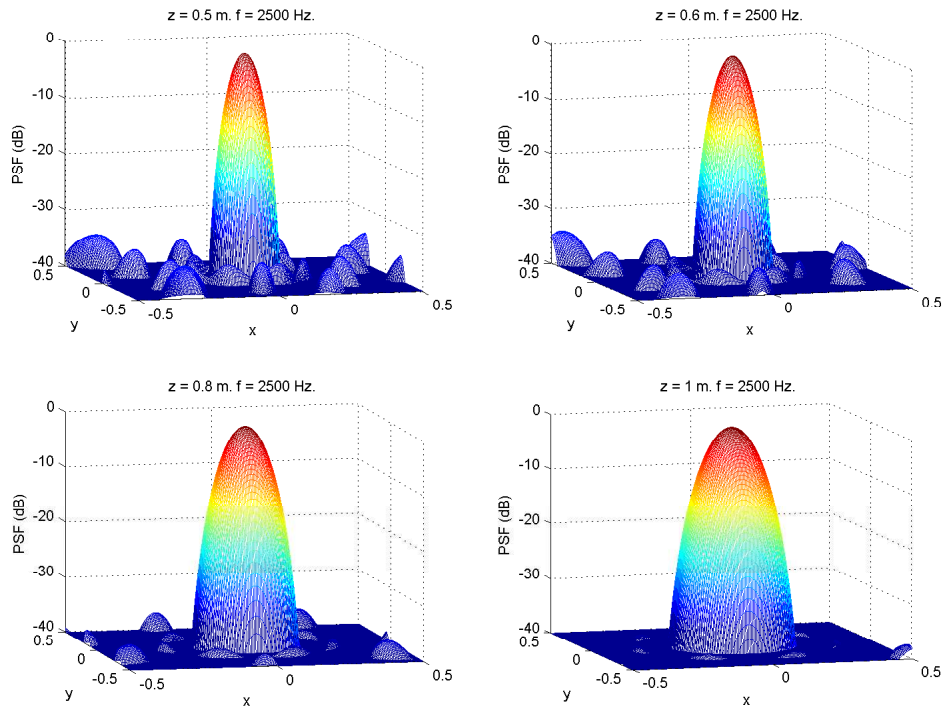

FIGURE A.7: Point Spread Functions of the 7×9 array for a point source centred on a scan plane. Scan planes at a perpendicular distance of 0.5, 0.6, 0.8 and 1.0 m from the array. $f = 2.5$ kHz.

more important than the slight increase in sidelobe levels. Figures A.7 and A.8 show the PSFs of the chosen array based on a 1×1 m scan plane at four perpendicular distances from the array. For a scan plane 1 m away from the array, the resolution of the array (3 dB bandwidth) is roughly 1.6λ [m]. For the same scan plane, the peak sidelobe level at 8 kHz is roughly 30 db lower than the source level.

One of the advantages of a microphone array is its inherent ability to suppress sources coming from directions other than the array's "look" direction. Such sources have maximum influence when located "behind" the scan plane (as viewed from the array). Figures A.9 and A.10 show PSFs based on the same scan planes as in figures A.7 and A.8, however this time the source is 2.1 m away from the array and slightly off-centre (exact coordinates are $x = 0.1, y = -0.1, z = 2.1$, with respect to the origin at the array centre). The influence of the source increases as the scan plane moves towards it, and is much more significant at the lower frequencies. This is because the array's resolution is poor on the axis perpendicular to the array's plane. The average sidelobe level is somewhat increased by this "spurious" source.

The PSF is a simulated response, and represents a "best case scenario". In practice

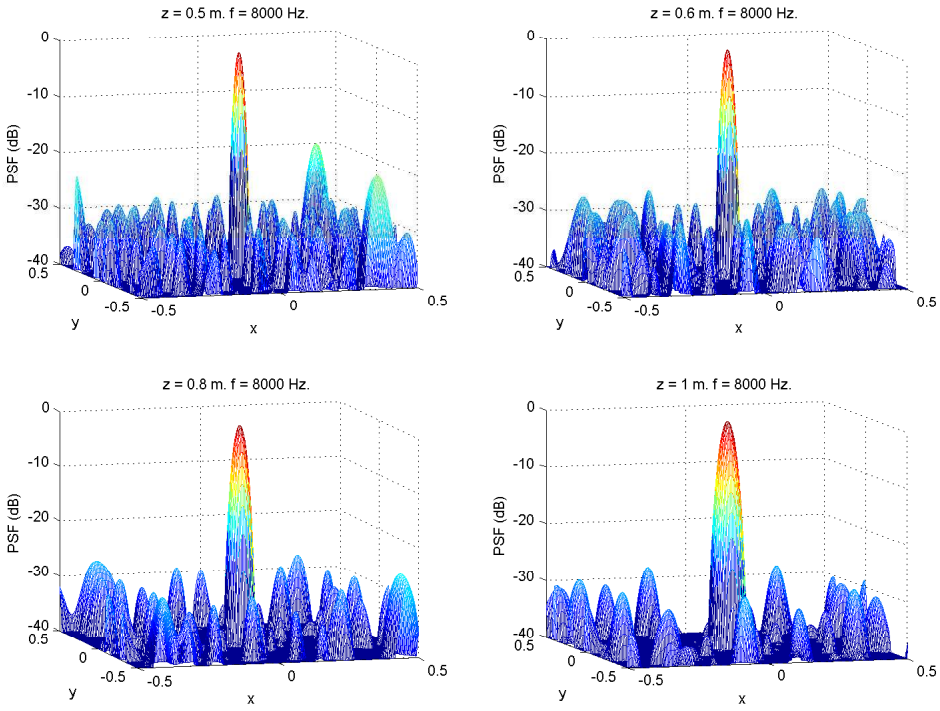

FIGURE A.8: Same plots as in figure A.7, but at $f = 8.0\,\text{kHz}$.

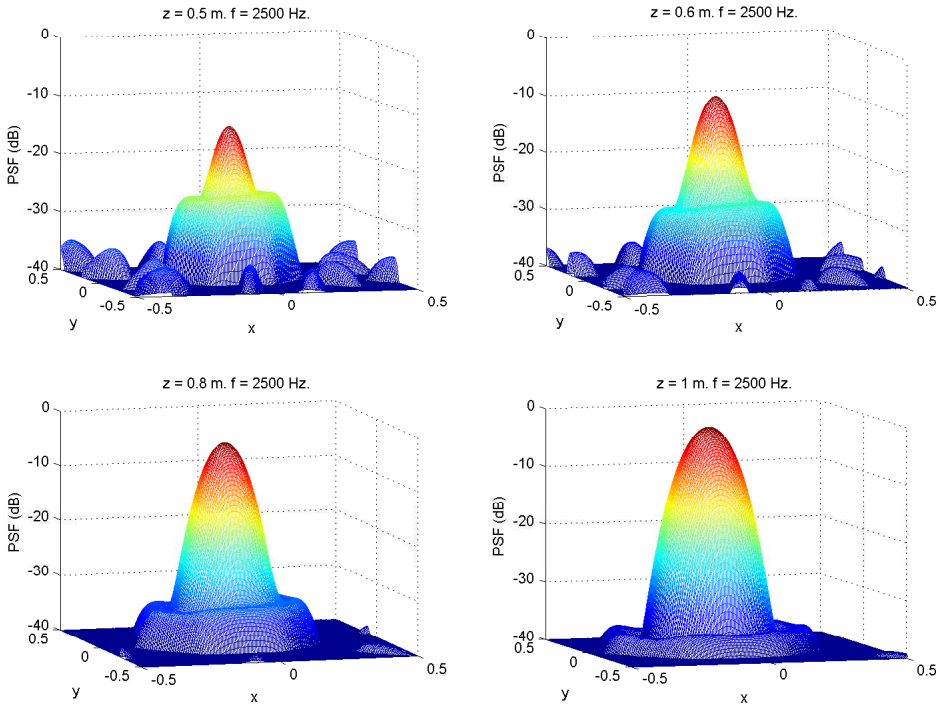

FIGURE A.9: PSF of a 7×9 array with source behind scanning plane ($x = 0.1, y = -0.1, z = 2.1$), $f = 2.5\,\text{kHz}$.

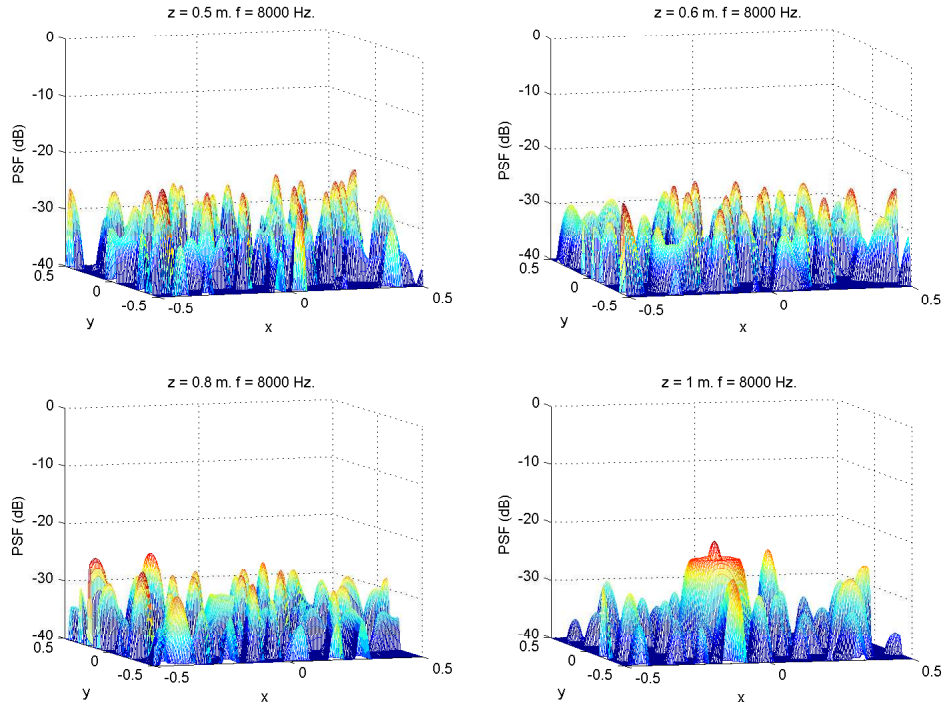

FIGURE A.10: PSF of a 7×9 array with source behind scanning plane ($x = 0.1, y = -0.1, z = 2.1$), $f = 8\,\text{kHz}$.

magnitude and phase mismatches, inaccuracies of the sensor placement and the reverberant field in the wind tunnel will have an adverse effect on the array's performance. Figure A.11 shows beamforming plots using a measured data set. The simulated point source is the same as that used in Section 4.2, in the form of a high intensity source coupled to a radiating orifice. The measurements were carried out without flow. Due to hardware limitations, only 56 out of the 63 microphones were used (the microphones on the sixth concentric circle from the inside were not used). The scan plane is $1.2 \times 0.8\,\text{m}$. The peak sidelobe level in the measured results is approximately 18 dB less than the source level. This discrepancy from the PSF values is partly due to using 11% less channels.

A.1.3.1 Array shading

The plots in figure A.11 indicate that results at the lower frequencies ($\leq 2\,\text{kHz}$) will have limited usability, due to the poor resolution. Given that the aperture size and the number of sensors were fixed, the only way how the resolution could be improved was by having a larger concentration of sensors on the outside of the array. One way of doing this is to design a higher-count multi-arm log-spiral array,

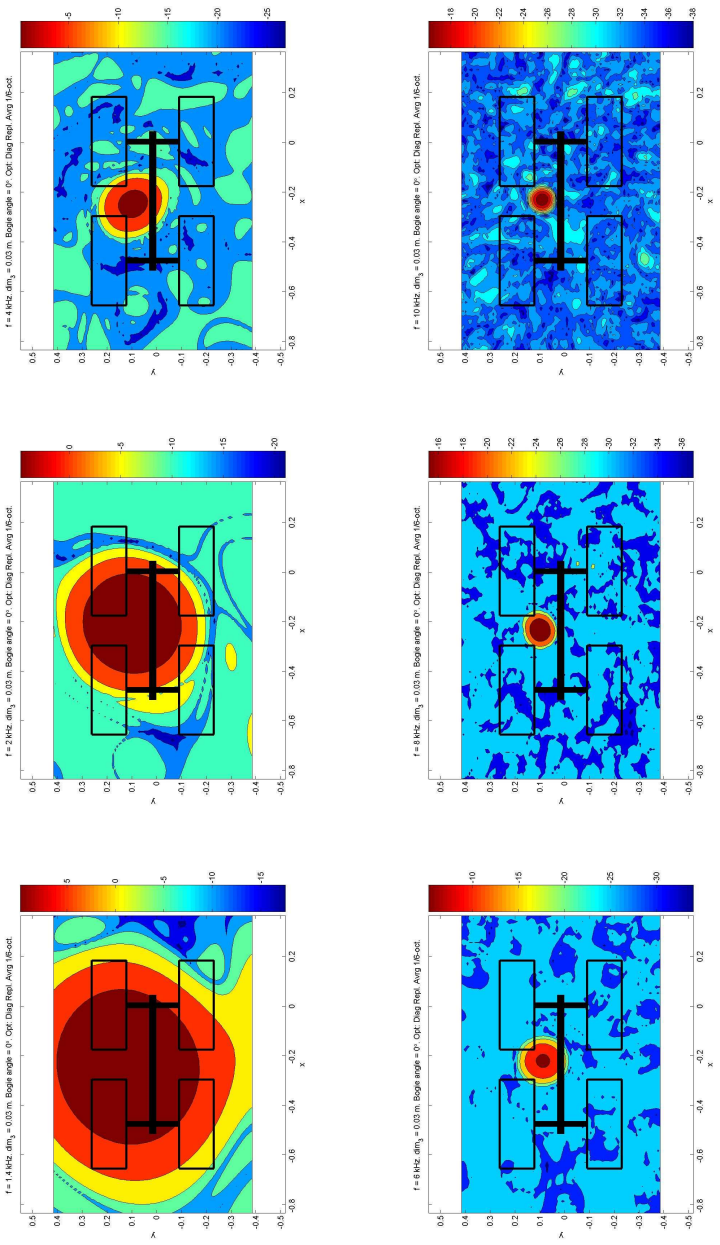

FIGURE A.11: Beamformer maps at various frequencies generated from measured data. Point source at $x = -0.225, y = 0.085$. See text for further details.

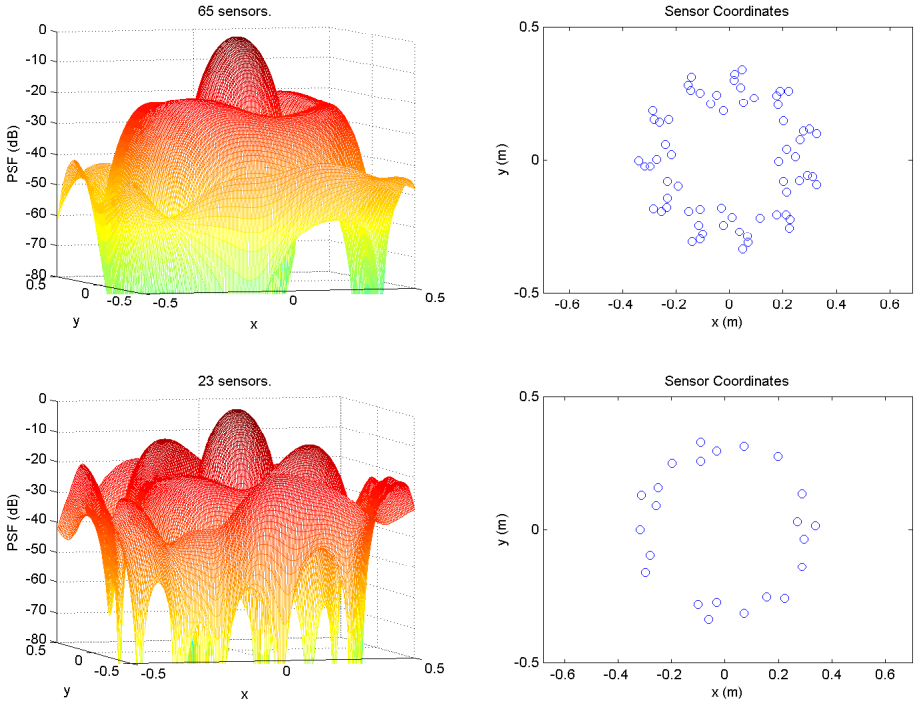

FIGURE A.12: Comparison between the point spread function and sensor distribution of two arrays having different configurations but one aim: that of concentrating more sensors on the outside of a 0.7 m diameter array. $f = 2.5$ kHz, $z = 1$m.

and then use selections of sensors for different frequencies. For example, the upper left hand plot of figure A.12 shows a selection of the outermost 64 sensors chosen from a 111-channel array . The resulting PSF (shown on the right hand side) can be compared with the bottom right hand plot in figure A.7. With the same amount of sensors and same aperture size, the beamwidth for this array design is effectively half the original one. However this comes at a price: namely a much higher sidelobe level (nearly 20 dB higher), which, being so close to the mainlobe, would have detrimental effects on nearby weaker sources, thus counteracting all the improvements which a thinner mainlobe was supposed to give.

Yet another alternative is to start with the original 7×9 array, and use only a subset of sensors for a particular frequency (this is often termed as "shading" in phased array literature). The major advantage of this is that one array is installed with all the sensors connected, and particular sensors are "engaged/disengaged" at the post-processing stage. The two plots on the bottom of figure A.12 show the sensor coordinates and corresponding PSF when ignoring the innermost 42 sensors. For this case the beam width is also reduced, however the sidelobes are even higher than in the previous case. Therefore array shading is not a viable solution with

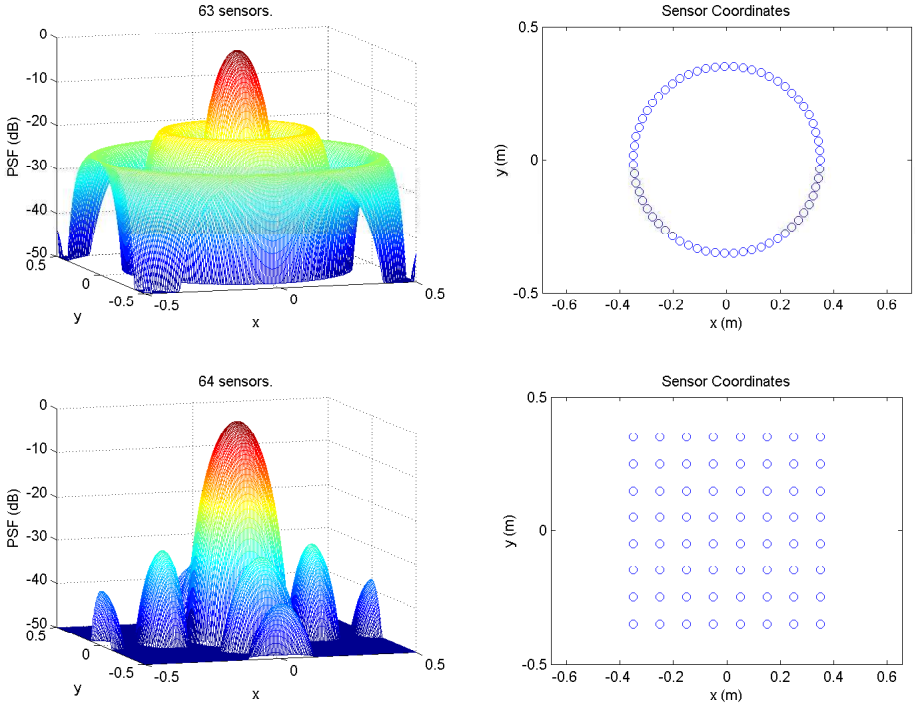

FIGURE A.13: Comparison between the point spread function and sensor distribution of two arrays: a circular array with $F = 1$ and a square array with $F = 0.46$. $f = 2.5\,\text{kHz}$, $z = 1\text{m}$.

such a low channel count.

For a fixed sensor count and aperture size, the thinnest beam width possible at a particular frequency is given by an array consisting of all the sensors sitting on the circumference of a circle of diameter equal to the aperture size. In this case, with 63 sensors and a maximum aperture of 0.7 m, the point spread function at 2.5 kHz of a scan plane parallel to the array and at a distance of 1 m away from it is shown in the top left hand plot of figure A.13. Once again, a good resolution comes at the expense of high sidelobes, which arise due to the uneven spatial sampling of the array's aperture. In contrast a square array gives a beam width of comparable size but with significantly lower sidelobes. Obviously this kind of array is not suitable for high frequencies, as discussed previously.

A.1.4 Array Calibration

When using single microphone measurements, accurate results depend on a proper calibration – normally a simple pistonphone calibration is sufficient. A microphone array also needs to be calibrated, however there are more parameters involved. The

array can be thought as a combination of the sum of the individual channels, and the assembly as a whole.

Beamforming relies essentially on magnitude and phase differences between channels, so ideally the response of each channel should be identical. In practice, if the same reference signal is applied to each channel, the amplitude and phase of the recorded signals will vary across channels. Each stage of the data acquisition contributes to this mismatch.

With respect to the array as a whole, installation errors are usually the most significant, especially at high frequencies. These errors arise because microphones are rarely at the exact specified position. Such errors can only be corrected by an in-situ array calibration.

There are various types of calibration tests which can be applied to arrays [4]:

- *injection calibration*, where a known signal (pure tone or white noise) is injected simultaneously into all microphone channels to detect microphone sensitivity and phase drift;
- *geometric survey techniques*, used to locate the position of the model relative to a reference point on the array, usually the centre – various measuring techniques can be used, such as laser and tape measure, sonic digitiser and portable coordinate measurement machines [19];
- *isolated point source test*, preferably performed in an anechoic chamber (in a wind tunnel, an anechoic box can be used to enclose both source and array) – the processed output of the array when focusing directly on the source should give exactly the same level as a single microphone;
- *in-situ point source test*, where a point source is mounted at a specific position on the test model, and measurements are taken with and without flow — this is a good check for geometry effects and convected source corrections.

The calibration for SotonArray is done in two stages. First the microphones are calibrated individually. Since electret microphones are used, a full frequency response function (FRF) calibration is preferred over a simple pistonphone measurement. Each array microphone is placed directly opposite an instrumentation grade GRAS Type 46BE transducer, consisting of a 1/4″ CCP preamplifier and a 1/4″ free field microphone, such that the diaphragms of the two microphones are separated by approximately 1 mm. This arrangement is then placed at approximately

1 m from a monitor speaker driven by white noise. The FRF between the two microphones (amplitude and phase) is determined and saved as a calibration file for each microphone. This information is then loaded by the beamforming software, and normalised by the sensitivity of the reference transducer (which is measured prior to the test using a Brüel and Kjær Acoustical Calibrator type 4230). Further details can be found in ref. [61].

Once the array and ancillary equipment is set up, a number of test cases are performed with a compact source (a PEI. Dome Component Tweeter[1] having a diameter of ~ 25 mm and a wide frequency range (typically 2.5 kHz – 30 kHz). The source plots can then be used to verify the location of the source and pinpoint any inaccuracies in the installation or geometry.

A.2 Wind Tunnel Duct Liner

In order to reduce the amount of reflections in a wind tunnel test section, the possibility of lining the boundaries with absorptive material was investigated. The chosen material is 25 mm-thick polyurethane foam[2] covered by an impervious plastic sheet. This sheet acts a smooth surface which theoretically would have no adverse affects on the flow, however, in spite of the manufacturer's claims, it seriously limits the absorption capabilities of the foam. This can be clearly seen in figure A.14, which shows the values of the absorption coefficient as measured in an impedance tube. Plots (a) show the liner with the plastic sheet cover as supplied, and plots (c) show the liner without the plastic sheet. Without the sheet, the foam has modest broadband absorption characteristics. The peak in absorption at approximately 1.6 kHz is possibly due to installation effects in the impedance tube, and most likely does not occur when mounting whole panels of the material. Therefore it is more safe to assume that the absorption coefficient of the covered foam has a maximum of 0.3. Figure A.14(b) shows another set of results that was performed with the plastic sheet perforated with a large number of minute holes. This gives a good compromise of smooth surface and decent absorption; and should be considered in future investigations.

As the duct liner was not meant to be a permanent modification to the test section, it was permanently bonded to aluminium sheets which were then attached to the wind tunnel test section.

[1] SoundLab Cat. No. B009W(RST13B).
[2] Tradename Wilhams PUNF Foam with Melinex Facing

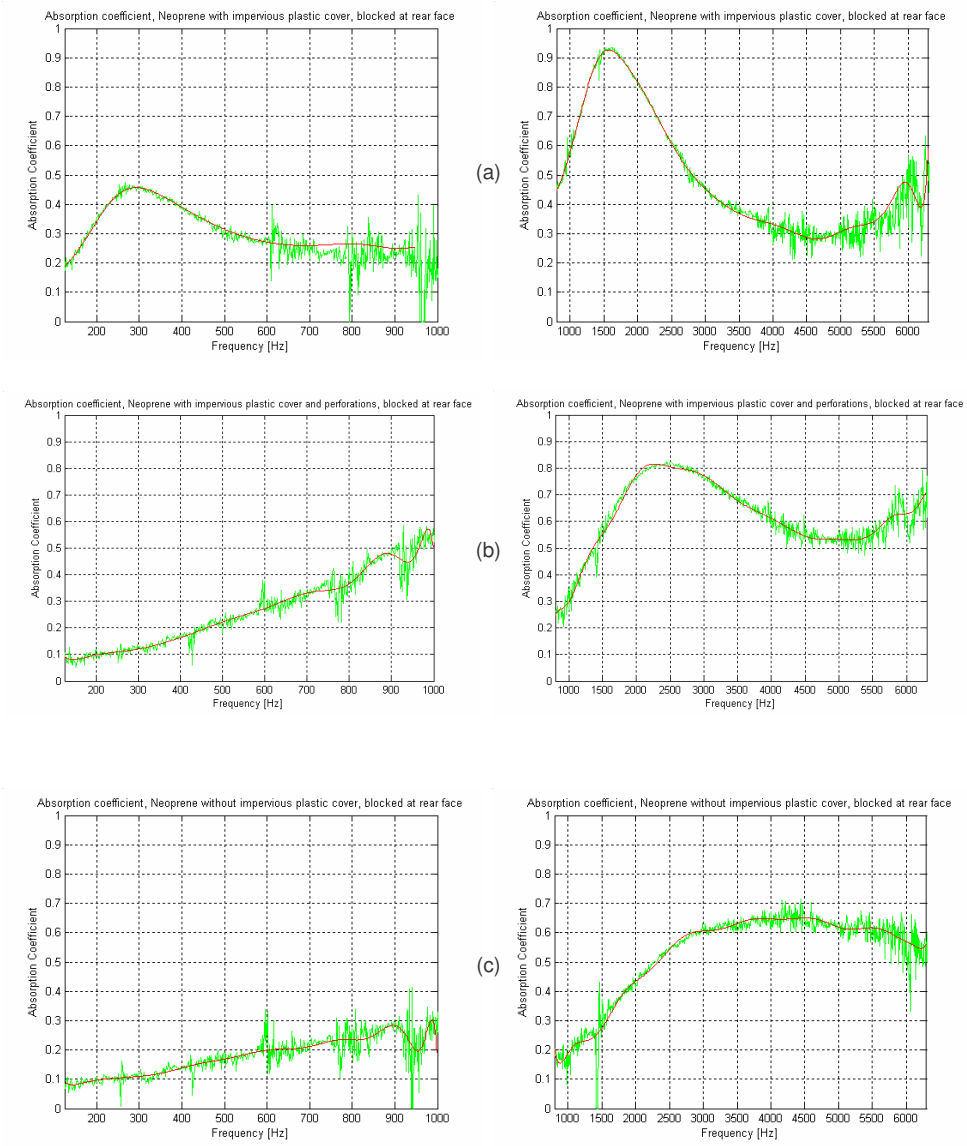

FIGURE A.14: Measured absorption coefficient, as a function of frequency of 25 mm-thick Wilhams PUNF Foam: (a) as supplied, (b) perforated plastic sheet, (c) no plastic sheet. From ref. [63].

A.3 Data Acquisition and Processing

The array microphones signals need to be preamplified, digitised and stored to some medium before the beamforming processing can commence. The pre-amplification is carried out using an in-house built 64-channel preamplifier system. The same system also provides the bias voltage necessary to power the electret microphones. The preamplifier was designed to have an ultra-wide frequency range (up to 60 kHz), a selection of gains (0 - 40 dB in 10 dB steps) and an option for a high pass filter with an adjustable cut-on frequency of 0/300/800 Hz. Overload indica-

tors matched to the input range of the data acquisition system is also present. All cabling is individually shielded.

Data acquisition is carried out using a National Instruments modular system based on the Dynamic Signal Acquisition (DSA) family of products. The system is based on a chassis housing various input/output cards interfaced by the PXI bus. These cards can be controlled either by an embedded controller housed in the same PXI chassis, or by an external PC through a software-transparent link. The current system consists of 8 PXI-4472 cards mounted in an 8-slot chassis. The PXI-4472 cards each have eight channels with a simultaneous sampling rate up to 102.4kSamples/s with a resolution of 24 bits. The acquisition process is controlled through software written in Labview. The software synchronises all the channels and acquires the predetermined number of samples, whilst simultaneously streaming the data to disk in binary format. Once the acquisition is finished, the saved data can be loaded into the beamforming software.

A.4 Post Processing

Post processing is carried out using Matlab, and is designed in the form of a number of "modules" that can be engaged or disengaged according to the user's preferences. It is a complete system whose input is the raw data from the array microphones, and the output consists of beamformer maps and integrated spectra. The software includes FFT with overlap, two types of calibration (pistonphone or full FRF curve), CSM averaging and optimisation, scan plane generation (with two axes of rotation), deconvolution (CLEAN and CLEAN-SC), de-reverberation and source power integration. Further details can be found in ref. [64].

The software is divided into two parts, which are shown in block diagram format in figures A.15 and A.16. The first part generates and saves the cross spectral matrix. A CSM needs only be generated once per data set: the same CSM is used for any grid point and irrespective of the type of steering vector. The code works on a sequential block group principle. If $L \times K$ samples were acquired per channel, where K is the number of samples per FFT block and L is the total number of blocks, then the code can generate n intermediate CSMs using $L_{\text{inter.}}$, where $L \leq nL_{\text{inter.}}$. This is done to reduce the huge computing memory requirements when processing large data sets.

The second part generates the beamforming plots. A scan plane is generated

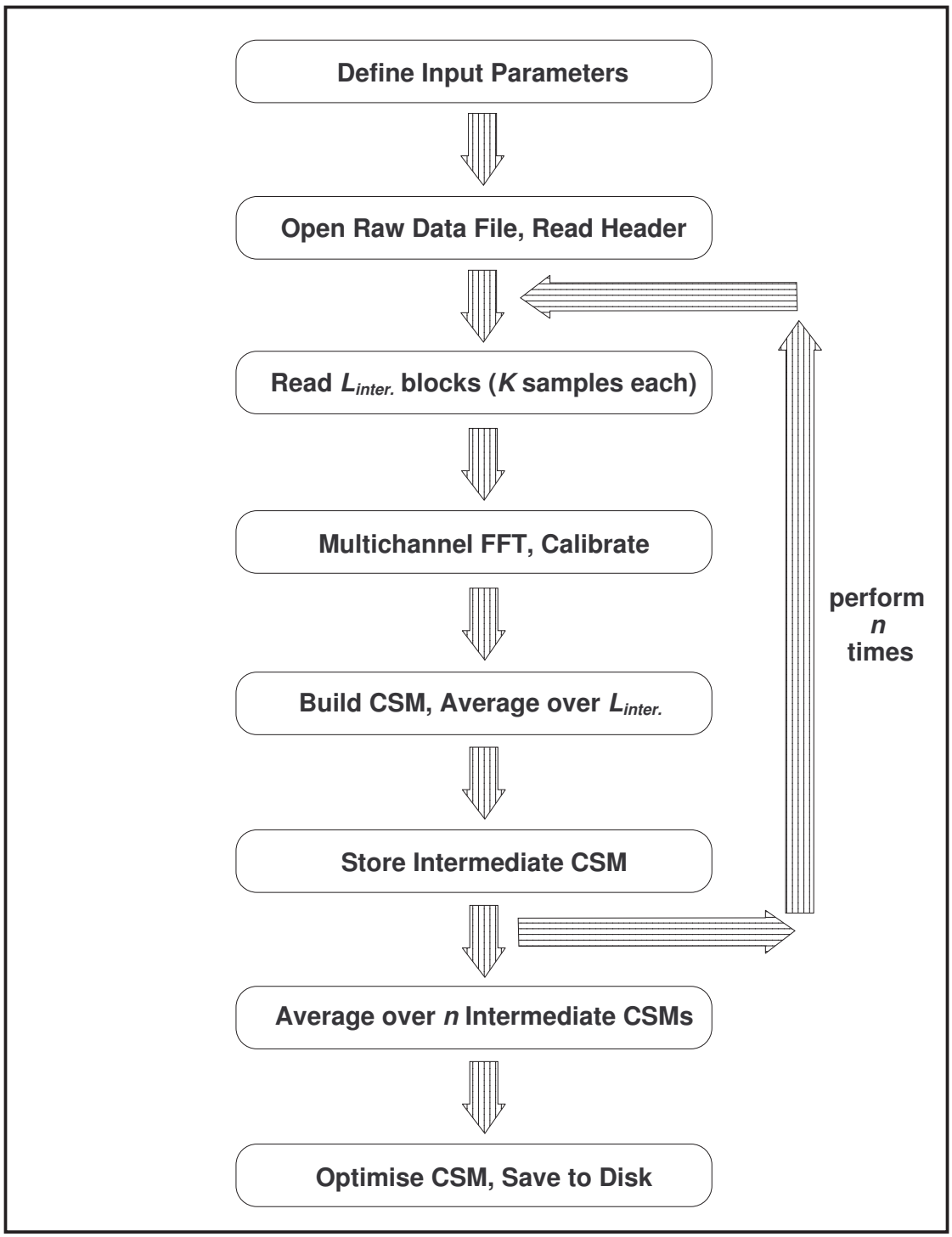

FIGURE A.15: Block Diagram of SotonArray Part I – CSM generation.

according to the input parameters, and sampled by a predefined number of grid points. The present code can only generate a 2-D plane which can rotate about arbitrary pivot axes parallel to the x and y axes. The code then enters into two frequency loops. The first loop is for a defined set of P frequency bands, normally one-third octave bands. Within this loop is a second loop for Q discrete frequencies within each band. For all quantitative analysis the frequency resolution $\Delta f = f_s/K$ matches that of the CSM, where f_s is the sampling frequency. For each frequency, the steering vector is built using the user's choice of Green's functions: free-space, image source model or measured. The conventional beamforming plot is computed using the pre-determined CSM and plotted and/or saved as a reference. This plot also serves as the "dirty" map for the deconvolution algorithms. Finally, spectra are generated for any user-defined areas using the Source Power Integration algorithm. The program can be used to plot and save beamforming maps in a variety of output formats.

A.5 Benchmarking

The beamforming software was benchmarked with similar software developed by the Dutch National Aerospace Lab (NLR), German Aerospace Centre (DLR), French Aerospace Lab (ONERA) and QinetiQ. The results from the SotonArray software were similar to those from the other partners, both qualitatively and quantitatively.

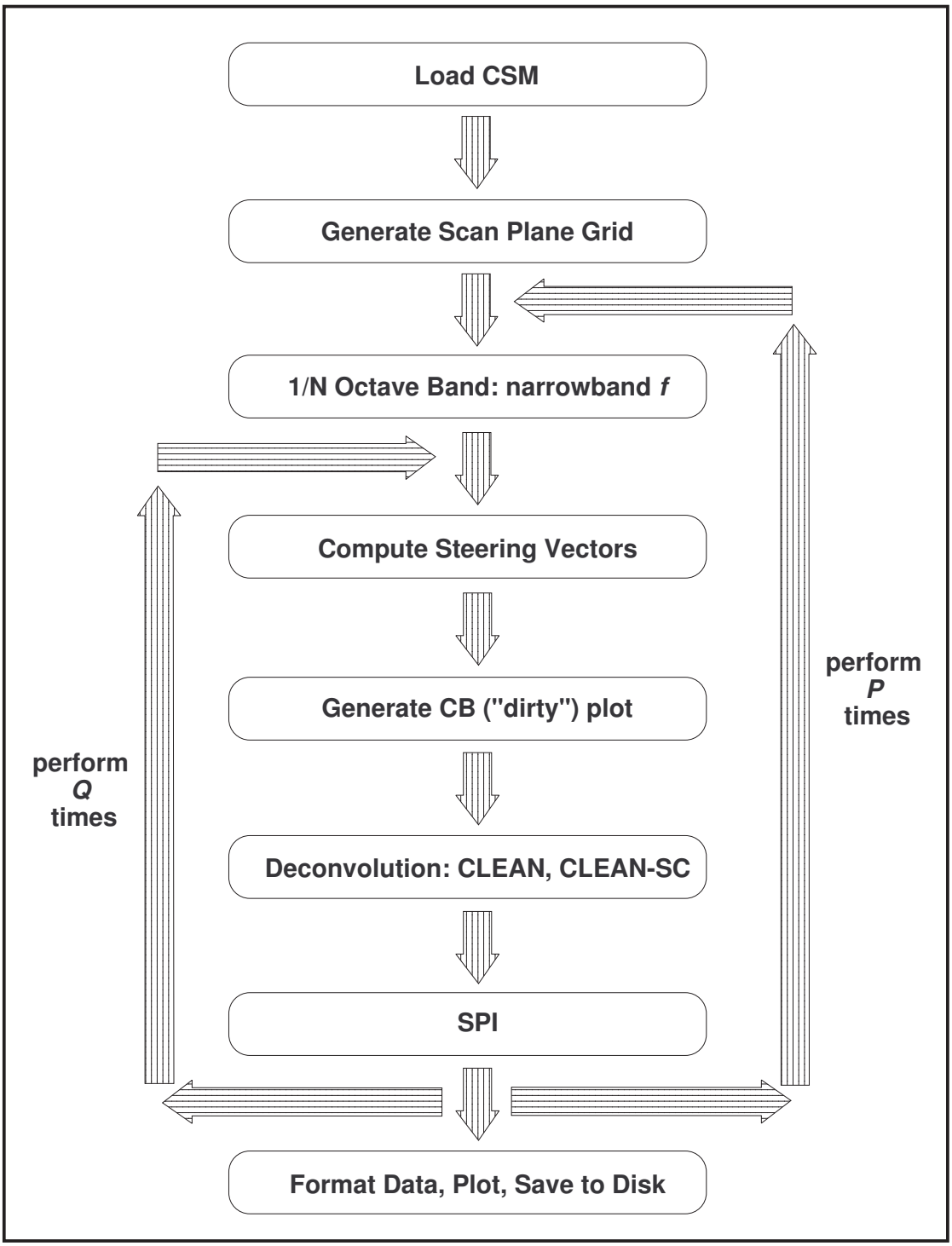

FIGURE A.16: Block Diagram of SotonArray Part II – Beamforming.

Appendix B

Challenges of implementing Impulse Response Measurements

Beamforming steering vectors obtained from analytical methods, such as an Image Source Model, were shown to offer a certain degree of improvement in the beamforming results. However, besides being susceptible to errors, such methods can only be applied for a very simple wind tunnel test section geometry; furthermore, diffraction and reflective effects by the test model itself are very difficult to account for. Measured Green's functions are not prone to such errors, and given that the measurements are free from errors, it should be the most accurate way of taking into account the real transfer function from source to receiver. This chapter describes an attempt that was made to measure Green's functions in the $2.1 \times 1.5\,\mathrm{m}$ wind tunnel in order to use them in the beamforming algorithm. In particular, a number of issues will be discussed why this attempt was unsuccessful in yielding more accurate beamforming results.

B.1 Impulse Responses

In Chapter 3, two ways of measuring Green's functions were described. The two main requirements are a compact source that does not significantly alter the measuring environment, and a very wide frequency band of interest. Unconventional sources that generate an impulse were deemed to satisfy these two conditions better than conventional electro-acoustic speakers. Furthermore, pseudo-impulsive sources were preferred over spark discharges, due to the ancillary hardware requirements of the latter. When using the former type, it can be feasible to arrange

FIGURE B.1: Device used to trigger the pseudo-impulsive sources. The markings are at 10 mm intervals, and give an indication of the size of the setup.

a number of identical sources in the form of a grid, which can be placed at the required imaginary scan plane.

In this case, readily available "caps" were used. These are cylindrical plastic capsules, approximately 1.5 mm in diameter and 2 mm long, filled with tiny amounts of explosive compounds that give an impulsive noise when struck mechanically. They work on the same principle as the separate percussion cap used to replace the flintlock in real firearms. These impulsive sources can produce sound pressure levels between 120 dB and 140 dB at a distance of 0.25 m [65].

One of the challenges with this type of source was how to trigger it remotely, given that it needs a mechanical impact. The solution was to use a spring-loaded clip that was armed manually and held in place by a magnetic field. By remotely displacing the magnets, the force in the spring overcame the magnetic force and triggered the hammer action to set off the impulsive source. This triggering device is shown mounted in situ in figure B.1.

The drawback of this setup was the physical size of the triggering device, which although relatively small, still affects the local sound field at high frequencies. This setup also gave rise to inaccuracies in the exact positioning of the impulsive sources; the resulting measurement locations are accurate to ± 5 mm. The triggering device also produced a certain degree of mechanical noise, however this is insignificant compared to the main impulse.

These sources were used to "map" the cavity area where the calibration source was positioned (shown in figure 5.3 on page 88) at 50 mm intervals (a total of 85 independent measuring locations). For each source position, data from the array microphones was simultaneously sampled at 96 kHz for a total duration of approximately 4.3 s (409600 samples). The maximum sampling frequency, which was limited by the data acquisition hardware, translates into a time resolution of $\Delta t \approx 10.4\,\mu$s. Measurements were done without flow, to reduce sources of noise.

The source was triggered manually after the acquisition was started, to make sure the electronic circuitry was in a settled state. This meant that at the post processing stage, a start and stop criterion had to be used to automatically extract the useful impulse data. In this case, the start criterion was a predefined number of samples before the "main" event (peak level corresponding to direct pressure wave from source). The stop criterion was chosen to be the point at which the fluctuations become a certain fraction of the main pulse, say 1×10^3 times less. This would included the initial reflections and a significant part of the reverberant field.

B.2 Issues with the Measurements

Figure B.2 shows one microphone signal for one source location. The left plot, depicting the full acquisition, clearly shows that the entire event was captured. However it is evident that the first part of the signal is not symmetric. This behaviour was observed throughout the acquired data, and can be seen more clearly in the right hand plot of the same figure. Although no definite reason was established, it is most likely due to inertia or saturation effects of the microphone diaphragm. The pressure due to the impulses might have caused too large a deflection, making the microphone unable to record pressure fluctuations just after this main event. Unfortunately it was not possible to make the impulses less loud in order to verify this hypothesis. The maximum recorded level was well within the maximum designed operating range of the microphone preamplifiers and data acquisition hardware (± 10 V).

In order to assess what effect this "saturation" effect would have on the impulse responses, one time history was manually manipulated to reconstruct a more realistic physical impulse. This can be seen in figure B.3. Two types of defects were edited: clipped spikes and a positive offset in the signal up to approximately 0.006 s. Note that the impulse in this figure was normalised such that the peak

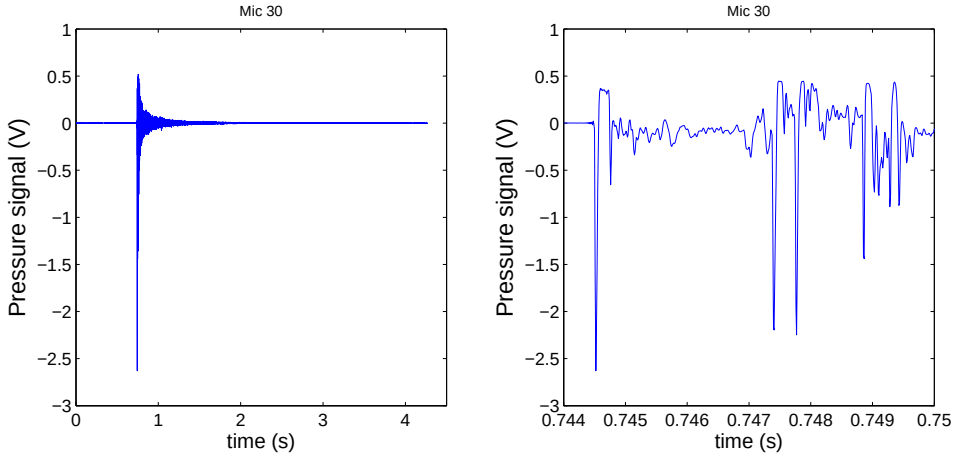

FIGURE B.2: Pressure signal (uncalibrated) from one of the array microphones when subjected to an impulsive source in the wind tunnel test section. (*left*) entire duration; (*right*) zoomed on the first part of the impulse.

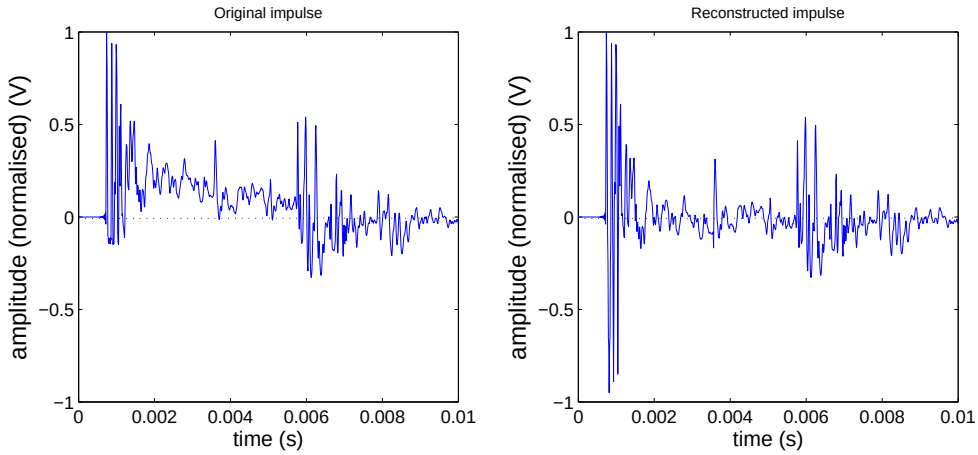

FIGURE B.3: First 0.01 s time history of an impulse recorded at a particular microphone: (*left*) as recorded by the microphone; (*right*) reconstructed in post processing.

value is unity. The reconstruction process was done purely on a visual basis, and does not reflect the true impulse.

Figure B.4 shows the resulting impulse response (measured and reconstructed) in the frequency domain, up to 20 kHz. There are noticeable differences in the two curves, particularly at around 10 and 18 kHz. It is also evident that the resulting curves are very noisy. Most of the noise is thought to be due to the reverberant field in the wind tunnel. Figure B.5 shows the time histories of three impulses for a particular source-receiver combination. The main spikes, corresponding to the direct reflections, are coincident, although the level relative to the main event changes. The smaller fluctuations in between the peaks vary, and therefore should average to zero. Unfortunately, given the experimental setup, and the need to

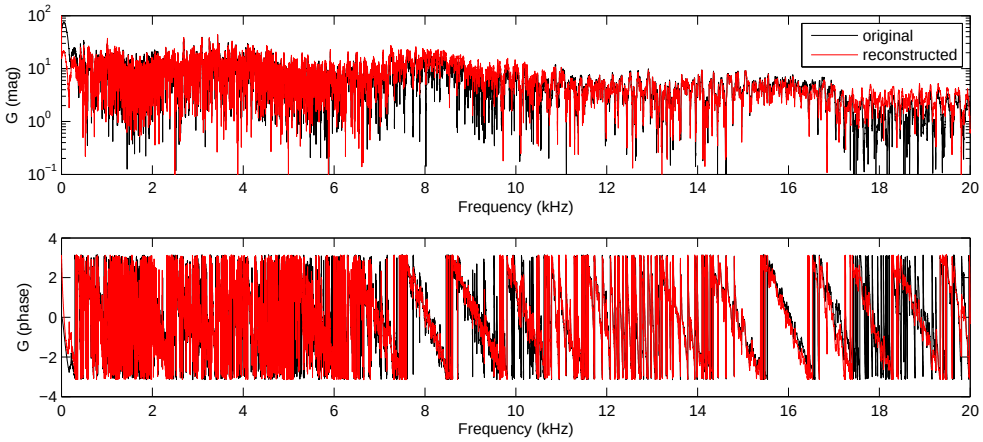

FIGURE B.4: FFT of the recorded impulse (original and reconstructed) shown in figure B.3.

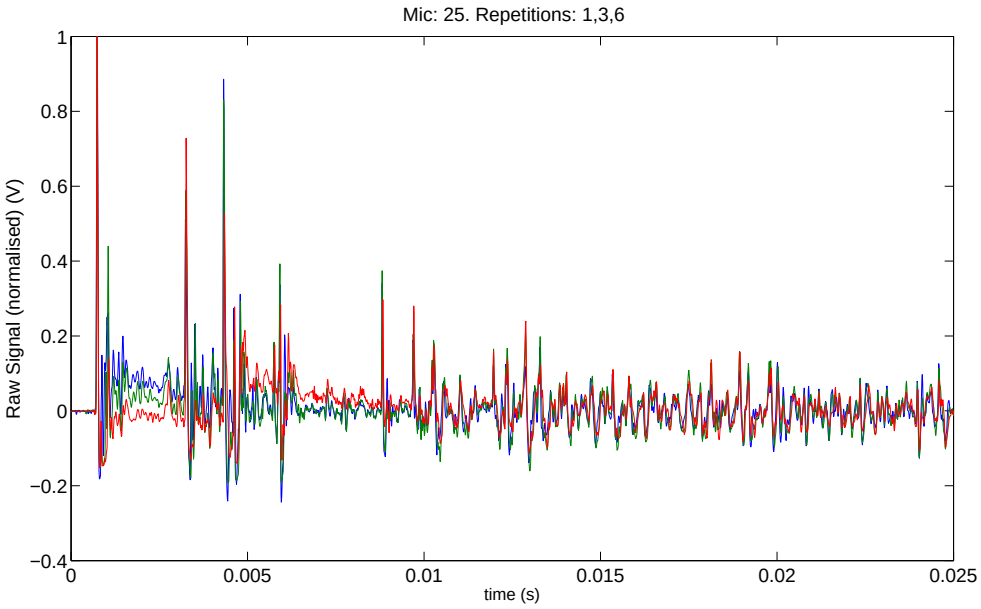

FIGURE B.5: Comparison of three impulses as recorded by an array microphone for a particular source position. Impulses are normalised with their respective maxima. Only the first 0.025s of the event is shown.

"map" a relatively large area, it was not possible to do averages at each location. As a substitute the impulse responses were artificially smoothed using a moving average algorithm based on 30 samples. The resulting responses for the measured and reconstructed impulses shown in figure B.3 are shown in figure B.6.

The measurements at each source location was due to a different impulsive source, which gave rise to a different peak level each time. This is partly due to variations in the amount of explosive compound in the individual caps, and partly due to the fact that the mechanical impact that triggers the impulse was not consistent.

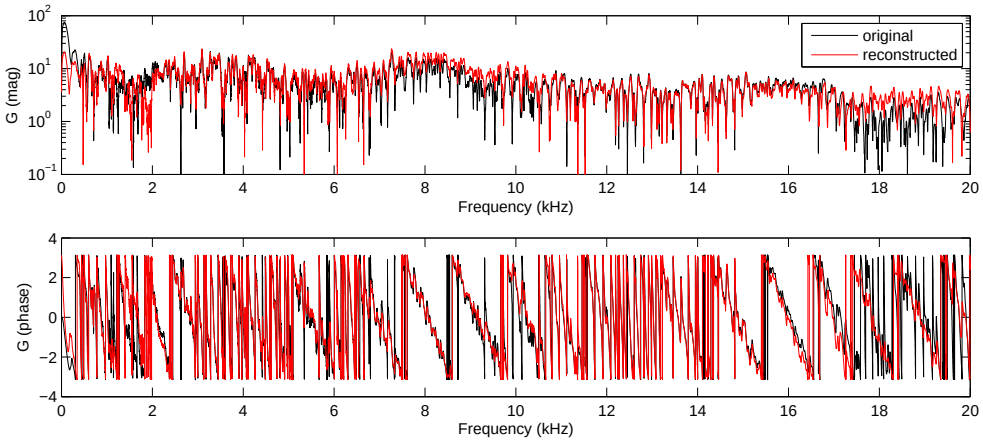

FIGURE B.6: Smoothed FFT of the recorded impulse (original and reconstructed) shown in figure B.3.

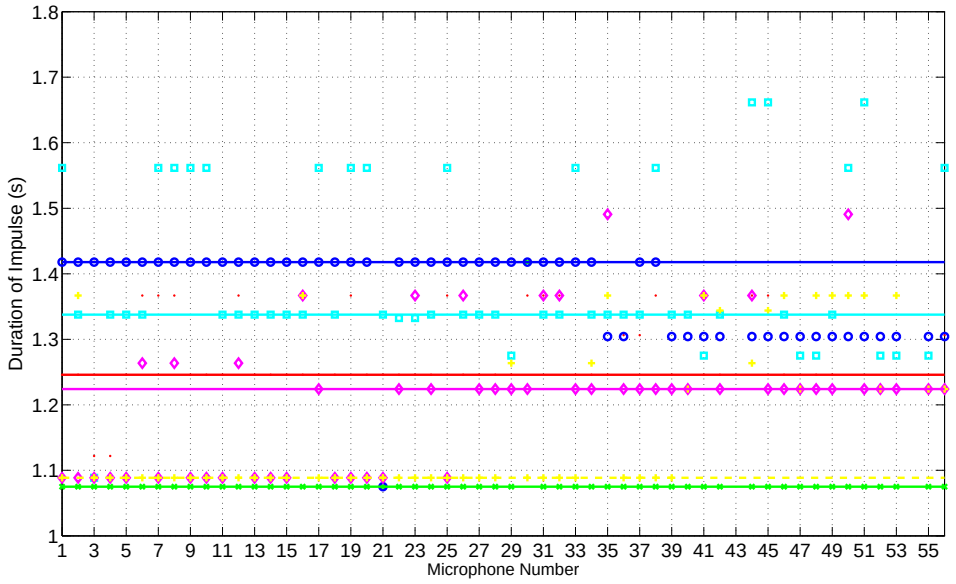

FIGURE B.7: Duration of six separate impulses as recorded by the 56 array microphones. Each impulse is truncated when the signal becomes 1×10^3 times smaller than the main pulse. The different data markers depict different trials. The continuous lines depict the mode across the array microphones.

Because of this, each impulse had to normalised to its peak level, so that the latter is equal to unity for all the recorded events.

It was also observed that the impulse duration varied for each discrete event. Figure B.7 shows the durations of six impulses at the same fixed position, as recorded by the 56 array microphones. Some of the impulses are more consistent than others with respect to the impulse duration across all the array microphones. Furthermore, the averaged duration varies between the six events.

In most cases the position of the impulses will not correspond to the exact locations of the grid points building up the scan plane of interest. Green's functions at the grid points have to be generated by a two-dimensional interpolation of the Green's functions "map" built using the available data at the impulse locations. In this case, a spline interpolation was used. As a first approximation this interpolation can be assumed to be valid if the grid point is less than half a wavelength away from the location of the measured Green's function. In this case, an impulse grid spacing of 50 mm gives a usable frequency range up to approximately 20 kHz.

B.3 PSF and SPI when using the measured Impulse Responses

Given the significant issues that affected the quality of the impulse measurements, it was unlikely that the calculated impulse responses could be used for a better estimate of the beamforming steering vectors. This is evident from the PSFs at four discrete frequencies: 2, 4, 8 and 16 kHz, shown on the left hand side of figure B.8. The microphone array and scan plane are the same as those considered in figure 2.6 on page 18 (using free-space Green's functions) and figure 4.1 on page 66 (using an image source model). Note that due to the spatial interpolation of the impulse responses, the PSF is defined only for part of the scan plane (impulse measurements were carried out within $-0.15 \leq x \leq 0.05$).

From the plots it is clear that the measured impulse responses are not suitable for beamforming. The imaginary point source situated in the middle of the plot is not well defined, especially at the lower frequencies. This will give rise to problems, even if deconvolution algorithms are employed.

Given that most of the issues could be arising from the poor quality of the measured phase data, an attempt to use a "hybrid" impulse model was made. This involved using the magnitude from the impulse measurements, and the phase from the free-space Green's functions. The resulting PSFs are shown on the right hand side of figure B.8. This yielded some improvements, however the source position in the low frequency plots is still not very well defined.

In order to verify if source powers could be accurately retrieved in spite of the poor PSF plot definition, the Source Power Integration (SPI) technique was applied to the data from the hybrid impulse model. The resulting integrated values, for the case of a full CSM and with diagonal removal, are given in Table B.1. Compared

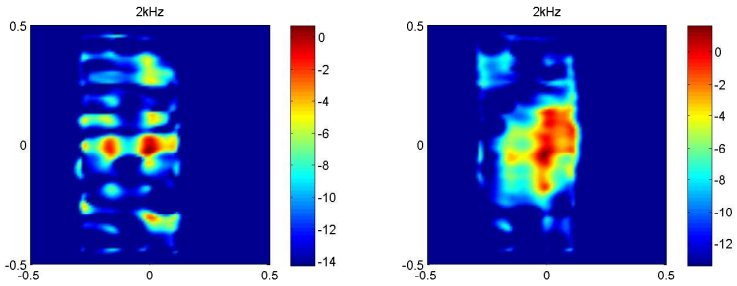

(a) 2 kHz

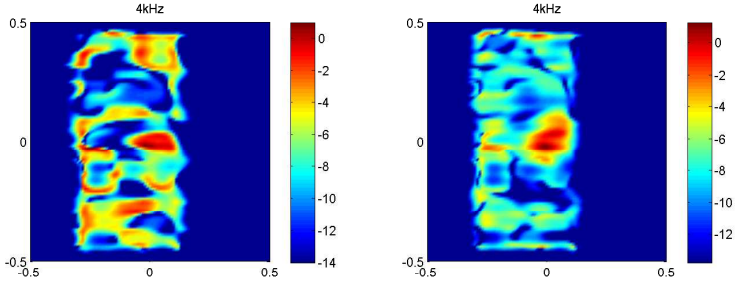

(b) 4 kHz

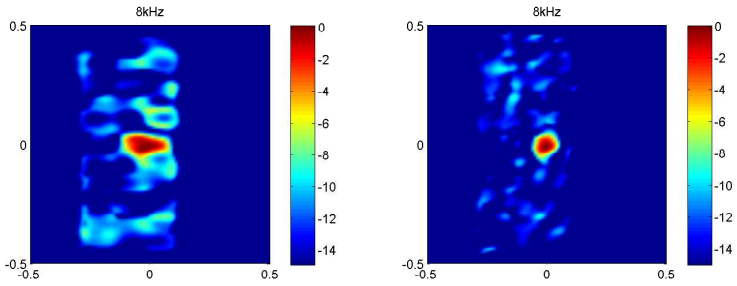

(c) 8 kHz

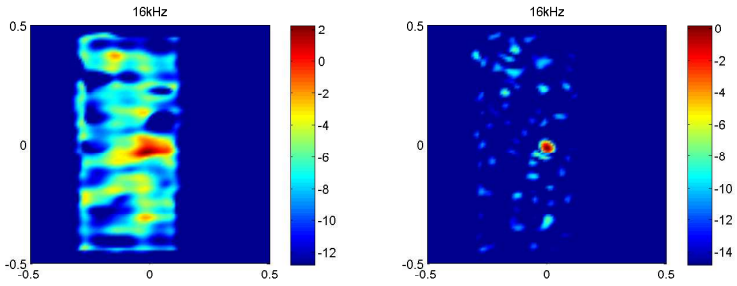

(d) 16 kHz

FIGURE B.8: Point Spread Functions using Green's functions estimated from impulse response measurements. Plots on the left are estimated using both the magnitude and phase, whilst plots on the right are from a hybrid model (see text for details).

TABLE B.1: Peak and integrated levels extracted from beamforming plots using impulse response measurements. Grid resolution is 0.01 m.

	Full CSM			Diagonal Removal		
freq (kHz)	Peak	Error(dB)		Peak	Error (dB)	
		Sum	SPI		Sum	SPI + threshold
2	1.46	27.9	0.007	1.47	26.9	0.26
4	1.33	28.7	0.006	1.30	21.5	1.47
8	1.00	22.0	0.027	1.00	10.5	2.65
16	1.04	20.1	0.042	1.03	9.22	2.68
32	1.00	24.6	0.015	1.00	2.33	3.02

to the equivalent tables given on pages 35 and 69 (for the free-space and ISM scenarios, respectively), table B.1 shows an extra column, giving the peak level of the mainlobe. In all the previous cases, the peak was always equal to unity, corresponding to the level of the imaginary unit point source. However in this case the peak level at low frequencies was somewhat larger. The reason for this is not clear. Also for this case, accurate levels when the diagonal removal technique is applied could not be achieved, even when using SPI with threshold.

These results show that the attempt to quantify the Green's functions in the $2.1 \times 1.5\,\mathrm{m}$ wind tunnel using measured impulse responses was not successful. This was most likely due to the choice of impulse source and acquisition hardware. Further work is recommended.

Appendix C

Additional Beamforming Plots

This Appendix contains additional results that compliment those presented in Chapter 5. Beamforming was carried out on a calibration source of known sound power to investigate if de-reverberation can give improvements in beamforming levels accuracy. The beamforming maps presented here are for one particular test case, i.e. with the source centred in the wind tunnel (position A in figure 5.5 on page 89), with no flow. Four sets of results are shown, the difference being the type of steering vectors used: free space, two Image Source Models (ISM-1.5 and ISM-0.8)[1], and measured steering vectors. For each set, three groups of figures are shown: conventional beamforming, deconvolution using CLEAN and deconvolution using CLEAN-SC.

A number of conclusions can be drawn from these plots. For the first set of plots using free space Green's functions it is evident that even for a single source scenario, deconvolution based on theoretical Point Spread Functions (PSFs), i.e. CLEAN, is not sufficient to remove the spatial noise at very high frequencies. When using an ISM additional sidelobes are introduced at low frequencies, however they are not as problematic as was shown in the PSFs shown in Chapter 4. The sidelobe structure changes according to the input parameters of the ISM. CLEAN does not completely remove these artifacts. For all the three sets of results, deconvolution based on CLEAN-SC was the most effective way how to improve the resolution of the plots and remove the influence of sidelobes.

In the case of measured impulses, the plots are unusable at low frequencies; however this is most likely due to problems with the impulse measurements, as discussed in Appendix B.

[1]These two ISMs are represented pictorially in figure 5.6 on page 91.

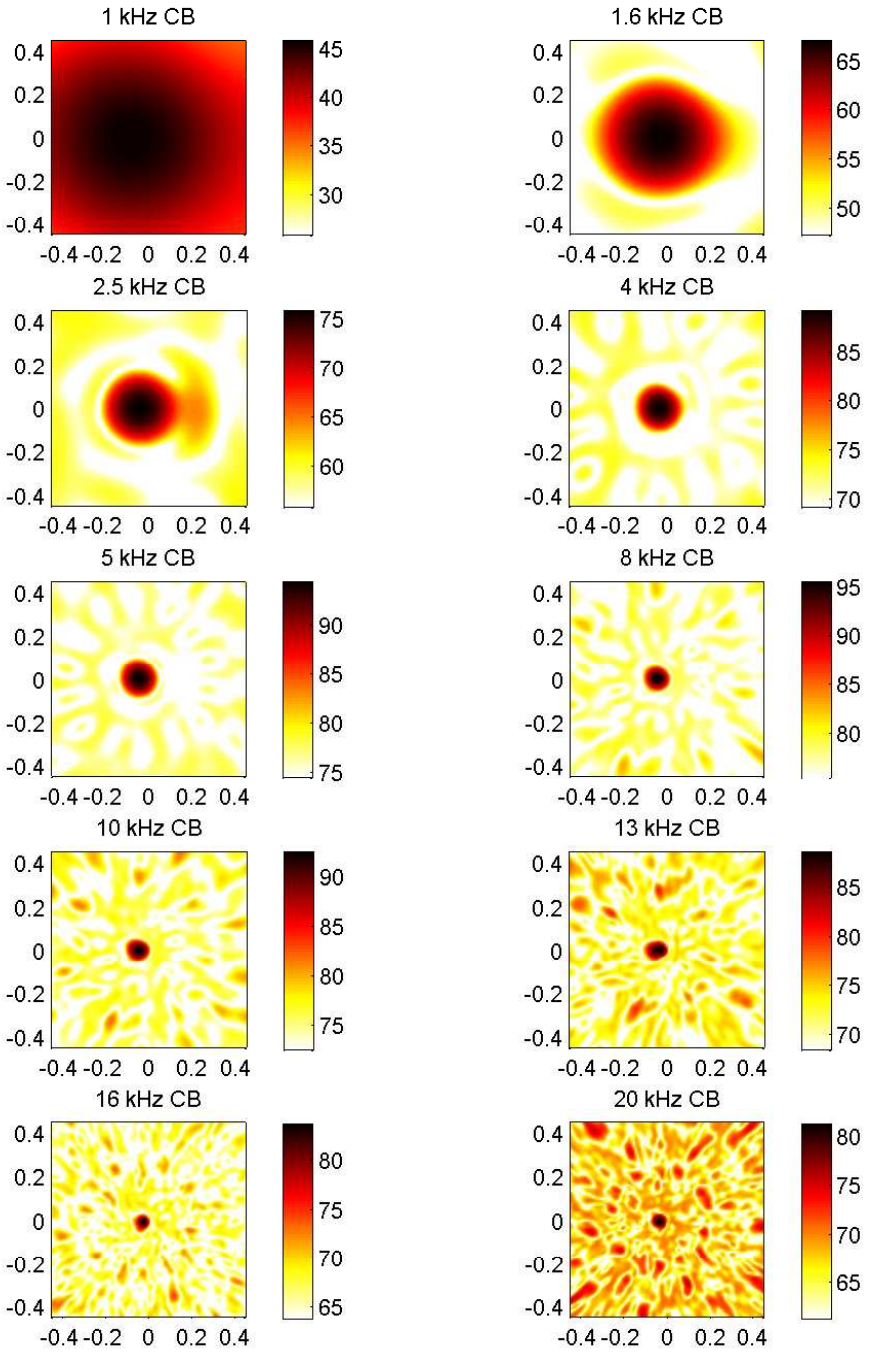

FIGURE C.1: Conventional beamforming maps of the calibration source using free space Green's functions.

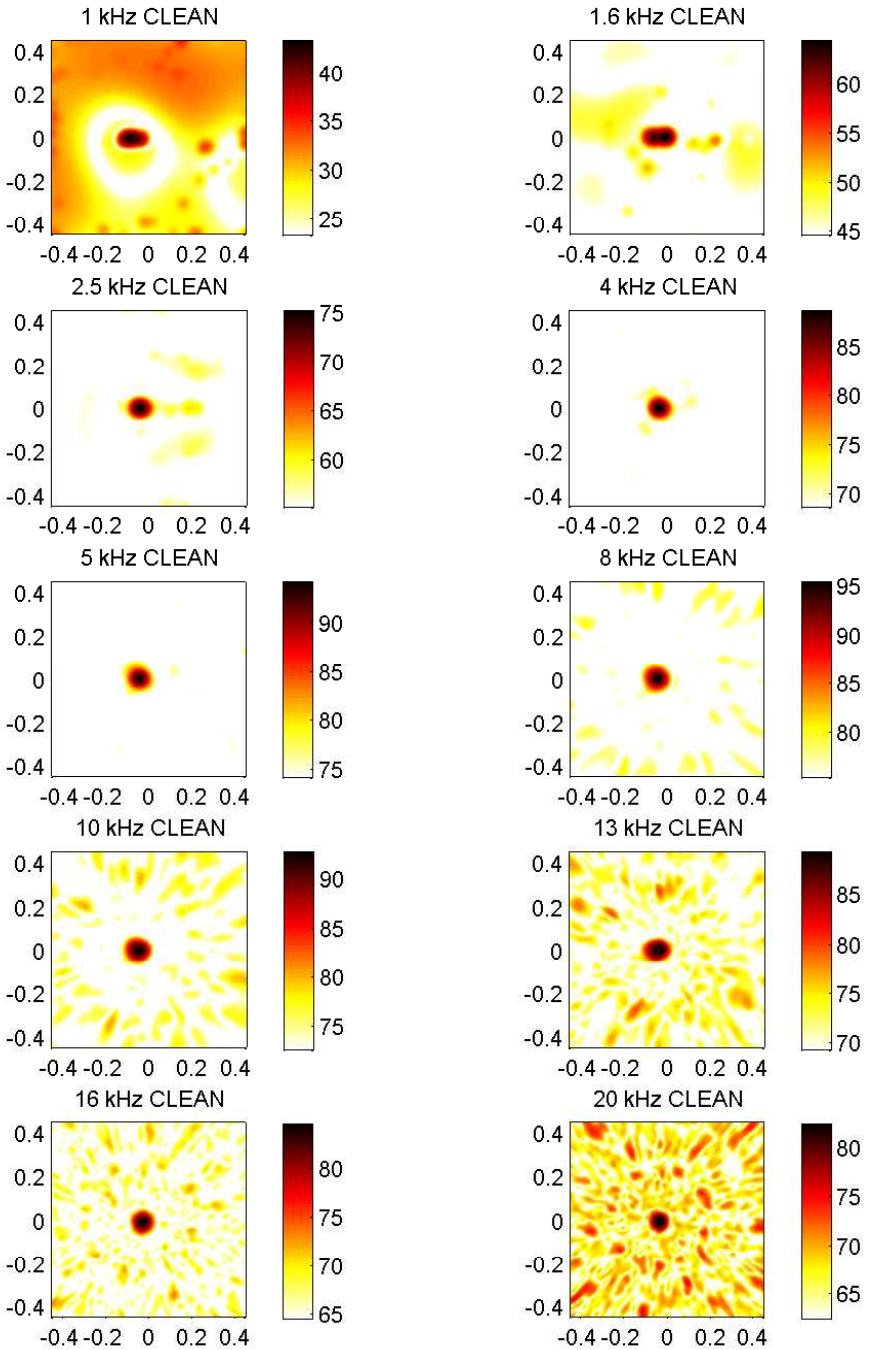

FIGURE C.2: Beamforming maps of the calibration source deconvolved with CLEAN, using free space Green's functions.

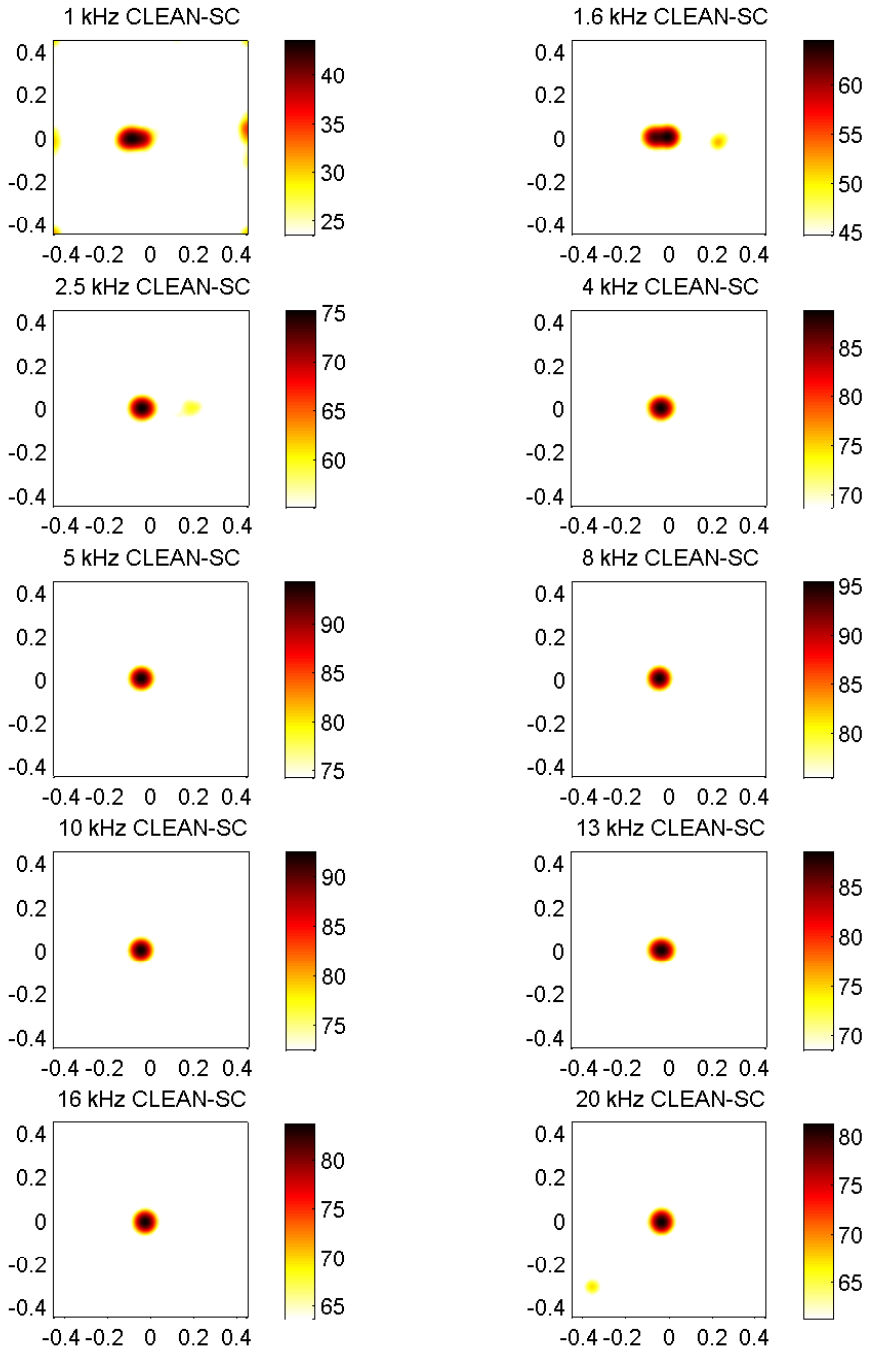

FIGURE C.3: Beamforming maps of the calibration source deconvolved with CLEAN-SC, using free space Green's functions.

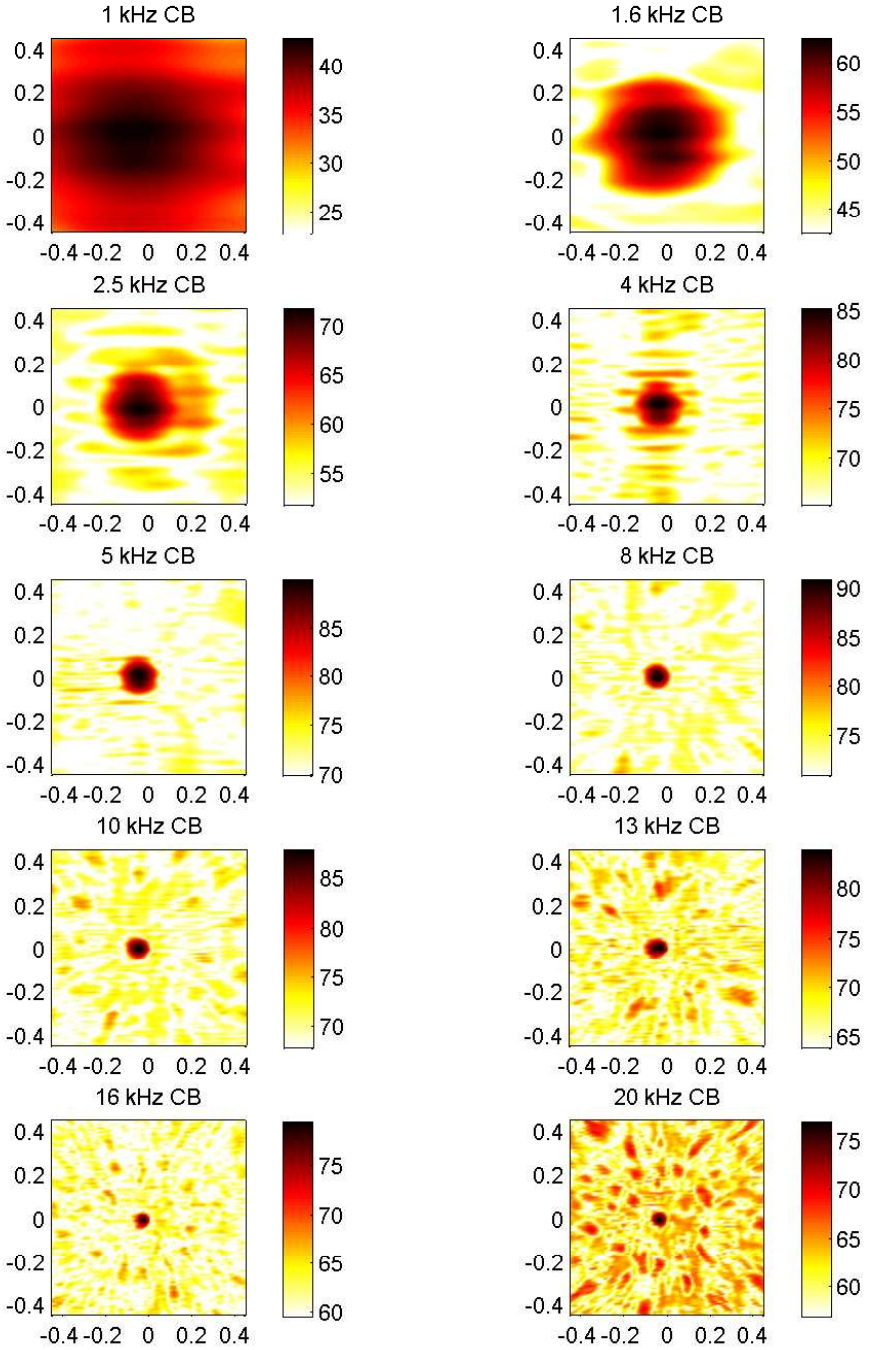

FIGURE C.4: Conventional beamforming maps of the calibration source using ISM-1.5.

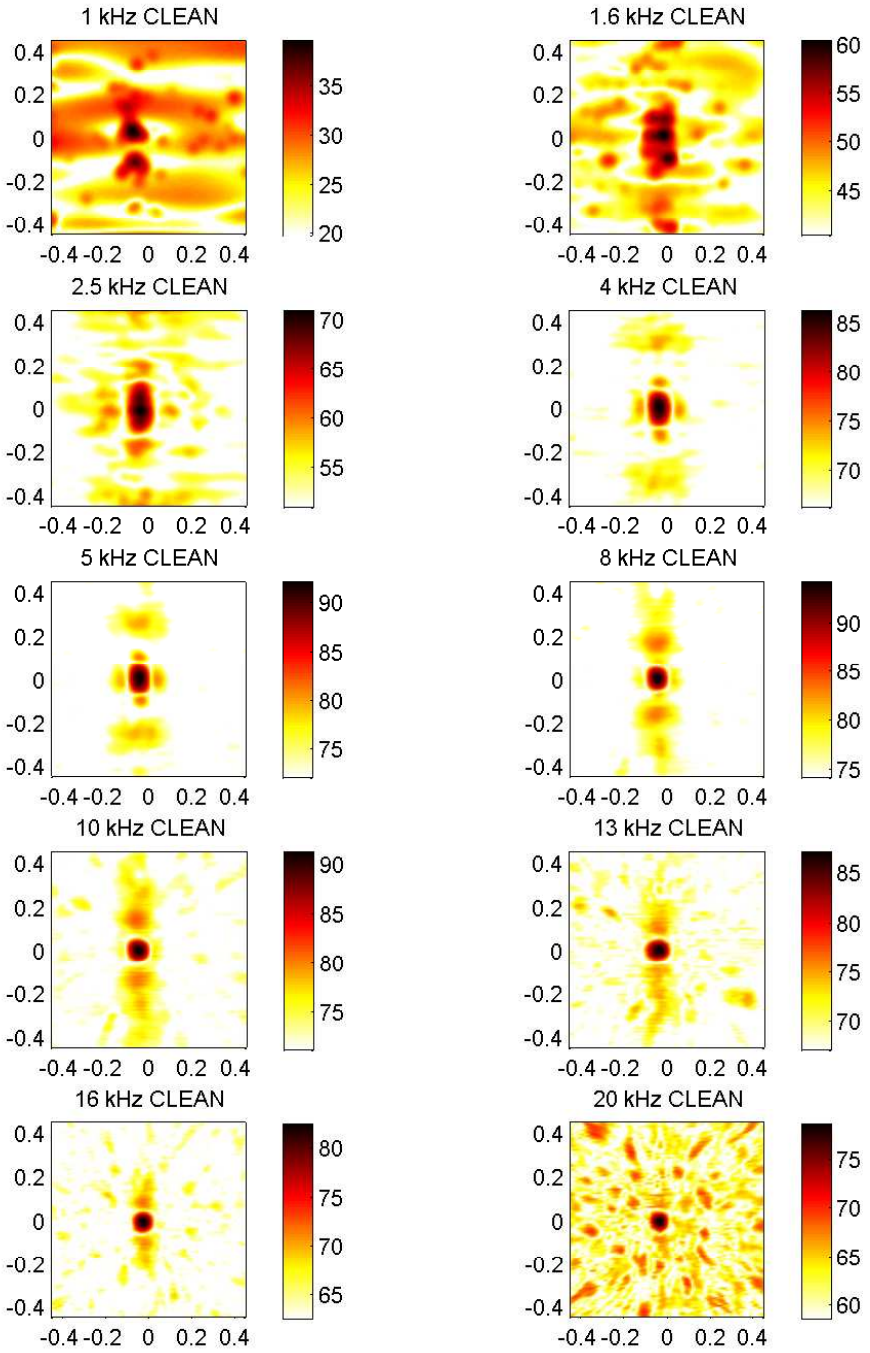

FIGURE C.5: Beamforming maps of the calibration source deconvolved with CLEAN, using ISM-1.5.

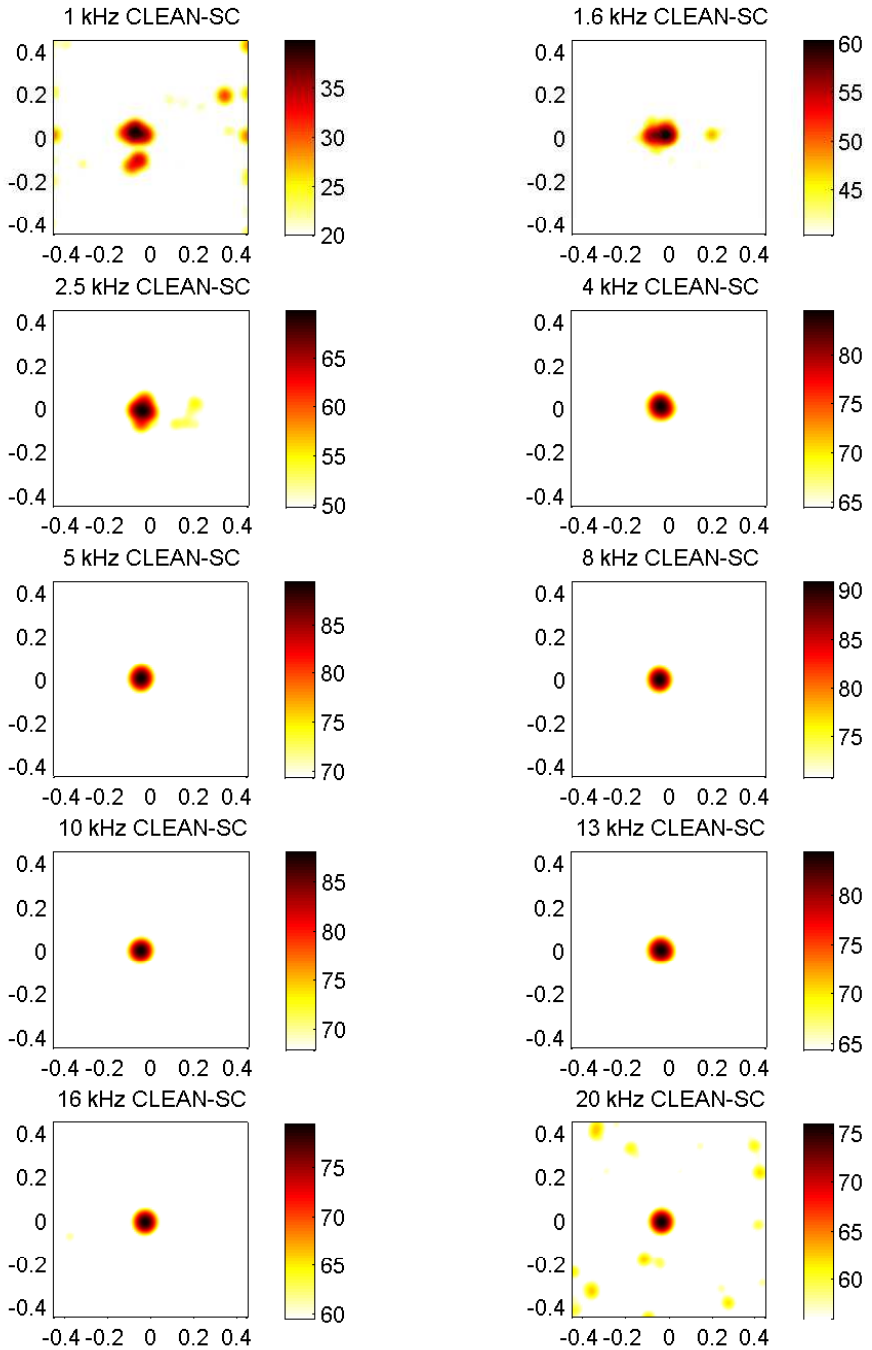

FIGURE C.6: Beamforming maps of the calibration source deconvolved with CLEAN-SC, using ISM-1.5.

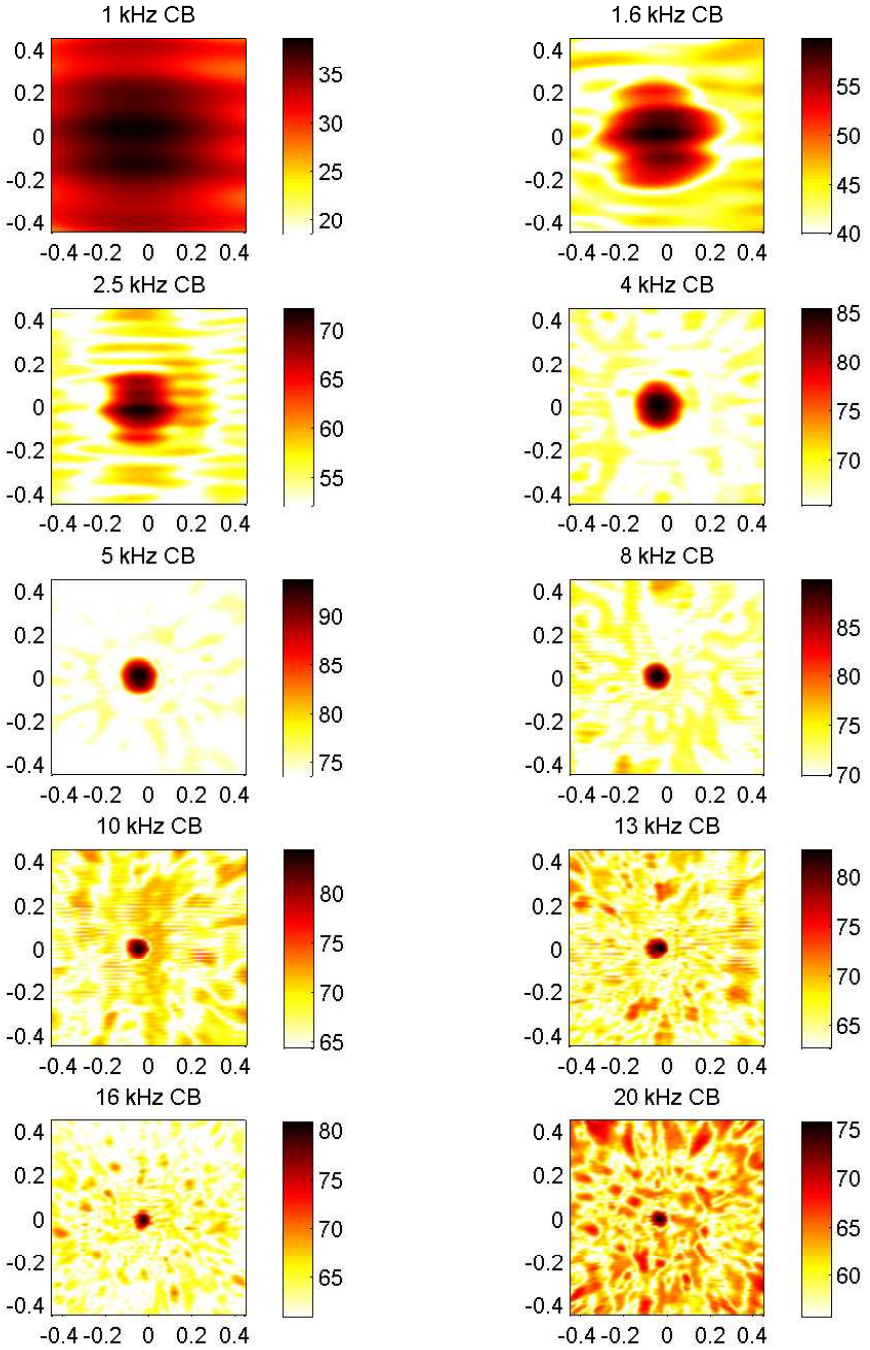

FIGURE C.7: Conventional beamforming maps of the calibration source using ISM-0.8.

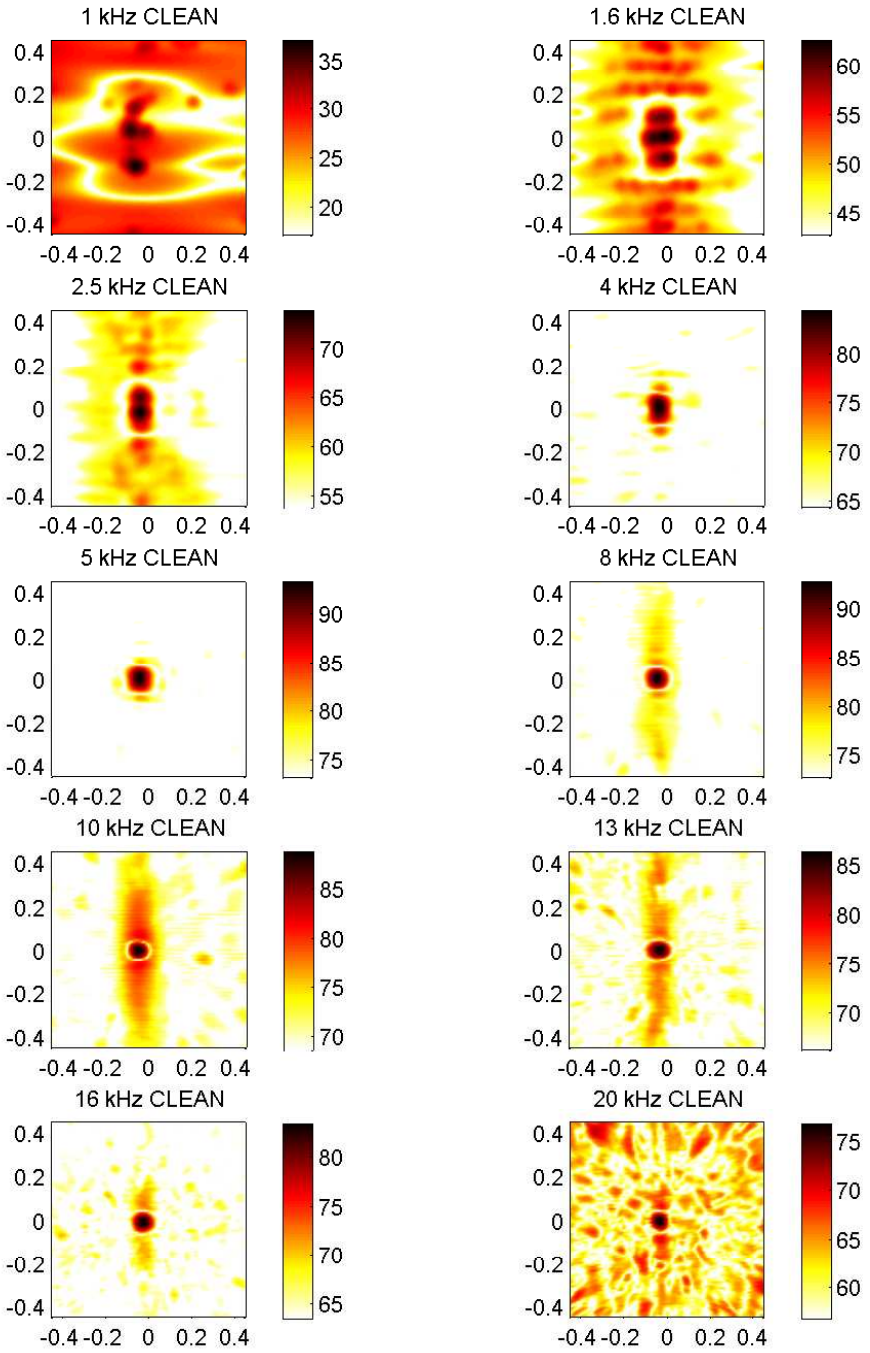

FIGURE C.8: Beamforming maps of the calibration source deconvolved with CLEAN, using ISM-0.8.

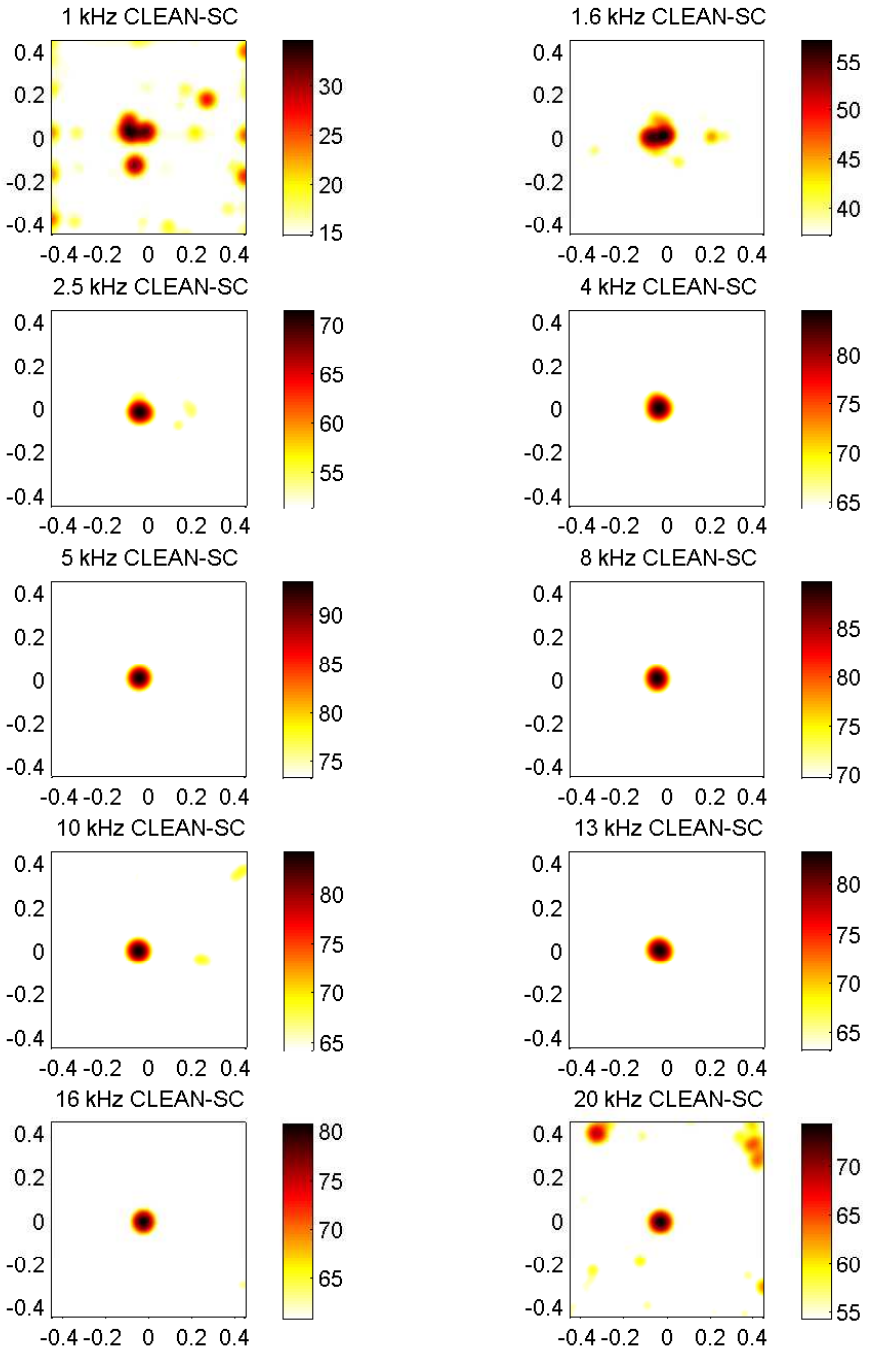

FIGURE C.9: Beamforming maps of the calibration source deconvolved with CLEAN-SC, using ISM-0.8.

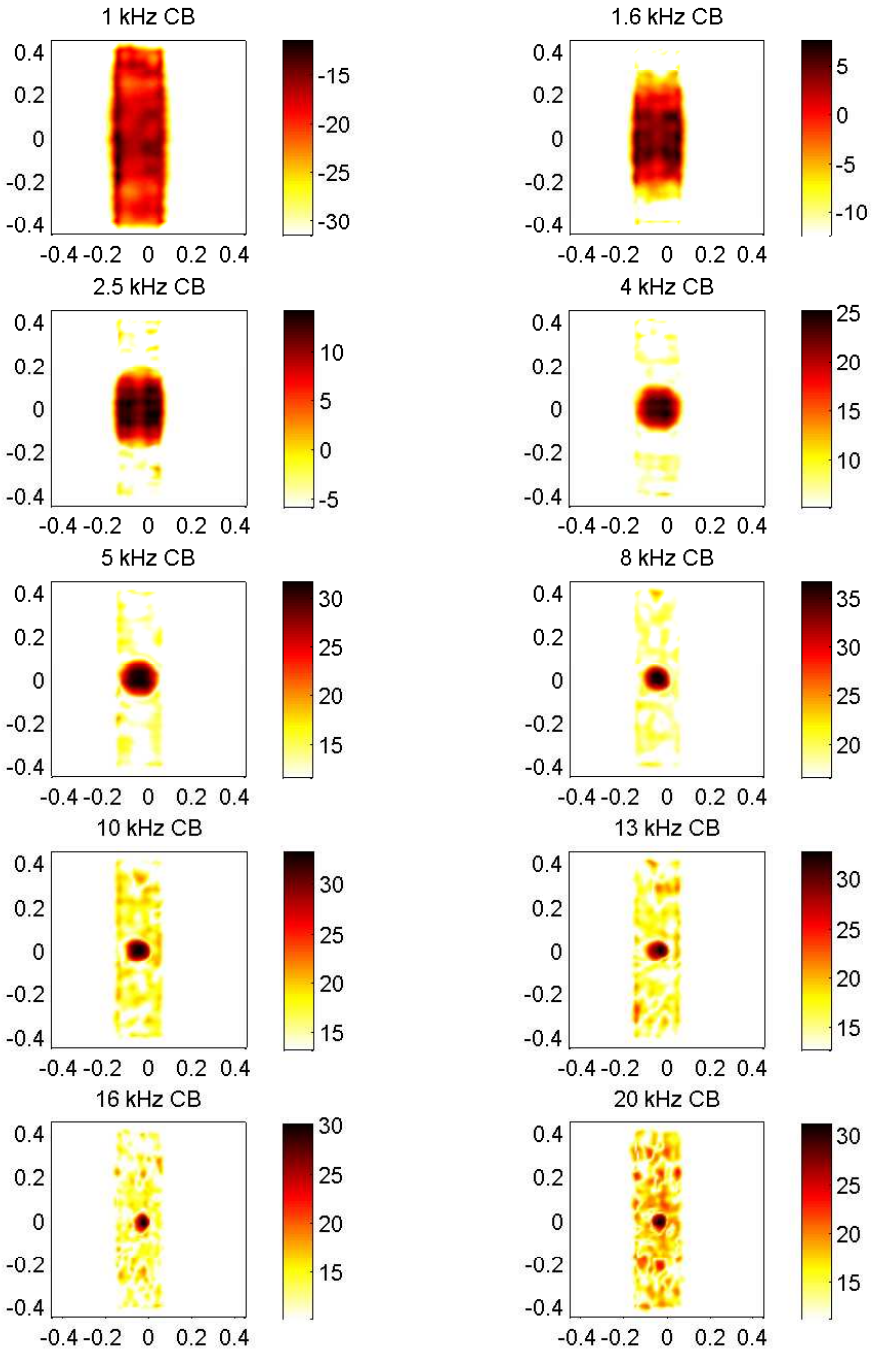

FIGURE C.10: Conventional beamforming maps of the calibration source using Green's functions estimates from measured impulse responses.

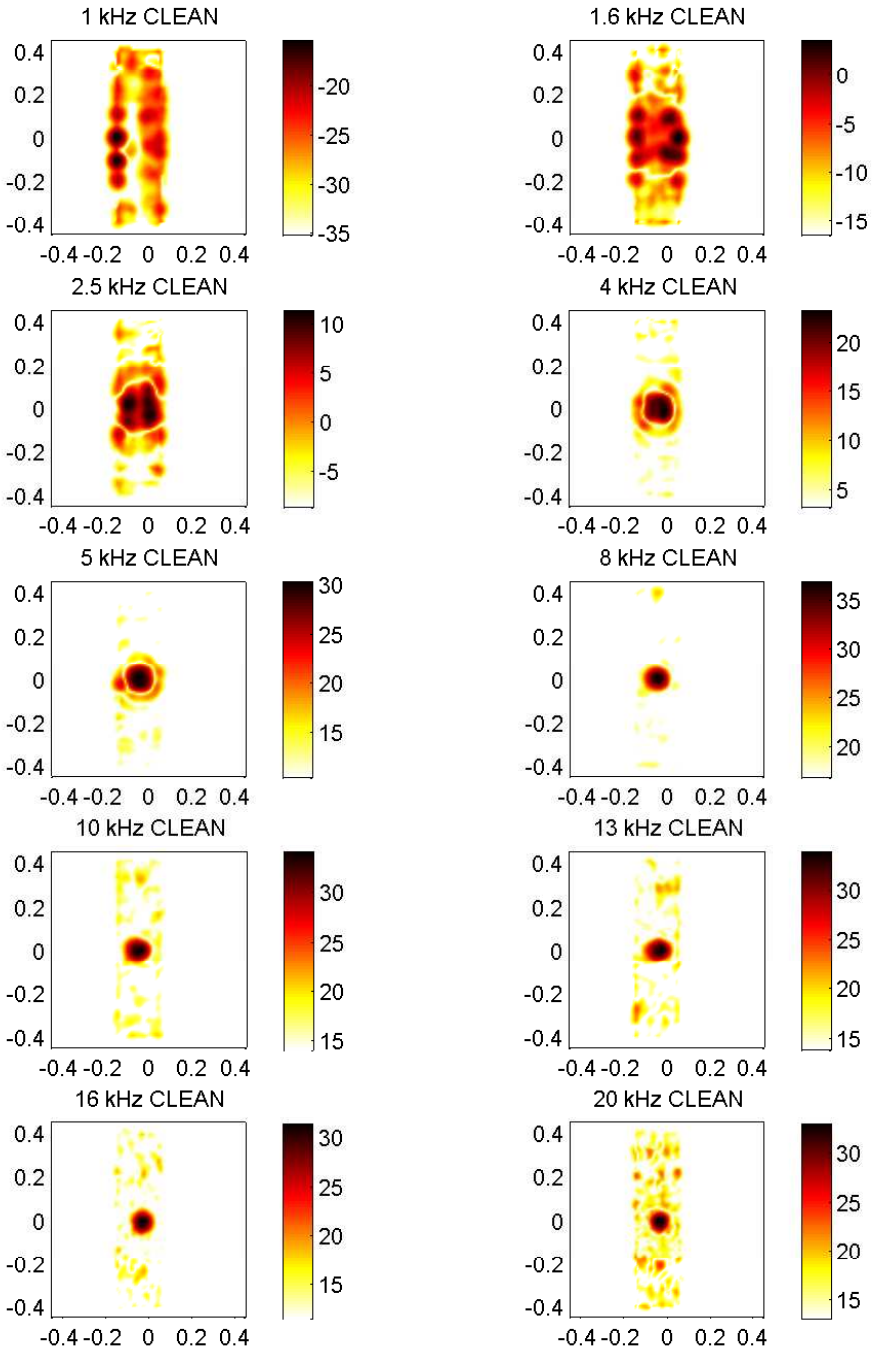

FIGURE C.11: Beamforming maps of the calibration source deconvolved with CLEAN, using Green's functions estimates from measured impulse responses.

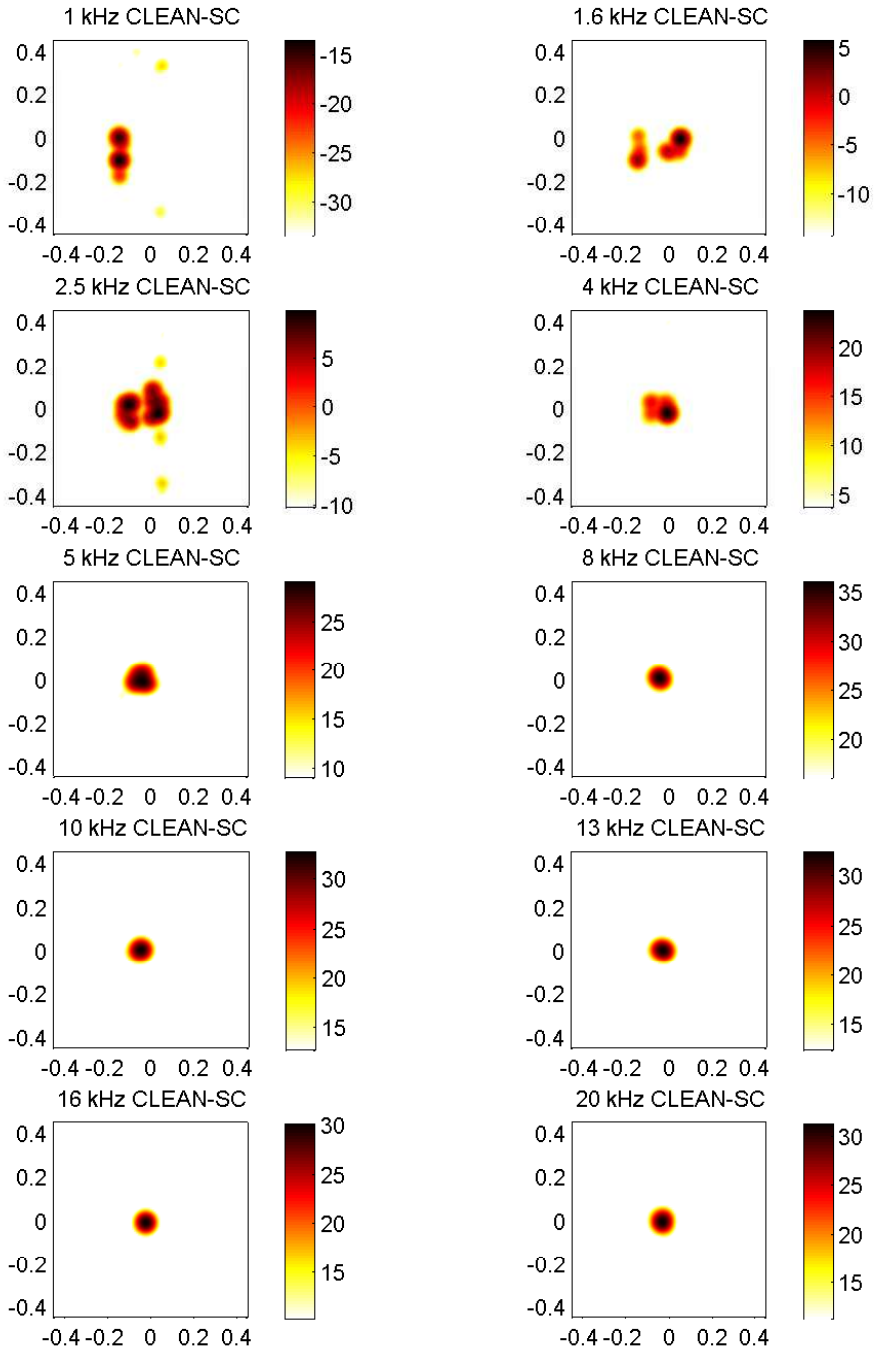

FIGURE C.12: Beamforming maps of the calibration source deconvolved with CLEAN-SC, using Green's functions estimates from measured impulse responses.

Appendix D

Publications

The following conference proceedings were published as part of the work contained in this thesis.

Fenech, B. and Takeda, K. (2008) Beamforming accuracy in closed-section wind tunnels. *AIAA*-2008-2908.

Fenech, B. and Takeda, K. (2007) Beamforming in highly reverberant wind tunnels - possibilities and limitations. In, *14th International Congress on Sound and Vibration (ICSV14)*, Cairns, Australia, 9-12 Jul 2007.

Fenech, B. and Takeda, K. (2007) Towards more Accurate Beamforming Levels in Closed-Section Wind Tunnels via De-Reverberation. *AIAA*-2007-3431.

Smith, M., Fenech B., Chow L., Molin N., Dobrzynski W. and Seror, C. (2006) Control of Noise Sources on Aircraft Landing Gear Bogies. *AIAA*-2006-2626, 2006.

References

[1] F.R. Grosche, H. Stiewitt, and B. Binder. Acoustic wind-tunnel measurements with a highly directional microphone. *AIAA Journal*, 15(11):1590–1596, 1977.

[2] W. Dobrzynski, L. C. Chow, P. Guion, and D. Shiells. A European study on landing gear airframe noise sources. *AIAA*, 2000-1971, 2000.

[3] D. H. Johnson and D. E. Dudgeon. *Array Signal Processing: Concepts and Techniques*. P T R Prentice Hall, 1993.

[4] W. Humphreys Jr., T. F. Brooks, W. W. Hunter Jr., and K. R. Meadows. Design and use of microphone directional arrays for aeroacoustic measurements. *AIAA*, 98-0471, 1998.

[5] M. Mosher, M. E. Watts, M. Barnes, and J. Bardina. Microphone array phased processing system (MAPPS): Phased array system for acoustic measurements in a wind tunnel. *SAE AIAA*, 1999-01-5576, 1999.

[6] S. Oerlemans and P. Sijtsma. Acoustic array measurements of a 1:10.6 scaled Airbus A340 model. *AIAA*, 2004-2924, 2004.

[7] P.T. Soderman, F. Kafyeke, N. J. Burnside, R. Chandrasekharan, S. M. Jaeger, and J. Boudreau. Airframe noise study of a CRJ-700 aircarft model in the NASA Ames 7- by 10- foot wind tunnel no. 1. *AIAA*, 2002-2406, 2002.

[8] M.G.Smith, B. Fenech, L.C. Chow, N. Molin, W. Dobrzynski, and C. Seror. Control of noise sources on aircraft landing gear bogies. *AIAA*, 2006-2626, 2006.

[9] A.R. Quayle, A.P. Dowling, H. Babinsky, W.R. Graham, H. Shin, and P. Sijtsma. Landing gear for a silent aircraft. *AIAA*, 2007-231, 2007.

[10] G. Wicken and N. Lindener. The Audi aeroacoustic wind tunnel: Final design and first operational experience. *SAE*, 2000-01-0868, 2000.

[11] K. Ehrenfried and L. Koop. Comparison of iterative deconvolution algorithms for the mapping of acoustic sources. *AIAA Journal*, 45(7):1584–1595, 2007.

[12] P. Sijtsma. CLEAN based on spatial source coherence. *International Journal of Aeroacoustics*, 6(4):357–374, 2007.

[13] L. Koop and K. Ehrenfried. Microphone-array processing for wind-tunnel measurements with strong background noise. *AIAA*, 2008-2907, 2008.

[14] C. Brauer S. Guidati and S. Wagner. The reflection canceller – phased array measurements in a reverberating environment. *AIAA*, 2002-2462, 2002.

[15] P. Sijtsma and H. Holthusen. Corrections for mirror sources in phased array processing techniques. *AIAA*, 2003-3196, 2003.

[16] F. Fahy and J. Walker, editors. *Advanced Applications in Acoustics, Noise and Vibration*, chapter 3. Source identification and location by P. A. Nelson, pages pp.100–153. Spon Press, 2004.

[17] JF Piet and G. Elias. Airframe noise source localization using a microphone array. *AIAA*, 97-1643-CP, 1997.

[18] P. Sijtsma. Experimental techniques for identification and characterisation of noise sources. In J. Anthoine and A. Hirschberg, editors, *VKI Lecture Series 2004-05*, Advances in Aeroacoustics and Applications, March 2004.

[19] T. J. Mueller, editor. *Aeroacoustic Measurements*. Springer, 2002.

[20] T. F. Brooks and W. M. Humphreys Jr. Flap-edge aeroacoustic measurements and predictions. *Journal of Sound and Vibration*, 261:31–74, 2003.

[21] T. F. Brooks and W. M. Humphreys Jr. Effect of directional array size on the measurement of airframe noise components. *AIAA*, 99-1958, 1999.

[22] W. K. Blake. *Mechanics of Flow-Induced Sound and Vibration, Volume II: Complex Flow-Structure Interactions*. Academic Press, 1986.

[23] S.M. Jaeger, W.C. Horne, and C.S. Allen. Effect of surface treatment on array microphone self-noise. *AIAA*, 2000-1937, 2000.

[24] N. J. Burnside, S. M. Jaeger, and B. R. Reinero. Array design and performance for a large scale airframe noise study. *AIAA*, 2002-2576, 2002.

[25] D. F. Long. Acoustic source location in wind tunnel tests via subspace BF. *AIAA*, 2003-0369, 2003.

[26] J.A. Högbom. Aperture synthesis with a non-regular distribution of interferometer baselines. *Astronomy and Astrophysics Supplement*, 15:417–426, 1974.

[27] T. F. Brooks and W. M. Humphreys Jr. A deconvolution approach for the mapping of acoustic sources (DAMAS) determined from phased microphone arrays. *AIAA*, 2004-2954, 2004.

[28] T. F. Brooks and W. M. Humphreys Jr. Three-dimensional application of DAMAS methodology for aeroacoustic noise source definition. *AIAA*, 2005-2960, 2005.

[29] R. P. Dougherty. Extensions of DAMAS and benefits and limitations of deconvolution in beamforming. *AIAA*, 2005-2961, 2005.

[30] S. Oerlemans and P. Sijtsma. Determination of absolute levels from phased array measurements using spatial source coherence. *AIAA*, 2002-2464, 2002.

[31] KR Holland and PA Nelson. Sound source characterisation: The focussed beamformer vs the inverse method. In *Tenth International Congress on Sound and Vibration*, July 2003.

[32] PA Nelson and SH Yoon. Estimation of acoustic source strength by inverse methods: Part I, conditioning of the inverse problem. *Journal of Sound and Vibration*, 233(4):643–668, 2000.

[33] E. W. Weisstein. *Frobenius Norm*. From MathWorld–A Wolfram Web Resource, `http://mathworld.wolfram.com/FrobeniusNorm.html`, Last accessed 28 July 2005.

[34] S. Patrick Grace, H. M. Atassi, and W. K. Blake. Inverse aeroacoustic problem for a streamlined body. Part 2: accuracy of solutions. *AIAA Journal*, 34(11):2241–2246, November 1996.

[35] KR Holland and PA Nelson. Minimising the number of microphones required for characterisation of distributed source regions. In *Thirteenth International Congress on Sound and Vibration*, July 2006.

[36] T. Suzuki. Generalised inverse beam-forming algorithm resolving coherent / incoherent, distributed and multipole sources. *AIAA*, 2008-2954, 2008.

[37] A. D. Pierce. *Acoustics - An Introduction to Its Physical Principles and Applications*. Acoustical Society of America, 1994.

[38] C.H. Jeong, J.G. Ih, and J.H. Rindel. An approximate treatment of reflection coefficient in the phased beam tracing method for the simulation of enclosed sound fields at medium frequencies. *Applied Acoustics*, 69(7):601–613, 2008.

[39] KR Holland. Personal communication, April 2009.

[40] D.D. Rife and J. Vanderkooy. Transfer-function measurement with maximum-length sequences. *Journal of the Audio Engineering Society*, 37(6):419–444, 1989.

[41] R. Singh and T. Katra. Development of an impulse technique for measurement of muffler characteristics. *Journal of Sound and Vibration*, 56(2):279 – 298, 1978.

[42] M. Salikuddin, P.D. Dean, H.E. Plumblee Jr., and K.K. Ahuja. An impulse test technique with application to acoustic measurements. *Journal of Sound and Vibration*, 70(4):487–501, 1980.

[43] M. Salikuddin, R.H. Burrin, and K.K. Ahuja. Development of an impulsive noise source to study the acoustic reflection characteristics of hard-walled wind tunnels. *AIAA*, 1986-1887, 1986.

[44] M. Arana, A. Vela, and L. San Martin. Calculating the impulse response in rooms using pseudo-impulsive acoustic sources. *Acta Acustica United with Acustica*, 89:377–380, 2003.

[45] P. Roux and M. Fink. Green's function estimation using secondary sources in a shallow water environment. *Journal of the Acoustical Society of America*, 113(3):1406–1416, 2003.

[46] M. J. Crocker. *Handbook of Acoustics*. Wiley-IEEE, 1998.

[47] ISVR Consulting. *Omni-directional Sound Sources*. World Wide Web, `http://www.isvr.co.uk/adau/adausourc.htm`, Last accessed 26 June 2006.

[48] H. Levine and J. Schwinger. On the radiation of sound from an unflanged circular pipe. *Physics Review*, 73(4):383–406, February 1948.

[49] K. Boorsma and X. Zhang. Perforated fairings for bluff body noise control. *AIAA*, 2007-3462, 2007.

[50] G. Marsaglia and A. Zaman. A new class of random number generators. *Annals of Applied Probability*, 3:462–480, 1991.

[51] P. Sijtsma. Personal communication, April 2009.

[52] B. Fenech and K. Takeda. Sound power and directivity pattern of microphone array calibration source KA558. Technical Report AFM 08/XX, SES, University of Southampton, 2008.

[53] G. Ashcroft and X. Zhang. Vortical structures over rectangular cavities at low speed. *Physics of Fluids*, 17(1), 2005.

[54] T. J. Mueller, editor. *Aeroacoustic Measurements*, chapter 3. Aeroacoustic Phased Array Testing in Low Speed Wind Tunnels by James R. Underbrink. Springer, 2002.

[55] Industrial aeroacoustic test. Unpublished, 2008.

[56] M. Mosher, M. E. Watts, S. Jovic, and S. M. Jaeger. Calibration of microphone arrays for phased array processing. *AIAA*, 97-1678-CP, 1997.

[57] W. M. Humphreys Jr., C. H. Gerhold, A. J. Zuckerwar, G. C. Herring, and S. M. Bartram. Performance analysis of a cost-effective electret condenser microphone directional array. *AIAA*, 2003-3195, 2003.

[58] D. P. Arnold, T. Nishida, L. N. Cattafesta III, and M. Sheplak. MEMS-based acoustic array technology. *AIAA*, 2002-0253, 2002.

[59] S. Chowhury, M. Ahmadi, G. A. Jullien, and W. C. Miller. A surface mountable MEMS beamforming microphone array and associated MEMS socket structure. In *Symposium on Microelectronics Research & Development in Canada*, 2001.

[60] J. P. King and J. R. Underbrink. Characterization of a microelectromechanical systems (MEMS) microphone. *AIAA*, 2008-2912, 2008.

[61] B. Fenech and K. Takeda. Frequency response analysis of microphone preamplifiers in the audible and ultrasonic regime. Technical Report AFM 07/02, SES, University of Southampton, 2007.

[62] G. Elias. Source localization with a two-dimensional focused array: Optimal signal processing for a cross-shaped array. In *Inter-Noise 95*, 1995.

[63] C. Karatsovis. Measurement results of acoustic liner. E-mail correspondence, 2nd June, 2005.

[64] B. Fenech and K. Takeda. SotonArray — Southampton University wind tunnel microphone array system guide. Technical Report AFM 07/03, SES, University of Southampton, 2007.

[65] B. Backus. *Study reveals noisy Christmas toys can damage hearing.* Deafness Research UK, `http://www.deafnessresearch.org.uk`, Last accessed 16 March 2008.